STUDIA UNIVERSITATIS
BABEŞ-BOLYAI

CHEMIA

3/2019

STUDIA UNIVERSITATIS BABEȘ-BOLYAI
CHEMIA

3/2019

EDITORIAL BOARD OF
STUDIA UNIVERSITATIS BABEŞ-BOLYAI CHEMIA

ONORARY EDITOR:

IONEL HAIDUC – Member of the Romanian Academy

EDITOR-IN-CHIEF:

LUMINIŢA SILAGHI-DUMITRESCU

EXECUTIVE EDITOR:

CASTELIA CRISTEA

EDITORIAL BOARD:

PAUL ŞERBAN AGACHI, Babeș-Bolyai University, Cluj-Napoca, Romania
LIVAIN BREAU, UQAM University of Quebec, Montreal, Canada
HANS JOACHIM BREUNIG, Institute of Inorganic and Physical Chemistry, University of Bremen, Bremen, Germany
JEAN ESCUDIE, HFA, Paul Sabatier University, Toulouse, France
ION GROSU, Babeș-Bolyai University, Cluj-Napoca, Romania
EVAMARIE HEY-HAWKINS, University of Leipzig, Leipzig, Germany
FLORIN DAN IRIMIE, Babeș-Bolyai University, Cluj-Napoca, Romania
FERENC KILAR, University of Pecs, Pecs, Hungary
BRUCE KING, University of Georgia, Athens, Georgia, USA
ANTONIO LAGUNA, Department of Inorganic Chemistry, ICMA, University of Zaragoza, Zaragoza, Spain
JURGEN LIEBSCHER, Humboldt University, Berlin, Germany
KIERAN MOLLOY, University of Bath, Bath, UK
IONEL CĂTĂLIN POPESCU, Babeș-Bolyai University, Cluj-Napoca, Romania
CRISTIAN SILVESTRU, Babeș-Bolyai University, Cluj-Napoca, Romania

http://chem.ubbcluj.ro/~studiachemia/;
studiachemia@chem.ubbcluj.ro
http://www.studia.ubbcluj.ro/serii/chemia/index_en.html

YEAR **Volume 64 (LXIV) 2019**
MONTH **SEPTEMBER**
ISSUE **3**

S T U D I A
UNIVERSITATIS BABEŞ–BOLYAI
CHEMIA

3

ISSUE DOI:10.24193/subbchem.2019.3

STUDIA UBB EDITORIAL OFFICE: B.P. Hasdeu no. 51, 400371 Cluj-Napoca, Romania, Phone + 40 264 405352

CUPRINS – CONTENT – SOMMAIRE – INHALT

Studia Universitatis Babes-Bolyai Chemia has been selected for coverage in Thomson Reuters products and custom information services. Beginning with V. 53 (1) 2008, this publication is indexed and abstracted in the following:

- Science Citation Index Expanded (also known as SciSearch®)
- Chemistry Citation Index®
- Journal Citation Reports/Science Edition

STUDIA UBB CHEMIA, LXIV, 3, 2019 (p. i-iv)
(RECOMMENDED CITATION)

CHEMIA NAPOCENSIS 1919-2019

Centenarul universității clujene ne oferă prilejul unei retrospective care să reflecte începuturile, dezvoltarea și contribuțiile școlii clujene de chimie in cercetarea științifică românească și prezența sa în știința chimică internațională. Trebuie să spunem de la început că acestea nu sunt neglijabile, deși multă vreme condițiile nu au fost comparabile cu cele din țările mai avansate.

În chimia clujeană s-au perindat mai multe generații, care dincolo de pregătirea de specialitate a studenților au adus fiecare ceva nou în preocupările științifice, în pas cu dezvoltarea chimiei și apariția unor noi domenii.

Încă de la începuturile sale, imediat după înființarea universității românești de la Cluj, chimia – încadrată în Facultatea de Științe, s-a manifestat și în cercetarea științifică, datorită profesorilor *întemeietori* care nu s-au mulțumit cu o activitate didactică remarcabilă, ci au introdus și spiritul științific în activitatea noii instituții. Aceștia sunt profesorii Adriano OSTROGOVICH (chimie organică), Dan RADULESCU (chimie organică, chimie fizică) și Gheorghe SPACU (chimie anorganică).

Activitatea profesorilor întemeietori s-a manifestat în perioada antebelică și a fost urmată de o generație de *continuatori*, care –formați înainte - au dus chimia clujeană și în perioada postbelică, în cadrul Facultății de Chimie. Aici se remarcă profesorii Raluca RIPAN (chimie anorganică), Ion TĂNĂSESCU (chimie organică), Candin LITEANU (chimie analitică), Ion CĂDARIU (chimie fizică), Gheorghe Constantin MACAROVICI (chimie generală). Activitatea acestor profesori a continuat până în deceniile 5-6.

O nouă generație cuprinde profesorii Emil CHIFU (chimie fizică), Gheorghe MARCU (chimie anorganică), Alexandru SILBERG, Maria IONESCU, Valer FĂRCĂŞAN, Nicolae ALMASI, Sorin MAGER (chimie organică), Ladislau KEKEDY (chimie analitică). A urmat o noua generație, cu profesorii Liviu ONICIU, Gheorghe NIAC, Janos ZSAKO, Ioan BÂLDEA (chimie fizică), Judith MUREŞAN (chimie macromoleculară). Crearea secției de inginerie chimică, datorată profesorului Liviu LITERAT, a adăugat o nouă dimensiune facultății.

Generația ultimă, contemporană, care și-a încheiat recent activitatea sau este în pragul pensionării, cuprinde – printre alții – profesorii Cătălin POPESCU, Maria TOMOAIA-COTIŞEL, Ossi HOROVITZ, Liana Maria MUREŞAN (chimie fizică),

Ioan SILBERG, Ion GROSU, Luminița SILAGHI-DUMITRESCU, Ioan CRISTEA, Mircea V. DIUDEA, Ioan OPREAN, Mircea VLASSA, Mircea DĂRĂBANŢU (chimie organică), Ionel HAIDUC, Cristian SILVESTRU, Stanislav COSTA, Mariana RUSU, Rodica MICU-SEMENIUC, Maria CURTUI, Letiția GHIZDAVU, Adrian PĂTRUŢ (chimie anorganică, organometalică și supramoleculară), Ioan SILAGHI-DUMITRESCU (chimie computațională), Costel SÂRBU, Emil CORDOS, Simion GOCAN, Teodor HODISAN, Iovanca HAIDUC (chimie analitică), Şerban AGACHI, Petru ILEA, Ioan BÂTIU, Eugenia GAVRILĂ (inginerie chimică), Florin Dan IRIMIE (biocataliză și inginerie biochimică).

Contribuțiile școlii clujene de chimie au fost recunoscute în țară prin alegerea unor profesori ca membri ai Academiei Române: profesorii Gheorghe SPACU, Raluca RIPAN (prima femeie academician), Ion TĂNĂSESCU, Gheorghe Constantin MACAROVICI, Ionel HAIDUC, Ioan SILBERG, Ioan SILAGHI-DUMITRESCU, Cristian SILVESTRU, Ion GROSU.

Generația contemporană de tineri conferențiari, ale căror nume nu le citățm deocamdată, își așteaptă rândul și promite continuarea la același nivel a cercetării științifice din Facultatea de Chimie și Inginerie Chimică.

Este dificil de prezentat într-un spațiu redus, domeniile abordate de-a lungul unui secol în cercetarea științifică clujeană în domeniul chimiei, preocupările și rezultatele, poate uneori performanțele mai deosebite. Încă de la începuturi, chimiștii clujeni au publicat nu numai în revistele naționale (se remarcă la început *Buletinul Societății de Ştiințe din Cluj*, apoi *Revue Roumaine de Chimie*, *Studia Universitatis Babeș-Bolyai-Chemia*, *Revista de Chimie*), ci au fost prezenți și în revistele internaționale. Mai ales în ultimii 30 ani, dar și înainte, nume ale chimiștilor universității clujene pot fi întâlnite în cele mai prestigioase reviste internaționale și uneori, ca autori, chiar pe coperțile unor cărți publicate în străinătate. Un rol însemnat au avut colaborările internaționale, desfășurate timp de mai mulți ani. Îmbunătățirea continuă a dotărilor facultății (de exemplu cu aparatură avansată de spectrometrie, cromatografie, spectroscopie și difractometrie de raze X) au facilitat cercetări independente, la nivel comparabil cu cel din universitățile europene.

Cercetările abordate în Facultatea de Chimie și Inginerie Chimică, cu contribuții recunoscute, se referă la sinteza organică (heterocicluri, sinteza *Tănăsescu*, substanțe biologic active), combinații coordinative (reactivul *Spacu*), polioxometalați, compuși organometalici, chimie supramoleculară, cicluri anorganice, biocataliză și tehnologii biochimice, radiochimie, chimie coloidală și chimia suprafețelor, electrochimie, cinetică chimică, chimie teoretică și computațională, analiza chimică, instrumentație, tehnologii de captare si stocare a carbonului, modelarea, simularea, intensificarea, automatizarea și optimizarea proceselor chimice si biochimice etc.

La împlinirea unui secol de activitate didactică și științifică, Facultatea de Chimie și Inginerie Chimică privește cu satisfacție în trecut și cu optimism în viitor.

REDACŢIA
Studia UBB Chemia

CHEMIA NAPOCENSIS 1919-2019

The centenary of the University of Cluj gives us the opportunity for a retrospective reflecting on the beginnings, development and contributions of the Cluj School of Chemistry to the Romanian scientific research and its presence in the international chemical science. We must say from the beginning that the outcomes are not negligible, although for a long time the conditions were not comparable to those in more advanced countries.

Several generations have succeeded in the Cluj School of Chemistry, each bringing beyond the specialized training of the students something new in scientific preoccupations, in accordance with the development of chemistry and the emergence of new fields.

Since its foundation, immediately after the establishment of the Romanian University in Cluj, the chemistry - enrolled in the Faculty of Sciences, has also became noticeable in scientific research, thanks to the founding teachers who were not satisfied with a remarkable didactic activity, but also lighted the scientific spirit in the activity of the new institution. These were professors Adriano OSTROGOVICH (organic chemistry), Dan RĂDULESCU (organic chemistry, physical chemistry) and Gheorghe SPACU (inorganic chemistry).

The activity of the founding academic teachers was carried out in the pre-war period and it was followed by a generation of continuators, who carried on the advance of Cluj School of Chemistry during the post-war period, within the Faculty of Chemistry. The professors Raluca RIPAN (inorganic chemistry), Ion TĂNĂSESCU (organic chemistry), Candin LITEANU (analytical chemistry), Ion CĂDARIU (physical chemistry), Gheorghe Constantin MACAROVICI (general chemistry) are to be noted here and their activity which continued until decades 5-6.

A new generation included professors Emil CHIFU (physical chemistry), Gheorghe MARCU (inorganic chemistry), Alexandru SILBERG, Maria IONESCU, Valer FĂRCĂŞAN, Nicolae ALMASI, Sorin MAGER (organic chemistry), Ladislau KEKEDY (analytical chemistry), followed by the generation of professors Liviu ONICIU, Gheorghe NIAC, Janos ZSAKO, Ioan BÂLDEA (physical chemistry), Judith MUREȘAN (macromolecular chemistry). The opening of the chemical engineering specialization, owed to the efforts of Professor Liviu LITERAT, added a new dimension to the faculty.

The latest, contemporary generation, which has recently completed its activity, or is about to retire, includes – among others – professors Cătălin POPESCU, Maria TOMOAIA-COTIŞEL, Ossi HOROVITZ, Liana Maria MUREŞAN (physical chemistry),

Ioan SILBERG, Ion GROSU, Luminița SILAGHI-DUMITRESCU, Ioan CRISTEA, Mircea V. DIUDEA, Ioan OPREAN, Mircea VLASSA, Mircea DĂRĂBANŢU (organic chemistry), Ionel HAIDUC, Cristian SILVESTRU, Stanislav COSTA, Mariana RUSU, Rodica MICU-SEMENIUC, Maria CURTUI, Letiția GHIZDAVU, Adrian PĂTRUŢ (inorganic, organometallic and supramolecular chemistry), Ioan SILAGHI-DUMITRESCU (computational chemistry), Costel SÂRBU, Emil CORDOS, Simion GOCAN, Teodor HODISAN, Iovanca HAIDUC (analytical chemistry), Șerban AGACHI, Petru ILEA, Ioan BÂTIU, Eugenia GAVRILĂ (chemical engineering), Florin Dan IRIMIE (biocatalysis and biochemical engineering).

The contributions of the Cluj School of Chemistry were recognized in the country by the election as members of the Romanian Academy of professors: Gheorghe SPACU, Raluca RIPAN (first woman academician), Ion TĂNĂSESCU, Gheorghe Constantin MACAROVICI, Ionel HAIDUC, Ioan SILBERG, Ioan SILAGHI-DUMITRESCU, Cristian SILVESTRU and Ion GROSU.

The contemporary generation of young lecturers from the Faculty of Chemistry and Chemical Engineering, whose names we do not mention at the moment, awaits their turn and promises the continuation of the scientific research at the same level.

It is difficult to outline in a limited space, the domains addressed over a century by scientific research in the field of chemistry, preoccupations and results, sometimes special performances. From the beginning, the chemists from the Cluj Chemistry School have published their scientific outcomes not only in the national journals (first in *Buletinul Societatii de Stiinte Cluj,* followed by *Revue Roumaine de Chimie*, *Studia Universitatis Babeș-Bolyai-Chemia*, *Revista de Chimie-Bucharest*), but they were also contributors with scientific articles published in international scientific journals. Especially in the last 30 years, but also before, the names of the chemists from the University of Cluj can be found in the most prestigious international journals and sometimes, as authors, even on the covers of books published abroad. International collaborations have played a significant role for several years.

The continuous improvement of the equipment achieved at the faculty (for example advanced spectrometry, chromatography, spectroscopy and X-ray diffractometry equipment) facilitated independent research at a level comparable to the one observed in the European universities.

The research areas developed in the Faculty of Chemistry and Chemical Engineering, with recognized contributions, cover organic synthesis (heterocycles, Tănăsescu synthesis, biologically active compounds), coordination compounds (Spacu reagent), polyoxometalates, organometallic compounds, supramolecular chemistry, inorganic chemistry, biocatalysis and biochemical technologies, radiochemistry, surface chemistry, electrochemistry, chemical kinetics, theoretical and computational chemistry, chemical analysis, instrumentation, carbon capture and storage technologies, modelling, simulation, intensification, control and optimization of chemical and biochemical processes, etc.

At the turn of a century of didactic and scientific activity, the Faculty of Chemistry and Chemical Engineering looks with satisfaction at the past and with optimism to the future.

The Editorial Board

STUDIA UBB CHEMIA, LXIV, 3, 2019 (p. 7-16)
(RECOMMENDED CITATION)
DOI:10.24193/subbchem.2019.3.01

CHALCHOGENIDE INDUCED INTRAMOLECULAR INTERACTIONS IN [2.2]PARACYCLOPHANES: A REVIEW

LAURA GABRIELA SARBU[a], LUCIAN GABRIEL BAHRIN[a,b], HENNING HOPF[c], MIHAIL-LUCIAN BIRSA[a,*]

ABSTRACT. The intramolecular interactions in *pseudo-geminally* substituted [2.2] paracyclophanes induced by chalchogenide halides is reviewed. The subtitution reactions with sulfur dichloride and disulfur dichloride and the addition reactions of selenium dihalides and diselenium dichlorides are highlighted.

Keywords: *acetylenes, allenes, [2.2]paracyclophane, propargylic alcohols, selenium halides, sulfur halides*

INTRODUCTION

Cyclophanes are strained organic molecules which contain aromatic ring(s) as well as aliphatic unit(s). The aromatic rings provide rigidity to their structure, whereas the aliphatic unit(s) forms bridge(s) between the aromatic rings and also provides flexibility to the overall structure. [2.2]Paracyclophanes ([2.2]PC) are a class of organic compounds which have drawn attention ever since their first appearance in the literature. The molecules of these compounds are made–up of two benzene rings placed one on top of the other, bound together by ethylene bridges in their *para* positions. The cyclophane chemistry is a fast developing field, as proven by a recent publication by Gleiter and Hopf, which describes the applications of cyclophanes in stereoselective synthesis and the incorporation of cyclophanes in complex molecular structures, like heterocycles and polymers [1]. Initially, [2.2]paracyclophane and its derivatives were studied because of their special geometry, sterical

[a] *Alexandru Ioan Cuza University of Iasi, Department of Chemistry, 11 Carol I Blvd., 700506 Iasi, Romania*
[b] *Petru Poni Institute of Macromolecular Chemistry, Aleea Grigore Ghica Vodă 41A, 700487 Iasi, Romania*
[c] *Technical University of Braunschweig, Institute of Organic Chemistry, Hagenring 30, D-38106 Braunschweig, Germany*
** Corresponding author: lbirsa@uaic.ro*

properties, transannular interactions and cycle tension [2]. Because of the rigid molecular frame, recent research suggests using the electronical properties of these compounds in the synthesis of polymers and charge-transfer complexes [3]. A number of cyclophanes have been designed and developed over the years for the selective recognition of various guest biomolecules [4]. Functional groups in *pseudo-geminally* substituted [2.2]paracyclophanes often undergo highly specific reactions. This is due to the rigid framework and the short distance between the two aromatic rings within the [2.2]paracyclophane unit. Thus, unsaturated cyclophane bis(esters) undergo intramolecular photocyclization, yielding the corresponding ladderane isomers [5-7].

The interaction of *pseudo-geminal* bis(propargylic)[2.2]PC alcohols with chalcogenide halides

Using *pseudo-geminally* substituted [2.2]paracyclophanes as spacers for bis(allenic) moieties, interesting starting materials for intra- or intermolecular reactions can be realized. An accessible entry to allenic systems consists of the [2,3]sigmatropic rearrangement of propargylic sulfenates to allenic sulfoxides. This reaction, which takes place spontaneously at low temperature, has been applied extensively in organic synthesis [8,9]. In order to follow this reaction type, the first step was to prepare *pseudo-geminal* bis(propargylic) alcohols **2a**–**c** (Scheme 1) by the reaction of the corresponding lithium acetylide with 4,15-diformyl[2.2]paracyclophane (**1**) [10]. To avoid side reactions the best results were obtained by adding **1** to the acetylenic salt solution, at –35 °C to –40 °C [11].

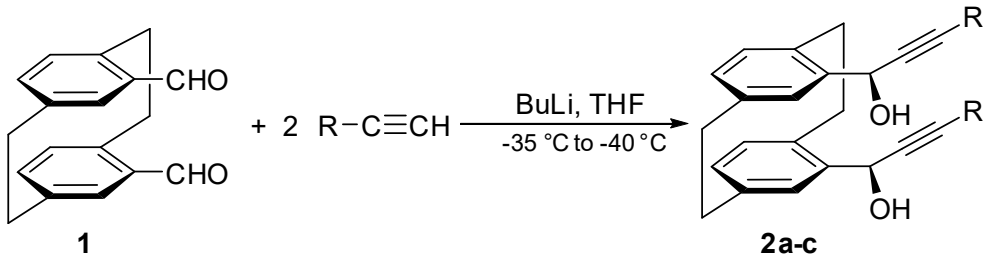

1 **2a-c**

2a R = *n*-Pr, 89%; **2b** R = *n*-Bu, 86%; **2c** R = Ph, 85%

Scheme 1. Synthesis of *pseudo-geminal* bis(propargylic) alcohols **2a-c**

The next step in the synthesis of *pseudo-geminal* bis(allenic) sulfoxides was to react the bis(propargylic) alcohols of type **2** with the most stable sulfenylchloride, perchloromethylmercaptane (PCMM). As expected, the double [2,3]sigmatropic rearrangement of the initially produced *pseudo-geminal* bis(propargylic)

trichloromethylsulfenates takes place spontaneously at low temperature affording the desired *pseudo-geminal* bis(allenyl) trichloromethylsulfoxides **3a**,**b** in good yields (Scheme 2) [11]. Both bis(allenyl) sulfoxides have been obtained as a mixture of four inseparable diastereoisomers. By using dimethyldioxirane (DMDO), a particularly mild oxidizing agent for our substrates, we obtained the desired *pseudo-geminal* bis(allenyl) sulfones **4a**,**b** as single isomers in moderate yields (Scheme 2).

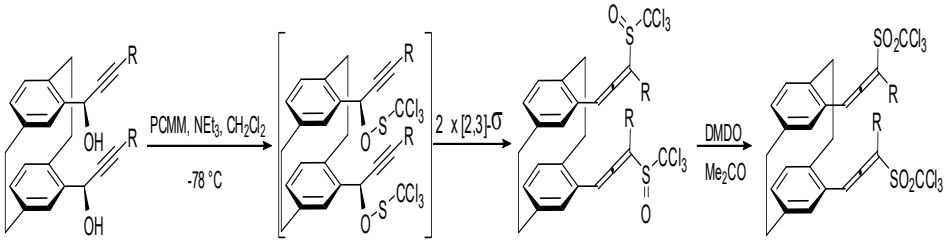

Scheme 2. Synthesis of *pseudo-geminal* bis(allenyl) sulfones **4**

Although the *pseudo-geminally* substituted [2.2]paracyclophane core holds the allenic moieties in favorable positions for further intramolecular interactions, none of these have been observed under various conditions. The lack of reactivity of these unsaturated systems could be due to both electronic and steric effects of the trichloromethyl sulfoxide or sulfone substituents, respectively.

Further investigations involved the replacement of the trichloromethyl group with a nitrophenyl substituent [12]. This was accomplished by the reaction of bis(propargylic) alcohols **2a,d** with *o*-nitrobenzenesulfenyl chloride *via* a double [2,3]sigmatropic rearrangement of the corresponding sulfenyl esters (Scheme 3) [8,9].

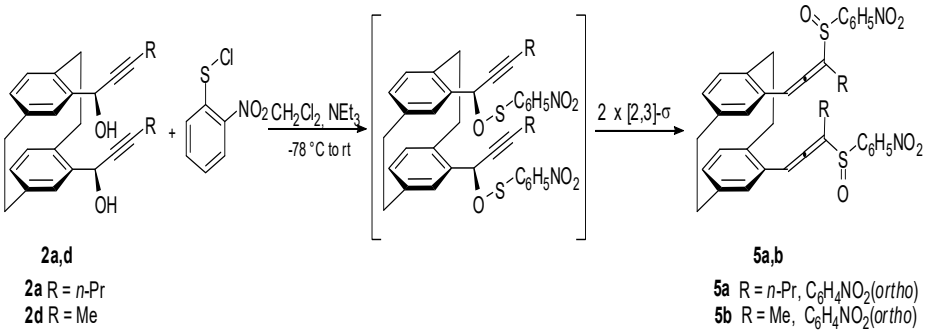

Scheme 3. Synthesis of *pseudo-geminal* bis(allenyl) nitrophenylsulfoxides **5**

A solution of **5** was then gently heated at 40 °C and after purification and separation of the crude mixture, two major compounds were isolated, an *α,β*-unsaturated ketone **6** and bis(*o*-nitrophenyl) disulfide **7** (Scheme 4) [12].

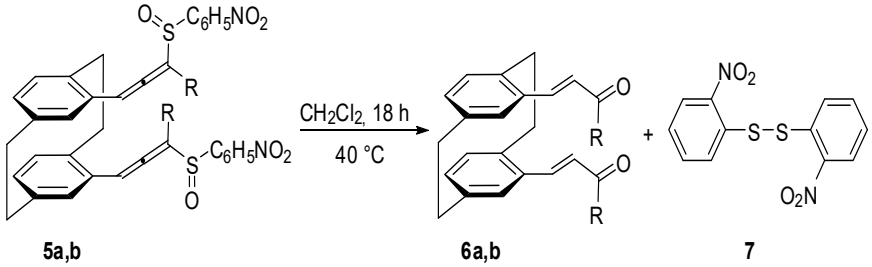

5a,b **6a,b** **7**

5a R = *n*-Pr, $C_6H_4NO_2$(*ortho*)
5b R = Me, $C_6H_4NO_2$(*ortho*)

6a R = *n*-Pr
6b R = Me

Scheme 4. Intramolecular interactions in *pseudo-geminal* bis(allenyl) nitrophenylsulfoxides

A survey of literature data on *ortho*-substituted phenyl sulfoxides revealed that mono-*ortho*-substitution prevents free rotation of the -S(O)R group. Consequently, it is reasonable to assume that the formation of *α,β*-unsaturated ketone is initiated by an interaction between the electron pairs of the sulfur and nitrogen atom, respectively, making the system flat and inducing a high rotational barrier around the S-C*ar* bond [13]. Thus, the conversion of **5a,b** to **6a,b** has involved the formation of a diradical intermediate of type **8** which then undergoes a dyotropic rearrangement as presented in Scheme 5 [14,15].

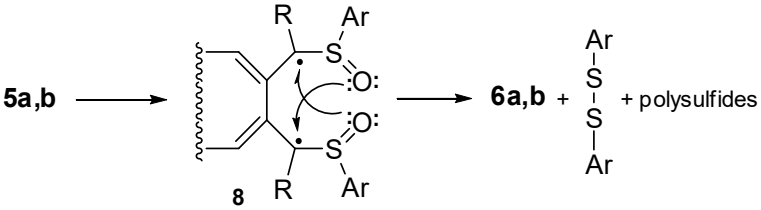

Scheme 5. The mechanism for the synthesis of bis(*α,β*-unsaturated) ketones **6**

Using the same type of substrate, the reactivity of the disulfur dichloride and sulfur dichloride towards *pseudo-geminally* substituted propargylic alcohols has been investigated. Thus, the reactions of *pseudo-geminal* bispropargylic alcohols **2c,d** with disulfur dichloride have been performed under high dilution conditions in the presence of triethylamine at -78 °C (Scheme 6) [16].

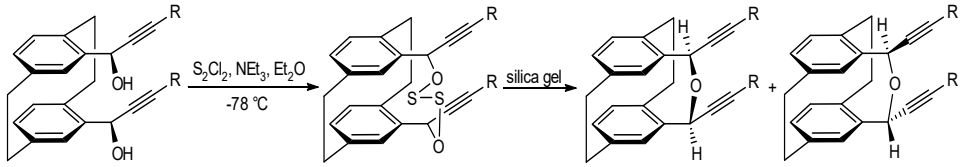

2c,d | **9a,b** | *meso*-**10a,b** | *dl*-**11a,b**

2c R = Ph
2d R = Me

9a R = Ph
9b R = Me

10a R = Ph
10b R = Me

11a R = Ph
11b R = Me

Scheme 6. Reaction of bis(propargylic) alcohols with disulfur dichloride

Purification of compounds **9** on silica gel, that provides mild acidic conditions, was always accompanied by sulfur extrusion, most likely as polysulfides, and by the formation of cyclic ethers **10** and **11**. The formation of cyclic ether from bispropargylic alcohols has also been observed by reacting the latter with pyridinium chloride [17]. The acid catalyzed rearrangement of dipropargyloxy disulfide **9** to the corresponding cyclic ethers appears to be kinetically favored, unlike the double sigmatropic rearrangement to the bisallenyl sulfone derivatives.

Using sulfur dichloride, a mixture of cyclic ethers **10** and **11**, and a compound related to disulfide **9** were obtained [16]. The dipropargyloxy sulfides **12** turned out to be more sensitive to acidic conditions provided by silica gel in the work-up process than the corresponding disulfides. This assumption was supported by an unexpected conversion of the crude reaction mixture to a single pinacolone type compound (**13**), process that involves an intramolecular hydride transfer (Scheme 7) [15].

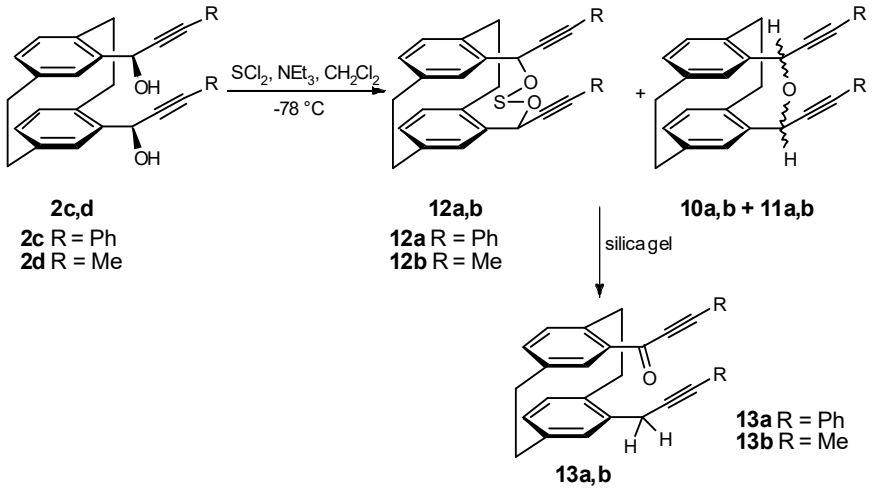

2c,d

2c R = Ph
2d R = Me

12a,b

12a R = Ph
12b R = Me

10a,b + 11a,b

13a R = Ph
13b R = Me

13a,b

Scheme 7. Reaction of bis(propargylic) alcohols with sulfur dichloride

The regio- and stereospecific addition of monoselenium monochloride to *pseudo-geminally* substituted bis(propargylic) alcohols has been performed under high dilution conditions. Along with the expected diselenides **14**, the monoselenides **15** and triselenides **16** were obtained (Scheme 8) [18]. The disproportionation reaction of selenium monochloride to selenium dichloride and triselenium dichloride [19] leads to the corresponding divinylic mono- and triselenides. For the *trans*-formation described in Scheme 8, in all cases *syn*-addition with *anti*-Markovnikov orientation was observed.

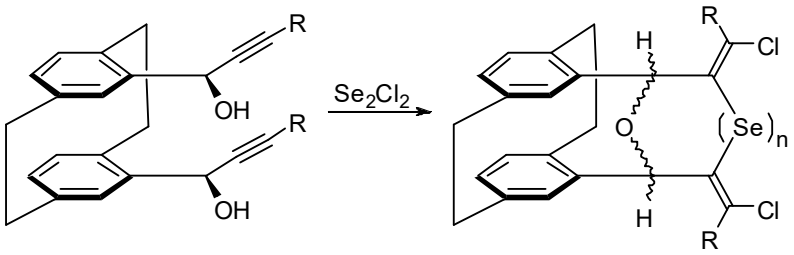

2c,d

2c R = Ph
2d R = Me

14a R = Ph, **14b** R = Me, n=2
15a R = Ph, **15b** R = Me, n=1
16a R = Ph, **16b** R = Me, n=3

Scheme 8. Addition of Se_2Cl_2 to *pseudo-geminally* substituted bis(propargylic) alcohols

The interaction of *pseudo-geminal* bis(ethynyl)[2.2]PC with chalcogenide halides

Following our interest in the introduction of new bridges to [2.2]paracyclophanes, we decided to investigate the reactivity of the chalchogenide halides towards 4,13-bis(ethynyl)[2.2]paracyclophanes. The ethynyl group is well known for its ability to undergo coupling reactions, making the *pseudo-geminal* bis(acetylene) **17** and its derivatives good candidates for building molecular scaffolding [20,21]. Thus, the reaction of *pseudo-geminal* bis(acetylene) **17** with *n*-BuLi in THF followed by treatment with SCl_2 resulted in the formation of thiophene substituted paracyclophane derivative **19** (Scheme 9) [22]. Most likely the cycloaromatization is induced by a nucleophilic attack of a THF-anion on one of the acetylelenic carbon atoms of the unstable intermediate sulfide **18**.

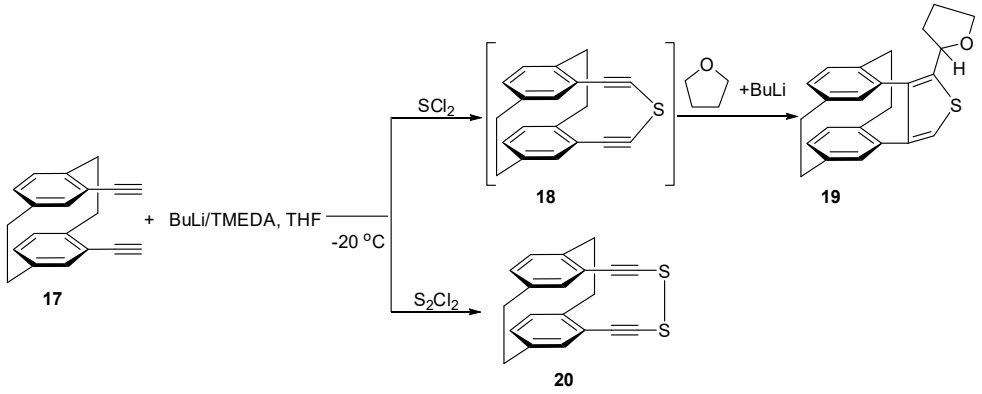

Scheme 9. Addition of SCl_2 and S_2Cl_2 to 4,13-bis(ethynyl)[2.2]paracyclophane

Under the same reaction conditions, the treatment of bis(acetylene) **17** with monosulfur monochloride led to the corresponding disulfide **20**, in 65% isolated yield (Scheme 9) [22]. The stability of this compound could be explained by a less hindered structure than that of the monosulfide **18** and the lack of cycloaromatization.

Other investigations involved the interactions of Se_2Cl_2 with *pseudo-geminal* bis(acetylene) **17**. The addition of electrophilic selenium reagent produced preferably the corresponding *E*-adduct, diselenide **21**, through an *anti*-addition with Markovnikov orientation (Scheme 10) [22].

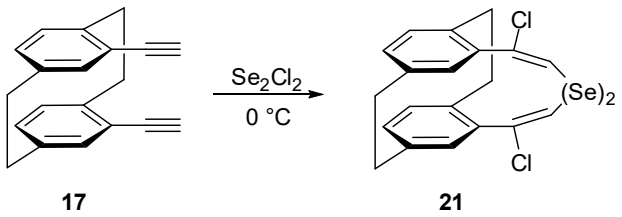

Scheme 10. Addition of diselenium dichloride to 4,13-bis(ethynyl)[2.2]paracyclophane

An addition/elimination sequence of selenium halides to *pseudo-geminally* bis(acetylene) substituted [2.2]paracyclophanes leads to new bridges with an *endo*-*exo*-diene substructure. Despite of the above reaction outcome, the addition of selenium dichloride and selenium dibromide to *pseudo-geminal* bis(ethynyl)[2.2]paracyclophane **17** provided a mixture of [2.3.2](1,2,4)cyclophane derivatives **22, 23, 25, 26** and tetrahaloderivatives **24, 27** (Scheme 11) [23].

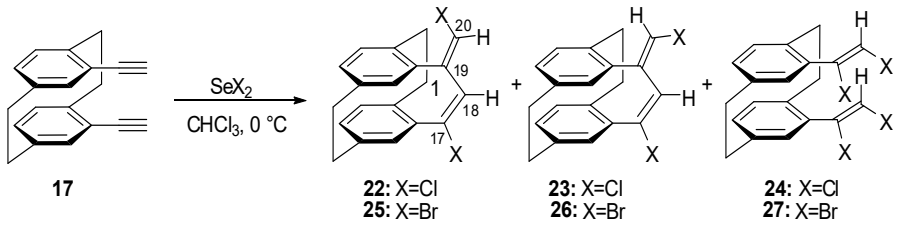

Scheme 11. Reactions of selenium dichloride and selenium dibromide with 4,13-bis(ethynyl)[2.2]paracyclophane

The configuration of compounds **22** and **25** as a (17*E*,19*E*)-diene was established from the mutual NOEs between H18 and H20. The relative *Z* stereochemistry of tetrabromo derivative **27** was unambiguously established by X-ray analysis. The unexpected formation of [2.3.2](1,2,4)cyclophane derivatives **22**, **23** and **25**, **26** prompted the investigation of the addition of phenylselenyl chloride to 4,13-bis(ethynyl)[2.2]paracyclophane. Surprisingly, the addition of 2 eq. of PhSeCl to bis(acetylene) **17** again provided a mixture of dienes **22** and **23** along with diphenyl diselenide. In a first step, the addition of one equivalent of PhSeCl to one of the triple bonds of **17** results in the formation of episelenonium ion **28** (Scheme 12). The episelenonium ion **28** should equilibrate with the ring-opened form, a benzylic type carbocation; the interaction of this intermediate with the opposing ethynyl substituent provides adduct **29**. For steric reasons, the chloride anion attacks from "outside" leading to intermediate **30**. The reaction of **30** with the second equivalent of PhSeCl leads to selenonium ion **31**; once the diphenyl diselenide leaving group is formed, the addition of chloride counter-anion from both directions is accompanied by the formation of [2.3.2](1,2,4)cyclophane derivatives **22** and **23**.

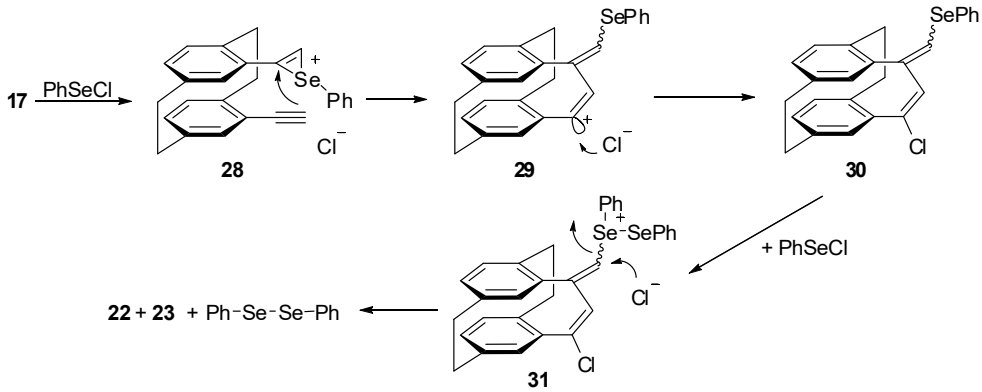

Scheme 12. Addition of phenylselenyl chloride to 4,13-bis(ethynyl)[2.2]paracyclophane

With regard to the addition of selenium dihalides to bis(acetylene) **17**, the reaction mechanism should follow a similar course, consisting of the formation of a selenonium ion of type **30** rather than the addition of the selenium electrophiles to the second triple bond. This involves elimination of diselenium dihalides with the formation of dienes **22**, **23** and **25**, **26**.

These reactions have been found to be sensitive to the substitution of the acetylenic bond. Thus, by reacting bis(acetylene) **32** with 1 eq. of selenium dichloride only the (17*E*,19*E*)-diene **33** and tetrachloride derivative **34** were isolated (Scheme 13) [23]. The lack of isomeric diene (17*E*,19*Z*) could be explained as the result of steric hindrance induced by the presence of methyl groups at the acetylenic carbon atoms. This forces the addition of a chloride anion to a methylated intermediate of type **31** to take place in the way that provides only the thermodynamically stable (17*E*,19*E*)-[2.3.2](1,2,4)cyclophane derivative **33**.

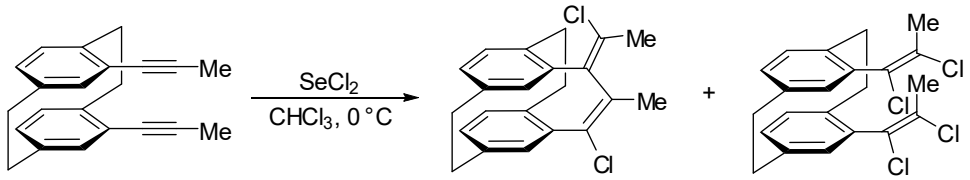

32 **33** **34**

Scheme 13. Reactions of selenium dichloride with 4,13-bis(propyn-1-yl)[2.2]paracyclophane **32**

CONCLUSIONS

The reactions of *pseudo-geminal* bis(ethynyl)[2.2]PC and of *pseudo-geminal* bis(propargylic)[2.2]PC alcohols with chalchogenide halides are presented. The intramolecular interactions generated by these interactions are underlined.

ACKNOWLEDGMENTS

CNCS - UEFISCDI support within PNCDI III is acknowledged by LGS and LGB for project numbers PN-III-PI-I.1-PD-2016-0962 and PN-III-PI-I.1-PD-2016-1117, respectively.

REFERENCES

1. H. Hopf; R. Gleiter; *Modern Cyclophane Chemistry,* Wiley-VCH, Weinheim, **2004**.
2. F. Vögtle; *Cyclophane Chemistry*, Wiley, Chichester, **1993**.
3. K.M. El-Shaieb; A F.E. Mourad; H. Hopf; *Arkivoc*, **2006**, 193-200.
4. S. Bartoli; S. Roelens; *J. Am. Chem. Soc.*, **2002**, *124*, 8307-8315.
5. H. Greiving; H. Hopf; P. G. Jones; P. Bubenitschek; J.-P. Desvergne; H. Bouas-Laurent; *Eur. J. Org. Chem.,* **2005**, 558–566.
6. H. Hopf; H. Greiving; C. Beck; I. Dix; P. G. Jones; J.-P. Desvergne; H. Bouas-Laurent; *Eur. J. Org. Chem.,* **2005**, 567–581.
7. For a review, see: H. Hopf; *Angew. Chem*., **2003**, *115,* 2928-2931; *Angew. Chem. Int. Ed*., **2003**, *42,* 2822–2825.
8. S. Braverman; *The Chemistry of Sulfenic Acids and their Derivatives*; S. Patai; Wiley, New York, **1990**, 311-359.
9. S. Braverman; *The Chemistry of Double-Bonded Functional Groups*, Suppl. A2; S. Patai; Wiley, Chichester, **1989**, 963-1060.
10. H. Hopf; F.-W. Raulfs; D. Schomburg; *Tetrahedron*, **1986**, *42*, 1655-1663.
11. M.L. Birsa; P.G. Jones; S. Braverman; H. Hopf; *Synlett*, **2005**, *4*, 640-642.
12. M.L. Birsa; H. Hopf; *Synlett*, **2007**, *17*, 2753-2755.
13. V. Baliah; A. Ekambaram; *J. Indian Chem. Soc.,* **1991**, *68*, 272-278.
14. For reviews see: (a) V. I. Minkin; L. P. Olekhnovich; Yu. A. Zhdanov; *Molecular Design of Tautomeric Compounds*; D. Reidel Publishing Co.: Dordrecht, **1988**, 221-246. (b) M. T. Reetz; *Adv. Organomet. Chem*., **1977**, *16*, 33-65.
15. K. Mackenzie; G. Proctor; D.J. Woodnutt; *Tetrahedron,* **1987**, *43*, 5981-5993, and references cited therein.
16. A. Birsa; L. Ignat; H. Hopf; M.L. Birsa; *Acta Chem. Iasi*, **2009**, *17*, 187-196.
17. M.L. Birsa; P.G. Jones; H. Hopf; *Eur. J. Org. Chem.*, **2005**, 3263-3270.
18. M.L. Birsa; H. Hopf; *Heteroatom Chem.*, **2010**, *21*, 126-130.
19. M. Lamoureux; J. Milne; *Can. J. Chem*., **1989**, *67*, 1936-1941.
20. L. Bondarenko; I. Dix; H. Hinrich; H. Hopf; *Synthesis,* **2004**, 2751–2759.
21. L. Bondarenko; S. Hentschel; H. Greiving; J. Grunenberg; H. Hopf; I. Dix; P. G. Jones; L. Ernst; *Chem. Eur. J.,* **2007**, *13,* 3950–3963.
22. L.G. Sarbu; A. Birsa; H. Hopf; M.L. Birsa; *Phosphorus, Sulfur and Silicon*, **2011**, *186*, 1246-1250.
23. L.G. Sarbu; H. Hopf; P.G. Jones; M.L. Birsa; *Beilstein J. Org. Chem.,* **2014**, *10,* 2550–2555.

STUDIA UBB CHEMIA, LXIV, 3, 2019 (p. 17-32)
(RECOMMENDED CITATION)
DOI:10.24193/subbchem.2019.3.02

EXPIRED DRUGS AS INHIBITORS IN ELECTROCHEMICAL PROCESSES – A MINI-REVIEW

NICOLAE VASZILCSIN[a], DELIA-ANDRADA DUCA[a,*], ADRIANA FLUERAŞ[a], MIRCEA-LAURENŢIU DAN[a]

ABSTRACT. Inhibitors of electrochemical processes have useful applications in corrosion protection of metals and alloys, as well as in galvanotechnics as levellers for the cathodic metal deposition. Active substances of drugs are good inhibitors, taking into account that they have in their molecules structures containing π electrons or lone pair electrons, being able to adsorb on the metal surfaces through weak physical or strong chemical interactions. Significant inhibition efficiency of several drugs have been proved many years ago, but unfortunately, drugs are expensive and their practical applications as corrosion inhibitors for metal and alloys has been delayed. In the present papers, the studies on the inhibition properties in metal corrosion processes of expired drugs have been emphasized, starting with the paper of R. S. Abdel Hameed, published in 2009. There are few studies on the expired drugs used as levellers in the cathodic metal deposition.

Keywords: *expired drugs, corrosion inhibitors, inhibition efficiency, galvanic levellers*

INTRODUCTION

In the most applied electrochemical processes the enhancement of the useful reaction is the major aim, having as a result a decrease of the electrode overpotential. In this respect, a conclusive example is given by water electrolysis in which the diminution of hydrogen, respectively oxygen evolution overpotential leads to an optimized voltage cell close to the difference between reversible potentials of oxygen and hydrogen evolution reactions. Consequently, the energy yield is maximized [1]. Similar situations are encountered in sodium chloride solution electrolysis, as well as in the electrode processes occurring in fuel cells [2,3].

[a] *University Politehnica Timişoara, Faculty of Industrial Chemistry and Environmental Engineering, Timişoara, Romania*
** Corresponding author: duca.delia@gmail.ro*

On the other hand, there are several cases in which an inhibition of electrode process is useful. The most compelling example is the corrosion of metals and their alloys. The decrease of the corrosion rate, for example in aggressive aqueous solutions, can be realized by the inhibition of the anodic metal ionization or/and cathodic hydrogen evolution or oxygen reduction reaction.

A special situation is encountered in galvanotechnics, more exactly in the metal electrodeposition, in which the quality of the deposited layer (adhesion, decorative aspect, compactness) is more important than the energy yield.

The study of the drugs inhibiting properties has been stimulated by the huge amount of expired or unused medicines. A part of them are destroyed by incineration, but an important amount is released in the residual water, thus polluting the environment [4,5]. Furthermore, drugs neutralization by incineration endangers the atmosphere with toxic compounds containing nitrogen, sulphur, phosphorus, fluorine and chlorine. On the other hand, the researches of the corrosion inhibitory properties of expired drugs are sustained by the report of US Food and Drug Administration that showed 90% of the massive drug stock of the US Army maintained their characteristics long time after the expiration dates [6].

Active substances from medicines have been intensively studied taking into account that in their molecules there are structures that facilitate physical or chemical interactions with metals: aromatic rings, multiple bonds, N, O or S atoms containing lone pair electrons [7,8]. An elaborate review on the drugs corrosion inhibitory effect on metals and alloys in various media has been published by G. Gece [9], while D. S. Chauhan et al. have summarized the results on expired drugs as novel corrosion inhibitors published up to 2016 [10].

EXPIRED DRUGS AS CORROSION INHIBITORS

By our knowledge, the study of expired drugs as corrosion inhibitor has been started by R. S. Abdel Hameed, in 2009, when he used expired Ranitidine (active substance: ranitidine hydrochloride) as corrosion inhibitors for aluminum in hydrochloric acid solutions [11,12].

Further, the research of unused drugs has been focused on corrosion inhibition of carbon steel in various aggressive media. Expired Carbamazepine and Paracetamol have been used as inhibitors for carbon steel in 0.1 M sulfuric acid solution, as well as in acetic acid/sodium acetate buffer solution [6]. Studies on the corrosion inhibition capacity of Citicoline, Carbocisteine and

Paracetamol, in 1 M hydrochloric acid, have been carried out by F. H. Ali et al [13]. Expired Declophen (active substance: diclofenac sodium) was evaluated by R. S. Abdel Hameed as non-toxic corrosion inhibitor for carbon steel in 1 M hydrochloric acid [14]. In the same medium, excellent results have been obtained by N. K. Gupta et al. in their investigation on the corrosion inhibition of carbon steel using expired Atenolol and Nifedipine [15]. Similar results have been obtained by P. Dohare, using expired Tramadol (active substance: tramadol hydrochloride) [16], as well as, A. K. Singh et al. using semi synthetic antibiotic Cefdinir [17]. Inhibition efficiencies up to 90 % have been reported by R. S. Abdel Hameed for expired Ranitidine [18]. Recently, R. A. Anaee et al. have reported the effect of expired Etoricoxib on the corrosion rate of carbon steel in 0.5 M H_3PO_4 solution, at 30° and 60°C [19]. In HCl solution, expired Citicoline, Carbocisteine and Paracetamol have been tested [13], while in neutral media, expired Fluconazole has been evaluated [20].

Weight loss measurement was a proper technique used in order to determine the inhibition efficiency (*IE*), defined by the equation (1) and expressed in % [21]:

$$IE = \frac{W - W_{inh}}{W} \cdot 100 \quad (1)$$

where W and W_{inh} are the corrosion rate in the absence, respectively presence of the drug, mg dm^{-2} h^{-1}.

Table 1 emphasizes inhibition efficiencies *IE* [%], obtained by different authors, using weight loss measurements.

In order to determine the inhibition efficiency many researchers prefer Tafel slope method based on the equation (2) [27]:

$$IE = \frac{i_{corr} - i_{corr(inh)}}{i_{corr}} \cdot 100 \quad (2)$$

where i_{corr} and $i_{corr(inh)}$ are corrosion current densities in the absence, respectively presence of the inhibitor, A m^{-2}.

It has to be mentioned that *IE* computed using weight loss measurements represents an average value during the test time, while *IE* determined by Tafel slope method is an instantaneous one. Also, instantaneous inhibition efficiency is obtained using electrochemical impedance spectroscopy (EIS) based on equation (3) [28, 29]:

$$IE = \frac{R_{ct(inh)} - R_{ct}}{R_{ct(inh)}} \cdot 100 \quad (3)$$

where R_{ct} and $R_{ct(inh)}$ are charge transfer resistance in the absence and presence of the inhibitor, Ω m^2.

Table 1. Inhibition efficiency of expired drugs for carbon steel in 1 M HCl (weight loss method).

Expired drug	Drug concentration	*IE* [%]	References	Remarks
Citicoline	0.008 M	28	[13]	Test time: 24 h Ambient temperature
	0.012 M	25		
Paracetamol	0.003 M	83	[13]	Test time: 24 h Ambient temperature
	0.006 M	77		
	0.009 M	80		
	0.012 M	87		
	0.017 M	88		
Carbocisteine	0.0055 M	54	[13]	Test time: 24 h Ambient temperature
	0.016 M	14		
	0.021 M	65		
	0.030 M	75		
Declophen	0.5 %	69	[14]	Test time: 168 h T = 303 K
	1.0 %	70		
	1.5 %	75		
	2.0 %	80		
	2.5 %	87		
Ranitidine	50 ppm	61	[18]	Test time: 168 h *T* = 303 K
	100 ppm	65		
	150 ppm	75		
	250 ppm	81		
	400 ppm	89		
Tramadol	25 mg L-1	83	[16]	Test time: 3 h Ambient temperature
	50 mg L-1	91		
	75 mg L-1	94		
	100 mg L-1	96		
Cefdinir	0.63·10-4 M	75	[17]	Test time: 3 h *T* = 308 K
	1.26·10-4 M	82		
	2.52·10-4 M	85		
	3.79·10-4 M	92		
	5.05·10-4 M	95		
	6.32·10-4 M	96		
Gentamicin	0.9%	92	[22]	Test time: 6 h *T* = 303 K
Carvedilol	$1.6 \cdot 10^{-4}$ M	99	[23]	Test time: 30 min *T* = 298 K
Ambroxol	9%	94	[24]	Test time: 4 h Ambient temperature
Pantoprazol	300 ppm	93	[25]	Test time: 2 h *T* = 303 K
Phenytoin	500 ppm	70	[26]	Test time: 72 h *T* = 298 K

Corrosion efficiencies for carbon steel obtained by Tafel slope method and EIS are given in table 2.

Table 2. Inhibition efficiency of expired drugs for carbon steel (Tafel slope method and EIS).

Expired drug	Drug concentration	Corrosive medium	Tafel *IE* [%]	EIS *IE* [%]	References
Atenolol	optimum value	1 M HCl	91	93	[15]
Nifedipine	optimum value	1 M HCl	93	96	[15]
Carbamazepine	$5 \cdot 10^{-3}$ M	0.1 M H_2SO_4	90	-	[6]
Paracetamol	saturated	acetic acid 0.25 M/ sodium acetate 0.25 M	85	-	[6]
Declophen	0.5 %	1 M HCl	64	-	[14]
	1.0 %		68	-	
	1.5 %		74	-	
	2.0 %		78	-	
	2.5 %		88	-	
Ranitidine	50 ppm	1 M HCl	62	60	[18]
	100 ppm		76	75	
	150 ppm		80	81	
	250 ppm		86	88	
	400 ppm		90	92	
Etoricoxib	75 ppm	0.5 M H_3PO_4 30°C	65	-	[19]
	125 ppm		58	-	
	175 ppm		70	-	
	225 ppm		81	-	
	275 ppm		68	-	
	75 ppm	0.5 M H_3PO_4 60°C	56	-	[19]
	125 ppm		64	-	
	175 ppm		54	-	
	225 ppm		55	-	
	275 ppm		60	-	
Cefdinir	0.63·10-4 M	1 M HCl 35°C	75	81	[17]
	1.26·10-4 M		82	85	
	2.52·10-4 M		85	87	
	3.79·10-4 M		92	92	
	5.05·10-4 M		95	97	
	6.32·10-4 M		96	97	
Paracetamol	10^{-3} M	0.1 M H_2SO_4	94	96	[30]
	10^{-3} M	1 M HCl	86	85	
Clopidogrel	250 ppm	2 M HCl	93	86	[31]
Podocip	100 mg L-1	1 M HCl	97.5	98	[32]
Doxelcalciferol	0.4 g L-1	3 M HCl	87	89	[33]

In order to improve the inhibitory activity a chemical modification of expired drugs has been reported. P. Singh et al. have used expired active substance of Dapsone modified with benzaldehyde and salicylaldehyde. Resulted Schiff bases were tested as corrosion inhibitors for carbon steel in aerated 0.5 M sulphuric acid solution. Based on the gravimetric measurements, inhibition efficiencies of 96% and 94% have been obtained at an optimum concentration of 0.219 mM Dapsone-benzaldehyde, respectively Dapsone-salicylaldehyde. An addition of about 0.6 mM KCl increased the inhibition efficiency up to 99% and 98% respectively [34]. Schiff bases derivate of expired antituberculosis drug Isoniazid were synthesized by A. K. Singh et al. using four 5-indol derivatives: 5-bromo-indole-3-carboxime, 5-chloro-indole-3-carboxime, 5-methoxy-indole-3-carboxime and indole-3-carboxime [35].

Very high inhibition efficiencies of expired Ethambutol (active substance: ethambutol hydrochloride) for mild steel in 0.5 M hydrochloric acid have been obtained by S. Dahiya et al.: 99,60% (weight loss), 99,35% (Tafel plot method), 93,72% (electrochemical impedance spectroscopy) [36].

P. Singh et al. have reported interesting results on the inhibition activity of fresh Atorvastatin (FA) and expired one (EA) (active substance: atorvastatin calcium). Both drugs have shown similar corrosion efficiency for mild steel in 1 M HCl with 150 ppm Atorvastatin: 98.4 and 99.1% (Tafel slope); 96.4 and 96.4% (electrochemical impedance), respectively 93.5 and 96.5% (weight loss) [37].

Expired Cefpodoxime, Levofloxacin, Ofloxacin and Linezolid were tested for mild steel in 1 M HCl. Generally, inhibition efficiencies over 90% have been obtained for 240 ppm drug concentration in the aggressive solution [38]. In 5% HCl, using expired Varenicline, an inhibition efficiency of 78% has been reported for mild steel in weight loss test during 10 h and 0.4 g L^{-1} drug [39]. Similar results have been registered in the case of Ceftin [40] and Amitriptyline expired drugs [41]. Raghavendra reported an inhibition efficiency up to 94% for mild steel in 3 M HCl, in the presence of 0.2 mg L^{-1} expired Fluoxymesterone [42].

Generally, it is accepted that inhibitory activity of organic compounds on the metal corrosion is closely linked to the bond strength between organic molecule and metal. Information on such interactions is given by the adsorption Gibbs energy ΔG_{ads}. A value more negative than -40 kJ mol^{-1} (ΔG_{ads} < -40 kJ mol^{-1}) indicates that the interaction between organic substrate and metal is very strong and it is given by a chemical sorption, whereas a value more positive than -20 kJ mol^{-1}(ΔG_{ads} > -20 kJ mol^{-1}) proves that the adsorption of inhibitor is physical [43]. Adsorption Gibbs energy depends on the equilibrium adsorption constant K_{ads}, obtained based on the adsorption isotherms [44, 45]:

$$\Delta G_{ads} = -2.303RT \lg(55.5 \cdot K_{ads}) \quad (4)$$

Adsorption Gibbs energy values obtained for various expired drugs are given in table 3, as well as the corresponding value of inhibitory efficiencies.

Data given in table 3 provide that higher inhibition efficiencies are obtained in the case of the chemical adsorption of expired drugs. The highest value of Gibbs energy (-51 kJ mol^{-1}) was noticed by N. Raghavendra, for expired Lorazepam as an inhibitor for mild steel in 3 M HCl [46].

Table 3. Adsorption Gibbs energy and inhibitory efficiencies.

Expired drug	-ΔGads [kJ mol-1]	Temperature [K]	IE [%]	References
Ranitidine	37	303 K	90 - 92	[18]
Declophen	41	303 K	88	[14]
Cefdinir	39	308 K	96-98	[17]
Tramadol	37	308 K	96	[16]
Isoniazid derivatives	35 - 39		91 - 96	[35]
Modified Dapsone	38 - 40		94 - 96	[34]
Etoricoxib	29	308 K	92	[19]
Lorazepam	51	333 k	96	[46]
Amlodipine	20.3	303 K	84	[47]
	18.5	318 K	69	
Acetazolamide	21	303 K	86 -96	[48]

Activation energy E_a is a general parameter that characterizes the rate of chemical or physical processes. Consequently, activation energy can emphasize the influence of inhibitors on the metal corrosion rate. The higher the activation energy in the presence of inhibitors, the better their inhibition efficiencies [49,50]. Activation energies for metal ionization in the absence and presence of the inhibitor, as well as the inhibitory efficiencies are given in Table 4.

Table 4. Activation energies for metal ionization in the absence E_a and presence of the inhibitor $E_{a(inh)}$ and corresponding inhibition efficiencies.

Expired drug	**E_a [kJ mol^{-1}]**	***$E_{a(inh)}$* [kJ mol^{-1}]**	**ΔE_a [kJ mol^{-1}]**	***IE* [%]**	*References*
Ranitidine	40	55	15	90 - 92	[18]
Declophen	41	66	25	88	[14]
Isoniazid derivatives	33	67 – 80	34 -47	91 - 96	[35]
Cefdinir	42	99	57	96 - 98	[17]
Pantoprazol	26	47	21	93	[25]
Ambroxol	61	41	20	61 - 65	[51]
Clopidogrel	82	94	12	83 - 93	[31]
Ethambutol	59	73	14	88 - 86	[52]

There are few studies related to the use of expired drugs as corrosion inhibitors for other metals than carbon steel. A. El-Aziz S. Fouda and A. M. El-Azaly have been studied the expired Concor as a potential non-toxic corrosion inhibitor for stainless steel (SS 304) in HCl solution. They have determined the inhibition efficiencies using weight loss measurements, Tafel slope method and electrochemical impedance spectroscopy. Weight loss procedure was applied for a few concentrations of the expired Concor drug between 50 and 300 ppm, in 2 M HCl. The inhibition efficiencies were included in the range of 40 – 70%. In the same aggressive medium, Tafel slope method gave inhibition activities between 36 and 64%, while using electrochemical impedance spectroscopy inhibition efficiencies between 71 and 86% have been obtained [53].

N. Raghavendra has reported the results obtained using expired Alprazolam as corrosion inhibitor for aluminum in 3 M hydrochloric acid solution. Among current methods, a volumetric evaluation of the corrosion rate was applied, based on the volume of hydrogen evolved during the test. In this case, the inhibition efficiency is given by the relationship:

$$IE = \frac{V_H - V_{H(inh)}}{V_H} \cdot 100 \quad (5)$$

where V_H and $V_{H(inh)}$ are the volume of hydrogen evolved during the corrosion test in the absence, respectively the presence of the inhibitor.

Based on volumetric technique, inhibition efficiencies of 87; 92; 95 and 98 have been obtained at 60°C, during 2 h, at following concentration of expired Alprazolam: 0.3; 0.6; 0.9, respectively 1.2 g L^{-1}. In the same conditions, electrochemical impedance spectroscopy gave efficiencies of 86; 95; 96 and 97%, while Tafel slope method gave about 99% for all drug concentrations [54].

Results obtained by M. M. Motawea et al. showed that expired Cidamex is good inhibitor for aluminum in 1 M HCl. Inhibition efficiency reached 99.6% at 300 ppm Cidamex [55]. In 1 M H_2SO_4, with 400 ppm expired Betnesol (active substance: betamethasone sodium) or Moxifloxacin (active substance: moxifloxacin hydrochloride), inhibition efficiencies reached 94 – 95%, respectively 85-86% [56]. For the same metal and solution, K. R. Jahromi et al. have reported that, as corrosion inhibitor, expired Pantoprazol (active substance: pantoprazole) is less efficient than fresh Pantoprazol. For a drug concentration of 1500 ppm, electrochemical impedance inhibition efficiency decreased from 71 to 59%, whereas Tafel slope one decreased from 71 to 51% [57]. Considerable efficiency for corrosion inhibition of aluminum was obtained using expired Voltaren (active substance: diclofenac sodium) (125 ppm in 1 M HCl): 92% (Tafel slope) and 90% (weight loss) [58].

The effect of expired Zosyn (active substances: piperacillin and tazobactam) on the corrosion rate of carbon steel in a standard 3.5% NaCl solution was investigated by M. Dan et al. Cyclic voltammograms drown on platinum in NaCl solution in the presence of Zosyn 10^{-3} M (10^{-3} M is an apparent molar concentration consisting in $0.7 \cdot 10^{-3}$ M Piperacillin and $0.3 \cdot 10^{-3}$ M Tazobactam, taking into account that in Zosyn, the mass ratio Piperacillin/ Tazobactam is 4/1) proved that the drug is stable in the test solution in the potential range of ±250 mV versus open circuit potential. Corrosion studies have been carried out in the absence and presence of 10^{-6}; 10^{-5}; 10^{-4} and 10^{-3} M Zosyn. Inhibition efficiencies of 6; 11; 77; respectively 79% have been obtained by Tafel plots method, at 298 K, whereas gravimetric procedure, in the same circumstances, gave 10; 17; 72; respectively 90% [59].

Ceftriaxone, the active substance of expired Cefort drug has been used as corrosion inhibitor for nickel in 0.5 M H_2SO_4 and 1 M HCl. Electrochemical behavior of Ceftriaxone and its stability have been examined by cyclic voltammetry on platinum electrode. In the presence of Ceftriaxone, in both solutions, open circuit potential was shifted toward more positive potential. It has to be mentioned that the optimum concentration of Ceftriaxone is about 10^{-4} M in 0.5 H_2SO_4 and 10^{-5} M in 1 M HCl. Inhibition efficiencies have been determined by weight loss measurements (WLM), Tafel slope method (TSM) and electrochemical impedance spectroscopy (EIS) (Table 5) [60].

Table 5. Inhibition efficiencies in the presence of Ceftriaxone.

Test solution	Ceftriaxone concentration [M]	Inhibition efficiency [%]		
		WLM	TSM	EIS
0.5 H_2SO_4	10^{-4} M	71.4	70.1	69.5
1 M HCl	10^{-5} M	69.6	73.0	73.9

For copper in 3 M HCl, Narasimha Raghavendra et al. used expired Famotidine as corrosion inhibitor with an efficiency of 86% after a weight loss test during 4 h, at 0.4 g L^{-1} drug concentration [61] and expired Naftifine (active substance: naftifine hydrochloride) in 5 M HCl, with 69% efficiency in the same test conditions [62].

EXPIRED DRUGS IN GALVANOTECHNICS

The use of expired drugs as levelling agents is an accessible and cheap alternative to replace the commercial additives. So far there is few data about their use in galvanotechnics and further investigations are necessary. Expired Cefort (active substance: ceftriaxone) drug has been tested as levelling agent in copper and nickel electrodeposition [63,64] and expired Midazolam and Caffeine in nickel electrodeposition [65,66].

First, their electrochemical behavior has been studied by cyclic voltammetry on Pt electrode, in acid electrolyte solutions, similar with those used at industrial level, in which different concentrations of expired drugs have been added. For copper deposition, 0.5 mol L^{-1} H_2SO_4 has been used, respectively 30 g L^{-1} H_3BO_3 + 0.5 mol L^{-1} Na_2SO_4 for nickel electrodeposition. As a preliminary result, it was found that all drugs will not undergo degradation during the metal deposition.

Further, to determine the kinetic parameters of copper, respectively nickel electrodeposition by Taffel slope method, linear voltammograms (LVs) have been drawn in quasi stationary conditions, at low scan rate, on Cu or Ni electrode in electrolyte solutions containing 5 g L^{-1} metal ions in 0.5 mol L^{-1} H_2SO_4 for copper bath and in 30 g L^{-1} H_3BO_3 for nickel bath, with addition of different concentrations of expired drugs. Based on LVs, Tafel plots were represented, from which the exchange current density i_o and charge transfer coefficient 1-α have been calculated according to the Butler-Volmer equation applied in the range of high overpotentials [67].

$$b = -\frac{2.303RT}{(1-\alpha)zF} \quad (6)$$

$$a = \frac{2.303RT}{(1 - \alpha)zF} \lg i_o \tag{7}$$

where: R is the gas constant, J mol^{-1} K^{-1}; T – thermodynamic temperature, K; 1-α – charge transfer coefficient; z – elementary charge number; F – Faraday constant, C mol^{-1}; i_o – exchange current density, A m^{-2}.

It has been reported that metal electrodeposition rate depends on the temperature, as well as the kinetic parameters (1-α) and i_o.

In table 6, the obtained results for ceftriaxone used as additive in copper electrodeposition are presented [63]. Similar, in table 7, the results for ceftriaxone [64], midazolam [65] and caffeine [66] in nickel deposition process are shown.

Table 6. Kinetic parameters for copper electrodeposition on copper in electrolyte solution containing 0.5 mol L^{-1} H_2SO_4 + 5 g L^{-1} Cu^{2+}, with and without different concentrations of ceftriaxone.

Concentration [mol L^{-1}]	Temperature [°C]	1–α	i_o [A m^{-2}]
0	25	0.16	8.90
	35	0.15	7.38
	45	0.22	4.38
	55	0.64	3.91
	65	0.46	3.24
10^{-6}	25	0.21	11.10
	35	0.21	7.80
	45	0.32	7.25
	55	0.69	7.27
	65	0.54	4.74
10^{-5}	25	0.23	11.40
	35	0.22	7.90
	45	0.41	8.84
	55	0.75	14.90
	65	0.54	11.40
10^{-4}	25	0.35	21.90
	35	0.32	18.40
	45	0.80	20.80
	55	0.82	38.00
	65	0.59	28.50
10^{-3}	25	0.60	45.90
	35	0.36	24.50
	45	0.85	25.40
	55	0.87	115.80
	65	0.67	62.30

Table 7. Kinetic parameters for nickel electrodeposition on nickel in electrolyte solution containing 30 g L^{-1} H_3BO_3 + 5 g L^{-1} Ni^{2+} in the absence and presence of different concentrations of expired drugs.

Expired drug	Concentration [mol L^{-1}]	Temperature [°C]	1–α	i_o [A m^{-2}]
Cetftriaxone	0	25	0.54	$1.5 \cdot 10^{-5}$
		35	0.52	$2.7 \cdot 10^{-4}$
		45	0.43	$1.0 \cdot 10^{-2}$
		55	0.41	$6.8 \cdot 10^{-2}$
		65	0.39	$6.7 \cdot 10^{-1}$
	10^{-6}	25	0.55	$8.2 \cdot 10^{-6}$
		35	0.54	$5.2 \cdot 10^{-5}$
		45	0.47	$1.1 \cdot 10^{-3}$
		55	0.41	$9.8 \cdot 10^{-3}$
		65	0.39	$2.9 \cdot 10^{-1}$
	10^{-5}	25	0.64	$6.7 \cdot 10^{-8}$
		35	0.63	$2.9 \cdot 10^{-6}$
		45	0.49	$1.5 \cdot 10^{-3}$
		55	0.42	$3.9 \cdot 10^{-3}$
		65	0.40	$8.47 \cdot 10^{-2}$
	10^{-4}	25	0.70	$1.7 \cdot 10^{-10}$
		35	0.64	$8.2 \cdot 10^{-9}$
		45	0.55	$1.8 \cdot 10^{-5}$
		55	0.42	$1.0 \cdot 10^{-3}$
		65	0.40	$1.3 \cdot 10^{-2}$
Midazolam	0	25	0.33	$7.3 \cdot 10^{-2}$
		35	0.30	$7.9 \cdot 10^{-2}$
		45	0.27	$9.2 \cdot 10^{-2}$
		55	0.16	$1.0 \cdot 10^{-1}$
		65	0.13	$1.1 \cdot 10^{-1}$
	10^{-6}	25	0.36	$6.8 \cdot 10^{-2}$
		35	0.32	$7.2 \cdot 10^{-2}$
		45	0.27	$8.7 \cdot 10^{-2}$
		55	0.19	$9.5 \cdot 10^{-2}$
		65	0.17	$1.0 \cdot 10^{-1}$
	$5 \cdot 10^{-6}$	25	0.38	$5.6 \cdot 10^{-2}$
		35	0.32	$5.2 \cdot 10^{-2}$
		45	0.29	$6.4 \cdot 10^{-2}$
		55	0.22	$7.1 \cdot 10^{-2}$
		65	0.19	$8.2 \cdot 10^{-2}$
	10^{-5}	25	0.41	$4.3 \cdot 10^{-2}$
		35	0.36	$4.5 \cdot 10^{-2}$
		45	0.30	$5.1 \cdot 10^{-2}$
		55	0.25	$6.2 \cdot 10^{-2}$
		65	0.20	$7.6 \cdot 10^{-2}$
	$5 \cdot 10^{-5}$	25	0.43	$3.3 \cdot 10^{-2}$
		35	0.40	$2.7 \cdot 10^{-2}$
		45	0.37	$3.4 \cdot 10^{-2}$
		55	0.27	$4.1 \cdot 10^{-2}$
		65	0.24	$5.8 \cdot 10^{-2}$
	10^{-4}	25	0.49	$2.7 \cdot 10^{-2}$
		35	0.47	$2.3 \cdot 10^{-2}$
		45	0.43	$3.2 \cdot 10^{-2}$
		55	0.36	$4.3 \cdot 10^{-2}$
		65	0.27	$5.1 \cdot 10^{-2}$
Caffeine	0	25	0.26	$26.6 \cdot 10^{-5}$
	10^{-6}		0.32	$16.7 \cdot 10^{-5}$
	10^{-5}		0.36	$10.5 \cdot 10^{-5}$
	10^{-4}		0.39	$9.2 \cdot 10^{-5}$
	10^{-3}		0.42	$7.6 \cdot 10^{-5}$
	10^{-2}		0.44	$6.6 \cdot 10^{-5}$

In both cases, the rate-determining step of the process is the monoelectronic charge transfer. The obtained results show both electrodeposition processes are influenced by the presence of a small concentration of expired drug in the electrolyte solution.

Temperature rise catalytic effect on nickel deposition is emphasized by the transfer coefficient 1-α decrease and increase of the exchange current density i_o.

The increase of the cathodic transfer coefficient with expired drug addition in the electrolyte solution is due to the shift of the reaction surface (inner Helmholtz plane) towards the bulk of solution [67]. This effect is diminished if the process takes place at high temperature.

For copper and nickel electrodeposition, using ceftriaxone from expired cefort drug as levelling agent, apparent activation energy was calculated from Arrhenius plots [63,64]. In has been observed an increase of the activation energy when ceftriaxone was added in the electrolyte solutions.

In copper deposition case, an increase from 30.8 KJ mol^{-1} (in 0.5 mol L^{-1} H_2SO_4 + 5 g L^{-1} Cu^{2+} electrolyte solution) to 57.3 KJ mol^{-1} was noticed when 10^{-3} mol L^{-1} ceftriaxone was added, suggesting the process is inhibited by the presence of the expired drug. A similar effect was observed when ceftriaxone has been added in 30 g L^{-1} H_3BO_3 + 5 g L^{-1} Ni^{2+} electrolyte solution; an increase from 27.2 KJ mol^{-1} to 48.6 KJ mol^{-1} has been seen at 10^{-4} mol L^{-1} ceftriaxone addition due to its adsorption onto the electrode surface.

For more precise characterization of the process occurring at interface during nickel electrodeposition and to observe ceftriaxone [64] and midazolam [65] influence on the process, electrochemical impedance spectroscopy (EIS) measurements have been done.

The shape of Nyquist spectra, a slightly suppressed semi-circle, indicates an electron transfer limiting process, characterised by the charge transfer resistance (R_{ct}).

A dependence between the diameter of the semi-circle and the concentration of expired drugs added in the electrolyte solution was observed. In both cases, the addition of expired drugs in the electrolyte solution leads to the increase of the semi-circle diameter and of R_{ct} values.

CONCLUSIONS

According to the literature data, active substances of drugs are good inhibitors for corrosion and metal deposition processes due to their molecular structure containing π and/or lone pair electrons. In the last decade, starting with the papers of R. S. Abdel Hameed, studies on the inhibition properties

have been focused on the expired drugs taking into account that, generally, fresh drugs are expensive. The report of US Food and Drug Administration, showing that 90% of the US Army drugs stock maintained their characteristics long time after expiration date, has stimulated the researches on the expired drugs as corrosion inhibitors and leveller agents in galvanotechnics.

Inhibition efficiencies over 90% have been reported especially for carbon steel in very aggressive media, like hydrochloric or sulphuric acid solutions. As well as, good efficiencies were obtained for anticorrosive protection of nickel, aluminum or copper.

There are few studies on the expired drugs used as levellers in galvanotechnics. Promising results were reported for copper and nickel electrodeposition.

Obtained results have proved that the expired drugs represents an interesting alternative to the recommended commercial substances used as corrosion inhibitors or levellers in the current technologies.

ACKNOWLEDGMENTS

This work was partially supported by University *Politehnica* Timisoara in the frame of PhD studies.

REFERENCES

1. A. Züttel, A. Borgschulte, L. Schlapbach, “Hydrogen as a Future Energy Carrier”, Wiley-VCH Verlag, Weiheim, **2008**, 156.
2. V.S. Bagotsky, “Fundamentals of Electrochemistry”, Wiley Interscience, Hoboken, **2006**, 321.
3. S. Srinivasan, “Fuel Cells – From Fundamentals to Applications”, Springer, **2006**, 209.
4. M.A. Kozak, J.R. Melton, S.A. Gernant, M.E. Snyder, *Research in Social and Administrative Pharmacy*, **2016**, *12*, 336.
5. A.Y.C. Tong, B.M. Peake, R. Braund, *Environ. Int.*, **2011**, *37*, 292.
6. N. Vaszilcsin, V. Ordodi, A. Borza, *Int. J. Pharm*., **2012**, *15*, 241.
7. B. Mernari, H. El Attari, M. Traisnel, F. Bentiss, M. Lagrenee, *Corros. Sci.*, **1998**, *40*, 391.
8. E.S.H. El Ashry, A. El Nemr, S.A. Esawyb, S. Ragab, *Electrochim. Acta*, **2006**, *51*, 3957.
9. G. Gece, *Corros. Sci.*, **2011**, *53*, 3873.

10. D.S. Chauhan, A.A. Sorour, M.A. Quraishi, *Int. J. Chem. Pharm. Sci.*, **2016**, *4*, 680.
11. R.S.A. Hameed, Al-Azhar Bull*, Science,* **2009**, *20*, 151.
12. R.S.A. Hameed, *Phys. Chem. Ind. J.*, **2013**, *8(4)*, 146.
13. F.H. Ali, T.A.M. Al-Shimiesawi, K.K. Hammud, S.A.A. Rahmman, "Carbon steel corrosion inhibition in acidic medium by expired drugs", The Fifth Scientific Conference of the College of Science University of Kerbala, **2017**, 115.
14. R.S.A. Hameed, H.I. Al Shafey, A.H. Abu-Nawwas, *Int. J. Electrochem. Sci.*, **2014**, *9*, 6006.
15. N.K. Gupta, C.S.A. Gopal, V. Srivastava, M.A. Quraishi, *Int. J. Pharm. Chem. Anal.,* **2017**, *4*, 8.
16. P. Dohare, D.S. Chauhan, A.A. Sorour, M.A. Quraishi, *Materials Discovery*, **2017**, *9*, 30.
17. A.K. Singh, B. Chugh, S.K. Saha, P. Banerjee, E.E. Ebenso, S. Thakur, B. Pani, *Results in Physics*, **2019**,*14*, 102383.
18. R.S.A. Hameed, *Port. Electrochim. Acta*, **2011**, *29*, 273.
19. R.A. Anaee, I.H.R. Tomi, M.H. Abdulmajeed, S.A. Naser, M.M. Kathem, *J. Mol. Liq.*, **2019**, *279*, 594.
20. V.B. Terrones, C.M. Campos, M.R. Romo, J.M. Esparza Schutz, A. Dominguez, J. Uruchurtu Chavarin, *Innovations Corr. Mat. Sci.*, **2015**, *5*, 31.
21. I.B. Obot, N.O. Obi-Egbedi, S.A. Umoren, *Corr. Sci.*, **2009**, *51*, 1868.
22. A. Srinivasulu, P.K. Kasthuri, *Oriental J. Chem.*, **2017**, *33*, 2616.
23. A.S. Fouda, M.A. El Morsi, T. El Mogy, *Green Chem. Lett. Rev.*, **2017**, *10*, 336.
24. P. Geethamani, P.K. Kasthuri, *Cogent Chem.*, **2015**, *1*, 1091558.
25. A.S. Fouda, H. Ibrahim, S. Rashwaan, A. El-Hossiany, R.M. Ahmed, *Int. J. Electrochem. Sci.*, **2018**, *13*, 6327.
26. A.H.I. Al-Shafey, R.S.A. Hameed, F.A. Ali, A.E.S. Aboul-Magd, M. Salah, *Int. J. Pharm. Sci. Rev. Res.*, **2014**, *27*, 146.
27. K.F. Khaled, *Applied Surface Science*, **2006**, *252*, 4120.
28. A. Samide, P. Ilea, A-C. Vladu, *Int. J. Electrochem. Sci.*, **2017**, *12*, 5964.
29. I. Rotaru, S. Varvara, L. Gaina, L.M. Muresan, *Appl. Surface Sci.*, **2014**, *321*, 188.
30. D.A. Duca, M.L. Dan, N. Vaszilcsin, *Materials Sci. Eng.*, **2018**, *416*, 012043.
31. A.S. Fouda, W.M. Mahmoud, K.M.A. Elawaye, *Prot. Met. Phys. Chem. Surf.*, **2017**, *53,* 139.
32. P. Dohare, D.S. Chauhan and M.A. Quraishi**,** *Int. J. Corr. Scale Inh.*, **2018**, *7*, 25.
33. N. Raghavendra, *J. Chem. Pharm. Res.*, **2018**, *10,*1.
34. P. Singh, D.S. Chauhan, S.S. Chauhan, G. Singh, M.A. Quraishi, *J. Mol. Liq.*, **2019**, *286*, 110903.
35. A.K. Singh, A.K. Pandey, P. Banerjee, S.K. Saha, B. Chugh, S. Thakur, B. Pani, P. Chaubey, G. Singh*, J. Environ. Chem. Eng.*, **2019**, *7*, 102971.
36. S. Dahiya, N. Saini, N. Dahiya, H. Lgaz, R. Salghi, S. Jodeh, S. Lata, *Port. Electrochim. Acta*, **2018**, *36*, 213.
37. P. Singh, D.S. Chauhan, K. Srivastava, V. Srivastava, M.A. Quraishi, *Int. J. Ind. Chem.*, **2017**, *8*, 363.

38. V. Rajeswari, K. Devarayan, P. Viswanathamurthi, *Res. Chem. Intermed.*, **2017**, *43*, 3893.
39. N. Raghavendra, L.V. Hublikar, A. S. Bhinge, P.J. Ganiger, *Int. J. Res. Advent Technol.,* **2019**, *7,* 675.
40. N. Raghavendra, L.V. Hublikar, P.J. Ganiger and A.S Bhinge*, Int. J. Green Herbal Chem. - Section A*, **2019**, *8*, 610.
41. N. Raghavendra, *Sci. Lett.*, **2019**, 7, 26.
42. N. Raghavendra, *Int. J. Chem. Mat. Res.,* **2018***, 6, 1.*
43. N.O. Eddy, S.R. Stoyanov. E.E. Ebenso, *Int. J. Electrochem. Sci.*, **2010**, *5*, 112.
44. M. Bobina, A. Kellenberger, J.P. Millet, C. Muntean, *Corr. Sci.*, **2013**, *69*, 389.
45. A. Samide, B. Tutunaru, *Central Eur. J. Chem.*, **2014**,*12*, 901.
46. N. Raghavendra, *Chem. Africa*, **2019**, doi.org/10.1007/s42250-019-00061-2.
47. A.S. Fouda, W.M. Mahmoud, H.A.A. Mageed, *J. Bio.Tribo. Corr.*, **2016**, *2*, 7.
48. L.P. Chaudhari, S.N. Patel, *J. Bio Tribo Corr.*, **2019**, *5*, 20.
49. L. Herrag, B. Hammouti, S. Elkadiri, A. Aouniti, C. Jama, H. Verzin, F. Bentiss, *Corr. Sci.*, **2010**, *52*, 3042.
50. J. Aljourani, K. Raeissi, M.A. Golozar, *Corr. Sci.*, **2009**, *51*, 1836.
51. P. Geethamani, M. Narmatha, R. Dhanalakshmi, S. Aejitha, P.K. Kasthuri, *J. Bio Tribo Corr.*, **2019**, *5*, 16.
52. A. Kumar, S. Bashir, *Russian J. Appl. Chem.*, **2016**, *89,* 1158.
53. A.S. Fouda, A. M. El-Azaly, *Zastita Materijala*, **2018**, *59*, 226.
54. N. Raghavendra, *J. Sci. Eng.Technol.*, **2018**, *6*, 35.
55. M.M. Motawea, H.S. Gadow, A.S. Fouda, *Global J. Res. Eng. C Chemical Eng.*, **2016**, *16*, 1.
56. R.S. Nathiya, S. Perumal, V. Murugesan, V. Raj, *J. Bio Tribo Corr.*, **2018**, *4*, 4.
57. K. Rezaei Jahromi, and C. Dehghanian, *Int. J. Curr. Res.,* **2017**, *9*, 44630.
58. R.S. Abdel Hameed, E.A. Ismail, A.H. Abu-Nawwas, and H.I. Al-Shafey, *Int. J. Electrochem. Sci.,* **2015**, *10*, 2098.
59. M. Dan, N. Vaszilcsin, M. Labosel, B. Pancan, *Chem. Bull. "POLITEHNICA" Univ. Timisoara*, **2014**, *59 (73)*, 13.
60. D.A. Duca, M.L. Dan, N. Vaszilcsin, *Adv. Eng. Forum*, **2018**, *27*, 74.
61. N. Raghavendra, L.V.Hublikar, A.S.Bhinge, P.J.Ganiger, *Int. J. Res. Appl. Sci. Eng.Technol.*, **2019**, *7*, 2289.
62. N. Raghavendra*, J. Adv. Electrochem.*, **2019**, *5*, 177.
63. D.A. Duca, M.L. Dan, N. Vaszilcsin, *Annals Univ. Oradea Environ. Protect.*, **2016**, *27*, 229.
64. D.A. Duca, M.L. Dan, N. Vaszilcsin, *Chem. J. Moldova*, **2017**, *12*, 87.
65. D.A. Duca, N. Vaszilcsin, M.L. Dan, *SGEM Conference Proceedings*, **2016**, *4*, 105.
66. D.A. Duca, M.L. Dan, N. Vaszilcsin, *Annals Univ. Oradea Environ. Protect.*, **2015**, *15*, 177.
67. J. O'M. Bockris, A.K.N. Reddy, M.E. Gamboa-Aldeco, "Modern Electrochemistry", Vol. 2A, Second edition, Kluwer Academic Publishers, New York, **2000**, 1479.

STUDIA UBB CHEMIA, LXIV, 3, 2019 (p. 33-46)
(RECOMMENDED CITATION)
DOI:10.24193/subbchem.2019.3.03

LAYERED DOUBLE HYDROXIDES, PECULIAR AND VERSATILE MATERIALS OFFERING MANY RESEARCH AND APPLICATION POSSIBILITIES

PÁL SIPOS[a,b] AND ISTVÁN PÁLINKÓ[a,c,*]

ABSTRACT. This review article describes the major structural features of layer double hydroxides (LDHs), gives an overview of their synthetic and modification methods as well as the structural characterization possibilities both the generally used and those, which can only be used for specific LDHs. The catalytic use of these materials without calcination, i.e. the layered structure is preserved, are also highlighted. The paper places the authors' works of about the last decade in the framework of recent papers and review articles of this broad field.

Keywords: *layered double hydroxides; synthetic and characterization methods; catalytic application of the as-prepared forms.*

INTRODUCTION

In the ninethies of the previous century, we entered the research field of layered double hydroxides by chance. At that time, we were working with the cation-exchanger montmorillonite, mostly we wanted to find ways of pillaring it with various complex inorganic cations, and use them in shape-selective catalytic reactions [1]. Then, the idea occurred to apply organic cations instead of the inorganic ones, perhaps if they are chiral, then enantioselective/ diastereoselective catalyst may be developed. Some amino acids, their protonated versions, seemed to be handy candidates to try. Having some organic chemistry background, it was clear that amino acids have amphoteric

[a] *University of Szeged, Institute of Chemistry Material and Solution Structure Research Group, Aradi Vértanúk tere 1, Szeged, H-6720 Hungary*
[b] *University of Szeged, Department of Inorganic and Analytical Chemistry, Dóm tér 7, Szeged, H-6720 Hungary*
[c] *University of Szeged, Department of Organic Chemistry, Dóm tér 8, Szeged, H-6720 Hungary*
** Corresponding author: palinko@chem.u-szeged.hu*

character, they can be deprotonated as well, then, why not use them as pillaring agents in anion-exchanger materials. To keep as close similarity to montmorillonite as it was possible, substances with layered structure were sought for. Thus, we arrived at the family of layered double hydroxides (LDHs). Even superficial literature search revealed that better not choose MgAl-LDH, since they were too popular, papers with ZnAl-LDH were significantly scarcer. The project went on, and we were able to produce amino acid pillared montmorillonite and amino acid pillared ZnAl-LDH using the protonated and the deprotonated versions of amino acids [2]. The paper was well received, since, by chance, we were among the first researchers to prepare amino acid intercalated LDHs, and this area of LDH research became popular soon after we published our results. Then, for some years, it looked like that this work was only an excursion to this area, until at the beginning of the twenties of this century, when new impetus came from an industrial collaboration. Then, we started to work with hydrocalumites [3], a subgroup of the hydrotalcite supergroup of LDHs [4]. We have learnt after conducting a thorough literature search, that the synthesis, structural modification, characterization of LDHs is very crowded area, thousands of papers are published annually, and LDHs also have many applications. From time to time excellent reviews provide with critical surveys of the area [5−18], and there are some books containing vital information both for the newcomers and the experienced researchers [19−22].

As far as their usages are concerned, we list some recent reviews, about a few important applications and application areas like drug delivery vehicles [23, 24], adsorbents [25], flame retardants [26], environmental protection [27, 28], electrochemistry and energy storage [29], photocatalysis [30, 31], catalysts after heat treatment and catalyst supports [32, 33], somewhat more about catalytic applications, when the layered structure is maintained [34−37]. This is the area we are working at.

METHODS OF SYNTHESIS AND POST-SYNTHESIS MODIFICATIONS

There are many frequently used ways of preparing LDHs, most of them are wet chemical methods [5, 38]; however, recently, increasing attention is turned towards less conventional ones, like mechanochemical synthesis methods (one- or two-step milling, in which the second step is usually wet milling) or ultrasonically-assisted mechanochemical synthesis (for recent reviews, see, e.g., refs. [13] and [17]. Ultrasonic irradiation can also be used in post-synthesis modifications efficiently.

Wet chemical methods

The main synthetic wet chemical techniques for the synthesis of LDHs are the co-precipitation [39] and the urea hydrolysis methods [40]. In the co-precipitation method, an aqueous solution of M(II) and M(III) cations (most often two components; however, layered hydroxides with three cationic components also emerge with increasing frequency) is applied as precursor. The solution is mixed together with aqueous base (usually NaOH) solution to reach the pH of precipitation. The urea hydrolysis method works similarly, but the urea hydrolysis, which is temperature-dependent provides the necessary pH value. The method affords more precise and constant pH.

It is known that the interlayer anions can be exchanged almost at will even bulky organic or complex ones can be introduced into the interlayer space [41, 42]. Among the methods generally applied for this purpose [43] one can find wet chemical as well as mechanochemical techniques. The wet chemical methods can be direct anion exchange from water [44], aqueous ethanol or acetone [45]; co-precipitation of the components including the anion to be intercalated [46]; the dehydration-rehydration method of intercalation [47, 48]. Occasionally, ultrasonic treatment increases the efficiency of the anion exchange or allows the introduction of anions, which would be difficult without its use [49, 50].

Mechanochemical methods

Basically, two methods are used. One-step milling is the simpler one, in which the solid components are milled together (dry milling). This was used, for instance in the synthesis of MgAl-LDHs using planetary ball mill [51]. In the two-step milling procedure [52], dry milling was performed first with the mixtures of the solid hydroxides of the M(II) and M(III) ions, then, milling was continued in the presence of small amount of water (wet-milling step). The presence of water ensured the formation of the LDH, since the amount of hydroxides in the metal salts was not sufficient for this. It was also shown that using a simple agate mortar and manual grinding also provided with the LDH [53]. This "soft" mechanochemical treatment − co-grinding the constituents in a mortar with a pestle − could also be used for the intercalation of various anions [54, 55]. CaAl- [56] and CaFe-LDH [57] could be prepared by the manual grinding as well as the two-step milling methods. It was shown manual grinding worked in producing LDH; however, the transformation was only partial, while it was complete on applying the two-step milling procedure.

It was found that certain LDHs like Ca(II)Sn(IV)-LDH could only be prepared by the two-step milling procedure [58]. Both the co-precipitation method and the one-step milling operation (milling without added liquid, i.e., dry milling) failed, physical mixtures of metal hydroxides and/or carbonates were only formed.

Upon mechanochemical treatment, the layered structure of CaFe-LDH) could be disordered and the deterioration steps were mapped [59]. Interestingly, the structural reconstruction of the mechanochemically disordered chloride-containing LDH was successful in distilled water as well as in nitrate-containing aqueous solution.

Ultrasonically-enhanced mechanochemical method

Ultrasonic irradiation alone is not sufficient for the synthesis of LDHs. However, when the mixture of metal hydroxides preactivated by dry milling was sonicated in the presence of distilled water, not only high-quality LDHs were formed, but various inorganic anions like CO_3^{2-}, OH^-, F^-, Cl^-, Br^-, I^-, N_3^-, NO_3^-, ClO_4^-could also be introduced among the layers with relative ease [49, 50].

Ultrasonic treatment could be used in the synthesis of close-to-phase pure ZnAl- [60] and CaAl-LDHs [49] or even CaFeAl-triple hydroxides [61]. Its use was imperative, since after the milling step, LDH could not be observed in the product.

Ultrasonic irradiation was found to be able to regulate the crystallization process of CaFe-LDH with chloride interlayer anions [62]. Low-performance ultrasonic irradiation provided with perfect conditions for the formation of LDH with well-developed hexagonally-shaped crystallites. At continuous emission, anion intercalation could be enhanced. At discontinuous radiation periodicity, the aggregation tendency of the particles formed was somewhat hindered. The method allowed the fine-tuning of the optical properties of the LDH samples, too.

METHODS OF STRUCTURAL CHARACTERIZATION

Methods of general use

There are many instrumental methods for the structural characterization of LDHs. Some has general applicability like powder X-ray diffractomery (XRD), infrared (mid and far) and Raman spectroscopies, X-ray photoelectron spectroscopy (XPS). These methods are largely available and relatively easily accessible even in any not so well-equipped research places. They provide with indirect information about the layered structure (XRD), and certain parts of the LDH like hydrogen bonding network of OH groups, interlayer anions, surface-adsorbed carbon dioxide, skeletal vibrations (vibrational spectroscopies), oxidation states of the cationic components (XPS). XRD is the major tool in structural characterization, since LDHs have typical X-ray traces, and certain crucial data can be deduced from the diffractograms like the basal distance (interlayer space plus the thickness of one layer) and its change due to

functionalization. Indexing and identifying the diffraction patterns can be done with the help of the JCPDS (Joint Committee of Powder Diffraction Standards) database.

LDHs give typical response on heat treatment. Three water types can be separated on thermal treatment. Thermogravimetric measurement usually reveal three distinctive forms of water molecules. On gradually increasing the temperature of heat treatment one can remove the physically adsorbed water molecules (100°C−150°C), the interlayer water molecules are next (175°C−325°C), finally, the dehydration of structural OH groups and their closely associated (hydrogen bonded) water molecules takes place (350°C−475°C). The latter are often called 'structural water', although it exists in the form of OH groups in the layer, but it becomes water on dehydration. The water forms can be distinguished with dielectric relaxation spectroscopy (DRS), and rehydration of the dehydrated LDH can also be followed by this method [63, 64].

For quantitative elemental analyses, various forms of the inductively coupled plasma analysis (ICP–MS, ICP–AES, ICP–OES) are available. This information is obtained after digesting the LDH [65-69].

Synchrotron-based methods like X-ray absorption spectroscopy, resonant inelastic X-ray scattering (RIXS), high resolution powder X-ray diffractometry, etc. are available in many places in the world, and accessible through obtaining beamtime after successful proposals. These methods provide with information on local structures or complete structural description at the atomic scale via the last method [65-68, 70-72].

Microscopic methods allow the researcher to see crucial features of the LDHs. Scanning electron microscopy (SEM) is applied for studying the morphologies of the crystals, the crystal shape can be examined and the lamellar structure of the LDHs can be observed. Obviously, changes in these features during and after treatments of various kinds can also be followed. Transmission electron microscopy (TEM), especially its high-resolution version (HRTEM) can be used for observing the layered structure directly, and, sometimes, if the orientation of the crystal allows, the thickness of the layer and the interlayer spacing can also be measured [59, 66]. If energy-dispersive X-ray analysis (EDX) is possible, then, the constituents can be qualitatively analysed, and even (half) quantitative measurements are also possible. If the EDX accessory is coupled to HRTEM, then elemental maps can be made at the atomic level, i.e. the evenness of elemental distribution can be observed.

Methods of limited use

EPR spectroscopy can be used for collecting structural information if any of the components is EPR active [65, 66].

Mössbauer spectroscopy is also a useful method providing structural information about the immediate environment of Mössbauer active nuclei. Sadly, there only a few ions (both, but more often iron(III)) are frequent constituents of LDHs [48, 73, 74].

In principle, molecular modelling is a method of general applicability; however, calculations at high theoretical levels are still problematic, because having meaningful data about a cluster representing well the LDH structure is still computationally expensive. Therefore, calculations are usually done at lower level of theory [75, 76], or combining molecular modelling and experimental data (XRD and TEM), and the purpose is mainly visualising the structural arrangements of intercalated complexes, for instance [65−69].

CATALYSIS WITH UNCALCINED LDHS

As it has already been mentioned, LDHs have many applications. One of the most important is their use in catalysis, mostly as catalyst precursors or catalysts in base-catalysed reactions. On calcination, the layered structure collapses and the catalytic activity of the resulting mixed oxide often increases, because of the presence of many defects in its structure.

In scarcer, but increasing number of cases, they are used in their as-prepared forms, and they were found to be active, selective and recyclable catalysts in a number of synthetically useful reactions. In the followings we attempt to give a brief overview about this kind of application.

Catalysts in various oxidative transformations

As-prepared MgAl-LDH selectively oxidized the olefinic double bond of enones using H_2O_2 for oxidation [77]. As-prepared CaAl-LDH or CaFe-LDH were found to be active as well [78]. Here, the compound was 2-cyclohexene-1-one, the oxidant was hydrogen peroxide, and the reaction was performed in the liquid phase in various solvents (Scheme 1). It was found that keeping the LDH structure was beneficial, since both uncalcined LDHs were more active than their calcined versions.

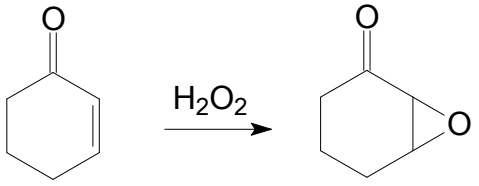

Scheme 1. Epoxidation of the C=C bond in a cyclic enone

Ca(II)Sn(IV)-LDH, which could only be made mechanochemically, worked well in the liquid-phase Baeyer-Villiger oxidation of cylohexanone (Scheme 2). Under the optimum conditions (reaction temperature: 70°C, reaction time: 24 h, solvent: benzonitrile) the conversion was 14%; however, this was the sole product.

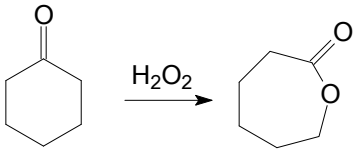

Scheme 2. ε-Caprolactam formation from cyclohexanone during Bayer-Villiger oxidation

The oxidative homocoupling reactions of aromatic amines (Scheme 3) as well as acetylenes (Scheme 4) were efficiently catalysed with as-prepared Cu(II)Fe(III)-LDH in a flow reactor at moderate pressure and temperature without added materials [79]. The catalyst remained very active even after 15-h time-on-stream, and displayed very high substance tolerance.

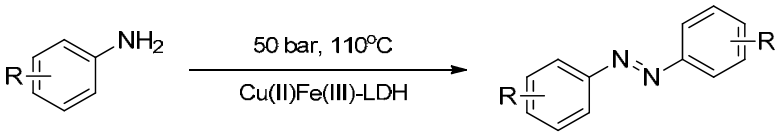

Scheme 3. As-prepared Cu(II)Fe(III)-LDH as catalyst in the homocoupling of anilines in a flow reactor

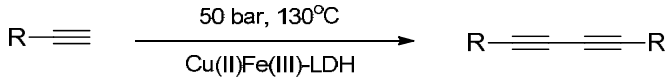

Scheme 4. As-prepared Cu(II)Fe(III)-LDH as catalyst in the homocoupling of terminal acetylenes in a flow reactor

Metal (ion) complexes intercalated in various LDHs were found to be active and selective catalysts. Mn(III)-sulfonato-salen−ZnAl-LDH intercalated material catalyzed the epoxidation of various prochiral alkenes with oxygen or even air [80−85]. Mn-salen−MgAl-LDH was efficient and recyclable catalyst in the N-oxidation of picoline [86]. Mn-porphyrin−ZnAl-LDH could catalyze the epoxidation of various olefins (cyclohexene, heptylene, phenylethylene, 3-methyl-3-buten-1-ol, ethyl cinnamate and chalcone) with oxygen [87].

The intercalated Cu(II)-2,2-bipyridine-5,5-dicarboxylate complex could catalyze the oxidation of styrene, ethylbenzene and cyclohexane producing benzaldehyde, acetophenone and a mixture of cyclohexanol and cyclohexanone, respectively [88]. The intercalated Cu(II)-sulphonato Schiff base complexes as well as the Fe(III)-Schiff base complex-LDH composites catalyzed the oxidation of glycerol to glyceric acid [89] and the selective oxidation of cyclohexane to a mixture of cyclohexanone and cyclohexanol [90]. Recently, Mo(II) complexed with bis(4-HOOC-phenyl)-acenaphthenequinone diimine) intercalated in MgAl- and ZnAl-LDH epoxidised *cis*-cyclooctene, styrene applying *tert*-butylhydroperoxide as the oxidant with 100% conversions [91].

In our experimental work [65−68], cyclohexene and two oxidants [peracetic acid and (diacetoxy)iodobenzene] were chosen as the probe molecules for studying the catalytic properties of Mn(II)- [65], Cu(II)- [66], Ni(II)- [67] or Fe(III)-amino acid [68] (L-histidine, L-cysteine or L-tyrosine) anionic complexes intercalated in CaAl-LDH. Epoxidation is the expected main reaction channel in the oxidation reaction of cyclohexene; however, other minor products may also be formed (Scheme 5).

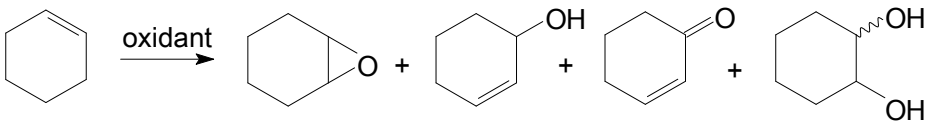

Scheme 5. The possible products in the oxidation reaction of cyclohexene

Acetone had to be the solvent, because peracetic acid does not decompose in it. The transformation of cyclohexene was significantly faster in the presence of the composites than in the blind tests (i.e. without the composites or in the presence of the LDH host only). Actually, it made almost no difference when the central ion and/or the ligands were varied. The overwhelming or the exclusive product was the epoxide, and the composites could be recycled several times with nearly retaining the original activity and composition of the product mixture.

Cyclohexene was oxidized, under similar conditions, with (diacetoxyiodo) benzene in aqueous acetone (5/95% by volume), too. The water content was imperative, since it was needed for hydrolysis, and thus the activation of (diacetoxyiodo)benzene by the following reaction [92]:

$$PhI(OOCH_3)_2 + H_2O \rightleftharpoons PhI(OH)_2 + 2\ CH_3COOH$$

It was observed that the *in situ* formed $PhI(OH)_2$, in the presence of added composites gave in close to 100% selectivity the diol even though epoxide was formed in appreciable quantities without them. The added composites acted as catalysts, and they could be recycled several times applying simple rinsing with the solvents between the repeated runs. Diol was a primary product over the fresh as well as the recycled catalysts, since the *cis* isomer was only found. If it had been originated from the ring opening of the epoxide, the *trans* isomer would have been formed.

The Cu(II)- [66] and the Fe(III)-containing [68] composites were probed in the Ullmann-type etherification (Scheme 6), and they also proved to be excellent catalysts in this reaction type. Recycling was possible and easy. The reactivity was maintained even after the third recycling reaction. For regeneration, a simple rinse with toluene proved to be sufficient.

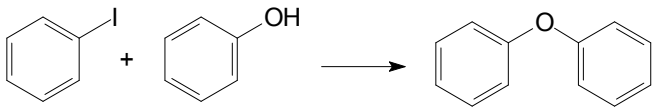

Scheme 6. Etherification of the Ullmann type
(in the original reaction, the catalyst was the Cu(I) ion [93, 94])

Catalysts of miscellaneous reactions

L-Prolinate-MgAl-LDH samples were tested in cross-aldol dimerization–condensation of benzaldehyde and acetone (Scheme 7). As it was expected, the dimerization was the main reaction (the catalyst was basic, and the temperature was low). Originally low (6%, [95]), but later appreciable (94%, [96]) enantioselective excess (ee) values were achieved. In the same reaction, the L-prolinate-CaFe-LDH composite did not perform so well [97], moderate ee values (53%) could only be obtained. After recycling the activity increased; however, both the dimerization selectivity and the enantioselectivity decreased. The latter is probably due the enolization of the carboxylate ions favoured by the basic conditions [98]. Due to this reaction the chirality of the α-carbon atom is lost.

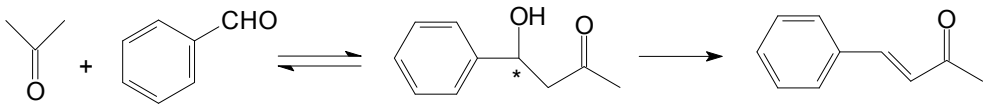

Scheme 7. The cross-aldol dimerization–condensation of benzaldehyde and acetone

The as-prepared Cu(II)Fe(III)-LDH actively and selectively catalysed the click reaction of organic azides and alkynes providing with 1,2,3-triazoles in a flow reactor under 50 to 100 bar pressure from room temperature to 100°C (Scheme 8) [99].

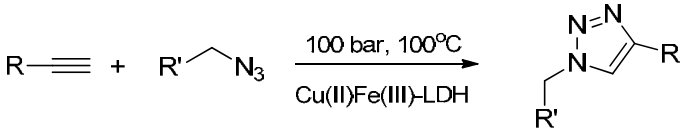

Scheme 8. 1,3-dipolar cycloaddition between terminal acetylenes and azides catalysed with uncalcined Cu(II)Fe(III)-LDH in a flow reactor

SUMMARY AND OUTLOOK

The research field dealing with various aspects of LDH chemistry spanning from their synthesis and modification methods through structural characterization till many kinds of applications is thriving. Thousands of papers are published annually. Here, hopefully, we were able to show recent developments of this broad field emphasizing the recently emerging area of their use as catalysts maintaining their layered structure. LDHs are versatile materials. It was also intended to show ways of their synthesis and structural modification, which is relatively easy; there are many methods available, slight and, occasionally, dramatic alterations occur. Some of them prove to be useful and are widely applied others prove to be impractical and forgotten. The authors are sure that research activity in this area will not diminish and we are going to see many new methods, with the help of which these versatile materials can be tuned to various applications even to those unknown today.

REFERENCES

1. I. Pálinkó; Á. Molnár; J. B.Nagy; K. Lázár; J. Valyon; I. Kiricsi; *J. Chem. Soc., Faraday Trans.*, **1997**, *93*, 1591–1599
2. Á. Fudala; I. Pálinkó; I. Kiricsi; *Inorg. Chem.*, **1999**, *38*, 4653–4658
3. I. Rousselot; C.T. Guého; F. Leroux; P. Léone; P. Palvadeau; J.-P. Besse; *J. Solid State Chem.*, **2002**, *167*, 137–144
4. S.J. Mills; A.G. Christy; J.-M.R. Génin; T. Kameda; F. Colombo; *Miner. Mag.*, **2012**, *76*, 1289–1336

5. G.D. Evans; R.C.T. Slade; *Struct. Bond.*, **2006**, *119*, 1–87
6. J. He; M. Wei; B. Li; Y. Kang; D.G. Evans; X. Duan; *Struct. Bond.*, **2006**, *119*, 89–119
7. G.R. Williams; A.I. Khan; D. O'Hare; *Struct. Bond.*, **2006**, *119*, 161–192
8. P. Nalawade; B. Aware; V.J. Kadam; R.S. Hirlekar; *J. Sci. Ind. Res.*, **2009**, *68*, 267–272
9. C. Taviot-Gueho; Y. Feng; A. Faour; F. Leroux; *Dalton Trans.*, **2010**, *39*, 5994–6005.
10. Ogawa, M.; Inomata, K. Preparation of layered double hydroxides. *Clay Sci.* **2011**, *15*, 131–137
11. Y. Lin; G. Wang; *Recent Patents on Nanotechnology*, **2012**, *6*, 169–173
12. G. Mascolo; M.C. Mascolo; *Mic. Mes. Mater.*, **2015**, *214*, 246–248
13. J. Qu; Q. Zhang; X. Li; X. He, X.; Song; *Appl. Clay Sci.*, **2016**, *119*, 185–192
14. M. Pavlovic; P. Rouster; T. Oncsik; I. Szilagyi; *ChemPlusChem,* **2017**, *82*, 121–131
15. V. Prevot; Y. Tokudome; *J. Mater. Sci.*, **2017**, *52*, 11229–11250
16. E. Conterosito; V. Gianotti; L. Palin; E. Boccaleri; D. Viterbo; M. Milanesio; *Inorg. Chim. Acta*, **2018**, *470*, 36–50
17. S. Intasa-ard; K. Imwiset; S. Bureekaew; M. Ogawa; *Dalton Trans.*, **2018**, *47*, 2896–2916
18. M.V. Bukhtiyarova; *J. Solid State Chem.*, **2019**, *269*, 494–506
19. *Layered Double Hydroxides: Present and Future*, V. Rives; Ed.; ISBN 978-1-61209-289-8, Nova Science Publishers, Inc, New York, 2001
20. *Handbook of Layered Materials*, S. M. Auerbach; K. A. Carrado; P. K. Dutta; Eds; ISBN 0-8247-5349-6, Marcel Dekker, Inc., New York, Basel, 2004
21. *Handbook of Clay Science Parts A and B, 2nd ed.*, F. Bergaya; G. Lagaly; Eds; ISBN-13: 978-0080993645, Elsevier, Amsterdam, 2013
22. *Layered Double Hydroxides (LDHs) – Synthesis, Characterisation and Applications*, I.T. Sherman; Ed.; ISBN 978-1-63482-024-0, Nova Science Publishers, Inc., New York, 2015
23. J.-H. Yang; J.-H. Lee; H.-J. Ryu; A.A. Elzatahry; Z.A. Alothman; J.-H. Choy; *Appl. Clay Sci.*, **2016**, *130*, 20–32
24. S. Saha; S. Ray; R. Acharya; T. K. Chatterjee; J. Chakraborty; *Appl. Clay Sci.*, **2017**, *135*, 493–509
25. J. Qu; L. Sha; C. Wu; Q. Zhang; *Nanomater.*, **2019**, *9*, 80:1–15
26. Y. Liu; Y. Gao; Q. Wang; W. Lin; *Dalton Trans.*, **2018**, *47*, 14827–14840
27. P. Gu; S. Zhang; X. Li; X. Wang; T. Wen; R. Jehan; A. Alsaedi; T. Hayat; X. Wang; *Environ. Poll.*, **2018**, *240*, 493–505
28. X. He; X. Qiu; C. Hu; Y. Liu; *J. Disp. Sci. Technol.*, **2018**, *39*, 792–801
29. X. Li; D. Du; Y. Zhang; W. Xing; Q. Xue; Z. Yan; *J. Mater. Chem. A*, **2017**, *5*, 15460–15485
30. L. Mohapatra; K. Parida; *J. Mater. Chem. A*, **2016**, *4*, 10744–10766
31. M.J. Wu; J.Z. Wu; J. Zhang; H. Chen; J.Z. Zhou; G.R. Qian; Z.P. Xu; Z. Du; Q. L. Rao; *Catal. Sci. Technol.*, **2018**, *8*, 1207–1228
32. K. Yan; Y. Liu; Y. Lu; J. Chai; L. Sun; *Catal. Sci. Technol.*, **2017**, *7*, 1622–1645.

33. M. Xu; M. Wei; *Adv. Funct. Mater.*, **2018**, *28*, 1802943:1–20
34. T. Li; H.N. Miras; Y.-F. Song; *Catalysts* **2017**, *7*, 260:1–17
35. K. Takehira; *Appl. Clay Sci.*, **2017**, *136*, 112–141
36. P. Sipos; I. Pálinkó; *Catal. Today*, **2018**, *306*, 32–41
37. S.B. Ötvös; I. Pálinkó; F. Fülöp; *Catal. Sci. Technol.*, **2019**, *9*, 47–60 (2019).
38. V. Tóth; M. Sipiczki; A. Pallagi; Á. Kukovecz; Z. Kónya; P. Sipos; I. Pálinkó; *Chem. Pap.*, **2014**, *68*, 633−637
39. F. Cavani; F. Trifiró; A. Vaccari; *Catal. Today,* **1991**, *11*, 173−301
40. A. Inayat; M. Klumpp; W. Schwieger; *Appl. Clay Sci.*, **2011**, *51*, 452–459
41. C. Forano; T. Hibino; F. Leroux; C. Taviot-Guého; Ch.13.1: Layered double hydroxides in *Handbook of Clay Science*, *Developments in Clay Science*, F. Bergaya; B.K.G. Theng; G. Lagaly; Eds; Elsevier Ltd 2006, Vol. 1, pp. 1021−1095.
42. I. Pálinkó; Nanostructures in confined environments in *Encyclopedia of Nanoscience and Nanotechnology*, H.S. Nalwa; Ed; American Scientific Publishers, 2011, Vol. 19, pp. 183–198.
43. A.I. Khan; D. O'Hare; *J. Mater. Chem.*, **2002**, *12*, 3191–31918
44. G. Choi; J.-H. Yang; G.-Y. Park; A. Vinu; A. Elzatahry; C.H. Yo; J.-H. Choy; *Eur. J. Inorg. Chem.*, **2015**, 925–930
45. Zs. Ferencz; M. Ádok-Sipiczki; I. Hannus; P. Sipos; I. Pálinkó; *J. Mol. Struct.*, **2015**, *1090*, 14−18
46. B.M. Choudary; B. Kavita; N.S. Chowdary; B. Sreedhar; M.L. Kantam; *Catal. Lett.*, **2002**, *78*, 373−377
47. S. Miyata; *Clays Clay Miner.*, **1980**, *28*, 50−56
48. M. Sipiczki; E. Kuzmann; I. Pálinkó; Z. Homonnay; P. Sipos; Á. Kukovecz; Z. Kónya; *Hyperfine Interactions*, **2014**, *226*, 171−179
49. M. Szabados; R. Mészáros; Sz. Erdei; Z. Kónya; Á. Kukovecz; P. Sipos; I. Pálinkó; *Ultrason. Sonochem.*, **2016**, *31*, 409−416
50. M. Szabados; G. Varga; Z. Kónya; Á. Kukovecz; S. Carlson; P. Sipos, I. Pálinkó; *Ultrason. Sonochem.*, **2018**, *40*, 853–860
51. V.R. Khusnutdinov; V.P. Isupov; *Chem. Sustain. Dev.*, **2007**, *15*, 367–372
52. W. Tongamp; Q. Zhang; F. Saito; *J. Mater. Sci.*, **2007**, *42*, 9210−9215
53. A.N. Ay; B. Zümreoglu-Karan; L. Mafra; *Z. Anorg. Allg. Chem.*, **2009**, *635*, 1470−1475
54. M. Milanesio; E. Conterosito; D. Viterbo; L. Perioli; G. Croce; *Cryst Growth & Des.*, **2010**, *10*, 4710–4712
55. A. Hayashi; H. Nakayama; *Chem. Lett.*, **2010**, *39*, 1060−1062
56. Zs. Ferencz; Á. Kukovecz; Z. Kónya; P. Sipos; I. Pálinkó; *Appl. Clay Sci.*, **2015**, *112–113*, 94–99
57. Zs. Ferencz; M. Szabados; G. Varga; Z. Csendes; Á. Kukovecz; Z. Kónya; S. Carlson; P. Sipos; I. Pálinkó; *J. Solid State Chem.*, **2016**, *233*, 236−243
58. Zs. Ferencz; M. Szabados; M. Ádok-Sipiczki; Á. Kukovecz; Z. Kónya; *J. Mater. Sci.*, **2014**, *49*, 8478−8486
59. M. Szabados; Z. Kónya; Á. Kukovecz; P. Sipos; I. Pálinkó; *Appl. Clay Sci.*, **2019**, *174*, 138−145

60. M. Szabados; Cs. Bús; M. Ádok-Sipiczki; Z. Kónya; Á. Kukovecz; P. Sipos; I. Pálinkó; *Particuology*, **2016**, *27*, 29–33
61. M. Szabados; K. Pásztor; Z. Csendes; Sz. Muráth; Z. Kónya; Á. Kukovecz; P. Sipos; I. Pálinkó; *Ultrason. Sonochem.*, **2016**, 32, 173−180
62. M. Szabados; A.A. Ádám; Z. Kónya; Á. Kukovecz; S. Carlson; P. Sipos; I. Pálinkó; *Ultrason. Sonochem.* **2019**, *55*, 165–173
63. V. Bugris; H. Haspel; Á. Kukovecz; Z. Kónya; M. Sipiczki; P. Sipos; I. Pálinkó; *J. Mol. Struct.*, **2013**, *1044*, 26−31
64. V. Bugris; H. Haspel; Á. Kukovecz; Z. Kónya; M. Sipiczki; P. Sipos; I. Pálinkó; *Langmuir*, **2013**, *29*, 13315−13321
65. G. Varga; Á. Kukovecz; Z. Kónya; L. Korecz; Sz. Muráth; Z. Csendes; G. Peintler; S. Carlson; P. Sipos; I. Pálinkó; *J. Catal.*, **2016**, *335*, 125−134
66. G. Varga; Sz. Ziegenheim; Sz. Muráth; Z. Csendes; Á. Kukovecz; Z. Kónya; S. Carlson; L. Korecz; E. Varga; P. Pusztai; P. Sipos; I. Pálinkó; *J. Mol. Catal. A*, **2016**, *423*, 49–60
67. G. Varga; Z. Timár; Sz. Muráth; Z. Kónya; Á. Kukovecz; S. Carlson; P. Sipos; I. Pálinkó; *Top. Catal.*, **2017**, *60*, 1429–1438
68. G. Varga; Z. Timár; Sz. Muráth; Z. Kónya; Á. Kukovecz; S. Carlson; P. Sipos; I. Pálinkó; *Catal. Today*, **2018**, *306*, 42–50
69. G. Varga; Z. Kónya; Á. Kukovecz; P. Sipos; I. Pálinkó; *J. Mol. Struct.*, **2019**, *1179*, 263–268
70. D. Srankó; A. Pallagi; E. Kuzmann; S.E. Canton; M. Walczak; A. Sápi; Á. Kukovecz; Z. Kónya; P. Sipos; I. Pálinkó; *Appl. Clay Sci.*, **2010**, *48*, 214–217
71. D. Srankó; M. Sipiczki; É.G. Bajnóczi; M. Darányi,; Á. Kukovecz; Z. Kónya; S. E. Canton; K. Norén; P. Sipos; I. Pálinkó; *J. Mol. Struct.*, **2011**, *993*, 62–66
72. M. Szabados; Z. Kónya; Á. Kukovecz; P. Sipos; I. Pálinkó; *J. Solid State Chem.*, **2019**, *272*, 227–233
73. M. Sipiczki; E. Kuzmann; Z. Homonnay; J. Megyeri; I. Pálinkó; P. Sipos; *J. Mol. Struct.*, **2013**, *1044*, 116−120
74. V. Bugris; M. Ádok-Sipiczki; T. Anitics; E. Kuzmann; Z. Homonnay; Á. Kukovecz; Z. Kónya; P. Sipos; I. Pálinkó; *J. Mol. Struct.*, **2015**, *1090*, 19−24
75. S.P. Newman; S.J. Williams; P.V. Coveney; W. Jones; *J. Phys. Chem. B*, **1998**, *102*, 6710−6719
76. P. Kovář; M. Pospíšil; M. Nocchetti; P. Čapková; K. Melánová; *J. Mol. Model.*, **2007**, *13*, 937−942
77. K. Yamaguchi; K. Mori; T. Mizugaki; K. Ebitani; K. Kaneda; *J. Org. Chem.*, **2000**, *65*, 6897–6903
78. M. Sipiczki; A.A. Ádám; T. Anitics; Z. Csendes; G. Peintler; Á. Kukovecz; Z. Kónya; P. Sipos; I. Pálinkó; *Catal. Today*, **2015**, 241, 231−236
79. S.B. Ötvös; Á. Georgiádes; R. Mészáros; K. Kis; I. Pálinkó; F. Fülöp; *J. Catal.*, **2017**, *348*, 90–99
80. E. Coronado; J.R. Galán-Mascarós; C. Martí-Gastaldo; A. Ribera; *Chem. Mater.*, **2006**, *18*, 6112–6114
81. S. Bhattacharjee; J.A. Anderson; *Chem. Commun.*, **2004**, 554–555
82. S. Bhattacharjee; J.A. Anderson; *Catal. Lett.*, **2004**, *95*, 119−125

83. S. Bhattacharjee; T.J. Dines; J.A. Anderson; *J. Catal.*, **2004**, *225*, 398−407
84. S. Bhattacharjee; J.A. Anderson; *Adv. Synth. Catal.*, **2006**, *348*, 151−158
85. S. Bhattacharjee; T.J. Dines; J.A. Anderson; *J. Phys. Chem. C*, **2008**, *112*, 14124–14130
86. L. Dai; J. Zhang; X. Wang; Y. Chen; *RSC Advances*, **2013**, *3*, 19885–19888
87. Y. Liu; Z. An; L. Zhao; H. Liu; J. He; *Ind. Eng. Chem. Res.*, **2013**, *52*, 17821−17828
88. B. Monteiro; S. Gago; S.S. Balula; A.A. Valente; I.S. Gonçalves; M. Pillinger; *J. Mol. Catal. A*, **2009**, *312*, 23–30
89. X. Wang; G. Wu; X. Liu; C. Zhang; Q. Lin; *Catal. Lett.*, **2016**, *146*, 620–628
90. K.M. Parida; M. Sahoo; S. Singha; *J. Mol. Catal. A*, **2010**, *329*, 7–12
91. J. Marreiros; M. Diaz-Coucea; M.J. Ferreira; D. Pedro; P.D. Vaz; M.J. Calhorda; C.D. Nunes; *Inorg. Chim. Acta*, **2019**, *486*, 274–282
92. J.-H. In; S.-E. Park; R. Song; W. Nam; *Inorg. Chim. Acta*, **2003**, *343*, 373−376
93. F. Ullmann; P. Sponagel; *Chem. Ber.*, **1905**, *38*, 2211−2212
94. F. Monnier; M. Taillefer; *Angew. Chem. Int. Ed.*, **2009**, *48*, 6954–6971
95. B.M. Choudary; B. Kavita; N.S. Chowdari; B. Sreedhar; M.L. Kantam; *Catal. Lett.*, **2002**, *78*, 373–377
96. Z. An; W. Zhang; H. Shi; J. He; *J. Catal.*, **2006**, *241*, 319–327
97. M. Sipiczki; D.F. Srankó; Gy. Szőllősi; Á. Kukovecz; Z. Kónya; P. Sipos; I. Pálinkó; *Top. Catal.*, **2012**, *55*, 858–864 (2012)
98. R. Bruckner in *Organic Reaction Mechanisms. Reactions, Stereochemistry and Synthesis*, M. Harmata; Ed; Springer-Verlag Berlin Heidelberg, 2010, p. 530.
99. S.B. Ötvös; Á. Georgiádes; M. Ádok-Sipiczki; R. Mészáros; I. Pálinkó; P. Sipos; F. Fülöp; *Appl. Catal. A*, **2015**, 501, 63−73 (2015)

STUDIA UBB CHEMIA, LXIV, 3, 2019 (p. 47-58)
(RECOMMENDED CITATION)
DOI:10.24193/subbchem.2019.3.04

GREEN CATALYTIC SYNTHESIS OF PHENPROCOUMON

NATALIA CANDU[a], ANDRAS TOMPOS[b], EMILIA TALAS[b], MADALINA TUDORACHE[b], SIMONA M. COMAN[a,*]

ABSTRACT. The catalytic potential of triflate-based activated carbon composites has been investigated in phenprocoumon (C_3-alkylated compound) synthesis, through the alkylation of 4-hydroxycoumarin with phenyl-ethyl-carbinol. The main reaction products are O- and C_3-alkylated compounds. However, O-alkylated product is more easily produced to the detriment of the C_3-alkylated compound, the selective synthesis of the last being a challenge in these conditions. Both the conversion of 4-hydroxycoumarin and the selectivity to C_3-alkylated compound is highly influenced by the physico-chemical characteristics of the catalysts and the reaction conditions. The highest 4-hydroxycoumarin conversions (16.0-30.0%) and selectivity to phenprocoumon (94.0-99.7%) were achieved with triflate-based activated carbon composites, characterized by the existence of strong Brønsted acid sites, optimal Lewis/Brønsted acid ratio, and bimodal micro-/mesoporosity.

Keywords: *triflic acid; activated carbon, Friedel-Crafts alkylation, 4-hydroxycoumarin; phenprocoumon*

INTRODUCTION

Traditionally, the syntheses of fine chemicals and pharmaceutical intermediates are carried out in liquid-phase, either by using stoichiometric processes or homogeneous acid-base catalysis. Among these syntheses, the Friedel-Crafts alkylation is widely used in a great variety of commercially-important products. However, this process commonly encounters drawbacks such as problems of waste disposal, salt formation and difficulties for the catalyst separation and recycling.

[a] *University of Bucharest, Faculty of Chemistry, Department of Organic Chemistry, Biochemistry and Catalysis, 4-12 Blvd. Regina Elisabeta, Bucharest 030016, Romania*
[b] *Hungarian Academy of Sciences, Institute of Materials and Environmental Chemistry, Research Centre for Natural Sciences, 1117 Budapest, Hungary.*
** Corresponding author: simona.coman@chimie.unibuc.ro*

Two important examples which involve, as a key-step, the Friedel-Crafts alkylation are the synthesis of (all-*rac*)-[α]-tocopherol (Vitamin E) which displays important antioxidant properties, and the synthesis of vitamin K_1, an important compound in the control of blood clotting [1-5]. The processes use either trimethylhydroquinone (TMHQ) or menadiol acetate (MDA) as substrates and isophytol (IP) as alkylating agent. In both cases, the search for highly efficient, heterogeneous catalysts, which might replace presently used homogeneous catalysts, is a challenging task. In this context, we have recently shown that hydroxylated nanoscopic fluorides (MgF_2 and AlF_3), with bi-acidic (Lewis/Brønsted) properties, can be successfully applied as highly efficient catalytic alternative to the homogeneous ones [6, 7].

Coumarins are part of one of the most important classes of heterocyclic compounds, which possess a range of important biological activities such as anti-inflammatory, antioxidant, antiallergic, hepatoprotective, antithrombotic, antiviral, antibiotic, and cytotoxic [8-10]. In particular, 4-hydroxycoumarins and its C_3-alkylated derivatives are of great interest due to their use as anticoagulant rodenticides and antithrombotic agents (i.e., warfarin, difetialone, bromadiolone, coumatetralone, and flocoumafen). However, the selective C_3-alkylation of 4-hydroxycoumarin is one of the most difficult reactions in synthetic chemistry. As in the case of vitamins E and K_1, most of these methodologies use strong acids as homogeneous catalysts (*ie*, H_2SO_4, HCl, $Yb(OTf)_3$, $FeCl_3$ x $6H_2O$, $Bi(OTf)_3$, and TMSOTf) [11-14]. Therefore, these processes are also associated with problems such as high toxicity, corrosion, and difficulty in catalysts separation and recovery. Moreover, some of these catalytic systems have certain limitations such as long reaction time and low yields. Therefore, the development of novel heterogeneous catalytic methods for the selective C_3-alkylation of 4-hydroxycumarin with alcohols as alkylating agents, is highly desirable and of a great interest for pharmaceutical industry. In this context, sulfated tin oxide (SO_4^{2-}/SnO_2) has been found to be an efficient solid catalyst for the C_3-benzylation of 4-hydroxycoumarin with secondary benzyl alcohols as alkylating agents but also for the O-alkylation with secondary benzyl acetates [15]. However, information upon the catalyst recyclability and its reuse is totally missing.

Taking into account the above considerations and the high scientific and economic interest in the development of new efficient solid catalysts for alkylation processes, here we report the Friedel-Crafts alkylation of 4-hydroxycumarin with phenyl-ethyl-carbinol as alkylating agent, in the presence of acid-based solid catalysts, such as triflate-based activated carbons. The possibility of O-alkylated formation being formed is higher than the probability of C_3-alkylated product formation. However, as a function of the catalyst nature the C_3-alkylated product can be favoured to the detriment of O-alkylation, as the obtained results in this study demonstrated.

RESULTS AND DISCUSSION

It is already known that the general mechanism of the catalytic Friedel-Crafts alkylations involves an initial interaction of the alkylating agent (E) with the acid catalyst to form an activated electrophile, E^+, which subsequently adds to the nucleophile aromatic ring with the formation of the Wheland intermediate (**1**) [16]. The subsequent elimination of proton forms the Friedel-Crafts alkylated product and restores the acid sites of the catalyst (Eq. 1):

$$E^+ + ArH \longrightarrow \underset{\mathbf{1}}{[E\text{-}Ar\text{-}H^+]} \longrightarrow E\text{-}Ar + H^+ \qquad \text{Eq. 1}$$

In these conditions, the activated electrophile (E^+) exists as a more or less tight ion pair, with a considerable degree of covalent bonding between the carbocation and the catalyst macroanion. Therefore, the nature of the catalyst has a considerable influence on the reactivity and selectivity of the alkylating agent, its relative stability being very important for determining the rate of alkylation. On the other hand, the reactivity of the aromatic nucleophile is governed by its ability to delocalize the positive charge in the Wheland intermediate (**1**) by inductive and resonance effects [16].

The application of the earlier developed hydroxylated nanoscopic fluorides [6, 7] failed in the development of a selective C_3-alkylation process of 4-hydroxycoumarin. This situation demonstrate that, indeed, the successful application of the Friedel-Crafts alkylation is strongly influenced by the reaction system features as the catalyst nature, the reaction conditions and the alkylating agent reactivity, their optimal combination being essential for the selective alkylation, in this case - for the selective synthesis of phenprocoumon (namely, C_3-alkylation in the detriment of O-alkylation). Scheme 1 shows the reaction pathways alkylation of 4-hydroxycoumarin with phenyl-ethyl-carbinol.

Initial catalytic tests (Table 1) were made by uses of different commercial carbon carriers (Ketjenblack EC-300J (KB), Vulcan XC-72R (V) and Black Pearls 2000 (BP)) impregnated with Nafion (*ie*, 40wt% and 80wt%). Obtained materials contained strong ~SO_3H groups with measured densities (meq/g_{cat}) of 0.29 and 0.45, respectively. Also, in order to modulate the optimum density of strong ~SO_3H Brønsted acid sites for the selective C_3-alkylation process to phenprocoumon, the Nafion content was varied from 10 wt% to 80wt% and the materials were calcined in nitrogen, at 200°C, for 4h, in order to make the surface layer more compact. Obtained samples contain 0.09-0.45 meq/g_{cat} of ~SO_3H groups.

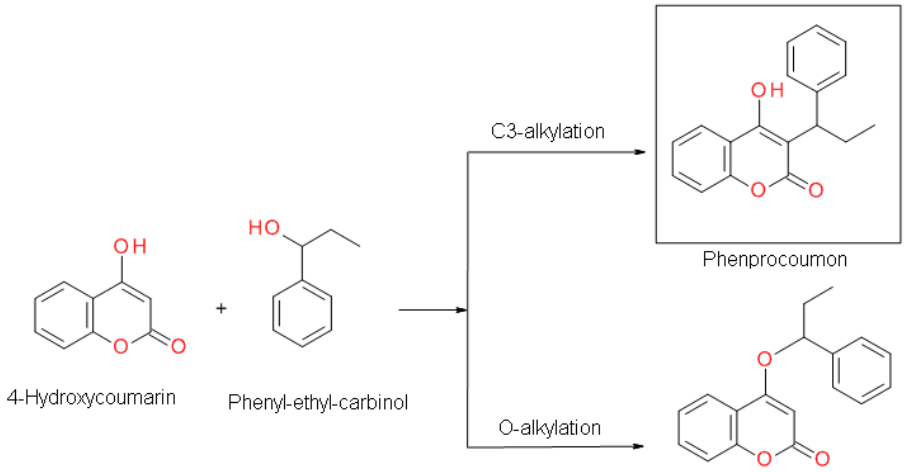

Scheme 1. The O-/C_3-alkylation of 4-hydroxycoumarin with phenyl-ethyl-carbinol

As Table 1 shows, the catalysts became active only for a –SO_3H sites densities of 0.45 meq_{SO3H}/g_{cat}.

Table 1. Catalytic performances of nafion-based catalysts

Entry	**Catalyst**	**Meq_{SO3H}/g_{cat}**	**X (%)**	**TOF (h^{-1})**	**TON**	**$S_{C\text{-alkylated}}$ (%)**	**$S_{O\text{-alkylated}}$ (%)**
1	V-40	0.29	0	0	0	0	0
2	KB-40	0.29	0	0	0	0	0
3	BP-40	0.29	1.6	0.6	1.1	100	0
4	V-80	0.45	5.6	1.2	2.5	100	0
5	BP-80	0.45	0.5	0.1	0.2	100	0
6	KB-80	0.45	0.1	0.02	0.04	100	0
7	BP-10-200*	0.09	0.2	0.2	0.4	0	100
8	BP-20-200*	0.17	1.1	0.6	1.3	0	100
9	BP-40-200*	0.29	0.8	0.3	0.6	0	100
10	BP-80-200*	0.45	0.9	0.2	0.4	0	100

*KB - Ketjenblack EC-300J, V - Vulcan XC-72R, BP - Black Pearls 2000; * - samples calcined in nitrogen, at 200°C, for 4 h Reaction conditions: 1mmol 4-hidroxycoumarin, 1mmol phenyl-ethyl-carbinol, 50 mg catalyst, 10 ml methanol, 80°C, 2h*

Even so, alkylation reaction takes place with low conversions of 4-hydroxycoumarin. Very important, the selectivity toward C_3-alkylated product was 100%, irrespective of the conversion level. The highest conversion was obtained in the presence of V-48 sample (Table 1, entry 4). After 24h, in the

presence of the same catalyst, the 4-hydroxycoumarin conversion increased at 11.0%, while, changing the solvent from methanol to acetonitrile, after a similar reaction time, the conversion increased 17.1%. In both cases the selectivity remained 100% in the favour of C_3-alkylated product.

Unexpected, in the presence of calcined samples (Table 1, entries 7-10), O-alkylated compound was the only evidenced product (100% selectivity), even if the density of the $–SO_3H$ sites remained unchanged after the calcination process. At the moment it is not clear what provoked this inversion in the alkylation selectivity as the Nafion is considered as a stable compound up to 300°C [17]. However, since in the case of non-calcined samples part of Nafion was leached during the catalytic reactions, we may assume that the presence of Brønsted acid sites in the homogeneous phase favours the C_3-alkylation pathway in the detriment of the O-alkylation. Nevertheless, due to its chemical instability the catalytic system was abandoned.

A second type of tested acid-based composites involved the oxidation of the activated carbons followed by their impregnation with triflic acid (Scheme 2). Most probably, the functionalization of the activated carbons surface with triflate groups takes place through a similar mechanism to that proposed by Perego et al. [18] and confirmed by Coman et al. [19], in which triflic acid reacts with vicinal hydroxyl groups yielding a bipodally anchored triflate to the carrier surface. Moreover, the resulting water from the esterification reaction may be coordinated to the grafted triflate, generating a strongly hydrated triflic acid onto the activated carbon surface, less prone to leaching.

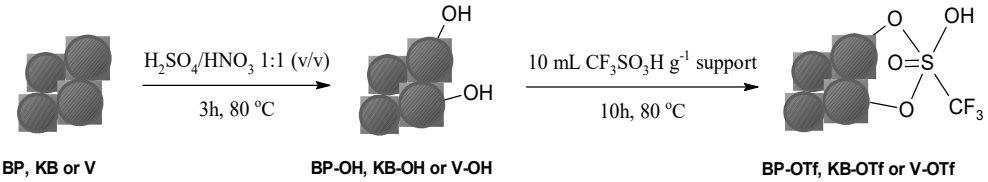

Scheme 2. The preparation of triflic acid-based activated carbon catalysts

Indeed, the FTIR analysis of the triflate-based AC samples (V-OTf, KB-OTf and BP-OTf) evidenced the successful anchoring of triflic acid. Therefore, in the IR spectra, the two bands located at 3410 cm^{-1} (νsOH) and 1695 cm^{-1} (νsC=O) indicate the successful oxidation of AC. However, very important are the bands located at 950 cm^{-1} and 1120 cm^{-1}, respectively, which correspond to the νsC-F and νsS=O of triflic acid, in agree with literature [20, 21]. For exemplification, the FTIR spectrum of V-OTf sample is given in Figure 1.

The XRD patterns of V-OTf sample before and after the grafting of triflic acid display the characteristic diffraction lines of the carbon materials, at 2θ of approximately 25° and 44°, respectively [22]. The presence of the diffraction line at around 24.85° (Figure 2) confirms that Vulcan carrier possesses an intermediate structure between amorphous and graphitic, called turbostratic structure, in agree with literature [23].

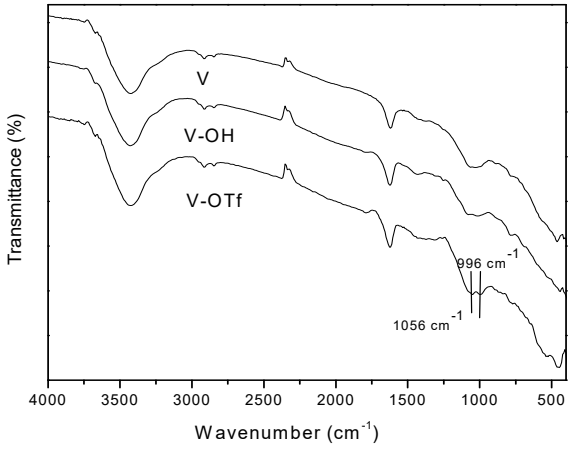

Figure 1. FTIR spectra of V, V-OH and V-OTf samples

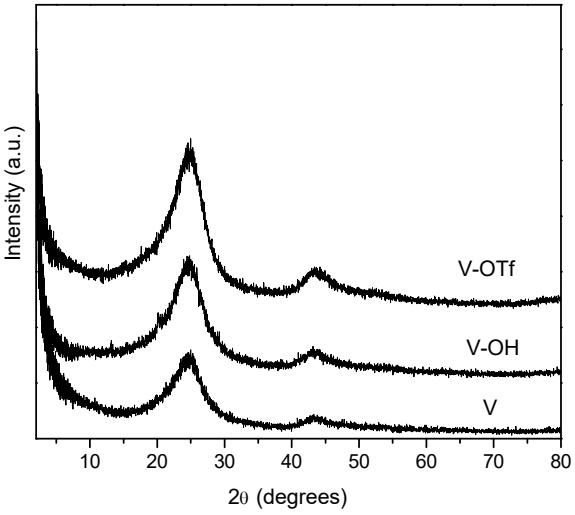

Figure 2. XRD patterns of V, V-OH and V-OTf samples

Due to its structure, black carbon Vulcan exhibits a high resistance to thermal decomposition. Indeed, the thermogravimetric (TG) analysis of the black carbon Vulcan (V) shows a mass loss of 53.74% at temperatures higher than 700°C. Oxidized sample (V-OH) loses only 34.58% from the initial mass while the sample modified with triflic acid (V-OTf) registered a total loss mass (100%) (Figure 3).

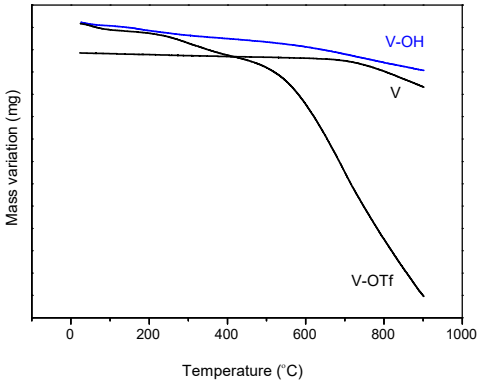

Figure 3. TG analysis of the V, V-OH and V-OTf samples

A water loss, accompanied by an endothermic effect, was observed in both V-OH and V-OTf samples, at temperatures lower than 100°C (Figure 4). An exothermic decomposition, with a maximum at 760°C was registered for the pristine carrier (sample V) while, the exothermic decomposition of the V-OH sample registered a maximum at 668°C. However, in the case of V-OTf sample, two exothermic effects, with maximum at 611 and 738°C, respectively, were registered.

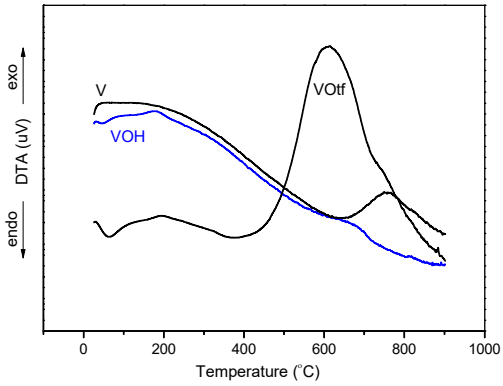

Figure 4. DTA analysis of the V, V-OH and V-OTf samples

Clearly, the functionalized V-OTf sample is less resistant to the thermal decomposition, this behavior being attributed to the partial destruction of its morphology during the treatment with triflic acid.

Pristine Vulcan sample had a relatively high surface area (S_{sp} = 254 m^2/g), a total pore volume of 0.67 cm^3/g and a bimodal meso-microporosity. After its oxidation and treatment with triflic acid a decrease of surface area till 225 m^2/g was registered, most probably due to a partially destruction of the carbon morphology, in agree with TG-DTA results.

In the case of triflate-based samples, the best results under reflux conditions were obtained in the presence of V-OTf catalyst and acetonitrile solvent. Therefore, after 24h of reaction the 4-hydroxycoumarin conversion reached 11.9%, with a total selectivity to the target product (C_3-alkylated product, namely phenprocoumon). Longer reaction times result in an increased conversion but a highly decreased selectivity to C_3-alkylated product (14.1%). The difference till 100% was completed by O-alkylated product, and low amounts of ethers produced from two molecules of phenyl-ethyl-carbinol.

Important improvements were, however, obtained when the alkylation reactions were rune in steel autoclave, under autogenic pressure (Table 2).

Table 2. Catalytic performances of the triflic acid-based catalysts under autogenic pressure

Entry	Catalyst	Time (h)	X (%)	$S_{C3\text{-alkylated}}$ (%)
1	V-OTf	12	28.2	99.7
2		24	30.1	98.7
3	KB-OTf	12	16.5	99.4
4		24	27.2	94.0
5	BP-OTf	12	23.3	95.8
6		24	28.2	94.4

Reaction conditions: 0.2 g 4-hydroxycoumarin, 0.2 g phenyl-ethyl-carbinol, 0.05 g catalyst, 5 ml acetonitrile, 150 ºC.

As Table 2 shows the presence of the V-OTf catalyst containing strong acid sites generated by the grafted triflate groups lead to a high increase of the conversion of 4-hydroxycoumarin (28.2%, Table 2, entry 1) after 12 h reaction yielding phenprocoumon (C3-alkylated products) with a remarkable 99.7% selectivity level. Unfortunately, a prolongation of the reaction time does not improve in high extend the conversion (30.1%, Table 2, entry 2) and lead to a decreased selectivity to phenprocoumon (98.7%, Table 2, entry 2), due to the formation of O-alkylated product. However, the

high selectivity to phenprocoumon has been well preserved during the V-OTf catalyst recycling, thus, confirming the presence of sulfonic species covalently bonded to the V carbon surface. Similar trends were observed irrespective of the used catalyst. Neither the change of the solvent nature or the variation of the reaction temperature was able to combine a high conversion of the 4-hydroxycoumarin with a high selectivity to phenprocoumon. Nevertheless, such performances can be obtained by adding higher amounts of catalyst in the reaction system.

At the moment, it is not entirely clear as to whether the total number of acidic sites has an influence upon the alkylation reaction, but it is obvious that both the presence of Brønsted acid sites and the Lewis/Brønsted acid site ratio are essential to promote the C_3-alkylation synthesis. It seems that the optimal acidic strength and the optimal combination of Lewis/Brønsted acid sites were generated in the sample V-OTf. Moreover, the decreasing alkylation rate is accompanied by an increasing of the C_3-alkylation selectivity. This effect may seem to be disadvantageous but catalytic syntheses with high selectivity into the target product are always preferred to those able to convert a substrate in high level to a large number of reaction products with individual low yields.

CONCLUSIONS

The synthesis of phenprocoumon is part of the organic synthesis from pharmaceutical industry which generates large amounts of waste, environmentally damaging.

A greener alternative to the classical methodology is the catalytic alkylation of 4-hydroxycoumarin with phenyl-ethyl carbinol. The O-/C_3-alkylation reaction rate ratio can be modulated in the favor of the C_3-alkylation by varying the chemical properties of the catalysts and the reaction conditions. The presented work showed that, irrespective of the catalysts nature, the 4-hydroxycoumarin conversions were from low to moderate levels. However, this cannot be considered a disadvantage as long as the selectivity to the target product can be improved till 100%. The developed systems bring a number of advantages in line with the principles of green chemistry, such as: the use of an alcohol (ie, phenyl-ethyl-carbinol) as alkylating agent, the use of substrate/reactant ratio of 1/1, the use of stable and recyclable solid catalysts, the synthesis of the target product (*ie*, C_3-alkylated product, phenprocoumon) with 100% selectivity. The above reaction system features eliminate a potential risk to the environment and simplify the product purification procedure, bringing essential advantages from the green chemistry point of view.

EXPERIMENTAL SECTION

Catalysts preparation

Commercial active carbon (AC) supports, purchased from Akzon Noble and Cabot, such as Ketjenblack EC-300J (KB, S_{sp} = 829 m^2/g; size particles of 30-40 nm), Vulcan XC-72R (V, S_{sp} = 254 m^2/g; size particles of 30 nm), and Black Pearls 2000 (BP, S_{sp} = 1475 m^2/g; size particles of 15 nm) were used for the preparation of the catalytic composites.

Nafion (ie, perfluorosulfonic polymer with terminal sulfonic groups) was deposited on each of the supports by wet impregnation, as follows: 3g of active carbon were dispersed in 150ml of 1-propanol. The obtained mixture was maintained under magnetic stirring for 30 minutes, at room temperature, and another 30 minutes under ultrasound radiation. Then, the corresponding amount of Nafion (10-80 wt%) was added under stirring and maintained for 30 minutes at room temperature, and another 30 minutes under ultrasound radiation. The solvent was evaporated at 85°C under vacuum and the obtained sample was dried at 110°C for 12h. Other serie of Nafion-based activated carbon composites, with different amounts of Nafion were calcined in nitrogen, at 200°C, for 4h.

The grafting of triflic acid onto V, KB and BP active carbons followed a procedure in two steps. In the first step, the activated carbon was oxidized with HNO_3 and H_2SO_4 under the following conditions: 1g of active carbon was kept in 50 ml of acid (25 ml of HNO_3 + 25 ml of H_2SO_4) under ultrasound radiation, for 1h, at 60°C, then washed to pH neutral and dried at 120°C, for 24 hours. Subsequently, the obtained material was treated with concentrated triflic acid (CF_3SO_3H, 10ml) and heated at 80°C for 10h. To remove the physical adsorbed residual triflic acid, the samples were washed with distilled water to neutral pH and dried at 120°C for 8 h. The obtained samples were abbreviated as V-OTf, KB-OTf and BP-OTf, respectively.

Catalysts characterisation

The obtained catalysts have been characterized by techniques such as TG-DTA, XRD and IR spectroscopy. TG-DTA characterization was performed with a TA Instruments SDT Q600, in the range of 25-900°C (10°C/min) and under nitrogen flow (20mL/min). XRD measurements were made with a Siemens D5000 diffractometer with CuK_α radiation (X = 1.5418 Å) with a scanning speed of 2 degrees/min, between 2° and 80°. FTIR spectra were measured with a Thermo-Nicolet FTIR apparatus, in the range of 500-4000 cm^{-1}, at room temperature (400 scans with a resolution of 4 cm^{-1}).

Catalytic tests

In a round bottom flask was added 10 ml of solvent (methanol or acetonitrile), 0.162 g (1 mmol) of 4-hydroxycoumarin and 0.136 g (1 mmol) of phenyl-ethyl-carbinol. Once the reactants have been dissolved, 50 mg of the catalyst was added, and the temperature has been raised at the boiling temperature typical of the solvent. The reaction is allowed to stir and reflux continuously for 2 - 48 h. Parallel tests have been made in steel autoclave, under autogenic pressure, as follow: 10 ml of solvent was added followed by the addition of 0.081 g - 0.162 g (0.5 mmol / 1.0 mmol) of 4-hydroxycoumarin and 0.136 g (1 mmol) of phenyl-ethyl carbinol. Once the reactants have been dissolved, 50 mg of the catalyst is added and the autoclave closed. The reaction is allowed to stir for 24 hours at the boiling temperature characteristic of the solvent.

After reaction, irrespective of the applied methodology, after the catalyst separation by filtration, the reaction products were analyzed by liquid chromatography (HPLC, Zorbax Eclipse Plus C18 column, eluent: AcCN:H_2O (75:25), wavelength: 274 nm) and identify by ^{1}H- and ^{13}C-RMN spectroscopy (Bruker Fourier, 300 MHz, standard: TMS (trimethyl silane), solvent: deuterated dimethyl sulfoxide (d-DMSO)).

ACKNOWLEDGMENTS

The authors are grateful to Dr. Florea Cocu (National Institute for Chemical-Pharmaceutical Research and Development, Bucharest, Romania) who took care on the synthesis of the investigated organic substrates.

REFERENCES

1. W. Bonrath, M. Eggersdorfer, T. Netscher, *Catal. Today*, **2007**, *121*, 45-57.
2. C. Schneider, *Mol. Nutr. Food Res.*, **2005**, *49*, 7-30.
3. J.M. Tucker, D.M. Townsend, *Biomed. Pharmacother.,* **2005**, *59*, 380-387.
4. K. Saldeen, T. Saldeen, *Nutr. Res.*, **2005**, *25*, 877-889.
5. A. Rüttimann, *Chimia*, **1986**, *40*, 290-306.
6. S.M. Coman, S. Wuttke, A. Vimont, M. Daturi, E. Kemnitz, *Adv. Synth. & Catal*., **2008**, *350*, 2517-2524.
7. S.M. Coman, V.I. Parvulescu, S. Wuttke, E. Kemnitz, *Chem. Cat. Chem,* **2010**, *2*, 92–97.

8. Ch. Raji Reddy, B, Srikanth, N. Narsimha Rao, D.-S. Shin, *Tetrahedron,* **2008**, *64*, 11666-11672.
9. R.D.H. Murray, J. Mendez, S.A. Brown, “The Natural Coumarins: Occurrence, Chemistry, and Biochemistry”, John Wiley & Sons, New York, NY, USA, **1982**.
10. V. Narayana, R. Varala, V. Kotra, P.K. Zubaidha, *Research & Reviews: J. Chem*., **2013**, *2*, 1-6.
11. E. Enders*, Angew. Chem.,* **1957**, *69*, 481-481.
12. W. Huang, J. Wang, Q. Shen, X. Zhou, *Tetrahedron,* **2007**, *63*, 11636-11643.
13. R. Rueping, B.J. Nachtsheim, E. Sugiono, *Synlett*, **2010**, 1549-1553.
14. P. N. Chatterjee, S. Roy, *Tetrahedron,* **2011**, *67*, 4569-4577.
15. V. Narayana, R. Varala, P. Zubaidha, *Int. J. Org. Chem.*, **2012**, *2*, 287-294.
16. M.C. Clark, C. Morris Smith, D.L. Stern, J.S. Beck, "Handbook of Heterogeneous Catalysis (second, completely revised and enlarged edition)", G. Ertl, H. Knozinger, F. Schuth, J. Weitkamp (Eds.), vol. 7, WILEY-VCH Verlag GmbH & Co.KGaA, **2008**, pp.3153.
17. Q. Deng, C.C. Wilkie, R.B. Moore, K.A. Mauritz, *Polymer*, **1998**, 39, 5961-5972.
18. A. De Angelis, C. Flego, P. Ingallina, L. Montanari, M. Clerici, C. Carati, C. Perego, *Catal. Today*, **2001**, *65*, 363-371.
19. I. Podolean, F. Anita, H. García, V.I. Parvulescu, S.M. Coman, *Catal. Today*, **2017**, *279*, 45-55.
20. L. Plasseraud, B. Therrien, A. Růžička, H. Cattey, *Inorg. Chem. Acta,* **2012**, *380,*50-56.
21. A. de Angelis, C. Flego, P. Ingallina, L. Montanari, M.G. Clerici, C. Carati, C. Perego, *Catal. Today,* **2001**, *65,* 363-371.
22. JCPDS (**2001**) International Centre for Diffraction Data 25-0284. (www.icdd.com)
23. M.J. Lázaro, L. Calvillo, V. Celorrio, J.I. Pardo, S. Perathoner, R. Moliner, "Carbon Black: Production, Properties and Uses", I.J. Sanders, T.L. Peeten (Eds.), Ch. 2, "Study and application of carbon black Vulcan XC-72R in polymeric electrolyte fuel cells", **2011** Nova Science Publishers, Inc.

STUDIA UBB CHEMIA, LXIV, 3, 2019 (p. 59-66)
(RECOMMENDED CITATION)
DOI:10.24193/subbchem.2019.3.05

IMIDAZOLIUM YLIDES: CYCLOADDITION *versus* HYDROLISIS

DUMITRELA CUCU[a,b], VIOLETA MANGALAGIU[b], DORINA AMARIUCAI-MANTU[a], VASILICHIA ANTOCI[a], IONEL I. MANGALAGIU[a,b,*]

ABSTRACT. Reactions of imidazolium ylides with dimethyl acetylenedicarboxylate in polar solvents (methanol) were studied. In the competition between cycloaddition *versus* hydrolysis, the last one prevails leading to base heterocycle, diene structures and benzoate esters. A feasible reaction mechanism is presented. When fused pyrrolo-imidazole derivatives are desirable to be obtained, polar solvents should be avoided.

Keywords: *imidazolium ylides, hydrolysis, cycloaddition, reaction mechanism, diene, pyrrolo-imidazole derivatives*

INTRODUCTION

Imidazole derivatives are indispensable structural scaffolds of substantial interest in both academic and industrial research. This five member ring azaheterocycle is considered to be one of the most vital heterocyclic scaffold found in a large number of natural products and pharmacologically active compounds, having a wide range of interesting biological activities, for example, anti-HIV [1,2], antimicrobial (antibacterial, antimycobacterial, antimycotic) [3-7], anticancer [6-8], anti-Alzheimer [9-11], antidepressant, analgesic, antihypertensive, antioxidant, anti-inflammatory [10,11].

Despite of their huge importance from pharmacological, industrial, and synthetic points of view, there are only a limited method for the synthesis of the imidazole derivatives, cycloaddition reactions of cycloimmonium ylides to variously dipolarophiles (activated alkenes and alkynes) being one choice [12,13].

[a] *Alexandru Ioan Cuza University of Iasi, Faculty of Chemistry, 11 Carol I Bd., Iasi 700506, Romania*
[b] *Alexandru Ioan Cuza University of Iasi, Interdisciplinary Research Institute - CERNESIM Center, 11 Carol I Bd., Iasi 700506, Romania,*
** Corresponding author: ionelm@uaic.ro*

Taking into consideration our expertise in the area of cycloimmonium ylides chemistry [13-21], and with the aim of obtaining new biologically active compounds with imidazole skeleton, we decided to study the reactions of imidazolium ylides with dimethyl acetylenedicarboxylate (DMAD), as a symmetrically activated alkyne.

RESULTS AND DISCUSSION

A literature survey show that the reactions of imidazolium ylides with activated symmetrically or non symmetrically substituted alkynes occur usually as a typically Huisgen 3+2 cycloadditions [12, 22-29], leading to the corresponding fused azaheterocycles type **II**, Scheme 1.

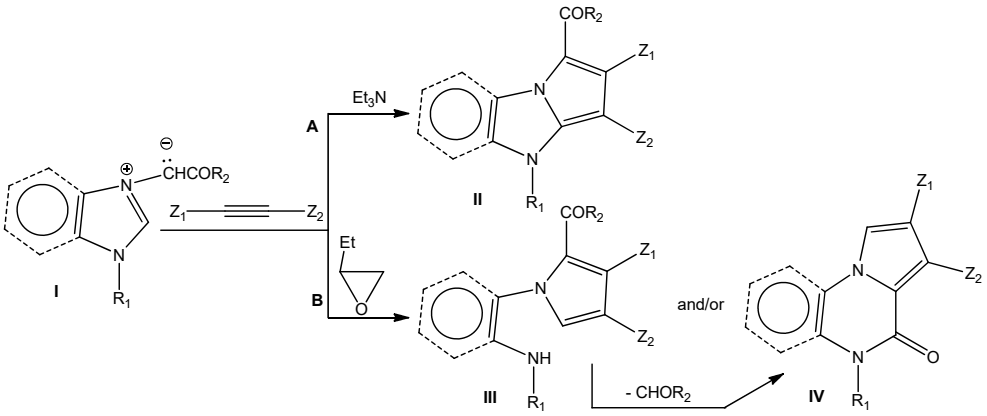

Scheme 1. Reaction pathway of imidazolium ylides **I** with activated symmetrically or non symmetrically substituted alkynes

However, according with the ylides structure and reaction conditions (in term of solvent and catalyst), the primary cycloaddition could be followed by a ring opening of the imidazole unit from structure **II**, leading to the pyrrole derivatives type **III** and/or fused pyrroloquinoxaline **IV**. Thus, when reaction took place in the presence of triethylamine in nonpolar solvents (usually benzene, pathway **A**), only azaheterocycles type **II** are formed, but in very low yields (trace to about 10%). When reaction took place in 1,2-epoxybutane (used as solvent and as scavenger for hydrobromic acid), the pyrrole derivatives type **III** and/or fused pyrroloquinoxaline **IV** are formed [30-34].

Having in view the above aspects and with the main aim of increasing the yields of reactions, we decide to study the reactions of imidazolium ylides **2a-d** with DMAD, in polar solvents, using triethylamine as catalyst and hydrobromic acid scavenger. In this respect, pyridine-*bis*(methylene)-*bis*(imidazole) ylides **2a-d** (generated *in situ* from the corresponding imidazolium salts **1a-d,** in the presence of triethylamine) were treated with DMAD in methanol, Scheme 2.

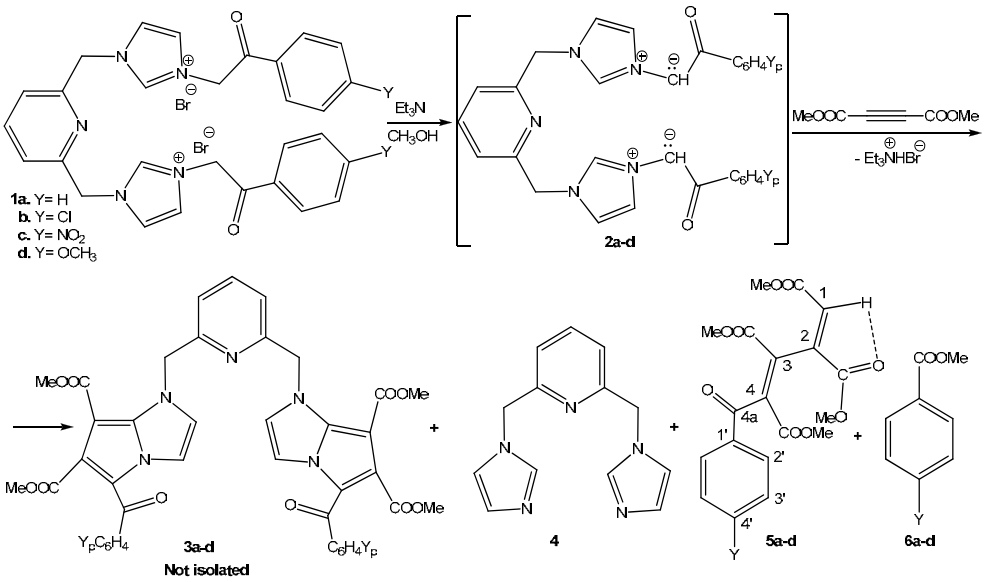

Scheme 2. Reaction pathway of pyridine-*bis*(methylene)-*bis*(imidazole) ylides **2a-d** with DMAD in polar solvents (MeOH)

Surprisingly, instead of the desired azaheterocycles type **3a-d** (which are obtained *via* a 3+2 dipolar cycloaddition reaction), compounds **4-6** are obtained. The formation of **4-6** could be explained by the following reaction mechanism: after the initial formation of ylides **2a-d**, a hydrolysis (methanolysis) took place on the ylide bond, with the formation of the 2,6-*bis*((1*H*-imidazol-1-yl)methyl) pyridine **4** and the unstable carbanion **A**.

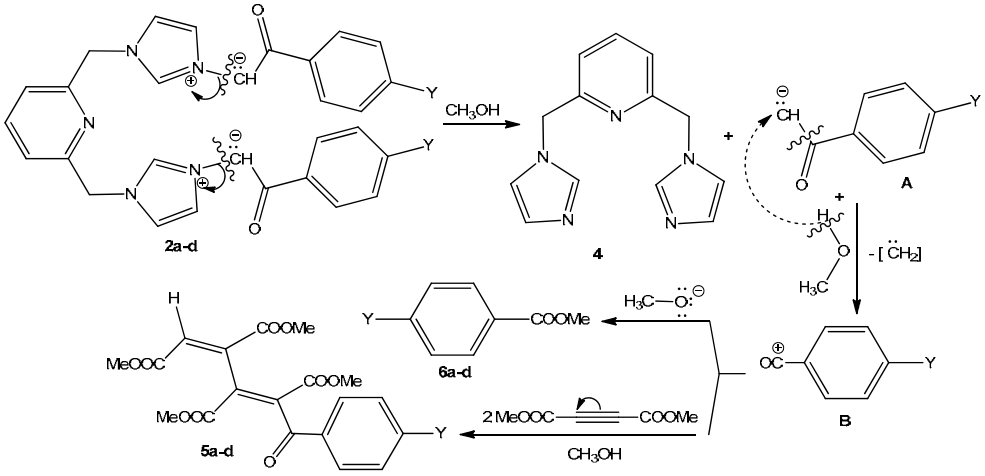

Scheme 3. Reaction mechanism of imidazolium ylides **2a-d** with DMAD in polar solvents (MeOH)

The carbanion **A** react immediately with methanol, eliminate carbene and generate the extremely unstable carbocation **B**. The stabilisation of cation **B** could occur in two different ways. One option is to react with the anionic methoxide, leading to the stable 4-Y-benzoate esters **6a-d**. In the same time, a competitive and successive reaction of addition of carbocation **B** to two molecules of DMAD took place, leading to the newly compounds with 1,3-diene structure **5a-d**.

The structure of compounds was proven by elemental (C, H, N) and spectral analysis (IR, 1H-NMR, 13C-NMR and two-dimensional experiments 2D-COSY, 2D-HMQC, 2D-HMBC). If we consider compound **5c** as representative for the series of compounds with 1,3-diene structure, the most important data furnished by 1H-NMR spectrum are the following: the most unshielded proton is the diene one H_1 (8.51 ppm, s) because of the powerful deshielding effect exerted by the two carboxymethyl groups from proximity and a possible hydrogen bond with the CO carbonyl group from the ester unit of the 2 position of diene skeleton (Scheme 2). The aromatic protons from 4-nitrobenzoyl ring appear to 8.29 ppm (d, $J_{3'2'}$ = 8.0 Hz, α-nitro, β-carbonyl) respectively at 7.88 ppm (d, $J_{2'3'}$ = 8.0 Hz, β-nitro, α-carbonyl). The methyl protons (from the four carboxymethyl groups) appear to 3.95 ppm (6H, from 1 and 4 positions) and 3.59 ppm (6H, from 2 and 3 positions). In the 13C-NMR spectrum, the most unshielded carbons are those one of carbonyl ketone group which appear at 192.64 ppm (C_{4a}, α-aryl, α-conjugated diene), followed by the carbons of the four carbonyl ester groups at 165.99 ppm (C_2, C_3) respectively 164.82 ppm (C_1,

C_4). The carbon atoms from benzene ring appear as follow: 150.78 ppm ($C_{4'}$), 140.72 ppm ($C_{1'}$), 130.63 ppm ($C_{2'}$), 123.04 ppm ($C_{3'}$), typical for aromatic *para* substituted carbons. The four diene carbons appear to 138.42 ppm (C_2), 136.04 ppm (C_3), 132.53 ppm (C_4), 132.29 ppm (C_1), in accordance with the proposed structure. At 53.53 ppm and 53.30 ppm appear the two methyl carbons from carboxymethyl groups located in positions 2 and 3, while at 52.60 ppm and 52.39 ppm appear the two methyl carbons from ester groups located in positions 1 and 4.

Compounds **4** and **6**, as well as their structures are known from the literature.

CONCLUSIONS

The reactions pathway of imidazolium ylides with dimethyl acetylenedicarboxylate, in polar solvents, and using triethylamine, were studied. In polar solvents, methanol, a competition between cycloaddition and hydrolysis (methanolysis) reactions took place, the last one prevailing. No cycloaddition reactions have been observed. The reaction mechanism supposes a primary hydrolysis of the ylides on the ylide bond, with the formation of base heterocycle and an unstable carbanion. This carbanion react immediately with methanol and generate an extremely unstable carbocation, which are stabilising itself either reacting with two molecules of DMAD (generating the 1,3-diene compounds **5a-d**) either reacting with the anionic methoxide (leading to the 4-Y-benzoate esters **6a-d**).

EXPERIMENTAL SECTION

All the reagents and solvents employed were used without further purification. The nuclear magnetic experiments (1H-NMR, 13C-NMR, 2D-COSY, 2D-HMQC, 2D-HMBC) were recorded using Bruker Avance III 500 spectrometer operating at 500 and 125 MHz for 1H and respectively 13C nuclei. The following abbreviations were used to designate chemical shift multiplicities: s = singlet, d = doublet, t = triplet. All chemical shifts are quoted on the δ-scale in ppm. Coupling constants are given in Hz. The microanalyses were in satisfactory agreement with the calculated values: C, ± 0.15; H, ± 0.10; N, ± 0.30. Thin layer chromatography (TLC) was carried out on Merck silica gel 60F254 plates. Column chromatography was carried out on silica gel (Roth 60, 0.04-0.063 mm). Visualisation of the plates was achieved using a UV lamp (λmax = 254 or 365 nm). All commercially available products were used without further purification unless otherwise specified.

General procedure for synthesis

The cycloimmonium salts **1a-d** (1 mmol) and dipolarophile (DMAD), (2.2 mmol) were dissolved in 20 mL of anhydrous methanol. Then triethylamine (3 mmol) was added. The resulting mixture was heated on reflux (with stirring) for 1 hour. The obtained solution was evaporated on vacuum, and the crude product was purified by flash chromatography on silica, using dichloromethane/ methanol 98:2.

(1E,3E)-Tetramethyl-5-oxo-5-phenylpenta-1,3-diene-1,2,3,4-tetracarboxylate, **5a**.
Yellow oil. FT-IR (KBr) cm^{-1}: 3075, 2918, 1690, 1580, 1522, 1428. 1H-NMR (500 MHz, $CDCl_3$) *δ*: 8.50 (s, $1H_1$), 7.92 (d, $2H_{2'}$, *J*= 7.2 Hz), 7.73 (t, $1H_{4'}$, *J*= 7.2), 7.61 (d, $2H_{3'}$, *J*= 7.2 Hz), 3.94 (s, 6H: $2xCH_3(COOCH_3)$ from 1 and 4 positions), 3.58 (s, 6H: $2xCH_3(COOCH_3)$ from 2 and 3 positions). 13C-NMR (125 MHz, $CDCl_3$) *δ*: 190.89 C_{4a} (CO ketone), 165.41 (CO ester from 2 and 3 positions), 164.26 (CO ester from 1 and 4 positions), 138.41 C_2, 136.20 $C_{1'}$, 136.02 C_3, 132.52 C_4, 132.31 $C_{4'}$, 132.28 C_1, 128.94 $C_{2'}$, 128.46 $C_{3'}$, 55.52 and 53.28 (methyl carbon ($COOCH_3$) from 2 and 3 positions), 52.54 and 52.35 (methyl carbon ($COOCH_3$) from 1 and 4 positions). Anal. Calcd. for $C_{19}H_{18}O_9$: C, 58.46; H, 4.65; Found: C, 58.56; H, 4.60.

(1E,3E)-Tetramethyl-5-(4-chlorophenyl)-5-oxopenta-1,3-diene-1,2,3,4-tetracarboxylate, **5b**.
Yellow-brownish oil. FT-IR (KBr) cm^{-1}: 3081, 2922, 1695, 1587, 1552, 1425, 760. 1H-NMR (500 MHz, $CDCl_3$) *δ*: 8.50 (s, $1H_1$), 7.96 (d, $2H_{3'}$, *J*= 8.0 Hz), 7.66 (d, $2H_{2'}$, *J*= 8.0 Hz), 3.94 (s, 6H: $2xCH_3(COOCH_3)$ from 1 and 4 positions), 3.59 (s, 6H: $2xCH_3(COOCH_3)$ from 2 and 3 positions). 13C-NMR (125 MHz, $CDCl_3$) *δ*: 189.92 C_{4a} (CO ketone), 165.26 (CO ester from 2 and 3 positions), 164.18 (CO ester from 1 and 4 positions), 138.76 $C_{4'}$, 138.40 C_2, 136.01 C_3, 132.52 C_4, 132.28 C_1, 132.10 $C_{1'}$, 130.32 $C_{2'}$, 129.02 $C_{3'}$, 55.50 and 53.26 (methyl carbon ($COOCH_3$) from 2 and 3 positions), 52.53 and 52.31 (methyl carbon ($COOCH_3$) from 1 and 4 positions). Anal. Calcd. for $C_{19}H_{17}ClO_9$: C, 53.72; H, 4.03; Found: C, 53.87; H, 4.13.

(1E,3E)-Tetramethyl-5-(4-nitrophenyl)-5-oxopenta-1,3-diene-1,2,3,4-tetracarboxylate, **5c**.
Yellow oil. FT-IR (KBr) cm^{-1}: 3120, 2931, 1698, 1578, 1521, 1470, 1350. 1H-NMR (500 MHz, $CDCl_3$) *δ*: 8.51 (s, $1H_1$), 8.29 (d, $2H_{3'}$, *J*= 8.0 Hz), 7.88 (d, $2H_{2'}$, *J*= 8.0 Hz), 3.95 (s, 6H: $2xCH_3(COOCH_3)$ from 1 and 4 positions), 3.59 (s, 6H: $2xCH_3(COOCH_3)$ from 2 and 3 positions). 13C-NMR (125 MHz, $CDCl_3$) *δ*: 192.64 C_{4a} (CO ketone), 165.99 (CO ester from 2 and 3 positions),

164.82 (CO ester from 1 and 4 positions), 150.78 $C_{4'}$, 140.72 $C_{1'}$, 138.42 C_2, 136.04 C_3, 132.53 C_4, 132.29 C_1, 130.63 $C_{2'}$, 123.04 $C_{3'}$, 55.55 and 53.30 (methyl carbon ($COOCH_3$) from 2 and 3 positions), 52.60 and 52.39 (methyl carbon ($COOCH_3$) from 1 and 4 positions). Anal. Calcd. for $C_{19}H_{17}NO_{11}$: C, 52.42; H, 3.94; N, 3.22; Found: C, 52.27; H, 3.84; N, 3.02.

(1E,3E)-Tetramethyl-5-(4-methoxyphenyl)-5-oxopenta-1,3-diene-1,2,3,4-tetracarboxylate, **5d**.
Pale yellow oil. FT-IR (KBr) cm^{-1}: 3079, 2927, 1682, 1600, 1240, 1161. 1H-NMR (500 MHz, $CDCl_3$) *δ*: 8.49 (s, $1H_1$), 8.00 (d, $2H_{2'}$, *J*= 8.4 Hz), 7.12 (d, $2H_{3'}$, *J*= 8.4 Hz), 3.93 (s, 6H: $2xCH_3(COOCH_3)$ from 1 and 4 positions), 3.80 (s, 3H from OCH_3), 3.58 (s, 6H: $2xCH_3(COOCH_3)$ from 2 and 3 positions). 13C-NMR (125 MHz, $CDCl_3$) *δ*: 189.10 C_{4a} (CO ketone), 165.04 (CO ester from 2 and 3 positions), 164.00 (CO ester from 1 and 4 positions), 163.92 $C_{4'}$, 138.40 C_2, 136.02 C_3, 132.49 C_4, 132.28 C_1, 130.60 $C_{1'}$, 126.31 $C_{2'}$, 114.23 $C_{3'}$, 55.80 (carbon from OCH_3), 55.50 and 53.25 (methyl carbon ($COOCH_3$) from 2 and 3 positions), 52.50 and 52.30 (methyl carbon ($COOCH_3$) from 1 and 4 positions). Anal. Calcd. for $C_{20}H_{20}O_{10}$: C, 57.14; H, 4.80; Found: C, 57.04; H, 4.85.

ACKNOWLEDGMENTS

Funding for this research was provided by UEFISCDI within the project CNFIS-FDI-2019-0129. Authors are also thankful to the POSCCE-O 2.2.1, SMIS-CSNR 13984-901, No. 257/28.09.2010 Project, CERNESIM, for the NMR experiments.

REFERENCES

1. E. Serrao; Z. L. Xu; B. Debnath; F. Christ; Z. Debyser; Y.Q. Long; N. Neamati; *Bioorg. Med. Chem*., **2013**, *21*, 5963–5972.
2. Y. Al-Soud; N. Al-Masoud; E. de Clerck; C. Pannecouque; *Acta Pharm*., **2007**, *57*, 379–393.
3. Y.L. Fan; X. H. Jin; Z.P. Huang; H.F. Yu; Z.G. Zeng; T. Gao; L.S. Feng; *Eur. J. Med. Chem.*, **2018**, *150*, 347-365.
4. A. Campaniço; R. Moreira; F. Lopes; *Eur. J. Med. Chem*., **2018**, *150*, 525-545.
5. V. Antoci; D. Cucu; G. Zbancioc; C. Moldoveanu; V. Mangalagiu; D. Amariucai-Mantu; A. Aricu; I.I. Mangalagiu; *Future Med. Chem.*, **2019**, *11*, in press.
6. C.N. Lungu; B.I. Bratanovici; M.M. Grigore; V. Antoci; I.I. Mangalagiu; *Curr. Med. Chem.*, **2019**, *26*, in press.

7. D. Mantu; V. Antoci; C. Moldoveanu; G. Zbancioc; I.I. Mangalagiu; *J. Enzyme Inhib. Med. Chem.*, **2016**, *31(S2)*, 96–103.
8. A.M. Zbancioc; Ghe. Zbancioc; C. Tanase; A. Miron; C. Ursu; I.I. Mangalagiu; *Lett. Drug. Des. Discov.*, **2010**, *7*, 644-649.
9. Y.X. Xu; H. Wang; X.K. Li; S.N. Dong; W.W. Liu; Q. Gong; T.D. Wang; Y. Tang; J. Zhu; J. Li; H.Y. Zhang; F. Mao; *Eur. J. Med. Chem.*, **2018**, *143*, 33-47.
10. P. Molina; A. Tárraga; F. Otón; *Org. Biomol. Chem*., **2012**, *10*, 1711–1724.
11. M. Gaba; C. Mohan; *Med. Chem. Res.*, **2016**, *25*, 173–210.
12. I. Zugravescu; M. Petrovanu; *N-Ylid Chemistry*, McGraw-Hill, London, New York, **1976**, pp. 100-117.
13. I.I. Mangalagiu; I. Druta; M. Constantinescu; I. Humelnicu; M. Petrovanu; *Tetrahedron*, **1996**, *52 (26)*, 8853-8862.
14. I.I. Mangalagiu; G. Mangalagiu; G. Drochioiu; C. Deleanu; M. Petrovanu; *Tetrahedron*, **2003**, *59*, 111-114.
15. M. Caprosu; Ghe. Zbancioc; C. Moldoveanu; I.I. Mangalagiu; *Collect. Czech Chem. C.*, **2004**, *69*, 426-434.
16. G. Zbancioc; V. Bejan; M. Risca; C. Moldoveanu; I.I. Mangalagiu; *Molecules*, **2009**, *14(1)*, 403-411.
17. R. Tucaliuc; V. Cotea; M. Niculaua; C. Tuchilus; D. Mantu; I.I. Mangalagiu; *Eur. J. Med. Chem.*, **2013**, *67*, 367-372.
18. G. Zbancioc; I.I. Mangalagiu; C. Moldoveanu; *Ultrason. Sonochem.*, **2015**, *23*, 376-383.
19. C.I. Ciobanu; V. Antoci; D. Mantu; I.I. Mangalagiu; *Rev. Chim. Bucharest*, **2015**, *66(4)*, 497-498.
20. G. Zbancioc; C. Moldoveanu; I. Humelnicu; V. Vasilache; I.I. Mangalagiu; *Rev. Chim. Bucharest*, **2016**, *67(8)*, 1516-1519.
21. C. Moldoveanu; G. Zbancioc; D. Mantu; D. Maftei; I.I. Mangalagiu; *Plos One,* **2016**, *11 (5)*, e0156129 (1-9).
22. H. Ogura; K. Kikuchi; *J. Org. Chem.*, **1972**, *37*, 2679-2682.
23. I. Zugravescu; J.M. Herdan; I. Druta; *Rev. Roum. Chim.*, **1974**, *19*, 649-658.
24. I. Zugravescu; J.M. Herdan; I. Druta; *Rev. Roum. Chim.*, **1974**, *19*, 659-664.
25. O. Meth-Cohn; *Tetrahedron Lett.*, **1975**, 413-416.
26. B. Wang; J. Hu; X. Zhang; Y. Hu; H. Hu; *J. Heterocycl. Chem*., **2000**, *37*, 1533-1537.
27. E. Georgescu; F. Georgescu; C. Roibu; P. C. Iuhas; C.Draghici; M. T. Caproiu; *Rev. Roum. Chim.*, **2002**, *47*, 885-891.
28. K. Wu; Q.Y. Chen; *Synthesis*, **2003**, 35-40.
29. X. Fang; Y.X. Wu; J. Deng; S.W. Wang, *Tetrahedron*, **2004**, *60*, 5487-5493.
30. A. Nicolescu; C. Deleanu; E. Georgescu; F. Georgescu; A.M. Iurascu; S. Shova; P. Filip; *Tetrahedron Lett.*, **2013**, *54*, 1486-1488.
31. E. Georgescu; A. Nicolescu; F. Georgescu; F. Teodorescu; D. Marinescu; A.M. Iurascu-Macsim; C. Deleanu; *Beilstein J. Org. Chem.*, **2014**, *10*, 2377-2387.
32. E. Georgescu; A. Nicolescu; F. Georgescu; F. Teodorescu; S. Shova; A.M. Macsim; C. Deleanu; *Synthesis*, **2015**, *47*, 1643-1655.
33. E. Georgescu; A. Nicolescu; F. Georgescu; S. Shova; B.C. Simionescu; C. Deleanu; *Rev. Roum. Chim*., **2016**, *61(4-5)*, 283-290.
34. E. Georgescu; A. Nicolescu; F. Georgescu; F. Teodorescu; S. Shova; A.T. Marinoiu; A.F. Dumitrascu; C. Deleanu; *Tetrahedron,* **2016**, *72*, 2507-2520.

STUDIA UBB CHEMIA, LXIV, 3, 2019 (p. 67-80)
(RECOMMENDED CITATION)
DOI:10.24193/subbchem.2019.3.06

SYNTHESIS AND ANTIBACTERIAL EVALUATION OF NEW PYRROLO[3',4':3,4]PYRROLO[1,2-*a*]QUINOLINE AND PYRROLO[3',4':3,4]PYRROLO[2,1-*a*]ISOQUINOLINE DERIVATIVES

CRISTINA M. AL MATARNEH[a], MONICA C. SARDARU[a], MIRCEA O. APOSTU[a], IRINA ROSCA[b], CATALINA I. CIOBANU[c], IONEL I. MANGALAGIU[a], RAMONA DANAC[a,*]

ABSTRACT. Two series of new fused pyrrolo[3',4':3,4]pyrrolo[1,2-*a*]quinoline and pyrrolo[3',4':3,4]pyrrolo[2,1-a]isoquinoline derivatives were synthesized and evaluated for the antimicrobial activity. The synthetic approach involves cycloimmonium ylides as 1,3-dipol intermediates. The structures of all synthesized compounds were proved by analytical and spectroscopic data. Crystal structure of compound **11a** has been also determined by single crystal XRD. The synthesized compounds were evaluated for their expected antimicrobial activity against *Staphylococcus aureus* ATCC25923, *Escherichia coli* ATCC25922 and *Candida albicans* ATCC10231, but no one showed activity against all the reference strains.

Keywords: *heterocycles, cycloaddition, quinolines, isoquinolines, antibacterial*

INTRODUCTION

In recent years, medicinal chemistry has been focused on the development of new potent antimicrobial agents, to overcome the problem of bacterial resistance, which became a very serious medical problem for health care systems in the entire world [1,2].

In this respect, fused N-heterocyclic systems attracted an important interest, since their molecules contain two or more widely known pharmacophoric fragments [3].

[a] *"Al. I. Cuza" University of Iasi, Faculty of Chemistry, Department of Chemistry, 11 Carol I, 700506 Iasi, Romania*
[b] *Institute of Macromolecular Chemistry "Petru Poni" Iasi, Romania*
[c] *"Al. I. Cuza" University of Iasi, Faculty of Chemistry, Research Department, 11 Carol I, 700506 Iasi, Romania*
** Corresponding author: rdanac@uaic.ro*

Pyrrolo[2,1-a]isoquinolines are particular structural units in the heterocycle class, some of them occurring in biologically active compounds, the best known being lamellarine and jamtine groups of alkaloids (fig. 1). Some representatives of the group are known for their inhibitory properties of topoisomerase or HIV-1 integrase enzymes, while others showed anticancer activity, anti-inflammatory or cardiovascular properties [4].

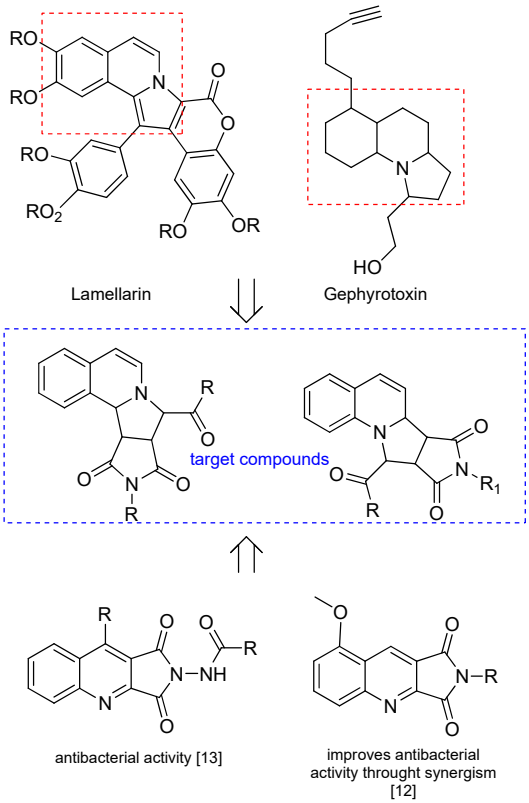

Figure 1. Design of the target compounds

Pyrrolo[1,2-a]quinolines are also present in marine alkaloids as gephyrotoxin (fig. 1) that is reported as a muscarinic antagonist and presents interesting neurological activities [5,6].

For these reasons, the synthesis of pyrrolo[1,2-*a*]quinolines and pyrrolo[2,1-*a*] isoquinolines has drawn much recent research interest. Several synthetic methods for these fused N-heterocycles have been reported, including the reactions of 2-alkylpyridine with aldehydes or α-haloketone [7], 1,3-dipolar

cycloadditions of quinolinium or isoquinolinium methylides to electron deficient dipolarofiles [8], 1,5-electrocyclizations and metal-catalyzed intramolecular C–N bond formation of alkynyl pyridines or propargylic pyridines [9].

In the same time, cyclic imides and their N-derivatives are reported to exhibit valuable biological effects including antifungal [10] and antibacterial [11-13] (fig. 1).

In this context, as part of our ongoing research aiming at the design and synthesis of new fused N-heterocyclic compounds with biological activities [14-18], we present here the synthesis, structure and the antimicrobial evaluation of two series of compounds with pyrrolo-pyrrolo[2,1-a]isoquinoline and pyrrolo-pyrrolo[1,2-a]quinoline structures (fig. 1), both series having the end pyrrole cycle as N-substituted cyclic imide.

RESULTS AND DISCUSSION

We decided to synthesize the pyrrolo-pyrrolo(iso)quinolone skeleton through the 3+2 cycloaddition of azomethineylide as the 1,3-dipole. This strategy has been used widely to construct complex cyclic systems from relatively simple precursors [19-22].

First step of our synthetic strategy was the synthesis of (iso)quinolinium monoquaternary salts **3-4** and **6-7** by an *N*-alkylation reaction with reactive halide type **2**, of isoquinoline and quinoline, respectively (Scheme 1). Reactions took place at room temperature with good to excellent yields. The structure of the new salts (**4** and **7**) was assigned by elemental and spectroscopic analysis: IR, ^{1}H and ^{13}C NMR.

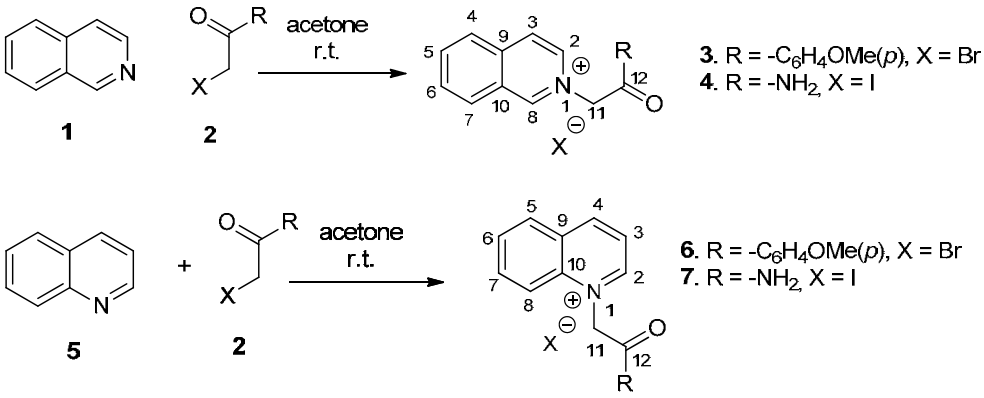

Scheme 1. Synthesis of monoquaternary salts **3-4** and **5-6**

Next, the synthesis of pyrrolo[1,2-*a*]quinoline and pyrrolo[2,1-*a*]isoquinoline derivatives took place by 3+2 cycloaddition of N-ylides generated *in situ* from salts **3-4** and **6-7** to N-ethyl or N-phenylmaleimide as symmetrically substituted electron deficient alkenes.

Thus, by deprotonation of salts **3-4** and **6-7** under triethylamine treatment, the resonance stabilized N-ylides were *in situ* generated and reacted with N-ethyl or N-phenylmaleimide giving tetrahydropyrrolo[3',4':3,4]pyrrolo[2,1-a]isoquinoline derivatives **9a-b** or pyrrolo[3',4':3,4]pyrrolo[2,1-a]isoquinoline derivatives **10a** (Scheme 2) and tetrahydropyrrolo[3',4':3,4]pyrrolo[1,2-a]quinolines **11a-b** and **12a**, respectively (Scheme 3). The cycloaddition reactions with N-ethyl or N-phenylmaleimide occur highly stereoselective, a single isomer being obtained in all cases.

The formation of compound **10a** could be explained by an oxidative dehydrogenation of the initial formed corresponding type **9** derivative, leading to the thermodynamically more stable product.

Interesting, the reaction of salts **4** and **7** with N-phenylmaleimide **8b** proved to be very difficult, complex and inseparable mixtures of compounds being obtained.

The structures of the new compounds **9a-b**, **10a**, **11a-b** and **12a** were assigned by elemental and spectroscopic analysis (IR, ^{1}H and ^{13}C-NMR).

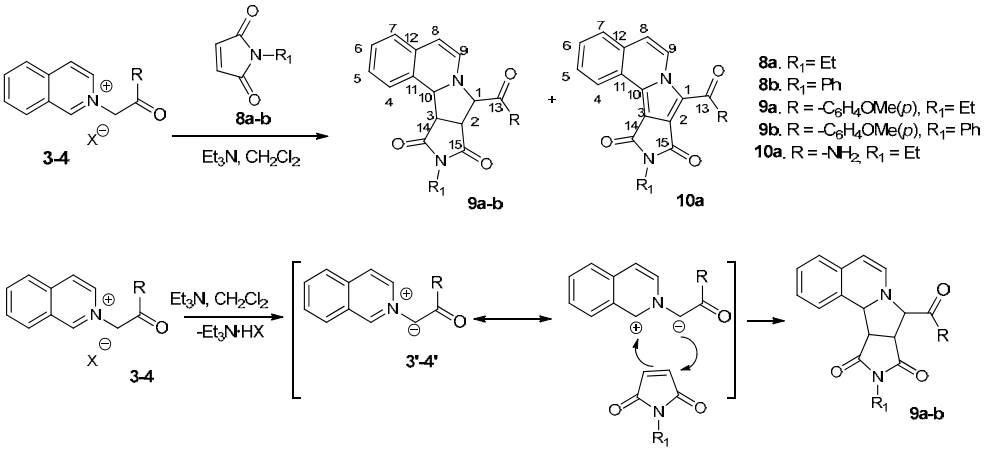

Scheme 2. Synthesis pathway for the tetrahydropyrrolo[3',4':3,4]pyrrolo[2,1-a]isoquinoline derivatives **9a-b** and the pyrrolo[3',4':3,4]pyrrolo[2,1-a]isoquinoline derivative **10a** and the proposed reaction mechanism

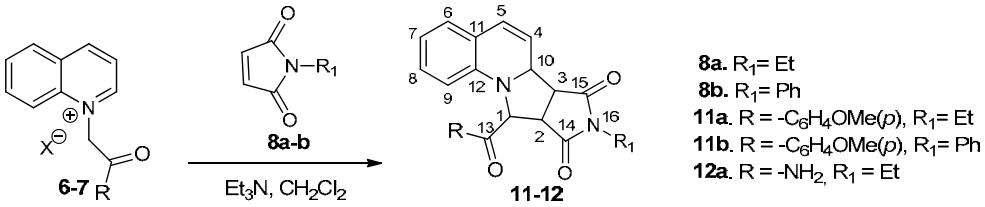

Scheme 3. Synthesis of tetrahydropyrrolo[3',4':3,4]pyrrolo[1,2-a]quinolines **11a-b** and **12a**

The IR spectra of polycyclic compounds type **9a-b** show absorption bands between 1774-1761 cm^{-1} characteristic for in phase stretching vibrations of C=O imide groups and between 1696-1692 cm^{-1} for out of phase vibrations of the same C=O imide group in some cases overlapped with ketone or amide carbonyl group absorption. In ^{1}H NMR spectrum of compounds **9a-b**, the signals at δ= 3.28-3.59 ppm have been assigned to H3 atom, the most shielded proton of the tetrahydropyrrole cycle. Protons 2 and 10 supply signals at δ= 3.76-4.15 ppm and δ=4.70-4.89 ppm, respectively. The signal delivered by H1 appears as singlet at weak fields (δ= 5.25-5.51 ppm) because of its electron withdrawing neighbours. The lack of coupling for H1 proton is a proof for a *trans* position relative to proton 2. The big values for the coupling constants $J_{2,3}$ (7.5-8.0 Hz) and $J_{3,10}$ (8.0 Hz) show us that hydrogen atoms H2, H3 and H10 lay on the same side of the tetrahydropyrrole ring, but on the opposite side of H1. ^{13}C-NMR spectra show two different signals for the two carbonyl imide carbon atoms at 174.1-174.6 ppm and 177.6-177.7 ppm respectively, while the carbonyl C13 furnishes signals at 192.0-192.3 ppm.

Compound **10a** furnishes a much simpler NMR spectrum with only two signals in the aliphatic region supplied by the ethyl group. Also the singlet signals of two amidic NH distinguish from the spectrum at 5.62 ppm and 8.71 ppm, respectively.

In ^{1}H NMR of compounds **11-12**, there are also four distinct signals in the aliphatic region corresponding to the four hydrogen atoms on the tetrahydropyrrole ring. The signals delivered by H1 appear as broad singlets, the small coupling ($J_{1,2}$= 1.0 Hz) with H2 proton being a proof for a *trans* position relative to proton 1. On the other hand, the big values for the coupling constants $J_{2,3}$ (8.0 Hz) and $J_{3,10}$ (8.0 Hz) show us that hydrogen atoms H2, H3 and H10 lay on the same side of the pyrrole ring, but on the opposite side of H1.

The above-mentioned conclusions for compounds type **11-12** were fully sustained by the structure obtained by single-crystal X-ray diffraction. Thus, the X-ray crystal structure of compound **11a**, is depicted in Figure 2.

Concerning the space disposal of the four fused rings we may notice that the end pyrrole cycle (former N-ethylmaleimide) is almost perpendicular to the quinoline plane. Full information concerning X-ray structure could be found in the Cambridge Crystallographic Data Centre (CCDC 1936035).

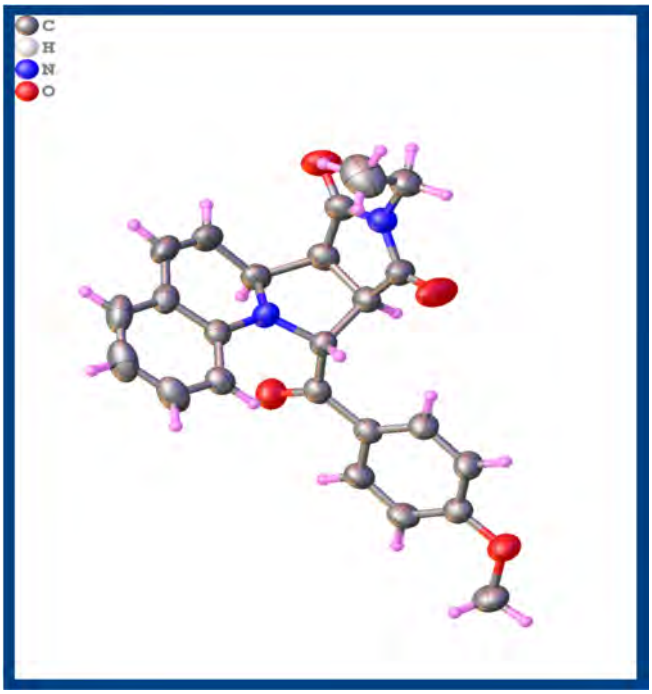

Figure 2. X-ray crystal structure of compound **11a** with thermal ellipsoids at 50% probability level

A perspective view of the **11a** compound is shown in Figure 3. From the analysis of molecules packing we can conclude that the crystals are stabilized mainly by rather weak H-bonds (H-O length 2.43 Å, C-O length 3.17 Å and C-H···O angle 136.4°). Also, we noticed the absence of π-π interactions which is probably a consequence of the nonplanar character of those molecules. Despite those facts the crystal structure is rather compact, the voids size being too small to accommodate solvent molecules.

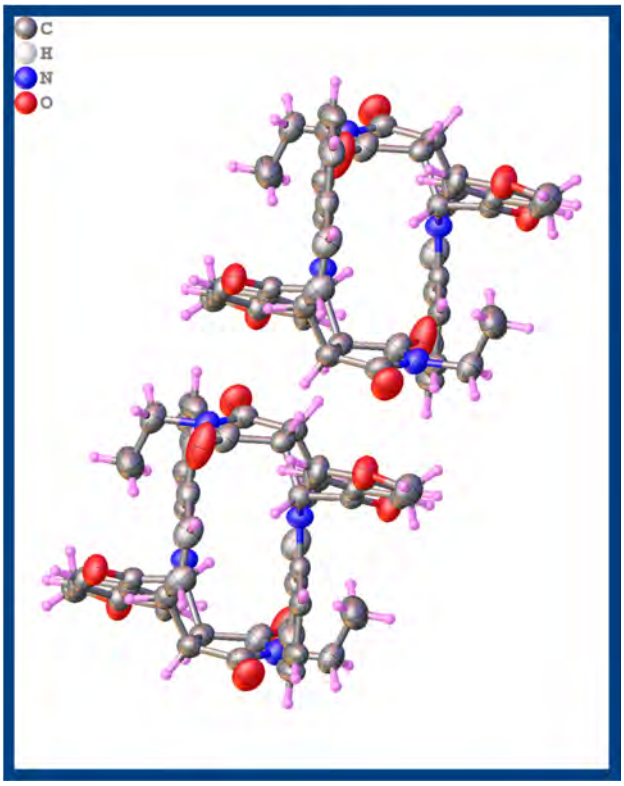

Figure 3. Packing (view along the c axis) of the molecules in the case of compound **11a**

Antimicrobial activity

Our group has previously reported several 1,10-phenanthrolinium monoquaternary salts [23] possessing antibacterial and antifungal activities. Thus, we decided to evaluate the antimicrobial activity for all synthesized compounds, including isoquinolinium salts **3-4** and quinolinium salts **6-7** (excepting salt **7** whose antibacterial evaluation was already reported. [24]. The antimicrobial activity of compounds **3**, **4, 6**, **7, 9-10** and **11-12** was measured by the agar disk diffusion method [25] which consists of addition of the sterile disks containing the compounds on the culture medium pre-inoculated with the microbial suspension, and measuring of the clear zone caused by the growth inhibition around the disks after 24 h of incubation. Unfortunately, all tested compounds showed no antimicrobial activity against all the reference strains.

CONCLUSIONS

The synthesis of new fused polycyclic indolizines derived from quinoline and isoquinoline is presented. The strategy adopted for construction of new pyrrolo[1,2-*a*]quinoline and pyrrolo[2,1-*a*]isoquinoline derivatives, including a typical Huisgen [3+2] dipolar cycloaddition of the corresponding isoquinolinium and quinolinium N-methylides to N-ethyl and N-phenylmaleimide proved to be straightforward and efficient. The cycloaddition reactions occur highly stereoselective (a single isomer being obtained). X-ray diffraction of compound **11a** proved unambiguously the compounds structure and brings information concerning lattice structure. The antibacterial activity of the synthesized compounds was measured, but all the investigated compounds showed no antimicrobial activity against the three reference strains.

EXPERIMENTAL SECTION

Chemistry

Melting points were recorded on an A. KrüssOptronic Melting Point Meter KSPI and are uncorrected. Proton and carbon nuclear magnetic resonance (δ_H, δ_C) spectra were recorded on a Bruker Avance III (500 MHz). All chemical shifts are quoted on the δ-scale in ppm. Coupling constants are given in Hz. IR spectra were recorded on a FTIR Shimadzu or Jasco 660 *plus* FTIR spectrophotometer. Thin layer chromatography (TLC) was carried out on Merck silica gel $60F_{254}$ plates. Column chromatography was carried out on silica gel (Roth 60, 0.04-0.063mm). Visualisation of the plates was achieved using a UV lamp (λ_{max}= 254 or 365 nm). All commercially available products were used without further purification unless otherwise specified.

General procedure for synthesis of isoquinolinium and quinolinium salts 3 and 5

1 mmol of quinoline or isoquinoline was dissolved in 5 mL acetone. Then 1.1 mmol of reactive halide was added and the resulted mixture was stirred at room temperature for 24 hours. The formed precipitate was filtered and washed with acetone to give the desired product.

General procedure for synthesis of isoquinoline and quinoline derivatives 7 and 8

The cycloimmonium salt (1 mmol, 1 equiv.) and dipolarophile (NEMI or NFMI), (1.1 mmol, 1.1 equiv), were added to 5 mL of dichloromethane and the obtained suspension was stirred at room temperature (rt) under N_2 atmosphere. Triethylamine (TEA) (3 mmol, 3 equiv.) was added drop-wise over 1 hour (magnetic stirring) and the resulting mixture was then stirred for 24 hours at rt. Methanol (5 mL) was added ant the resulting mixture is kept for 24 hours without stirring. The formed precipitate was collected by filtration to give a solid which was washed with methanol. The product was crystallized from dichloromethane/methanol (1/1, v/v).

Spectral data

2-(2-(4-methoxyphenyl)-2-oxoethyl)isoquinolin-2-ium bromide (**3**). Grey solid, η= 95%, m.p.= 215-217°C, IR (KBr, cm^{-1}): 3009, 2947, 1684, 1604, 1237, 1162, 974. ^{1}H-NMR (DMSO-d_6, 500 MHz): δ= 3.91 (s, 3H, OMe), 6.61 (s, 2H, H_{11}), 7.20 (d, *J*= 8.0 Hz, 2H, 2 x Ph-H), 8.09-8.13 (overlapped signals , 3H, H_6, 2 x Ph-H), 8.33 (t, *J*= 7.5 Hz, 1H, H_5), 8.42 (d, *J*= 8.5 Hz, 1H, H_4), 8.55 (d, *J*= 8.0 Hz, 1H, H_7), 8.68 (d, *J*= 7.0 Hz, 1H, H_3), 8.75 (d, *J*= 6.5 Hz, 1H, H_2), 10.05 (s, 1H, H_8). ^{13}C-NMR (DMSO-d_6, 125 MHz): δ= 55.9 (OMe), 65.8 C_{11}, 114.5 (2 x CH-Ph), 125.4 C_3, 126.4 Cq-Ph, 126.9 C_{10}, 127.4 C_4, 130.6 C_7, 130.8 (2 x CH-Ph), 131.4 C_6, 136.4 C_2, 137.2 C_5, 137.4 C_9, 151.7 C_8, 164.4 Cq-Ph, 189.2 C_{12}.

2-(2-amino-2-oxoethyl)isoquinolin-2-ium iodide (4). Yellow solid, η= 97%, m.p.= 199-201°C, IR (KBr, cm^{-1}): 3334, 3147, 2927, 1691, 1649, 1393, 1292 823.^{1}H-NMR (DMSO-d_6, 500 MHz): δ= 5.53 (s, 2H, H_{11}), 7.77 (s, 1H, NH), 8.10 (as, 2H, H_6, NH), 8.30-8.37 (overlapped signals, 2H,H_5, H_4), 8.52-8.70 (overlapped signals, 3H, H_2, H_3, H_7), 10.01 (s, 1H, H_8). ^{13}C-NMR (DMSO-d_6, 125 MHz): δ= 61.5 C_{11}, 125.1 C_3, 126.7 C_{10}, 127.3 C_4, 130.5 C_7, 131.3 C_6, 136.4 C_2, 137.1 C_9, 137.3 C_5, 151.6 C_8, 166.2 C_{12}.

1-(2-(4-methoxyphenyl)-2-oxoethyl)quinolin-1-ium bromide (**6**). Grey solid, η= 89%, m.p.= 221-223 °C; IR (KBr, cm^{-1}): 3024, 2956, 1673, 1598, 1519, 1359, 1240, 1175. ^{1}H-NMR (DMSO-d_6, 500 MHz): δ= 3.92 (s, 3H, OMe), 7.00 (s, 2H, H_{11}), 7.22 (d, *J*= 8.5 Hz, 2H, 2 x Ph-H), 8.13 (d, *J*= 8.5 Hz, 2H, 2 x Ph-H), 8.06 (t, *J*= 7.5 Hz, H_6), 1H, 8.22 (t, *J*= 7.5 Hz, 1H, H_7), 8.33 (dd, *J*= 8.5; 5.5 Hz, 1H, H_3), 8.40 (d, *J*= 8.5 Hz, 1H, H_5), 8.55 (d, *J*= 8.5 Hz, 1H, H_8),9.45 (d, *J*= 8.5 Hz, 1H, H_4), 9.55 (d, *J*= 5.5 Hz, 1H, H_2). ^{13}C-NMR (DMSO-d_6, 125 MHz): δ= 55.9 (OMe), 62.9 C_{11}, 114.4 (2 x CH-Ph), 119.1 C_5, 122.2 C_3, 126.4 Cq-Ph, 129.4 C_9, 130.0 C_6, 130.6 C_8, 131.2 (2 x CH-Ph), 135.9 C_7, 138.6 C_{10}, 148.5 C_4, 151.0 C_2, 164.5 Cq-Ph, 189.0 C_{12}.

1-(2-amino-2-oxoethyl)quinolin-1-ium iodide (7). Yellow solid, η= 68%, m.p.= 236-239°C, IR (KBr, cm^{-1}): 3361, 3154, 2980, 1678, 1620, 1523, 1356, 778. ^{1}H-NMR (DMSO-d_6, 500 MHz): δ= 5.85 (s, 2H, H_{11}), 7.84 (s, 1H, NH), 8.05 (dt, *J*= 8.0 ; 2.0 Hz, 1H, H_6), 8.17 (s, 1H, NH), 8.25-8.31 (m, 3H, H_3, H_7, H_5),8.51 (d, *J*= 8.0 Hz, 1H,H_8), 9.38 (d, *J*= 8.0 Hz, 1H, H_4), 9.52 (d, *J*= 5.5 Hz, 1H, H_2).^{13}C-NMR (DMSO-d_6, 125 MHz): δ= 58.8 C_{11}, 118.4 C_5, 122.0 C_3, 129.3 C_9,129.9 C_6, 130.6 C_8, 135.9 C_7,138.2 C_{10}, 148.2 C_4, 151.1 C_2, 165.8 C_{12}.

10-ethyl-8-(4-methoxybenzoyl)-8,8a,11a,11b-tetrahydro-9H-pyrrolo[3',4':3,4]pyrrolo[2,1-a]isoquinoline-9,11(10H)-dione (**9a**). Yellow crystals, η= 60%, m.p.= 208-210°C; IR (KBr), ν(cm^{-1}): 2978, 1774, 1696, 1670, 1600, 1399, 1225. ^{1}H-NMR ($CDCl_3$, 500 MHz): δ= 0.90 (t, *J*= 7.0 Hz, 3H, $CH_2C\underline{H_3}$), 3.25 (q, *J*= 7.0 Hz, 2H, $C\underline{H_2}CH_3$), 3.28 (t, *J*= 8.0 Hz, 1H, H_3), 3.73 (1H, s, OMe), 3.76 (d, *J*= 7.5 Hz, 1H, H_2), 4.70 (d, *J*= 8.0 Hz, 1H, H_{10}), 5.16 (d, *J*= 7.5 Hz, 1H, H_8), 5.29 (s, 1H, H_1), 6.05 (d, *J*= 7.5 Hz, 1H, H_9), 6.77 (d, *J*= 7.5 Hz, 1H, H_4), 6.83 (d, *J*= 8.5 Hz, 2H, 2 x Ph-H), 7.00 (as, 2H, H_5, H_6), 7.03 (dd, *J*= 7.5; 4.0 Hz, 1H, H_7), 7.95 (d, *J*= 8.5 Hz, 2H, 2 x Ph-H). ^{13}C-NMR ($CDCl_3$, 125 MHz): δ= 11.4 ($CH_2\underline{C}H_3$), 33.8 ($\underline{C}H_2CH_3$), 45.8 C_2, 51.3 C_3, 55.4 (OMe), 61.7 C_{10}, 72.1 C_1, 102.5 C_8, 113.8 (2 x CH-Ph), 124.2 C_4, 125.7 C_6, 125.8 C_{11}, 126.5 Cq-Ph, 127.3 C_5, 128.2 C_7, 130.8 C_{12}, 131.4 (2 x CH-Ph), 134.9 C_9, 163.9 Cq-Ph, 174.6 C_{14}, 177.7 C_{15}, 192.0 C_{13}.

8-(4-methoxybenzoyl)-10-phenyl-8,8a,11a,11b-tetrahydro-9H-pyrrolo[3',4':3,4]pyrrolo[2,1-a]isoquinoline-9,11(10H)-dione (**9b**). Yellow solid, η= 90%, m.p.= 208-210°C; IR (KBr), ν(cm^{-1}): 1761, 1692, 1671, 1595, 1507, 1394, 1240, 1167. ^{1}H-NMR ($CDCl_3$, 500 MHz): δ= 3.59 (t, *J*= 8.0 Hz, 1H, H_3), 3.86 (1H, s, OMe), 4.15 (d, *J*= 8.0 Hz, 1H, H_2), 4.89 (d, *J*= 8.0 Hz, 1H, H_{10}), 5.49 (d, *J*= 7.5 Hz, 1H, H_8), 5.51 (s, 1H, H_1), 6.25 (d, *J*= 7.5 Hz, 1H, H_9), 7.12-7.20 (m, 3H, H_4, H_6, H_5), 6.96 (ad, *J*= 8.5 Hz, 3H, 2 x Ph-H, H_7), 7.09 (d, *J*= 7.5 Hz, 2H, 2 x Ph-H), 7.33 (t, *J*= 7.5 Hz, 1H, Ph-H), 7.40 (t, *J*= 7.5 Hz, 2H, 2 x Ph-H), 8.09 (d, *J*= 8.5 Hz, 2H, 2 x Ph-H). ^{13}C-NMR ($CDCl_3$, 125 MHz): δ= 46.5 C_2, 51.9 C_3, 55.7 (OMe), 62.5 C_{10}, 73.3 C_1, 103.1 C_8, 114.2 (2 x CH-Ph), 124.8 C_7, 126.0 (2 x Ph-CH, C_{11}), 126.5 C_6, 126.9 C_{14}, 127.8 C_4, 128.6 (Ph-CH), 128.9 C_5, 129.2 (2 x Ph-CH), 130.9 C_{12}, 131.8 (2 x CH-Ph), 132.1 C_q-Ph, 135.3 C_9, 164.4 C_{17}, 174.1 C_{14}, 177.6 C_{15}, 192.3 C_{13}.

10-ethyl-8-(4-methoxybenzoyl)-9H-pyrrolo[3',4':3,4]pyrrolo[2,1-a]isoquinoline-9,11(10H)-dione (**10a**). Brown solid, η= 60%, m.p.= 239-240°C. IR (KBr, cm^{-1}): 3394, 3182, 1741, 1687, 1618, 1408, 1221, 1018. ^{1}H-NMR ($CDCl_3$, 500 MHz): δ= 1.33 (t, *J*= 7.0 Hz, 3H, $CH_2C\underline{H_3}$), 3.79 (q, *J*= 7.0 Hz, 2H, $C\underline{H_2}CH_3$), 5.62 (s, 1H, NH), 7.22 (d, *J*= 7.5 Hz, 1H, H_8), 7.67-7.76 (overlapped signals, 3H, H_5, H_6, H_7), 8.71 (s, 1H, NH), 9.11 (d, *J*= 7.5 Hz, 1H, H_4), 9.64 (d, *J*= 7.5 Hz, 1H, H_9).^{13}C-NMR ($CDCl_3$, 125 MHz): δ= 14.3 ($CH_2\underline{C}H_3$),33.7 ($\underline{C}H_2CH_3$), 111.0 C_3, 114.8 C_1, 115.9 C_8, 124.0 C_{11}, 125.8 C_9, 126.8 C_7, 127.4 C_4, 129.0 C_5, 129.5 C_2, 130.4 C_6, 131.6 C_{12}, 151.8 C_{10}, 161.2 C_{14}, 163.7 C_{13}, 166.2 C_{15}.

8-ethyl-10-(4-methoxybenzoyl)-6a,6b,9a,10-tetrahydro-7H-pyrrolo [3',4':3,4]pyrrolo[1,2-a]quinoline-7,9(8H)-dione (**11a**). Yellow crystals, η= 70%, m.p.= 190-192^{o}C; IR (KBr), ν(cm^{-1}): 3056, 2974; 2930, 2827, 1783, 1698, 1598, 1491, 1446, 1397, 1233, 1166, 759. ^{1}H-NMR ($CDCl_3$, 500 MHz): δ= 1.03 (t, *J*= 7.0 Hz, 3H, $CH_2C\underline{H}_3$), 3.41 (t, *J*= 8.0 Hz, 1H, H_3), 3.52 (q, *J*= 7.0 Hz, 2H, $C\underline{H}_2CH_3$), 3.57 (dd, *J*= 8.0, 1.0 Hz, 1H, H_2), 3.91 (1H, s, OMe), 5.20 (td, *J*= 8.0, 2.0 Hz, 1H, H_{10}), 5.63 (s, 1H, H_1), 6.05 (dd, *J*= 10.0, 2.0 Hz, 1H, H_4), 6.18 (d, *J*= 8.0 Hz, 1H, H_9), 6.40 (dd, *J*= 10.0, 2.0 Hz, 1H, H_5), 6.65 (t, *J*= 7.5 Hz, 1H, H_7), 6.92 (d, *J*= 7.0 Hz, 1H, H_6), 6.96 (t, *J*= 8.5 Hz, 2H, H_8), 7.04 (d, *J*= 8.5 Hz, 2H, 2 x Ph-H), 8.28 (d, *J*= 8.5 Hz, 2H, 2 x Ph-H). ^{13}C-NMR ($CDCl_3$, 125 MHz): δ= 12.9 ($CH_2\underline{C}H_3$), 34.5 ($\underline{C}H_2CH_3$), 47.0 C_2, 48.2 C_3, 55.7 (OMe), 60.7 C_{10}, 63.8 C_1, 110.7 C_9, 114.5 (2 x CH-Ph), 118.8 C_7, 121.1 C_4, 122.2 C_{11}, 126.6 Cq-Ph, 126.7 C_5, 127.5 C_6, 129.2 C_8, 131.6 (2 x CH-Ph), 141.8 C_{12}, 164.5 Cq-Ph, 175.7 C_{14}, 177.6 C_{15}, 194.2 C_{13}.

10-(4-methoxybenzoyl)-8-phenyl-6a,6b,9a,10-tetrahydro-7H-pyrrolo [3',4':3,4]pyrrolo[1,2-a]quinoline-7,9(8H)-dione (**11b**). Yellow crystals, η= 80%, m.p.= 198-199^{o}C; IR (KBr), ν(cm^{-1}): 3042, 2962, 2909, 1779, 1715, 1676, 1599, 1489, 1379, 1172, 746. ^{1}H-NMR ($CDCl_3$, 500 MHz) : δ= 3.59 (t, *J*= 8.0 Hz, 1H, H_3), 3.82 (d, *J*= 8.0 Hz, 1H, H_2), 3.91 (1H, s, OMe), 5.24 (td, *J*= 8.0, 2.0 Hz, 1H, H_{10}), 5.80 (s, 1H, H_1), 6.09 (dd, *J*= 10.0, 2.5 Hz, 1H, H_4), 6.31 (d, *J*= 8.0 Hz, 1H, H_9), 6.46 (dd, *J*= 10.0, 2.0 Hz, 1H, H_5), 6.71 (t, *J*= 7.5 Hz, 1H, H_7), 6.97 (d, *J*= 7.5 Hz, 1H, H_6), 7.01 (t, *J*= 8.0 Hz, 2H, H_8), 7.03 (d, *J*= 8.5 Hz, 2H, 2 x Ph-H), 7.10 (d, *J*= 7.5 Hz, 2H, 2 x Ph-H), 7.35-7.43 (m, 3H, 3 x Ph-H), 8.29 (d, *J*= 8.5 Hz, 2H, 2 x Ph-H). ^{13}C-NMR ($CDCl_3$, 125 MHz): δ= 47.1 C_2, 48.7 C_3, 55.8 (OMe), 61.0 C_{10}, 64.6 C_1, 110.9 C_9, 114.5 (2 x CH-Ph), 119.1 C_7, 121.0 C_4, 122.2 C_{11}, 126.5 (2 x Ph-CH), 126.6 Cq-Ph, 127.0 C_5, 127.7 C_6, 129.0 (CH-Ph), 129.3 (2 x Ph-CH), 129.4 C_8, 131.6 (C_{15}, C_{19}, Ph-Cq), 141.7 C_{12}, 164.6 Cq-Ph_{17}, 175.0 C_{14}, 177.0 C_{15}, 194.1 C_{13}.

8-ethyl-7,9-dioxo-6b,7,8,9,9a,10-hexahydro-6aH-pyrrolo[3',4':3,4] pyrrolo[1,2-a]quinoline-10-carboxamide (12a). Brown solid, η= 70%, m.p.= 213-217^{o}C. IR (KBr, cm^{-1}): 3401, 3259, 2984, 1762, 1690, 1600, 1406, 1218, 1125, 759, 614. ^{1}H-NMR (DMSO-d6, 500 MHz): δ= 0.81 (t, *J*= 7.0 Hz, 3H, $CH_2C\underline{H}_3$), 3.3 (q, *J*= 7.0 Hz, 2H, $C\underline{H}_2CH_3$),3.55 (overlapped signals, 2H, H_3, H_2), 4.59 (s, 1H, H_1), 5.11 (m, 1H, H_{10}), 5.88 (dd, *J*= 10.0, 2.5 Hz, 1H, H_4), 6.34 (dd, *J*= 10.0, 2.0 Hz, 1H, H_5), 6.52 (d, *J*= 8.0 Hz, 1H, H_9), 6.58 (t, *J*= 7.0 Hz, 1H, H_7), 6.89 (dd, *J*= 7.5; 1.0 Hz, 1H, H_6), 6.98 (dt, *J*= 8.5; 1.0 Hz, 1H, H_8), 7.39 (s, 1H, NH), 7.92 (s, 1H, NH).^{13}C-NMR ($CDCl_3$, 125 MHz): δ= 12.4($CH_2\underline{C}H_3$), 33.2 ($\underline{C}H_2CH_3$), 47.3 C_2, 48.5 C3, 59.4 C_{10}, 62.0 C_1, 110.5 C_9, 117.8 C_7, 121.1 C_{11}, 121.6 C_4, 125.4 C_5, 126.9 C_6, 128.9 C_8, 142.1 C_{12}, 172.1 C_{13}, 175.9 C_{14}, 177.4 C_{15}.

X-Ray Crystallography

Crystallographic measurements for compound $C_{24}H_{22}N_2O_4$ were carried out on a SuperNova, Dual, Cu at zero, Eos diffractometer. The crystal was kept at 294 K during data collection. The unit cell determination and data integration were carried out using the CrysAlisPro package of Oxford Diffraction. Using Olex2 [26], the structure was solved with the Superflip [27] structure solution program using Charge Flipping and refined with the ShelXL [28] refinement package using Least Squares minimisation.

Table 1. Crystal data and structure refinement for **11a**

Identification code	**11a**
Empirical formula	$C_{24}H_{22}N_2O_4$
Formula weight	402.45
Temperature/K	294
Crystal system	triclinic
Space group	P-1
a/Å	8.9438(5)
b/Å	9.4257(4)
c/Å	13.1464(6)
α/°	92.456(3)
β/°	107.620(4)
γ/°	106.925(4)
Volume/Å^3	1000.05(9)
Z	2
ρ_{calc}mg/mm^3	1.3364
m/mm^{-1}	0.747
F(000)	425.4
Crystal size/mm^3	0.3200 × 0.2800 × 0.2200
Radiation	Cu Kα (λ = 1.54184)
2Θ range for data collection	7.12 to 140.88°
Index ranges	-10 ≤ h ≤ 10, -11 ≤ k ≤ 9, -16 ≤ l ≤ 15
Reflections collected	6411
Independent reflections	3732[R(int) = 0.0124]
Data/restraints/parameters	3732/0/272
Goodness-of-fit on F^2	1.059
Final R indexes [I>=2σ (I)]	R_1 = 0.0426, wR_2 = N/A
Final R indexes [all data]	R_1 = 0.0456, wR_2 = 0.1136
Largest diff. peak/hole / e Å^{-3}	0.17/-0.20

The main crystallographic data together with refinement details are summarized in Table 1. CCDC 1936035 contains the full crystallographic data. Those data can be obtained free of charge from the Cambridge Crystallographic Data Centre via *www.ccdc.cam.ac.uk/data_request/cif*.

Antimicrobial activity

The antimicrobial activity was determined by disk diffusion assay against three different reference strains: *Staphylococcus aureus* ATCC25923, *Escherichia coli* ATCC25922 and *Candida albicans* ATCC10231. All microorganisms were stored at -80°C in 20% glycerol. The bacterial strains (*S. aureus* and *E. coli*) were refreshed in Mueller-Hinton broth at 36±1°C and the yeast strain (*C. albicans*) was refreshed on Sabouraud dextrose broth at 36±1°C. Microbial suspensions were prepared with these cultures in sterile solution to obtain turbidity optically comparable to that of 0.5 McFarland standards (yielding a suspension containing $1x10^8$CFU ml^{-1} for all the microorganisms).

Volumes of 0.4 ml from each inoculum were spread onto Mueller-Hinton agar and Sabouraud dextrose agar and all the tested samples were added after the medium surface dried. The sterilized paper discs (6 mm) were placed on the plate and an aliquot (100 µl) of the tested compounds (concentration 10mg/ml, dissolved in DMSO) was added on the paper discs. To evaluate the antimicrobial properties, the growth inhibition was measured under standard conditions after 24 hours of incubation at 36±1 °C. After incubation, the diameters of inhibition zones were measured by using Image J software.

ACKNOWLEDGMENTS

We thank the POSCCE-O 2.2.1, SMIS-CSNR 13984-901, Project no. 257/28.09.2010, CERNESIM, for the NMR and XRD experiments.

REFERENCES

1. I.M. Gould; *Int. J. Antimicrob. Ag.*, **2008**, *32S*, S2-S9.
2. G L. French; *Int. J. Antimicrob.Ag.*, **2010**, *36S3*, S3–S7.
3. M.G. Ferlin; C. Marzano; L. Dalla Via; A. Chilin; G. Zagotto; A. Guiotto; S. Moro; *Bioorg. Med. Chem.,* **2005**, 13, 4733–4739.

4. J. Krishnan; B. Vedhanarayanan; B. S. Sasidhar; S. Varughese; V. Nai; *Chem. Asian J.*, **2017**, 12, 623 – 627.
5. J.W. Daly; B. Witkop; T. Tokuyama; T. Nishikawa; I.L. Karle; *Helv. Chim. Acta*, **1977**, 60, 1128-1140.
6. H. Ishibashi; S. Harada; K. Sato; M. Ikeda; S. Akai; Y. Tamura; V.U. Ahmad; A. Rahman; T. Rasheed; H. Rehman; *Heterocycles ,***1987**, 26, 1251.
7. D.S. Allgäuer; H. Mayr; *Eur. J. Org. Chem*., **2014**, 14, 2956–2963.
8. Y. Liu; Y. Zhang; Y.-M.Shen; H.-W. Hu; J.-H.Xu; *Org. Biomol. Chem.*, **2010**, 8, 2449–2456.
9. J. An; Q.-Q. Yang; Q. Wang; W.-J. Xiao*; Tetrahedron Lett*., **2013**, 54, 3834–3837.
10. R.S. Dhivare; S.S. Rajput; *Int. J. Chem. Tech. Res.,* **2016**, 9(3), 325-331.
11. A.M. Al- Azzawi; K.K.H. Al-Obiadi; *Int. J. Res. Pharm. &Chem.,* **2016**, 6(1), 1-8.
12. C. Jin; R. Alenazy; Y. Wang; R. Mowla; Y. Qin; J. Quan; E. Tan; N.D. Modi; X. Gu; S.W. Polyak; H. Venter; S. Ma; *Bioorg. Med. Chem. Let.,* **2019**, 19(7), 882-889.
13. T.H. Largani; G. Imanzadeh; S. Zahri; N.N. Pesyan; E. Şahin; *Green Chem. Lett. Rev.,* **2017**, 10, 387-392.
14. R. Danac; T. Daniloaia; V. Antoci; V. Vasilache; I.I. Mangalagiu; *Lett. Drug Des. Discov.,* **2015**, 12, 14-17.
15. A. Rotaru; R. Danac; I. Druta; G. Drochioiu; I. Cretescu; *Rev. Chim. (Bucharest, Romania),* **2005**, 56(2), 179-183.
16. C.M. Al Matarneh, C.I. Ciobanu; I.I. Mangalagiu; R. Danac; *J. Serb. Chem. Soc*., **2016**, 81(2), 133-140.
17. C.M. Al Matarneh; I.I. Mangalagiu; S. Shova; R. Danac; *J. Enz. Inhib. Med. Chem.,* **2016**, 31(3), 470-480.
18. A.-M. Olaru; V. Vasilache; R. Danac; I.I. Mangalagiu; *J. Enz. Inhib. Med. Chem*., **2017**, 32(1), 1291-1298.
19. S. Mondal; A. Maity; R. Paira; M. Banerjee; Y.P. Bharitkar; A. Hazra; S. Banerjee; N.B. Mondal; *Tet. Lett*., **2012**, 53, 6288-6291.
20. C.M. Al Matarneh; C.I. Ciobanu; M.O. Apostu; I. I. Mangalagiu; R. Danac; *C.R. Chimie,* **2018**, 21(1), 1-8.
21. C.M. Al Matarneh; M.O. Apostu; I.I. Mangalagiu; R. Danac; *Tetrahedron,* **2016**, 72, 4230-4238.
22. R. Danac; L. Leontie; A. Carlescu; G.I. Rusu; *Mat. Chem. Phys*., **2012**, 134(2-3), 1042-1048.
23. I. Druta; R. Danac; M. Ungureanu; G. Drochioiu; *Ann. Pharm. Fr.*, **2002**, 60, 348-351.
24. K.M. Khan; Z.S. Saify; Z.A. Khan; M. Ahmed; M. Saeed; M. Schick; H.J. Kohlbau; W. Voelter; *Arzneim.-Forsch.,* **2000**, 50(10), 915-924.
25. D.F. Brown; D. Kothari; *J. Clin. Pathol*., **1975**, 28, 779–783.
26. CrysAlis RED, Oxford Diffraction Ltd.,Version 1.171.36.32, 2003.
27. O.V. Dolomanov; L.J. Bourhis; R.J. Gildea; J A.K. Howard; H.J. Puschmann; *Appl. Cryst*., **2009**, *42*, 339-341.
28. G.M. Sheldrick; SHELXS, *Acta Crystallogr. A*, **2008**, *64*, 112-122.

STUDIA UBB CHEMIA, LXIV, 3, 2019 (p. 81-98)
(RECOMMENDED CITATION)
DOI:10.24193/subbchem.2019.3.07

THIN LAYER PHOTOCATALYSTS OF TiO_2-Ag COMPOSITES

BORBÁLA TEGZE[a], EMŐKE ALBERT[a], BOGLÁRKA DIKÓ[a], JÁNOS MADARÁSZ[b], GYÖRGY SÁFRÁN[c], ZOLTÁN HÓRVÖLGYI[a,*]

ABSTRACT. Mesoporous TiO_2 coatings were prepared by sol-gel dip-coating method on glass and SiO_2 coated glass substrates. They were modified with silver by two different methods: impregnation of as-prepared coatings in $AgNO_3$ aqueous solution; coating deposition from precursor sols containing $AgNO_3$. Transmittance spectra, refractive index, layer thickness and porosity were determined by UV-Vis spectroscopy. Crystallinity of the samples was characterized by XRD, and the morphology and structure by HR-TEM. Photoinduced wettability conversion of the samples was studied, and it was found that the presence of the SiO_2 barrier layer and the silver content had significant effect on the wetting behaviour. The photoactivity and reusability of the samples were investigated with methyl orange dye degradation under ultra-violet (UV) irradiation. TiO_2 coatings impregnated in 1M $AgNO_3$ solution were found to be the most stable photocatalyst system.

Keywords: *TiO_2, photocatalysis, self-cleaning, dye degradation, sol-gel coatings*

INTRODUCTION

Titania is a highly effective photoactive material, with great promise in the fields of photocatalysts, solar cells, *etc.*[1–5] For many applications it can be a great advantage to use TiO_2 in coating form: *e.g.* in air- and water purification via photocatalytic means, coatings offer easier separation of the photocatalyst from the polluted fluid and a more manageable system compared

[a] *Budapest University of Technology and Economics, Faculty of Chemical Technology and Biotechnology, Department of Physical Chemistry and Materials Science, Centre for Colloid Chemistry, H-1521 Budapest, Budafoki út 6-8, Hungary*
[b] *Budapest University of Technology and Economics, Faculty of Chemical Technology and Biotechnology, Department of Inorganic and Analytical Chemistry, Technical Analytical Chemistry Research Group, H-1521 Budapest, Szent Gellért tér 4, Hungary*
[c] *Centre for Energy Research, Institute for Technical Physics and Materials Science, H-1121, Budapest, Hungary*
** Corresponding author: zhorvolgyi@mail.bme.hu*

to other forms (*i.e.* powders).[6] TiO_2 films on solid substrates, such as glass, are a promising type of self-cleaning coating, used for *e.g.* windows, solar panel coverages.[7] Photoinduced wettability conversion is another commonly observed property of TiO_2: under UV light the surface becomes more hydrophilic, and this change in wettability is reversible. This behaviour has practical importance for several applications, especially for anti-fogging and self-cleaning coatings. The most accepted explanation for this phenomenon is that photogenerated holes in TiO_2 can react with lattice oxygen, which leads to the formation of surface defect sites (oxygen vacancies). Water molecules from the atmosphere dissociatively adsorb on these defect sites and form hydroxyl groups, causing increased hydrophilicity. Following the UV treatment, if the samples are kept in dark, under visible light or at a higher temperature, the surface gradually becomes more hydrophobic once again, as oxygen adsorption replaces the adsorbed water and “heals” the defect sites. [8–10]

An important aim of researchers is to increase the photoactivity of TiO_2 coatings: one known way to achieve this is through modification with noble metals, one of the most suitable options is silver.[11,12] Furthermore, silver particles on the surface provide antibacterial properties [13–15], which is also an attractive function for many practical uses. There are several reasons for the increased photoactivity of titania-silver composite coatings. The main reason is that silver particles can increase the time of the photo-induced charge separation of electrons and holes (silver particles act as electron traps by forming a Schottky barrier at the semiconductor-metal interface) [16]. In certain cases, surface plasmon resonance of silver nanoparticles [17], and band-gap narrowing of the photocatalyst [18] was observed, which can contribute to a wider wavelength range of solar light being utilized.

TiO_2 coatings can be prepared by a variety of methods. The sol-gel technique can produce thin coatings of high surface area with a mesoporous system, which provides possibilities of easy control of structure, composition and layer thickness [19]. There are different methods for the preparation of titania-silver sol-gel composite coatings: the most often used is simply adding silver-compound (e.g. $AgNO_3$) to the precursor sol [20–22]. The impregnation method is used less often: the advantage is that a greatly decreased amount of silver is needed, while the ordered pore structure of the coatings remains unchanged; the disadvantage is that this method needs an additional step during the preparation. In the impregnation method the coating is immersed in $AgNO_3$ solution, dried and then a post-treatment is carried out to reduce the silver ions, *e.g.* UV irradiation [23,24] or heat treatment [25]. The comparison of these different silver modification methods, and studying how the amount, location and other parameters of the silver particles present in the coatings influences the photoactivity and the stability of these photocatalysts can have relevance for future research and applications.

In this paper mesoporous titania sol-gel coatings on glass substrate are prepared and modified with silver by the impregnation method, using two different concentrations of $AgNO_3$ solution. For comparison, porous titania-silver composite coatings are also prepared by the more often used method of adding silver to the precursor solution. Compact SiO_2 barrier layer was deposited on the glass substrate, in order to inhibit ion diffusion (mainly Na^+) from the glass to the titania layer, which is known to decrease its photoactivity [26]. The coatings are characterized by UV-Vis spectroscopy, X-ray diffraction, transmission electron microscopy and wettability measurements, including the investigation of photoinduced wettability conversion. The photoactivity of the samples is studied with dye degradation under UV light, including repeated measurements, to evaluate the stability and reusability of the photocatalytic samples. The effectiveness of the SiO_2 barrier layer is also investigated. The results were analysed with the aim of discovering the connections between the parameters of the silver modification and the structure, photoactivity and photocatalytic stability of the titania coatings, in order to develop cost effective photocatalyst systems with highly increased photoactivity and good stability.

RESULTS AND DISCUSSION

The transmittance spectra of the prepared titania samples can be seen in Fig. 1a. SiO_2 coatings improve the light transmittance of the glass substrate, due to their lower refractive index, while TiO_2 – both as a first and as a second layer - causes a decrease in transmittance, since its refractive index is higher. Silver modification of the SiO_2/TiO_2 coatings by impregnation in $AgNO_3$ solution resulted in lowered light transmittance, due to the presence of silver particles: this change was minimal in the case of TiO_2-Ag(0.03M) samples, while more noticeable in the case of TiO_2-Ag(1M) coatings. This indicates that with higher $AgNO_3$ impregnating solution concentration a higher Ag content could be reached in the coatings. The TiO_2/Ag coatings, which were prepared by adding $AgNO_3$ directly to the precursor sol, had the lowest transmittance of all samples, as a result of their high Ag content. The absorbance spectra of the different silver modified coatings can be seen in Fig. 1b. Comparing the different silver modification methods, only a slight absorbance increase could be observed as a result of the impregnation in $AgNO_3$, while the TiO_2/Ag coatings showed significantly higher absorption. This difference could also be observed in the colour of the samples: TiO_2-Ag coatings were almost completely transparent, while TiO_2/Ag coatings showed a deeper grey colour. The TiO_2/Ag samples also show a peak around 506 nm, which can be attributed to the surface plasmon absorption of Ag particles [27]. The effective

refractive index (n), layer thickness (d) and porosity (P) values of the coatings determined from the transmittance data can be seen in Table 1. The titania coatings had a layer thickness around 100 nm, and a porosity of 32-37%. The titania layer thickness of the $SiO_2/TiO_2/Ag$ samples was estimated to be 116 nm, from the optical analysis of coatings that were prepared the same way, with the exception that no $AgNO_3$ was added to the precursor sol. The presence of the SiO_2 barrier layer caused a slight change in the properties of the TiO_2 coatings, with a small increase in refractive index and decrease in thickness values. The one-sided coatings made for the photocatalysis tests showed almost completely identical properties to the conventionally prepared two-sided coatings, thus, the experiments carried out on these two types of samples can be readily compared.

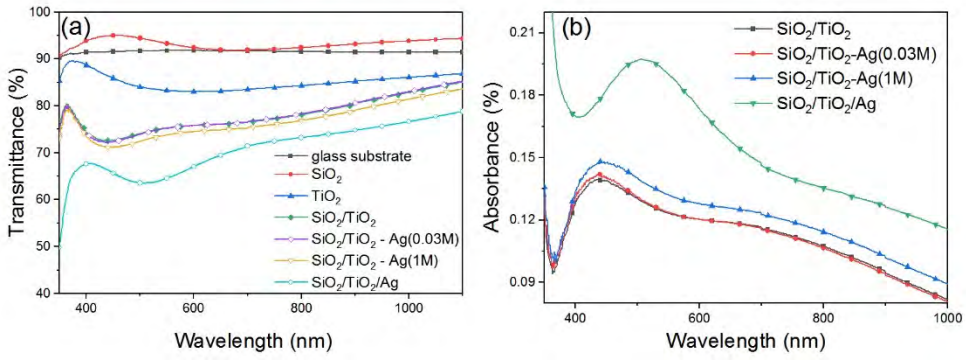

Figure 1. Transmittance (a) and absorbance (b) spectra of the coatings (two-sided samples)

Table 1. Effective refractive index (n), layer thickness (d) and porosity (P) values of the coatings

Sample type	n (-)	d (nm)	P (%)
SiO_2	1.447 ± 0.003	228 ± 23	-
TiO_2 on glass	1.696 ± 0.024	113 ± 2	37 ± 2
TiO_2 on SiO_2 coated glass	1.761 ± 0.016	83 ± 6	33 ± 1
SiO_2 (one-sided)	1.456 ± 0.002	226 ± 3	-
TiO_2 on SiO_2 coated glass (one-sided)	1.767 ± 0.030	87 ± 2	32 ± 1

The theoretical silver content of the TiO_2/Ag coatings calculated from the precursor sol composition is 11.8 wt%. During the calculation of the silver content of TiO_2-Ag coatings, it was assumed that the $AgNO_3$ impregnating solution completely filled the pore volume: silver content was estimated as 0.0421 wt% and 1.38 wt% for TiO_2-Ag(0.03M) and TiO_2-Ag(1M) samples, respectively. These estimated values can be compared with previous Rutherford backscattering spectroscopy measurements of TiO_2-Ag(1M) and TiO_2-Ag(0.03M) coatings prepared on silicon wafers, as reported in our paper [14]: the silver content was found to be 1.07 wt% for TiO_2-Ag(0.03M) samples and 2.37 wt% for TiO_2-Ag(1M) samples. The silver content increased with increasing concentration of $AgNO_3$ impregnating solution, although this increase was not linear. The theoretically calculated values are significantly lower than the measured silver content, suggesting strong adsorption of silver ions on the titania surface. The TiO_2/Ag coatings are estimated to have a silver content of one order of magnitude higher (~12 wt%) compared to the other silver modification method (1-2 wt%).

XRD measurements were first carried out on TiO_2 coatings on SiO_2 coated glass substrates. However, only a low intensity peak around $2\Theta = 25°$ (suggesting anatase crystal phase) could be seen on the XRD pattern (not shown). This weak signal was due to the very low layer thickness of the titania coatings. In order to get better XRD results, TiO_2 powder was prepared from the same precursor sol as used in the coating deposition, and different heat treatments were applied. Three types of silver modified TiO_2 samples were prepared to model the three types of coatings: TiO_2 powder was impregnated in 0.03 M and 1 M $AgNO_3$ solutions; while a TiO_2/Ag powder sample was also prepared from the precursor sol that contained $AgNO_3$. The XRD pattern of these powder samples showed well-defined and multiple peaks, as seen in Fig. 2. The average crystallite sizes and the phase content of the crystalline parts were determined from the XRD pattern, and can be seen in Table 2. TiO_2 powder sample heat-treated at 450 °C (the same as applied during coating preparation) was found to be of mainly anatase phase, with a very small amount of rutile phase. The same TiO_2 sample, when heat-treated at 600 °C, showed narrower, more separated peaks at its XRD pattern, suggesting that higher crystallinity was reached at this higher temperature. This was further confirmed by comparing the calculated crystallite sizes, as seen in Table 2. The composition of the crystalline phases was found to be the same (93 wt% anatase, 7 wt% rutile). No rutile phase was found in the TiO_2/Ag sample (100 wt% anatase), its XRD pattern indicated higher amorphous content compared to the other samples, and the average crystallite size was also estimated to be slightly lower. This difference is most likely due to the different precursor sol composition used for the preparation of these samples.

In comparison, the TiO_2-Ag(0.03M) and TiO_2-Ag(1M) powder samples also contained rutile phase in a small, but slightly higher amount (11 wt% rutile), and slightly higher average crystallite sizes were determined compared to the TiO_2 sample heat treated at the same temperature. The increase of both the crystallite size and the rutile phase content in these Ag modified samples can be a result of the much longer time spent at high temperature, as two consecutive heat treatments were applied during their preparation. However, it's still unexpected that these samples have higher rutile content than the TiO_2 sample treated at 600 °C, since anatase crystal phase transforms into rutile at 500-800 °C [28]. Another possibility is that the higher rutile content was due to the $AgNO_3$ decomposition during the heat treatment: the heat from this exothermic reaction can facilitate the anatase-rutile transformation [29]. Thus, the additional step needed in this silver modification method, which can be seen as a disadvantage, can also cause beneficial effects: the second heat treatment caused increased crystallinity and rutile phase content. Both of these can contribute to higher photocatalytic activity, since it was found in several studies that mainly anatase crystal phase with a low rutile content is a more effective system compared to pure anatase [2].

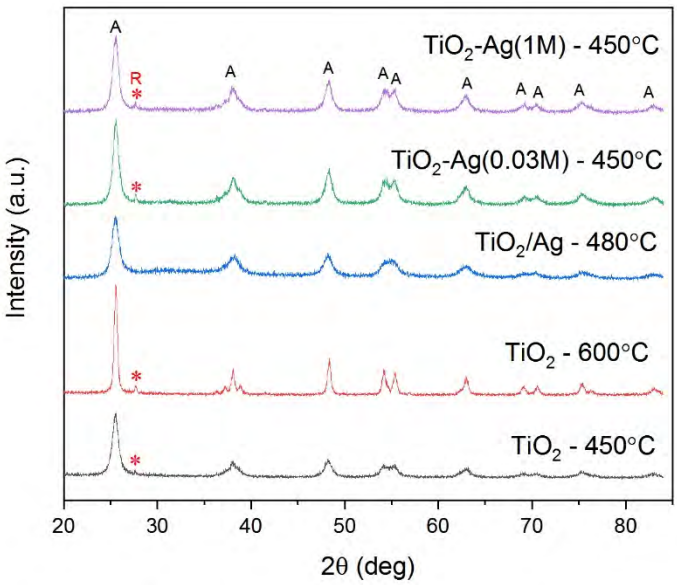

Figure 2. XRD pattern of TiO_2 powder samples (A: anatase, R: rutile)

Table 2. Average crystallite sizes and phase content of crystalline parts determined from the XRD pattern

Sample type	crystallite size	anatase wt%	rutile wt%
TiO_2 (450 °C)	11.8 nm	93	7
TiO_2 (600 °C)	20.2 nm	93	7
TiO_2/Ag (480 °C)	10.6 nm	100	-
TiO_2-Ag(0.03M) (450 °C)	12.7 nm	89	11
TiO_2-Ag(1M) (450 °C)	12.4 nm	89	11

Fig. 3. shows the cross-sectional TEM (a, b), HR-TEM (c) and EELS (d) images of TiO_2 (a) and TiO_2-Ag(1M) (b, c, d) coatings on Si substrates. The porous structure is visible and similar for both samples, and the layer thickness determined from the images (Fig. 3a-b) is the same for both coatings (72 nm, which is in good agreement with the value determined by optical analysis). Hence, the silver modification of the samples did not damage their initial pore system. The coatings are made of interconnected TiO_2 particles that form a pore system that is irregularly structured, but largely homogeneous throughout the coating. According to high resolution TEM (Fig. 3c), the coating consists of 6-11 nm sized crystalline (anatase) TiO_2 particles. The dark particle seen on the surface of the coating in this image is likely a silver metal particle. This can be confirmed by the EELS plasmon image of the TiO_2-Ag(1M) sample (Fig. 3d): the Ag particles appear as dark contrast features, while the oxide matrix exhibits bright contrast (the darker contrast is attributed to metallic behaviour). The sample contains clearly visible, relatively large Ag particles of 6-14 nm on the surface and also within the pores of the layer. It's suggested that in addition to the large particles there are also much smaller ones, inside the pores, which are too small to be detected.

Wettability of TiO_2 coatings and the photoinduced changes in this property were studied by measuring water contact angles. Advancing (Θ_A), receding (Θ_R) and Young's contact angles (Θ_{Young}), and contact angle hysteresis (H) values of the different samples on SiO_2 coated glass can be seen in Table 3. The as-prepared coatings were found to be hydrophilic, with a high contact angle hysteresis (15-20°). After 5 min UV irradiation, all samples showed complete wetting (contact angle 0°). After storing these samples in dark for several days, the contact angle values increased and reached values significantly above their initial value (by about 30°, see Table 3), and after various treatments (e.g. UV and Vis irradiation cycles) the lower original values that could be measured on the as-prepared samples were not recovered, most

likely due to photocorrosion processes. Generally, all samples on SiO_2 coated glass after longer Vis irradiation and/or storage in darkness showed advancing contact angle values between 45° and 80°. Samples modified by $AgNO_3$ solution impregnation showed similar contact angles to that of the pure TiO_2 coatings. In contrast, the TiO_2/Ag samples made from $AgNO_3$ containing precursor sol showed significantly lower contact angles. This can be explained by the differences in coating structure caused by the presence of $AgNO_3$ in the precursor sol; while it is also possible that this silver modification method resulted in a significant amount of highly dispersed, small Ag particles present on the surface, capable of fast silver ion diffusion into water, which caused higher polarity and hydrophilicity.

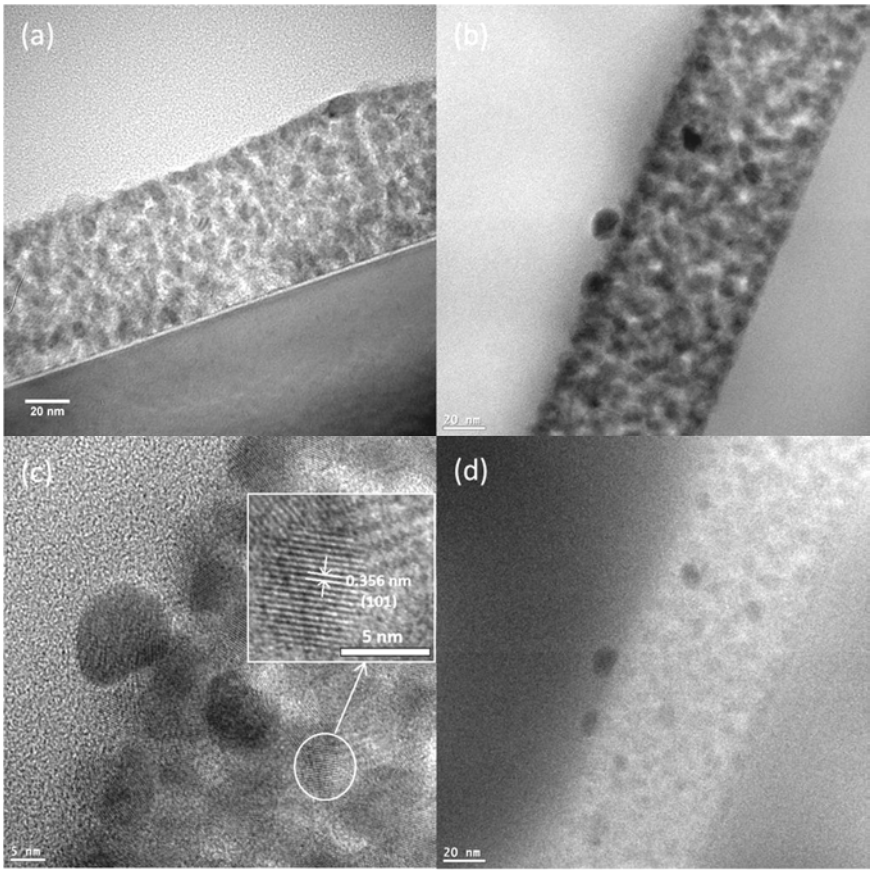

Figure 3. Cross-sectional TEM images of TiO_2 (a) and TiO_2-Ag(1M) (b) coatings; HR-TEM image (c) and EELS plasmon image (d) of the same TiO_2-Ag(1M) sample.

Table 3. Advancing (Θ_A), receding (Θ_R) and Young's contact angles (Θ_{Young}) and contact angle hysteresis (H) values of samples made on SiO_2 coated glass, measured right after preparation and after 5 min UV irradiation followed by 2 days in dark

	Θ_A (°)	Θ_R (°)	Θ_{Young} (°)	H (°)
	as-prepared			
TiO_2	31 ± 4	16 ± 3	24 ± 3	15 ± 1
TiO_2-Ag(0.03M)	31 ± 6	14 ± 5	24 ± 5	17 ± 4
TiO_2-Ag(1M)	37 ± 5	18 ± 5	29 ± 4	20 ± 4
TiO_2/Ag	12 ± 2	-	-	-
	5 min UV, 2 days in dark			
TiO_2	57 ± 8	34 ± 6	47 ± 7	23 ± 3
TiO_2-Ag(0.03M)	68 ± 10	43 ± 6	56 ± 8	25 ± 3
TiO_2-Ag(1M)	73 ± 7	48 ± 6	61 ± 6	25 ± 2
TiO_2/Ag	45 ± 9	30 ± 8	38 ± 8	15 ± 2

The TiO_2 coatings prepared on bare glass were found to be even more hydrophilic: all types of samples on bare glass showed complete wetting, even after 2 days of storage in dark (seen also in Fig. 4). This considerable difference between the same coating types prepared on different surfaces is due to the Na^+ migration from the glass into the titania layer during the heat treatment of the coating preparation, which is only possible in the absence of SiO_2 barrier layer. The high Na^+ content of TiO_2 samples on bare glass causes higher polarity and increased hydrophilicity. The Na ions can diffuse into the water droplets placed on the sample, further increasing the surface polarity.

Several cycles of UV irradiation/regeneration under visible light were repeated on the samples. The comparison of TiO_2 and $AgNO_3$ solution impregnated TiO_2 samples can be seen in Fig. 4. All samples showed photoinduced wettability conversion behaviour through multiple cycles. However, this effect was much smaller in the case of the coatings prepared on bare glass substrates, most likely due to their high Na^+ content. Slower regeneration of hydrophobicity was observed with increasing Ag content. Presumably, the Ag particles present in the samples can form silver ions, and may even diffuse into the water placed on the surface during the contact angle measurements, leading to a more hydrophilic surface when compared to pure TiO_2.

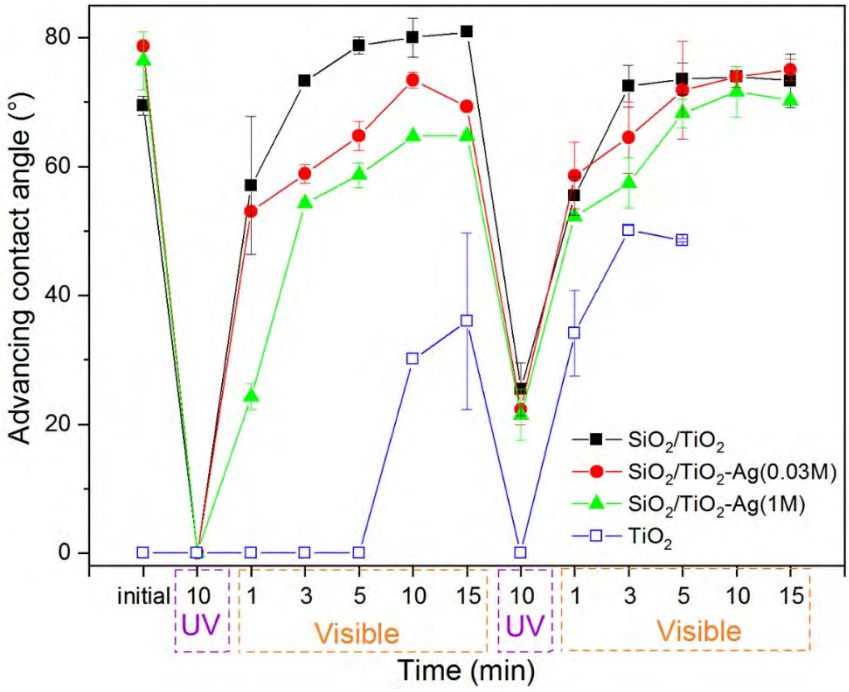

Figure 4. Advancing contact angles measured on TiO_2 and TiO_2-Ag samples during two UV/Vis cycles

Photoactivity of the samples was studied using methyl orange dye solution. In the first tests, the photocatalytic activity of TiO_2, TiO_2-Ag(0.03M) and TiO_2-Ag(1M) samples was compared. Fig. 5a shows the absorbance decrease of the dye solution during UV irradiation, on the example of a TiO_2 coating prepared on SiO_2 coated glass. A peak attributed to methyl orange can be seen at 465 nm [30]. Dye decolourization was compared for different samples by determining A/A_0, where A is the absorbance at 465 nm after t time of UV irradiation, and A_0 is the initial absorbance at 465 nm before irradiation (Fig. 5b). All TiO_2 samples on SiO_2 coated glass showed significant photoactivity. In comparison, the photoactivity of samples prepared on bare glass was found to be drastically decreased due to their high Na^+ content, dye degradation was minimal. Dye photodegradation was found to follow pseudo-first order reaction.The degradation rate constants (k) were determined by linearization of the measured $A/A_0 - t$ values, using the following equation:

$\ln(A/A_0) = -kt$. The k value was determined from the slope of the line fitted to the data points. The degradation rate constants were 0.12 ± 0.04 h^{-1} for SiO_2/TiO_2, 0.30 ± 0.04 h^{-1} for SiO_2/TiO_2-Ag(0.03M), 0.33 ± 0.08 h^{-1} for SiO_2/TiO_2-Ag(1M), and 0.35 ± 0.04 h^{-1} for SiO_2/TiO_2/Ag samples. These results show that the dye photodegradation was significantly faster in the silver modified coatings compared to the pure titania coatings. The silver content of the samples did not appear to influence the photoactivity: lower Ag content was enough to achieve a high photoactivity increase. However, another important question is the stability and reusability of these photoactive coatings: whether the samples can degrade the dyes in repeated tests with the same efficiency, or if over time their photoactivity would decrease. Furthermore, in our previous paper [14], it was found that the silver content of similarly prepared samples decreases in time while they are immersed in an aqueous solution – it's likely that this process can influence the photoactivity of the coatings. For this reason, the samples were further evaluated in repeated photocatalysis tests.

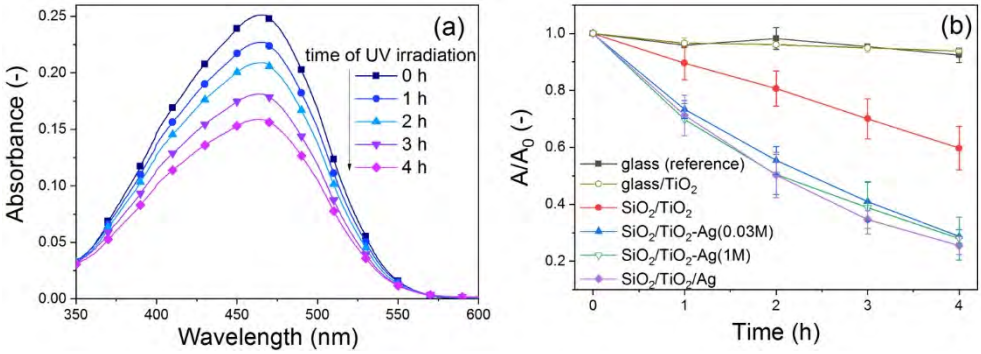

Figure 5. Photocatalysis measurements: (a) absorbance decrease of methyl orange solution containing SiO_2/TiO_2 sample under UV light; (b) A/A_0 – t curves of different samples

In these repeated measurements, the samples were irradiated for 4 × 4 h: after each 4 h irradiation a new dye solution was used for the same sample. The decrease in concentration of dye molecules was estimated by the A/A_0 value after each 4 h UV irradiation, and the dye degradation efficiency (D) of the different samples was calculated by the following equation: $D = (1\text{-}A/A_0) \times 100\%/a$, where a is the area of the coating sample.

In order to have a well determined area of coating in contact with the dye solution, coatings were deposited on only one side of the glass substrate using a special sample holder during the dip-coating process. All titania coatings were prepared on SiO_2 coated glass for these measurement.

As it can be seen in Fig. 6, the pure titania coatings showed a stable photoactivity during the full 16 h irradiation of the photocatalysis tests. Similarly, to the previously described experiments, the results of the repeated tests showed that all Ag modified coatings showed significantly increased dye degradation compared to the pure TiO_2 samples. It was found that dye degradation efficiency values (determined after the first 4 h of irradiation) did not increase with increasing the amount of silver in the samples. However, it was found that even though the TiO_2-Ag(0.03M) samples initially had the highest photoactivity, this photoactivity decreased after the test was repeated several times. In contrast, the TiO_2-Ag(1M) samples, which contained a higher amount of silver particles, did not show significant photoactivity decrease during the measured time interval (16 hours). It can be assumed that the silver particles on the titania surface start to dissolve and diffuse as silver ions into the aqueous solution during the measurement [14]. After a certain time, enough silver is removed from the coating that the photoactivity starts to decrease. While initially a lower surface coverage of silver might even be advantageous, during repeated use the photoactivity decrease would occur much slower in the impregnated samples with the higher Ag content. This is why TiO_2-Ag(0.03M) samples showed higher initial photoactivity, but TiO_2-Ag(1M) samples kept their high photoactivity for longer during repeated use. The speed of this process can also depend on the sizes and dispersity degree of the silver particles, and in this, there might also be differences between the samples. It's possible that bigger Ag particles could form in the TiO_2-Ag(1M) coatings due to the much higher $AgNO_3$ impregnating solution concentration used, which would also cause slower dissolution. Interestingly, the TiO_2/Ag coatings that contained the highest amount of silver also showed a slight decrease in photoactivity. Possibly the reason for this is that in the TiO_2/Ag coatings only some amount of the Ag particles are on the surface and accessible during the photocatalytic degradation, and silver is also incorporated into the TiO_2 matrix; while with the impregnated TiO_2-Ag coatings the accessibility of the silver particles is ensured. In these experiments, the silver particles present on the surface (or in the vicinity of the surface) seemed to play a more significant role in the rate of dye photodegradation, than the silver present in the matrix.

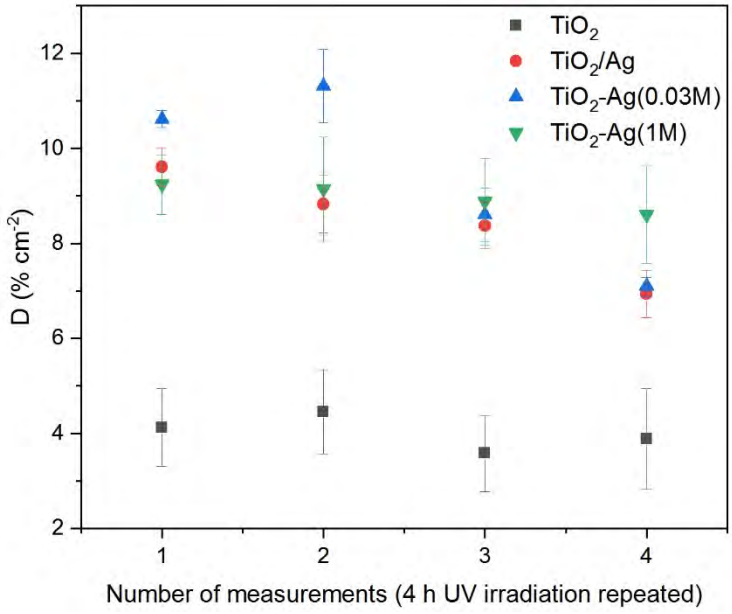

Figure 6. Repeated photocatalysis measurements

CONCLUSIONS

The results show that the method and parameters of silver modification have an important impact on the long-term photocatalytic activity of titania coatings. Silver modification via impregnation in $AgNO_3$ solution followed by a heat treatment is a promising method for increasing the photoactivity of self-cleaning TiO_2 coatings. The second heat treatment, which was carried out in order to reduce silver ions, was found to have further beneficial results: the crystallinity increased, and rutile-anatase mixed crystal phase was achieved, which can both improve photoactivity. The prepared titania coatings had a highly porous, crystalline structure. SiO_2 barrier layer was applied on the glass substrates, which led to improved photocatalytic properties and more pronounced photoinduced wettability conversion behaviour, both important for practical applications. Complete wetting was achieved under UV light, which means that water and aqueous media can penetrate the pores, and the high surface area provided by the porous structure can be fully utilized. The reusability and stability of the photocatalyst layer can be ensured by choosing an optimal silver content, which can be controlled by impregnation parameters (*e.g.* concentration of impregnating $AgNO_3$ solution).

EXPERIMENTAL SECTION

All reagents were analytical grade and used without further purification. The following materials were used for the preparation of the samples: hexadecyltrimethylammonium bromide (CTAB, 99+%, Acros Organics), Pluronic P123 (P123, average mol wt 40000, Sigma Aldrich), hydrochloric acid (HCl, 37%, Reanal), nitric acid (HNO_3, 65%, Lach-Ner), tetraethyl orthosilicate (TEOS, 99%, Merck), titanium (IV) butoxide (98%, Merck), titanium (IV) isopropoxide (98+%, Acros Organics), acetylacetone (99+%, Acros Organics), $AgNO_3$ (99.8%, Lach-Ner), 2-propanol (99+%, Acros Organics), ethanol (EtOH, 99.7+%, Reanal), purified distilled water (filtered with Millipore Simplicity 185 system to reach 18.2 MΩ cm). Methyl orange dye (95%, Acros Organics) was used in the photocatalysis tests.

Preparation of coatings

TiO_2 and two-layered SiO_2/TiO_2 coatings were prepared on glass substrates using sol-gel dip-coating. Silver modified TiO_2 samples were prepared by two methods: by adding $AgNO_3$ to the precursor sol, and by impregnation of as-prepared TiO_2 samples in $AgNO_3$ solutions followed by heat treatment. Some titania samples were also deposited on silicon wafers for the HR-TEM measurements. For the photocatalysis tests one-sided samples were prepared using a laboratory made sample holder that covered one side of the substrate. The synthesis of precursor sols via acid catalysed hydrolysis and polycondensation of silicon- and titanium-alkoxides was similar to that reported previously [14,31]. Compact SiO_2 barrier layers were prepared from precursor sols with molar ratios of TEOS : EtOH : HCl : H_2O - 1 : 4.75 : 7.2×10^{-4} : 4.00. For the porous TiO_2 coating preparation the molar ratios of titanium (IV) butoxide : EtOH : HNO_3 : H_2O : CTAB were 1 : 27.74 : 0.39 : 1.54 : 0.124 in the precursor sol. Porous TiO_2/Ag composite coatings were also prepared from precursor sols that contained $AgNO_3$, with molar ratios of titanium (IV) isopropoxide : EtOH : acetylacetone : H_2O : P123 : $AgNO_3$ - 1 : 33.80 : 0.97 : 2.19 : 0.034 : 0.1. Film deposition from the precursor sols onto clean glass and Si substrates (cleaned with 2-PrOH and distilled water) and SiO_2 coated glass substrates was carried out with a dip-coater (Plósz Mérnökiroda Kft., Hungary) using withdrawal speeds of 6 cm min^{-1} for SiO_2 barrier layers, and 12 cm min^{-1} for TiO_2 coatings. As the thickness of the coatings can be controlled by the withdrawal speed, these values were selected in order to prepare continuous, homogeneous and transparent films of desired layer thicknesses, with good repeatability. Samples were placed in an oven (Nabertherm B170) for heat treatment at 480 °C for 1 h (TiO_2/Ag

coatings), or 450 °C for 30 min (all other samples). The heat treatment parameters were chosen to reach suitable stability and avoid significant shrinkage of the coatings. To prepare two-layered SiO_2/TiO_2 coatings, the SiO_2 layer was dip-coated followed by a heat-treatment, and these steps were then repeated with the appropriate parameters to prepare the second, titania layer. Silver modified titania coatings denoted as TiO_2-Ag(0.03M) and TiO_2-Ag(1M) samples were prepared by impregnation of porous TiO_2 samples in $AgNO_3$ aqueous solutions of 0.03 M or 1 M concentrations. The impregnation was carried out with the dip-coater using a dipping speed of 1 cm min^{-1} and withdrawal speed of 10 cm min^{-1}. The samples were then washed with distilled water, dried, and placed in an oven for heat-treatment at 60 °C for 30 min, then 450 °C for 30 min.

Measurements and methods

The transmittance spectra of the glass substrates and the coated samples were measured by an Analytic Jena Specord 200–0318 UV-Vis spectrophotometer, in the wavelength range of 350-1100 nm, using air as reference, a scanning speed of 10 nm s^{-1} and a resolution of 1 nm. The refractive index (at 632.8 nm) and layer thickness values of SiO_2, TiO_2 and SiO_2/TiO_2 two-layered coatings on glass substrates were calculated from the transmittance spectra using thin layer optical models [32]. The porosity of these coatings was estimated from the measured effective refractive index using the Lorentz-Lorenz formula [33].

The crystallinity of titania coatings, and TiO_2 and silver modified TiO_2 powders was analysed using an X-ray diffractometer (Philips PANalytical X'pert Pro, Cu-K_α radiation). Powder samples were prepared in order to model the investigated TiO_2 and silver modified TiO_2 coatings: precursor sols (used in the preparation of TiO_2 and TiO_2/Ag coatings) were dried for 24 h until they formed a gel, then different heat-treatments were carried out. TiO_2 powders (heat-treated at 450 °C, 30 min) were impregnated in 0.03 M and 1 M $AgNO_3$ solution, filtered and dried, then heat-treated the same way as the respective coating samples after impregnation. From the XRD pattern the average crystallite sizes were determined from the highest intensity peak (corresponding to anatase (101) plane), using Scherrer's equation [34].

Transmission electron microscopy (TEM) and high-resolution transmission electron microscopy (HR-TEM) cross-sectional images of TiO_2 and TiO_2-Ag(1M) coatings on Si substrates were taken by a JEOL 3010 HRTEM (300 kV) with a point resolution of 0.17 nm). The microscope was equipped with a Tridiem GATAN Image Filter, making possible energy filtered TEM imaging, electron energy loss spectrum (EELS) measurements.

Wettability measurements of the samples were carried out using a drop shape analyser (DSA30, KRÜSS GmbH) device. Contact angles of distilled water were measured on TiO_2 coatings prepared on SiO_2 coated glass and on bare glass substrates. Advancing and receding contact angles were measured with the sessile drop method and the drop-build-up technique. The samples were placed in a closed chamber, where the relative humidity was kept above 90%, the temperature was 25 °C, and the following procedure was repeated three times on each sample: a water droplet of 10 µl was placed on the sample surface to measure the advancing contact angles, then 5 µl of water was removed to measure the receding angle. Contact angle hysteresis (H) was calculated as the difference of advancing (Θ_A) and receding (Θ_R) contact angles, and the Young's contact angle (Θ_{Young}) was calculated using the Wolfram-Faust equation [35]: $\Theta_{Young} = \arccos((\cos \Theta_A + \cos \Theta_R)/2)$. The photoinduced surface wettability conversion of the samples was studied by placing the samples under visible and UV light sources. The UV lamp was a Phillips CLEO UV-A light source (HPA 400 S, 400 W), with an emittance maximum in UV of 365 nm. The light arrived perpendicularly at the surface of the samples from a distance of 30 cm and intensity of 47.1 mW cm^{-2}. Two 57 W LED lamps (GE 93845, emission maximum at 600 nm) were used as visible light source, with a distance of 18 cm and intensity of 0.47 mW cm^{-2}.

Methyl orange dye, an anionic dye often used for the characterization of photocatalysts [36,37], was used as model pollutant in the photocatalysis tests: No methyl orange adsorption from their aqueous solution could be detected on the TiO_2 coating surface in preliminary experiments. 10^{-5} M methyl orange aqueous solutions were prepared using distilled water. The coatings were placed in glass crystallizing dishes, each containing 25 mL dye solution and irradiated with a UV lamp (the parameters of the UV irradiation were the same as described for the wettability measurements). Water bath and ventilation was used to counteract the heat generated by the high intensity UV lamp. The solution was mixed during the 4 × 1 h of UV irradiation. Before the measurement, and after each hour under UV light the absorption spectra of the dye solutions were measured in a quartz cuvette in the wavelength range of 350-600 nm, using distilled water as reference (otherwise using the same parameters as described above). In the repeated measurements, 4 × 4 h UV irradiation was repeated on TiO_2, TiO_2-Ag(0.03M), TiO_2-Ag(1M) and TiO_2/Ag coatings prepared only on one side of the glass substrate, using new dye solutions for each time. The samples were placed with the coated side upwards under the UV lamp. All photocatalysis test results were averaged from data measured on at least 3 identical samples in each case.

ACKNOWLEDGMENTS

The authors thank J. Sinclaire-Krasznai, P. Gömbös and E. Hild for their help. This work was supported by the Ministry of Human Capacities (BME FIKP-NAT); the National Research Development and Innovation Office (TNN-123631, K-128266); and the TÁMOP 4.2.1/B-09/1/KMR-2010-0002 (BME R + D + I project). Emőke Albert's research work was supported by the European Union and the State of Hungary, co-financed by the European Social Fund (TÁMOP-4.2.4.A/2-11/1-2012-0001).

REFERENCES

1. T. Ochiai; A. Fujishima; *J. Photochem. Photobiol. C Photochem. Rev.,* **2012**, *13*, 247–262.
2. M. Kapilashrami; Y. Zhang; Y.S. Liu; A. Hagfeldt; J. Guo; *Chem. Rev.,* **2014**, *114* (19), 9662–9707.
3. K. Nakata; A. Fujishima; *J. Photochem. Photobiol. C Photochem. Rev.* **2012**, *13* (3), 169–189.
4. C. Byrne; G. Subramanian; S.C. Pillai; *J. Environ. Chem. Eng.* **2018**, *6* (3), 3531–3555.
5. P. Hegedus; E. Szabó-Bárdos; O. Horváth; K. Horváth; P. Hajós; *Materials (Basel).* **2015**, *8* (1), 231–250.
6. M. Patil; S. Shaikh; I. Ganesh; *Curr. Nanosci.* **2015**, *11* (3), 271–285.
7. V.A. Ganesh; H.K. Raut; A.S. Nair; S. Ramakrishna; *J. Mater. Chem.* **2011**, *21* (41), 16304–16322.
8. R. Wang; K. Hashimoto; A. Fujishima; M. Chikuni; E. Kojima; A. Kitamura; M. Shimohigoshi; T. Watanabe; *Nature* **1997**, *338*, 431–432.
9. R.-D. Sun; A. Nakajima; A. Fujishima; T. Watanabe; K. Hashimoto; *J. Phys. Chem. B* **2002**, *105* (10), 1984–1990.
10. M. Miyauchi; N. Kieda; S. Hishita; T. Mitsuhashi; A. Nakajima; T. Watanabe; K. Hashimoto; *Surf. Sci.* **2002**, *511* (1–3), 401–407.
11. J. Schneider; M. Matsuoka; M. Takeuchi; J. Zhang; Y. Horiuchi; M. Anpo; D.W. Bahnemann; *Chem. Rev.* **2014**, *114* (19), 9919–9986.
12. S.G. Kumar; L.G. Devi; *J. Phys. Chem. A*, **2011**, *115*, 13211–13241.
13. J.G. McEvoy; Z. Zhang; *J. Photochem. Photobiol. C Photochem. Rev.* **2014**, *19* (1), 62–75.
14. E. Albert; P.A. Albouy; A. Ayral; P. Basa; G. Csík; N. Nagy; S. Roualdès; V. Rouessac; G. Sáfrán; Á. Suhajda; Z. Zolnai; Z. Hórvölgyi; *RSC Adv.* **2015**, *5* (73), 59070–59081.
15. S.P. Tallósy; L. Janovák; E. Nagy; Á. Deák; Á. Juhász; E. Csapó; N. Buzás; I. Dékány; *Appl. Surf. Sci.* **2016**, *371*, 139–150.

16. J.M. Herrmann; H. Tahiri; Y. Ait-Ichou; G. Lassaletta; A.R. González-Elipe; A. Fernandez; *Appl. Catal. B Environ.* **1997**, *13* (3–4), 219–228.
17. K. Awazu; M. Fujimaki; C. Rockstuhl; J. Tominaga; H. Murakami; Y. Ohki; N. Yoshida; T. Watanabe; *J. Am. Chem. Soc.* **2008**, *130* (5), 1676–1680.
18. K. Page; R.G. Palgrave; I.P. Parkin; M. Wilson; S.L.P. Savin; A.V. Chadwick; *J. Mater. Chem.* **2007**, *17* (1), 95–104.
19. W. Li; Z. Wu; J. Wang; A.A. Elzatahry; D. Zhao; *Chem. Mater.* **2014**, *26*, 287–298.
20. G. Zhao; H. Kozuka; T. Yoko; *Thin Solid Films* **1996**, *277* (1–2), 147–154.
21. M. Epifani; C. Giannini; L. Tapfer; L. Vasanelli; *J. Am. Ceram. Soc* **2000**, *83* (10), 2385–2393.
22. E. Traversa; M.L. Vona; D.I. Vona; P. Nunziante; S. Licoccia; T. Sasaki; N. Koshizaki; *J. Sol-Gel Sci. Technol.,* **2000**, *19*, 733–736.
23. I.M. Arabatzis; T. Stergiopoulos; M.C. Bernard; D. Labou; S.G. Neophytides; P. Falaras; *Appl. Catal. B Environ.* **2003**, *42* (2), 187–201.
24. P. Falaras; I.M. Arabatzis; T. Stergiopoulos; M.C. Bernard; *Int. J. Photoenergy* **2003**, *5* (3), 123–130.
25. L. Mai; D. Wang; S. Zhang; Y. Xie; C. Huang; Z. Zhang; *Appl. Surf. Sci.* **2010**, *257* (3), 974–978.
26. P. Novotna; J. Krysa; J. Maixner; P. Kluson; P. Novak; *Surf. Coatings Technol.* **2010**, *204* (16–17), 2570–2575.
27. M.M. Viana; N.D.S. Mohallem; D.R. Miquita; K. Balzuweit; E. Silva-Pinto; *Appl. Surf. Sci.* **2013**, *265*, 130–136.
28. C. Su; B.Y. Hong; C.M. Tseng; *Catal. Today* **2004**, *96* (3), 119–126.
29. J. Yu; J. Xiong; B. Cheng; S. Liu; *Appl. Catal. B Environ.* **2005**, *60* (3–4), 211–221.
30. D. Zhu; Z.A. Schelly; *Langmuir* **1992**, *8* (1), 48–50.
31. B. Tegze; E. Albert; B. Fodor; G. Sáfrán; Z. Hórvölgyi; *Dye. Pigment.* **2019**, *167*, 109–119.
32. E. Hild; A. Deák; L. Naszályi; Ö. Sepsi; N. Ábrahám; Z. Hórvölgyi; *J. Opt. A Pure Appl. Opt.* **2007**, *9* (10), 920–930.
33. W. Heller; *J. Phys. Chem.* **1965**, *69* (4), 1123–1129.
34. B.D. Cullity; *Elements of X-ray diffraction*, Addison-Wesley, London, **1956**, pp. 99.
35. E. Wolfram; R. Faust; *Wetting, Spreading Adhes.* **1978**, 213–222.
36. U.G. Akpan; B.H. Hameed; *J. Hazard. Mater.* **2009**, *170* (2–3), 520–529.
37. I.K. Konstantinou; T.A. Albanis; *Appl. Catal. B Environ.* **2004**, *49* (1), 1–14.

STUDIA UBB CHEMIA, LXIV, 3, 2019 (p. 99-109)
(RECOMMENDED CITATION)
DOI:10.24193/subbchem.2019.3.08

MORPHO-STRUCTURAL AND PHOTOCATALYTIC PROPERTIES OF SnO_2 NANOPARTICLES

MARIA ŞTEFAN[a,*], OVIDIU PANA[a], CRISTIAN LEOSTEAN[a], ADRIANA POPA[a], DANA TOLOMAN[a], SERGIU MACAVEI[a], DIANA LAZAR[a], LUCIAN BARBU-TUDORAN[a]

ABSTRACT. SnO_2 nanoparticles were successfully synthesized by precipitation method, in the presence of hexadecyltrimethyl ammonium bromide (CTAB) and polyethylene glycol 600 (PEG 600) as surfactants. The obtained SnO_2 nanoparticles were characterized by X-ray diffraction (XRD), porosity and surface area measurements (BET), high resolution transmission electron microscopy (HRTEM), X-ray photoelectron spectroscopy (XPS). Also, photocatalytic properties toward degradation of Rhodamine B (RhB) were investigated. It was found that morpho-structural properties are influenced by the preparative conditions of doped SnO_2 nanoparticles.

Keywords: *SnO_2; nanoparticles; photocatalytic properties*

INTRODUCTION

Wastewater decontamination is a stringent requirement in the research field of environmental protection [1-4]. Utilization of green and cheap technologies has been considered a convenient solution to complete degradation of organic pollutants released from industry [5-8].

Photocatalysis is an advanced oxidation method used for removing organic contaminants such as organic dyes, antibiotics, etc from aquatic system. Generally, semiconductor materials namely metal oxides have been employed for the photo-degradation of organic contaminants [9-10]. Among various oxides SnO_2 is one of the most popular and promising materials in wide range of applications such as gas sensing, photocatalytic applications, solar cells, lithium-ion batteries, because of its high stability, non-toxicity, eco-friendly and low cost [11-15].

[a] *National Institute for Research and Development of Isotopic and Molecular Technologies, 67-103 Donath Str., RO-400293 Cluj-Napoca, Romania.*
** Corresponding author: mstefan@itim-cj.ro*

The obtaining of nanoparticles with predetermined size and shape represents the target of materials chemistry [16-19]. The morpho-structural properties of oxide nanoparticles can be controlled by addition in synthesis procedure of various surfactants [20, 21]. It is known that organic surrounding environment and surface passivation can provide stability and additional functionality to the nanoparticles. In the present work we report influence of different surfactants on morpho-stuctural properties of SnO_2 nanoparticles. Also, the photocatalytic properties of samples for degradation of rhodamine B (RB) were evaluated.

RESULTS AND DISCUSSION

Generally, the properties of nanoparticles can be controlled by a rigorous modification of experimental parameters. SnO_2 nanoparticles were obtained by precipitation method in the presence of different surfactants. The general chemical equations for obtaining of SnO_2 nanoparticles are:

$$SnCl_2 + 2NaOH \rightarrow Sn(OH)_2 + 2NaCl \quad (1)$$
$$Sn(OH)_2 \rightarrow SnO + H_2O \quad (2)$$
$$SnO+1/2O_2 \rightarrow SnO_2 \quad (3)$$

The crystalline structure of the obtained nanoparticles was evidenced by X-ray diffraction. Figure 1 shows the diffraction patterns and corresponding indexation of S1, S2 and S3 samples. The diffraction peaks are sharp and strong indicating the good crystallinity of the samples. All of them together with corresponding reflection planes can be indexed to tetragonal SnO_2 nanoparticles (WWW-MINCRYST, CASSITERITE-779). No other peaks were observed such as Sn or any other Sn based oxide, indicating the high purity of the samples.

Using the Scherer formula, along (110) diffraction lines, the average crystallite sizes of all the samples have been determined. The calculated values are 10.8 nm (S1), 11.3 nm (S2) and 11.5 nm (S3), respectively. The addition of surfactants in the synthesis procedure for the obtaining of SnO_2 nanoparticles seems to favor the increase of the crystallite sizes.

Figure 2 shows the transmission electron microscopy (TEM) images of the SnO_2 nanoparticles obtained with/ without surfactants. It can be seen that nanoparticles consist of small particles with tetrahedral shape with diameters around 11 nm, showing a strong tendency toward agglomeration. It can be seen that the addition of surfactants slightly changes the morphology of SnO_2 nanoparticles.

The representative high-resolution TEM (HRTEM) images are given in figure 3. Lattice fringes are clearly visible in images revealing the crystalline nature of nanoparticles. Based on the Fourier analysis of this image, to crystalline planes of SnO_2 (110) was identified.

For qualitative analysis of samples, the following XPS core-level lines were recorded: Sn 3*d*, O 1*s* and C 1*s*. The C 1s line associated to C-C or C-H bindings positioned at 284.6 eV was used for spectra calibration. As an example, the XPS spectrum together with the corresponding deconvolutions of Sn 3*d* core-levels for sample S3 is shown in figure 4.

The restrictions used for fitting the spectrum refer to the relation between integral intensities of the doublet components $I_{(5/2)} = (2/3)I_{(3/2)}$ and doublet separation considered as 8.4 eV. The observed position of 488.0 eV for Sn 3*d* (5/2) and 496.4 eV for Sn 3*d* (3/2) is characteristic to Sn^{4+} oxidation state. Two shake-up satellites positioned at 491.5 eV and 499.9 eV were also used in the deconvolution process. Samples S1 and S2 show similar Sn 3*d* spectra, characteristic to Sn^{4+} oxidation state.

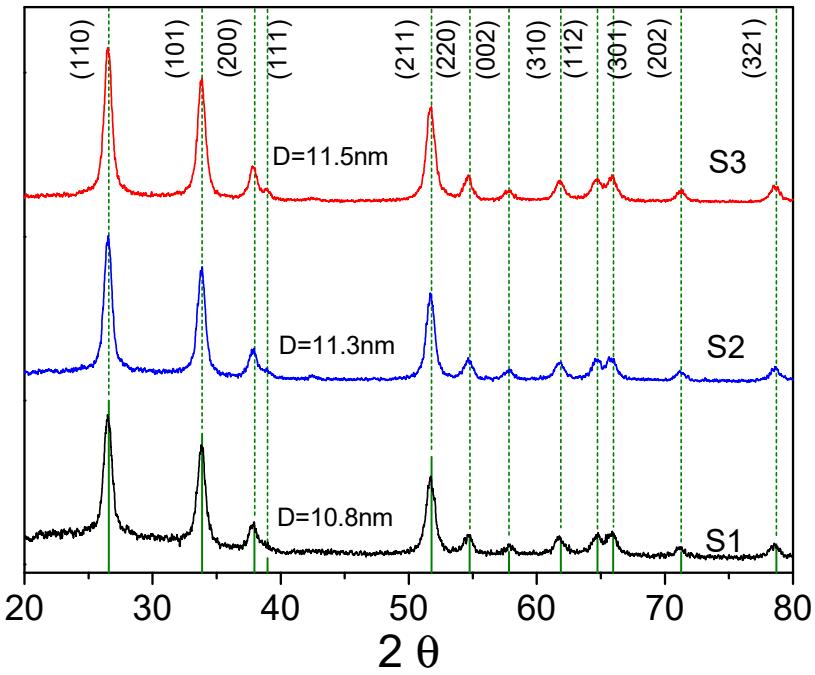

Figure 1. Diffraction patterns and corresponding indexation of S1(SnO_2), S2 (SnO_2-CTAB) and S3(SnO_2-PEG600) nanoparticles

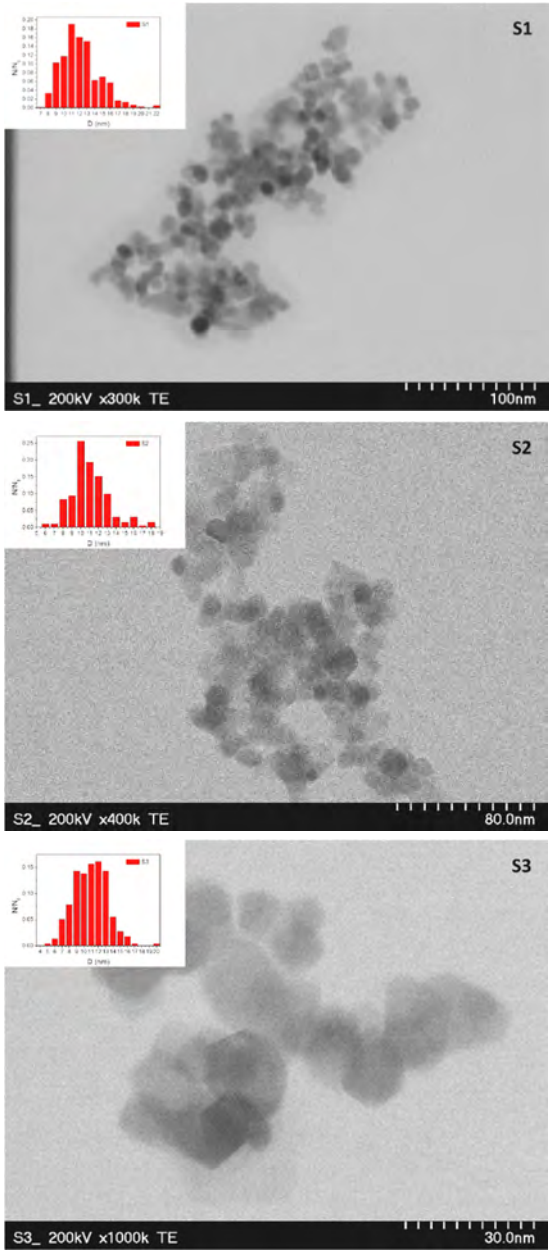

Figure 2. TEM images of SnO_2 nanoparticles obtained with different surfactants S1-SnO_2, S2-SnO_2-CTAB, S3- SnO_2-PEG600

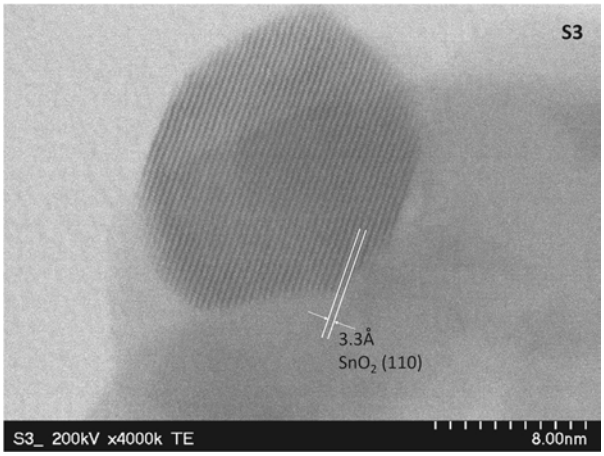

Figure 3. HRTEM image corresponding to S3(SnO_2-PEG600) sample

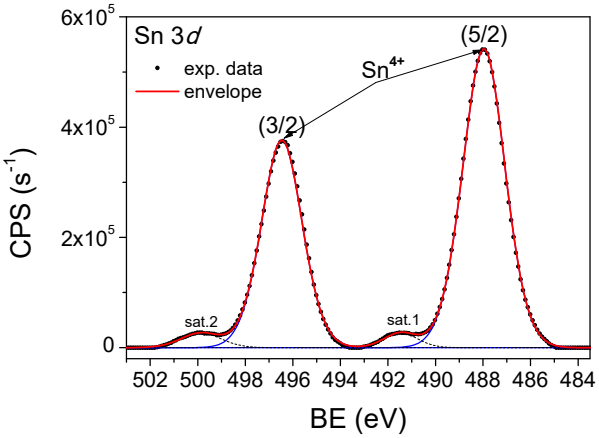

Figure 4. XPS spectrum of Sn 3*d* core-levels together with the corresponding deconvolutions in case of S3 (SnO_2-PEG600) sample.

The N_2 adsorption–desorption isotherms and corresponding pore size distribution of SnO_2 nanoparticles are shown in Figure 5 (a, b). The results indicate that for all samples the isotherms are of types IV with hysteresis loop on the desorption branch, sustaining the mesoporous structure of samples. Also, the pore size distribution shows mean diameter of 80 Å that confirmed the presence of mesopores. Other data such as BET surface area, pores volumes were also calculated and are given in Table 1.

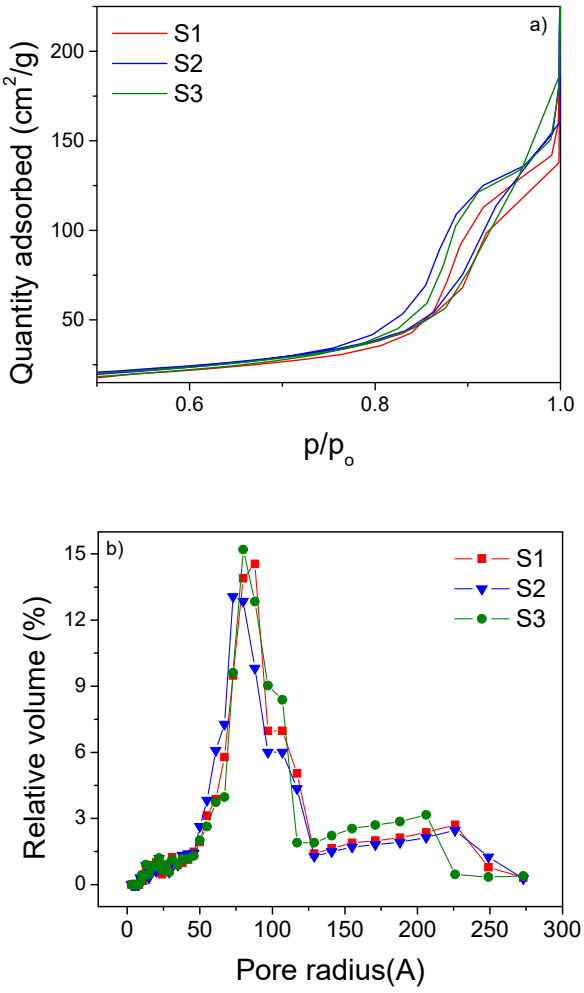

Figure 5. N_2 adsorbtion-desorption isotherms (a) and corresponding pore size distribution; (b) of nanoparticles: S1(SnO_2), S2(SnO_2-CTAB)and S3(SnO_2-PEG600)

The BET surface area of SnO_2 nanoparticles prepared with/without surfactants varies from 45.29 - 47.16 m^2/g, depending on surfactant type. The addition of CTAB seems to have no effect on surface area. Also, the pore volume was found to increase for sample with PEG 600. This behavior is due to the partial/total removing of surfactants in the calcinations process.

Table1. Surface area and pores characteristic of SnO_2 nanoparticles with/without surfactants

Sample	BET surface area (m^2/g)	Pore volume (cm^3/g)
S1(SnO_2)	47.16	0.24
S2 (SnO_2-CTAB)	47.16	0.23
S3(SnO_2-PEG600)	45.29	0.25

The photocatalytic activity of the synthesized samples was estimated by examining the degradation of Rhodamine B (RhB) pollutant. Prior to the photocatalytic process, the RhB adsobtion on SnO_2 nanoparticles surface, in the dark was tested. It was observed that the adsorption-desorption equilibrium was reach after 30min. All samples present similar adsorption, only a small amount of RhB molecules being adsorbed at the nanoparticles surface. After the equilibrium was reached, the RhB solution containing the nanoparticles was irradiated by visible light. The changes in intensity of the UV-VIS absorption peak of RhB situated at 554 nm as a function of irradiation time was monitored.

As an example, figure 6 presents the evolution of RhB absorption peak intensity in the presence of S1 sample at different irradiation time intervals. Based on the absorption changes, the photocatalytic activity was calculated. The photocatalytic activity of RhB in the presence of S1, S2 and S3 samples is shown in figure 7. After 180 min of visible light irradiation, only 19-24% of the RhB dye was degraded by S3 and S2 sample, whereas 98% of the RhB dye was degraded by S1 sample.

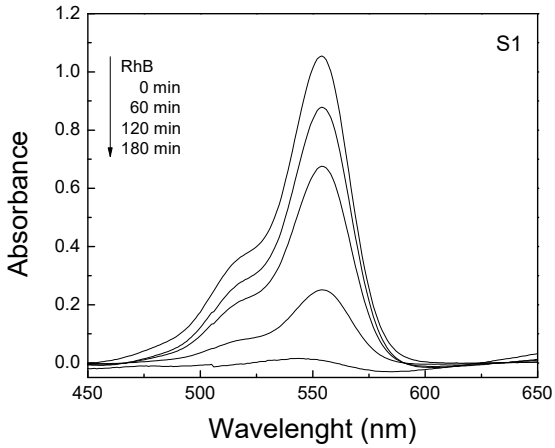

Figure 6. UV–vis absorption spectra of RhB aqueous solution in the presence of S1(SnO_2) sample at different irradiation time interval

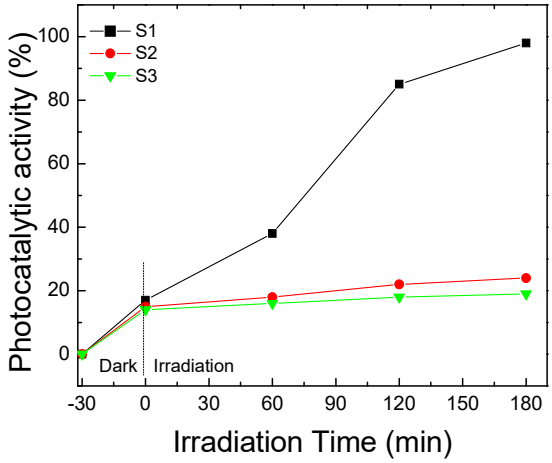

Figure 7. Photocatalytic degradation of RhB in the presence of S1(SnO_2), S2(SnO_2-CTAB) and S3(SnO_2-PEG600) nanoparticles

Since the photocatalytic process takes place mainly on the nanoparticles surface, the surface-to-volume ratio and the pore size are important parameters involved in pollutant degradation. Seems that the surfactants presence on the surface of SnO_2 inhibit the photocatalytic process.

EXPERIMENTAL SECTION

Materials

The chemical reagents used for the preparation of SnO_2 nanoparticles are: tin chloride $SnCl_2x2H_2O$ (for synthesis, Merck), sodium hydroxide (98% Alpha Aesar), hexadecyltrimethyl ammonium bromide $C_{19}H_{42}NBr$-CTAB (99%, Sigma) and polyethylene glycol 600 (PEG 600).

All chemicals are analytical grade without further purification and were used as received.

Sample preparation

The SnO_2 nanoparticles were obtained by chemical precipitation starting from aqueous solution of tin chloride dihydrate-$SnCl_2x2H_2O$ and sodium hydroxide-NaOH in the presence of different surfactants. In the synthesis procedure, 3.2 mM of $SnCl_2x2H_2O$ were dissolved in 100 ml water and then 100 ml NaOH solution (3.2 mM) was added drop wise in the solution. Different surfactants such as CTAB and PEG 600 were added into mixture.

After the addition of NaOH was finished, the reaction was kept 4h under vigorous stirring. The as prepared SnO_2 nanoparticles were separated by centrifugation and washed with water and ethanol (1:1 v/v) for several times to remove the excess of reactants and then dried at 65 ^{0}C, in air. Finally, the dried samples were thermally treated for 2 h at 500^{0}C in furnace, at a rate of 10^{0}C/min, in order to get the crystalline SnO_2 nanoparticles. In order to evidenced the influence of organic additive on properties of the SnO_2 nanoparticles different samples were prepared as follows: S1-SnO_2, S2-SnO_2 -CTAB, S3- SnO_2 -PEG600.

Samples characterization

The crystalline structures were evidenced by X-ray diffraction (XRD), recorded by using a Bruker D8 Advance X-ray diffractometer set-up, at 40 kV and 40 mA equipped with a germanium monochromator in the incident beam. The X-ray diffraction patterns were collected in a step-scanning mode with steps of $\Delta\theta = 0.02°$ using Cu Kα1 radiation ($\lambda = 1.54056$ Å) in the 2θ range 10^o-80^o. Pure silicon powder was used as standard for instrument broadening correction.

The morphology of the composite nanoparticles was determined by transmission electron microscopy (TEM) and high resolution TEM (HRTEM). The TEM measurements were performed with Hitachi SU8230 Transmission Electron Microscope equipped with a cold field emission gun. The powders were dispersed in ethanol, with a BANDELIN SONOREX homogenizer and deposited on 400 meshes copper grid, which was coated with carbon film. The HRTEM images were collected with Hitachi H9000NAR transmission electron microscope. The qualitative and quantitative compositions of samples were investigated by using X-Ray Photoelectron Spectroscopy (XPS) assisted by Ar ions etching. The XPS spectra were recorded by using a SPECS spectrometer working with Al anode (1486.6 eV) as X-rays source. Each sample was subject of several Ar ions etchings until the XPS spectra remained unchanged in shape and intensity. At this stage the XPS spectra reflect the real composition of samples. In order to avoid artificial reduction of different oxidation stats of elements the etching was performed by using Ar ions accelerated at a maximum 1000 V voltage with a filament current of 10 mA.

Surface area measurements were performed with a Micromeritics TriStar II 3020 instrument, nitrogen adsorption at 77 K. All samples were degassed at 150 ^{o}C for 24 h in nitrogen flow) Brunauer - Emmett – Teller (BET) analysis and BJH analysis (Baret, Joyner, and Halenda method) was used to determine area and volume of the mezo and macropores using adsorption and desorption techniques.

The photocatalytic activity of the SnO_2 nanoparticles was evaluated by photodegradation of Rhodamine B (RhB) in a Laboratory-Visible-Reactor system with a 400 W halogen lamp (Osram) which emits in visible range. The irradiation was performed under ultrasonically stirring. The catalyst (12 mg) was suspended in aqueous solution of RhB (1.0×10^{-5} mol L^{-1}, 8 mL) and then the mixture was stirred in the dark to achieve the adsorption equilibrium on the catalyst surface. Each degradation experiment was continuously conducted for 180 min. 3.5 mL of the mixed suspension was extracted at given intervals of illumination and separated with a magnet to remove the photocatalysts.

Finally, the clear supernatant was measured by recording the maximum absorbance of RhB at 554 nm. To separate the nanocomposites from the solution after the photodegradation of RhB a magnet was used. The photocatalyst was recycled three times and each experiment cycle used a fresh RhB solution under the same experimental conditions.

Photocatalytic activity is calculated using the following equation:

$$\text{Photocatalytic activity} = \frac{A}{A_0} \text{ x } 100 \quad (4)$$

where, A_0 and A represent the initial and the changed absorbance of RhB at 553 nm, respectively.

CONCLUSIONS

SnO_2 nanoparticles were prepared in the presence of different surfactants: hexadecyltrimethyl ammonium bromide (CTAB) and polyethylene glycol 600 (PEG 600). XRD investigations evidenced the crystalline nature of samples. The formation of crystalline nanoparticles with polyhedral shape was confirmed by TEM/HRTEM. The surface area measurements evidenced that SnO_2 nanoparticles have mesoporous structure with average pore size 80 nm. The surface area of nanoparticles varies from 45.29 - 47.16 m^2/g, depending on surfactant type. XPS investigations show the oxidation state Sn^{4+} in the samples. The photocatalytic measurements reveal that SnO_2 nanoparticles have photocatalytic efficiency toward the degradation of RhB solution. The presence of surfactants inhibits the photocatalytic response.

ACKNOWLEDGEMENTS

The authors would like to express appreciation to the Romanian Ministry of Research and Innovation for the financial support through Project PN19 35 02 03 (Core Program).

REFERENCES

1. Z.L. Wang, W.Z. Wu, *Angew. Chem*. **2012**, *51*, 11700.
2. K. Sornalingam, A. McDonagh, J. L Zhou, M.A.H. Johir, M.B. Ahmed, *Sci. Tot. Env.* **2018**, *610*, 521.
3. H.J. Zhang, G.H. Chen, D.W. Bahnemann, Photoelectrocatalytic materials for environmental applications, *J. Mat. Chem*., **2009**, *19*, 5089.
4. K. Prakash, P.S. Kumar, K. Saravanakumar, S. Karuthapandian, *J. Exp. Nanosci.*, **2016**,1, 1.
5. S. Zang, M. Zeng, J. X. Li, *J. Mater. Chem. A*, **2014**, *2*, 4391.
6. M. Abdullah, A. Hamdi, M. Sillanpaa, *J. Mater. Sci*., **2014**, *49*, 5151.
7. Q. Du, G. Lu, *Appl. Surf. Sci.*, **2014**, *305*, 235.
8. C. Tang, V. Chen, *Water. Res*., **2004**, *38*, 2775.
9. P.S. Kumar, M. Selvakumar, P. Bhagabati, et al, *RSC Adv*., **2014**, *4*, 32977.
10. R. Zhang, H. Wu, D.D. Lin, W. Pan, *J. Am. Ceram. Soc*., **2009**, 92, 2463.
11. A. Ahmed, M.N. Siddique, U. Alam, T. Ali, P. Tripathi, *Appl. Surf. Sci*., **2019**, 463, 976.
12. M.S. Park, G.X. Wang, Y.M. Kang, D. Wexler, S.X. Dou, H.K. Liu, *Angew. Chem*. **2007**,119764–767
13. A. Borhaninia, A. Nikfarjam, N. Salehifar, *Trans. Nonferrous Met. Soc. China,* **2017**, 27, 1777.
14. Y. Li, Q. Yang, Z. Wang, G. Wang, B. Zhang, Q. Zhang, D. Yang, *Inorg. Chem. Front.,* **2018**, ***5***, 3005.
15. R. Mani, K. Vivekanandan, K. Vallalperuman, *J. Mater. Sci. Mater. Electron*., **2017**, *28*, 4396.
16. K. Prakash, P. Senthil Kumar, S. Pandiaraj, K. Saravanakumar, S. Karuthapandian, *J. Exp. Nanosci.,* **2016**, *11*, 1138.
17. S. Shi, D. Gao, Q. Xu, Z. Yang, D. Xue, *RSC Adv*., **2014**, *4*, 45467.
18. B. Babu, A.N. Kadam, G.T. Rao, S.W. Lee, C. Byon, J. Shim, *J. Lumin*., **2018**,*195*, 283.
19. K. Anandan, V. Rajendran, *Superlattices Microstruct*. **2015**, *85*, 185.
20. A. Bhattacharjee, M. Ahmaruzzaman, T. Sinha, *RSC Adv*., **2014**, *4*, 51418.
21. H. Choi, E. Stathatos, D. D. Dionysiou, *Topics in Catal.*, **2007**, *44*, 513.

STUDIA UBB CHEMIA, LXIV, 3, 2019 (p. 111-120)
(RECOMMENDED CITATION)
DOI:10.24193/subbchem.2019.3.09

ENHANCEMENT OF FUMARIC ACID PRODUCTION BY *RHYZOPUS ORYZAE* USING OXYGEN - VECTOR

CORINA CIOBANU[a], ALEXANDRA TUCALIUC[a,*], ALEXANDRA CRISTINA BLAGA[a], ANCA-IRINA GALACTION[b], DAN CAȘCAVAL[a]

ABSTRACT. Fumaric acid, one of the most important organic acids with various applications in industries, can be obtained by fungal fermentation processes, mainly by using *Rhizopus oryzae* as producing microorganism. The challenges are to maintain pellet morphology of fungy and to optimize the multiple factors that influence fumaric acid production. The main objective of this study is to improve fumaric acid production by varying *n*-dodecane concentration levels in batch fungal fermentations. This strategy leads to an increase of fumaric acid concentration for about 1.2 times in system with 5% *n*-dodecane but a higher hydrocarbon concentration induced inhibition phenomenon to fumaric acid production.

Keywords: *fumaric acid, fermentation, Rhizopus oryzae, oxygen-vector, n-dodecane*

INTRODUCTION

Fumaric acid (*trans*-butenedioic acid) is a four carbon dicarboxylic acid, one of the two isomeric unsaturated dicarboxylic acids, alongside maleic acid. Fumaric acid is found in certain species of fungus, lichen, and other plants, including *Fumaria officinalis*, from which it was first isolated [1].

It is a very important compound due to its numerous applications in food, feed and beverages, used as acidulant, preservative and flavoring agent; as intermediate for L-malic and L-aspartic acid production, and also as chemical feedstock for the production of paper resins, unsaturated polyester resins, alkyd resins, plasticizers, and miscellaneous industrial products [1, 2].

[a] *"Gheorghe Asachi" Technical University of Iasi, "Cristofor Simionescu" Faculty of Chemical Engineering and Environmental Protection, 73 Prof. Dimitrie Mangeron str., RO-700050, Iasi, Romania*

[b] *"Gr.T. Popa" University of Medicine and Pharmacy of Iasi, Dept. of Biomedical Science, 9-13 M. Kogalniceanu str., RO-700454, Iasi, Romania*

** Corresponding author: tucaliucalexandra@gmail.com*

The petrochemical routes for the fumaric acid production via catalytic isomerization of maleic acid or through maleic anhydride requires high material and energy consumptions, leading to the increased interest for fermentative processes. Some microorganisms, such as bacteria *E. coli*, *Lactobacillus sp.* produce fumaric acid in small amounts, as a key intermediate in the citrate cycle. Fumaric acid is produced especially by fungus; some identified genera are *Rhizopus*, *Mucor*, *Cunninghamella*, and *Circinella*. Among these strains, *Rhizopus* species (*nigricans*, *arrhizus*, *oryzae*, and *formosa*) were the best-producing, yielding fumaric acid under aerobic and anaerobic conditions [3, 4].

Although high fumaric acid yields have been obtained from fungi such as *Rhizopus oryzae* and *Rhizopus arrhizus*, the process might be limited at the industrial scale because these fungi are difficult to grow and their morphology can strongly affect production characteristics [5, 6].

Fungi can be grown in submerged cultures in several different morphological forms: suspended mycelia, clumps, or pellets [7, 8]. In terms of fumaric acid production, fungal growth in pellet form is a favorable alternative because significantly improves the rheology of the fermentation broth which results in efficient mass and oxygen transfer rates into the biomass and reduces energy consumption for aeration and agitation [9].

Rhizopus species are aerobic microorganisms that require a continuous supply of oxygen during the fermentation process. Variations in the dissolved oxygen (DO) level might have a significant effect on the production of fumaric acid and byproducts. Malic acid and ethanol are produced as byproducts, but in small concentrations. Ethanol production usually occurs under anaerobic conditions or when oxygen is limited in the culture, and thus can be decreased by providing sufficient oxygen to the culture [10].

Fumaric acid production depends on fungal cells growth and pellet formation in submerged cultures, process controlled by multiple factors such as nutrients, pH, agitation, aeration, inoculum level, substrate concentration, polymer additives, the broth viscosity, and surface-active agents [11]. Among these factors, oxygen transfer rate (aeration) or the control of dissolved oxygen in the medium during fermentation is considered very important for organic acid production. In the case of fumaric acid, high concentrations of oxygen in the broth yield high titers of the acid, but low productivities, while at low DO the situation is reversed. A combination of high and low dissolved oxygen, in this order, permits high titers of fumaric acid and high glucose conversions [12].

An alternative of this strategy (combination of high and low dissolved oxygen) and without needing a supplementary intensification of mixing may be represented by the addition of some immiscible liquids in the aqueous phase which could induce a significant increase of oxygen transfer rate from air to microorganisms' cells. These compounds, in which oxygen is highly soluble, are known in literature as oxygen-vectors [13]. Some studies reporting the use of oxygen-vectors to improve the performance of fermentations processes [14, 15].

The aim of this study was to investigate the possibility to optimize the dissolved oxygen control for improving fumaric acid production by adding different levels of oxygen-vectors in fungal fermentation.

RESULTS AND DISCUSSION

Important parameters that require optimization in the fermentation process are medium composition and oxygen transfer rate (aeration) or the control of dissolved oxygen in the medium during fermentation. Factors affecting cell growth and pellet formation, including the strain, spore inoculum size, and culturing conditions (medium composition, temperature, pH, and agitation speed) have been extensively studied [16].

For batch fermentations without oxygen-vector Figure 1 shows slow glucose consumption by the fungus pellets with a fast increase in fumaric acid accumulation in the broth after 100 hours, indicating that the carbon sources is consumed for pellets formation instead of acid biosynthesis.

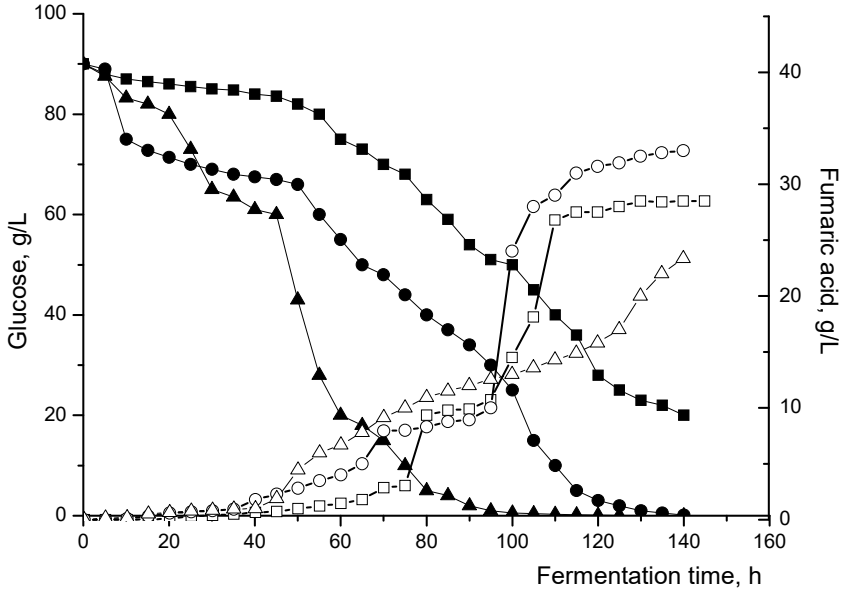

Figure 1. Variation of glucose and fumaric acid concentrations during fungal fermentation (glucose concentration: ■ - 0 % *n*-dodecane, ● - 5% *n*-dodecane, ▲- 10% *n*-dodecane; fumaric acid concentration: □ - 0 % *n*-dodecane, ○ - 5% *n*-dodecane, Δ - 10% *n*-dodecane)

Hydrocarbon concentration exhibits a significant influence on fumaric acid production mainly by accelerating the oxygen transfer rate, therefore in the presence of 5% *n*-dodecane the decrease of glucose consumption is more pronounced attaining the maximum final concentration of fumaric acid (33 $g \cdot L^{-1}$) in the broth. The concentration of fumaric acid remains at a constant level in absence of *n*-dodecane after 100 h of fermentation, but increases slowly in the presence of hydrocarbon. The oxygen vector addition improved glucose consumption: the substrate was completely exhausted for the fermentation with *n*-dodecane in 140 h, while for the control system, the residual glucose was about 20 $g \cdot L^{-1}$. Therefore, due to a reduced concentration of dissolved oxigen in the absence of hydrocarbon, pellets could not use all the assimilable nitrogen, this leading to a slow fermentation and the process was stopped before the end of fermentable sugars.

For the system with 10% *n*-dodecane, Figure 1 shows the significant decrease of glucose concentration during the first 60 h, this substrate being almost entirely consumed over 80 h. The *n*-dodecane addition leads to a superior rate of glucose consumption, due to an increased rate of pellets multiplication under higher dissolved oxygen concentration. This phenomenon is followed by exponential increasing of fumaric acid concentration, probably due to the consumption of *n*-dodecane as alternative source of carbon and energy, but at the end of fermentation process fumaric acid concentration in broth reached a low value (23.35 $g \cdot L^{-1}$), as compared with systems without and with 5% hydrocarbon. This variation is a result of inhibition effect which appeared at higher hydrocarbon concentration. The increased values of DO determined by the high amount of oxygen vector in the medium were extremely beneficial for the biomass growth at the expense of acid production, since *Rhizopus* strains accumulate fumaric acid in stress conditions. If the medium offers optimum conditions (DO over 80%) the carbon source will be used only for biomass accumulation, fungi being able to grow on hydrocarbon substrates [17, 18].

Fumaric acid production by fungal culture is limited by the dissolved oxygen in the broth, thus one way to minimize oxygen mass transfer limitation to the cells is to stimulate the formation of small, spherical, cell pellets, which can reduce clump formation and broth viscosity. During fungal fermentation of *R. oryzae* the process was towards pellets formation and pellets with a diameter over 1 mm were obtained (Figure 2.A.) in the absence of hydrocarbon, whereas in the presence of *n*-dodecane smaller pellets (<1 mm diameter) (Figure 2.B. and Figure 2.C.) were formed.

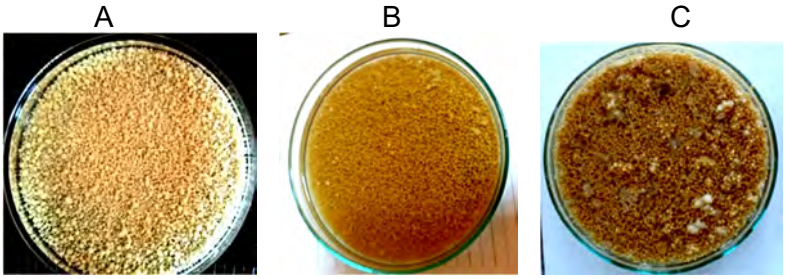

Figure 2. Close-up of the pellets formed in fermentation systems: A. without *n*-dodecane, B. with 5% *n*-dodecane and C. with 10% *n*-dodecane.

In the systems with smaller pellets more biomass was formed, leading to maximum biomass concentration of 5.5 $g \cdot L^{-1}$ d.w. for system with 10% *n*-dodecane (Figure 3.), but it was not correlated with a higher content of fumaric acid. This fact indicates that a higher concentration of hydrocarbon (10% *n*-dodecane) leads to biomass growth and inhibit the fumaric acid production.

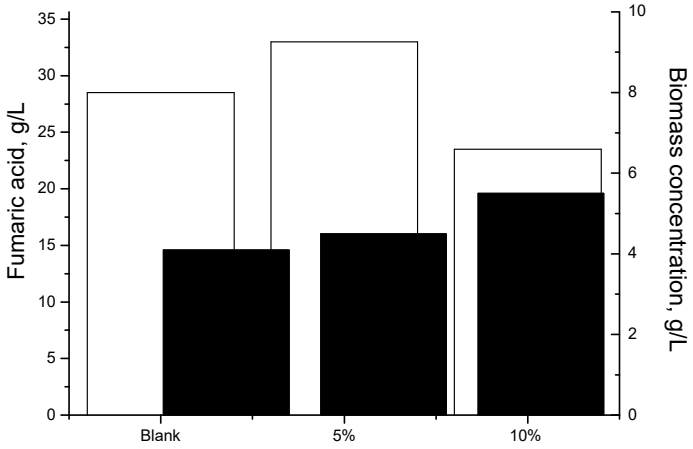

Figure 3. Correlation of fumaric acid production with biomass concentration (□ - fumaric acid concentration, ■ – biomass concentration).

Smaller pellets formation correlated with higher biomass concentration indicated an optimal oxygen mass transfer in the inner region of pellets due to the higher concentration of dissolved oxygen in the fermentation broth, generating a gradient concentration between pellets and culture medium. A more intensive metabolism of the smaller pellets and the presence of oxygen vector in the broth could prompt the dissolved oxygen, the most important substrate, to be easier and faster transferred into pellets. Decreasing the

oxygen-vector concentration (5% *n*-dodecane) the inhibition effect to fumaric acid production was eliminated, this leading to higher accumulation of fumaric acid (33 $g \cdot L^{-1}$) at the end of fermentation under limited pellets growth (biomass concentration 4.5 $g \cdot L^{-1}$ d.w.).

Oxygen is the most difficult substrate to be supplied to aerobic cultures of *R. oryzae* pellets. According to Figure 4, the values of dissolved oxygen concentration are significantly higher in presence of hydrocarbon comparatively with control fermentation processes. This variation is due to the positive effect on the appearance of limiting steps, such as mass transfer of oxygen from bulk to boundary layer (the film surrounding the pellets) and to inner pellet diffusion step. For maintaining a constant level of oxygen in the pellets is important to provide a high level of oxygen in the fermentation broth, leading to a high concentration gradient between bulk and inner of the pellets. Therefore, the level of fumaric acid biosynthesised by pellets depends directly on substrate and oxygen concentration into the broth. After 80 h of fermentation the fumaric acid concentration increased continuously, but over 120 hours it reached a constant level in the system without *n*-dodecane, indicating that the conditions discussed above were not maintained and the substrate was consumed in a superficial region of the pellets, inducing the lyses of the cells in the inner of the pellets.

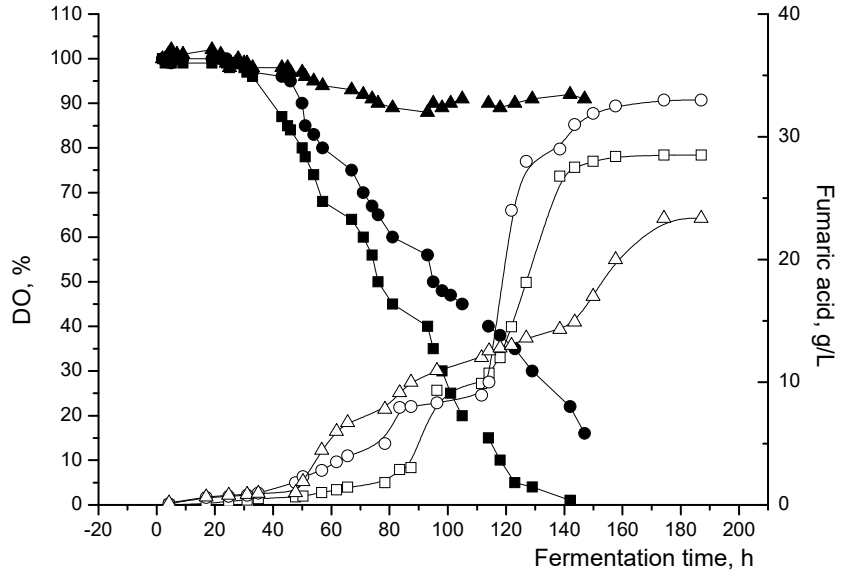

Figure 4. The profile of dissolved oxygen during fungal fermentation (dissolved oxygen concentration: ■ - 0 % *n*-dodecane, ● - 5% *n*-dodecane, ▲- 10% *n*-dodecane; fumaric acid concentration: □ - 0 % *n*-dodecane, ○ - 5% *n*-dodecane, ∆ - 10% *n*-dodecane).

Whereas in the presence of 5% *n*-dodecane, the pellets still produce fumaric acid after 120 h of fermentation, and reach a high concentration level in the broth as a result of the increased biomass amount and due to the positive influence of hydrocarbon on the oxygen mass transfer in the inner region of the pellets. Regarding the system with 10% *n*-dodecane, the dissolved oxygen is maintained at relatively high values during the entire fermentation processes (Figure 4) and limits the fumaric acid biosynthesis rate due to the inhibitory effect on the pellets production step.

Oxygen mass transfer proprieties are very important in the complex media of fungal fermentation, this representing an important key for process scale-up and commercialisation. Therefore, the influence of *n*-dodecane concentration on oxygen transfer rate, *via* oxygen transfer coefficient (k_La, s^{-1}), was analysed. According to Figure 5 the positive influence of hydrocarbon is correlated by the amplification of the oxygen mass transfer coefficient for about 1.3 times by increasing the volumetric concentration of dodecane from 0 to 5%.

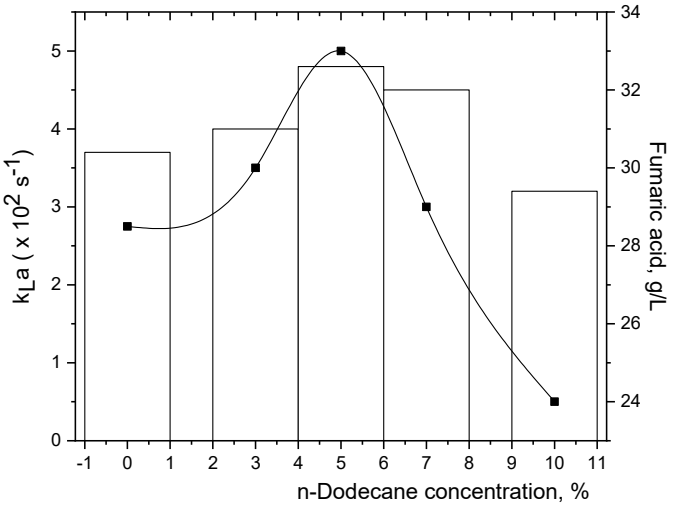

Figure 5. Influence of *n*-dodecane concentration on oxygen mass transfer coefficient and fumaric acid concentration.

As mentioned above, higher hydrocarbon concentration led to the appearance of the inhibition effect for fumaric acid production, which is confirmed by the decrease of the k_La coefficient for about 1.5 times in systems with 10% n-dodecane. Therefore, higher concentration of oxygen-vectors limits the production of fumaric acid, but this negative influence is partially countered by pellets accumulation in the fermentation broth.

CONCLUSIONS

Fumaric acid production by fungal fermentation is strongly dependent on dissolved oxygen concentration, therefore a strategy to improve the biosynthesis performance was proposed. The experiments were carried out in batch systems and fungus morphology was controlled for pellets formation. Batch fermentations were performed in the absence and presence of *n*-dodecane, used as oxygen vector. Hydrocarbon concentration exhibits a significant influence on fumaric acid production. Therefore, in the presence of 5% *n*-dodecane, the decrease of glucose consumption is more pronounced, leading to an increase of fumaric acid concentration of about 1.2 times. At higher hydrocarbon concentration (10% *n*-dodecane) an inhibition effect on fumaric acid production appeared which can be assumed to the cumulative negative effect of two factors: attaining the inhibition level of hydrocarbon and the high amounts of biomass in the fermentation broth. The maximum amount of fumaric acid was reached with 5% n-dodecane, while in systems with 10% *n*-dodecane the fumaric acid production decreased with almost 50%.

EXPERIMENTAL SECTION

The fungal batch fermentations were performed in a laboratory stirred bioreactor (2 L Fermentor Fermac 360, Electrolab, UK) with 1.4 L. working volume. The characteristics of bioreactor are given in Table 1.

Table 1. Geometric characteristics of bioreactor (d = impeller diameter, mm; D = bioreactor diameter, mm; h = distance from the stirrer to the bioreactor bottom, mm; H = bioreactor height, mm; l = impeller blade length, mm; l' = oxygen electrode immersed length, mm; w = impeller blade height, mm)

d	d/D	H/D	w/d	l/d	h/d	d'/d	l'/d	no. blades
55	0.46	1.46	0.27	0.31	0.64	0.018	1.82	6

As producing microorganism, *Rhizopus oryzae* ATCC 20344 was used. *R. oryzae* was cultured on malt extract agar at 35 °C for 7 days. The agar with fungi spores was washed with sterile water. The spore suspensions were used to inoculate the pre-culture medium. The composition of the growth medium for spores was: glucose 30 $g \cdot L^{-1}$, yeast extract 2.5 $g \cdot L^{-1}$, KH_2PO_4 0.6 $g \cdot L^{-1}$, $MgSO_4$ 0.25 $g \cdot L^{-1}$, $ZnSO_4$ 0.044 $g \cdot L^{-1}$, $FeCl_3$ 0.0075 $g \cdot L^{-1}$.

The medium without the glucose was heat sterilized (20 minute at 121 °C), the glucose was sterilized separately. Precultures were carried out at 35 °C and 180 rpm in a gyratory incubator-shaker for 1-2 days. After cultivation, the obtained pellets were transferred immediately into a fermenter containing the production medium: glucose 90 $g \cdot L^{-1}$, $(NH_4)_2SO_4$ 2 $g \cdot L^{-1}$, KH_2PO_4 0.3 $g \cdot L^{-1}$, $MgSO_4$ 0.25 $g \cdot L^{-1}$, $ZnSO_4$ 0.044 $g \cdot L^{-1}$, $FeCl_3$ 0.0075 $g \cdot L^{-1}$. *n*-Dodecane was used as oxygen vector at volumetric concentration of 5% and 10%. For the pH control a saturated solution of Na_2CO_3 sterilized by filtration was used. Silicone-based antifoam agent for controlling foam generation during batch fermentations was used.

Fermentation processes were carried out in the following conditions: 35 °C, 400 rpm, pH 5.5, aeration rate 2 $L \cdot min^{-1}$, fermentation time approx. 160 – 180 hours. Samples were taken periodically and the glucose and fumaric acid contents were monitored using a HPLC system (Dionex Ultimate 3000). Glucose analysis was performed on a HPLC system equipped with refractive index detector using HyperRez carbohydrate column (300 x 7.7 mm, 8 µm) with water as mobile phase at 0.6 $mL \cdot min^{-1}$ and column temperature of 80 °C, while the fumaric acid was analyzed by a PDA detector and Acclaim OA column (150 x 4.5 mm, 5 µm). The mobile phase consisted in 100mM Na_2SO_4 solution, pH 3.65 corrected with methane sulfonic acid, at a flow rate of 0.6 $mL \cdot min^{-1}$ and 30 °C.

ACKNOWLEDGMENTS

This work was supported by a research grant of the TUIASI, project number 0973/2018.

REFERENCES

1. A.C. Roa Engel, A.J.J. Straathof, T.W. Zijlmans, W.M. van Gulik, L.A.M. van der Wielen, *Appl. Microbiol. Biotechnol.,* **2008**, *78*, 379–389.
2. Q. Xu, S. Li, H. Huang, J. Wen, *Biotechnol. Adv.*, **2012**, *30*, 1685–1696.
3. E. Riscaldati, M. Moresi, F. Federici, M. Petruccioli, *Biotechnol. Lett.*, **2000**, *22*, 1043–1047.
4. E. Podgórska, M. Kasprzak, D. Szwajgier, *Pol. J. Food Nutr. Sci.*, **2004**, *54*, 47–50.
5. Y.Q. Fu, Q. Xu, S. Li, Y. Chen, H. Huang, *Korean J. Chem. Eng.*, **2010**, *27*, 183–186.
6. W. Kenealy, E. Zaady, J.C. Dupreez, B. Stieglitz, I. Goldberg, *Appl. Environ. Microbiol.,* **1986**, *52*, 128–133.

7. B. Metz, N.W.F. Kossen, *Biotechnol. Bioeng.,* **1977**, *19*, 781–799.
8. W. Liao, Y. Liu, S. Chen, *Appl. Biochem. Biotechnol.*, **2007**, *137*, 689–701.
9. J.C. van Suijdam, N.W.F. Kossen, P.G. Paul, *Eur. J. Appl. Microbiol. Biotechnol.,* **1980**, *10*, 211–221.
10. N. Cao, J. Du, C.S. Gong, G.T. Tsao, *Appl. Environ. Microbiol.*, **1996**, *62*, 2926–31.
11. J. Zhang, J. Zhang, *Crit. Rev. Biotechnol.*, **2016**, *36*, 1066–1077.
12. Y.Q. Fu, S. Li, Y. Chen, Q. Xu, H. Huang, X. Y. Sheng, *Biotechnol. Appl. Biochem.*, **2010**, *162*, 1031–1038.
13. J.L. Rols, J.S. Condoret, C. Fonade, G. Goma, *Biotechnol. Bioeng.,***1990**, *35*, 427–435.
14. S. Jia, M. Wang, P. Kahar, Y. Park, M. Okabe, *J. Ferment. Bioeng.*, **1997**, *84*, 176–178.
15. A.C. Blaga, C. Ciobanu, D. Cascaval, A.-I. Galaction, *Biochem. Eng. J.*, **2018**, *131*, 70–76.
16. M. Papagianni, *Biotechnol. Adv.,* **2004**, *22*, 189–259.
17. F.X. Prenafeta-Boldú, A. Kuhn, D.M.A. M. Luykx, H. Anke, J.W. van Groenestijn, J.A.M. de Bont, *Mycol. Res.*, **2001**, *105*, 477–484.
18. F.X. Prenafeta-Boldú, R. Summerbell, G. Sybren de Hoog, *FEMS Microbiol. Rev.*, **2006**, *30*, 109–130.

STUDIA UBB CHEMIA, LXIV, 3, 2019 (p. 121-128)
(RECOMMENDED CITATION)
DOI:10.24193/subbchem.2019.3.10

SHEAR FLOW OF BOVINE SERUM ALBUMIN SOLUTIONS

MARIA BERCEA[a,*], SIMONA MORARIU[a], IOANA-ALEXANDRA PLUGARIU[a], DOINA BĂRÂLĂ[b]

ABSTRACT. In this paper, the flow of bovine serum albumin (BSA) solutions in physiological serum was investigated at different concentrations from 1 to 10 g/dL and temperatures from 4°C to 80°C. Some peculiar behaviours were depicted as a function of thermodynamic and shear conditions. The intermolecular interactions, the electroviscous effects, the shear forces as well as the temperature influence the shear viscosity of BSA solutions.

Keywords: *BSA, shear flow, shear induced aggregation, activation energy, associates*

INTRODUCTION

Serum albumin, as a model for globular proteins, is synthesized by the liver in mammals and has a half-life in the circulatory system of approx. 19 days, being the most abundant globular protein in blood plasma (approx. 60%) Its function is to bind and transport small molecules, such as fatty or amino acids, metals, dyes, or pharmaceutical compounds [1]. Bovine serum albumin (BSA) presents a high stability due to its primary structure of 585 amino acid residues and the secondary structure formed by 67% α-helix [1, 2].

The protein-protein interactions in solution in different concentration regimes attracted a high interest during the last years. Very often, the proteins are investigated in dilute solutions (bellow 0.1 g/dL) in order to understand their behaviour at molecular level. Efforts were carried out to evaluate the first order deviations from thermodynamic ideality in semidilute regime (between 0.1 and 1 g/dL) [3]. However, in physiological environment the protein content is of approx. 3.5–4.3 g/dL [4] or even higher, as for example the concentration of

[a] *Petru Poni Institute of Macromolecular Chemistry, 41-A Grigore Ghica Voda Alley, 700487 Iasi, Romania*

[b] *S.C. BARALCHIM S.R.L., Dumbravei Str., Nr. 17, 060044 Dumbrava Roşie, Romania*

** Corresponding author bercea@icmpp.ro*

mammalian hemoglobin in erythrocytes can exceed 30 g/dL [3]. A highly concentrated protein solution is generally considered the system in which more than 10% volume represents the solute (proteins can occupy up to 40% of the cellular volume). Usually, such solution is regarded as crowded [5], when the behaviour of the protein is influenced by the interactions with other like or unlike molecules [6]. Increased concentration leads to a smaller distance between the protein molecules and, as a consequence, the probability of protein–protein interactions is higher [7]. The resulting interactions are influenced by the net charge of the protein [8].

In salted solution, the deviation from the ideal behaviour is more pronounced as the protein concentration increases, structured aggregates appear due to short-range attractive interactions between protein molecules [3].

Small-angle X-ray scattering investigations have shown that at high protein concentrations, the balance between attractive and repulsive forces, controlled by pH, influences the aggregation or extensive morphological changes [4]. Under physiological conditions (concentrations of 3.5 g/dL – 5.5 g/dL), the globular proteins keep the native structure in neutral and basic environments.

Globular proteins influence the flow properties, phase behaviour, microstructure and transport of biomolecules and biofluids in the mammalian body. These proteins are used in different formulations for food, drugs or cosmetics and the knowledge of their rheological behaviour is an important key in application of the multicomponent materials [9-11].

The present investigation is focused on flow behaviour of BSA in physiological serum at pH = 7.4, varying concentration from 1 g/dL to 10 g/dL and temperatures from 4°C to 80°C.

RESULTS AND DISCUSSION

Figure 1 shows complete flow curves registered for 2 g/dL BSA in physiological serum at 4°C. The flow behaviour can be observed either from viscosity or shear stress as a function of shear rate. At low shear rates, the solution behaves as Newtonian fluid, the shear viscosity (η) is independent on the applied shear rate ($\dot{\gamma}$). In this region, the relaxation time of the deformed solute is shorter than the characteristic time of the flow, keeping the rest structure of the solution which is formed by BSA associates and clusters. By increasing the shear rates, the BSA structures have no time to fully relax, the intermolecular interactions are in competition with the flow forces and the BSA molecules tend to orient along the flow direction. Thus, for shear rates in the range 0.0215 s^{-1} – 100 s^{-1}, the flow becomes non-Newtonian, the viscosity

depends on the applied shear rate, varying as $\eta \sim \dot{\gamma}^{-0.79}$. At high shear rates ($\dot{\gamma}$ > 100 s^{-1}), the intermolecular interactions are completely overcomed by the shear forces and the behaviour is again Newtonian.

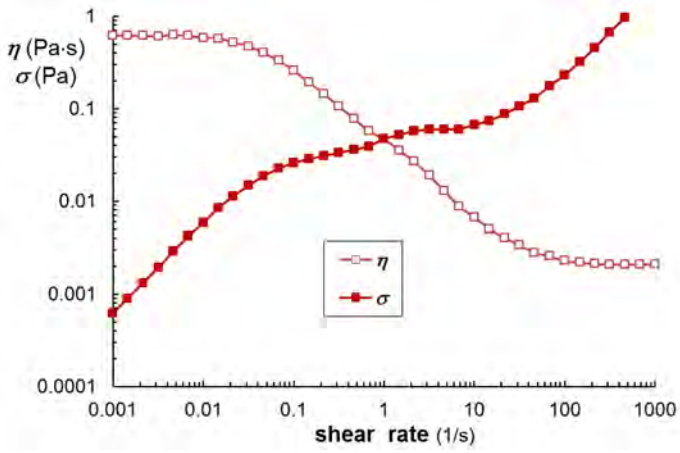

Figure 1. Viscosity and shear stress as a function of shear rate for 2% BSA solution at 4°C

The flow curves are very sensitive to temperature as well as shear regime. As the temperature increases, the flow is Newtonian from 20°C to 45°C (Figure 2). For temperatures between 55°C and 65°C and 0.1 s^{-1} < $\dot{\gamma}$ < 20 s^{-1}, the curves present maxima due to shear induced aggregation occurring between BSA molecules. For $\dot{\gamma}$ > 20 s^{-1}, all curves show Newtonian behaviour. The shear induced aggregation was observed previously in dilute and semidilute polyelectrolyte aqueous solutions [12,13]. For BSA solutions, the electroviscous effects are in competition with Brownian motion, induced by temperature increase, and with the shear forces. At low temperatures and shear rates, the electroviscous effects are dominant for BSA concentrations up to 4 g/dL. The solution viscosity is influenced mainly by the charge of BSA molecules and counterions present in solution. Weak attractive interactions and long-range interactions exhibited at low concentrations coexist with the Coulombic and electroviscous repulsions and determine a shear thickening effect for moderate shear forces. High shear forces overcome these effects, the clusters and aggregates are destroyed and molecules flow easily and the viscosity approaches the second Newtonian region. At high concentrations, the contribution of attractive short-range interactions becomes significant and

in salted solution the charge-induced repulsions are minimal [7,14]. At high temperatures (70°C and 80°C), the predominance of attractive interactions induces a self-assembling behaviour of BSA molecules into a transient network with high resistance to flow (high viscosity of all systems, regardless concentration, Figure 3). Moreover, a heat denaturation with some changes in conformation of BSA molecules occurs, some aggregates are formed and a large unfolding takes place [15].

By following the viscosity at constant shear rate of 1 s^{-1} (similar to flow conditions of proteins in plasma of normal cells [16]) as a function of temperature for low BSA concentrations (1 g/dL, 2 g/dL and 4 g/dL), it can be observed that a sharp decrease occurs up to 20°C, followed by a region where the viscosity slowly decreases as the temperature increases (Figure 3). Above 50°C – 60°C one observes a maximum value of viscosity, then a decrease and a significant increase at 70°C and 80°C. The full symbols represent the maxima from η - $\dot{\gamma}$ curves.

BSA presents in its structure 17 intrachain disulphide bridges and one sulfhydryl group (Cys-34) [2]. The disulphide bonds confer certain rigidity, but allow a significant conformational change under different external conditions. At neutral pH, the disulphide bridges are hidden in the protein molecule and are not exposed to the solvent interactions.

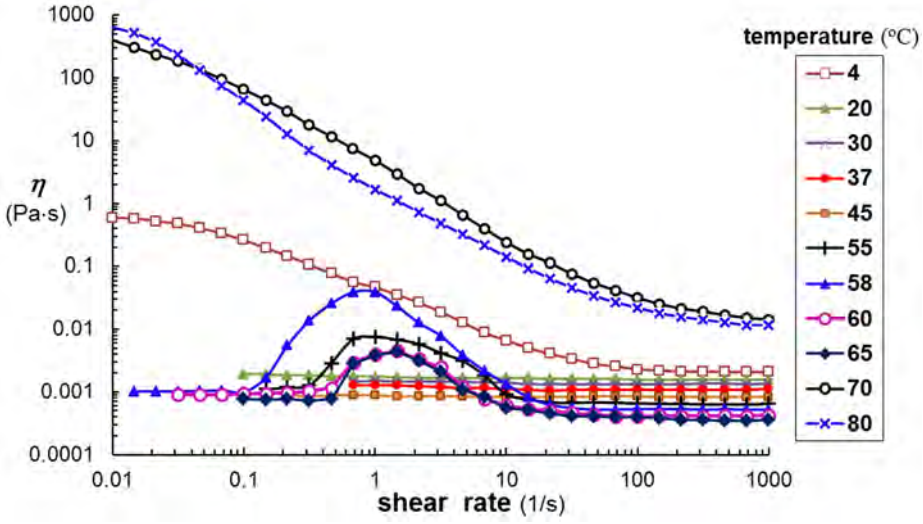

Figure 2. Viscosity as a function of shear rate for 2% BSA solution at various temperatures

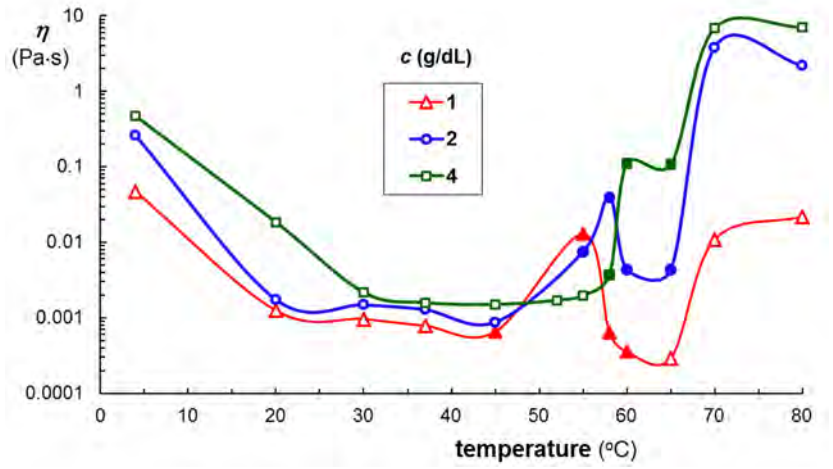

Figure 3. Viscosity as a function of temperature for 2% BSA solution at 1 s^{-1}. The full symbols represent the maxima from η - $\dot{\gamma}$ curves

The activation energy of flow (E_a) was determined from the plot of $\log\eta$ *vs*. 1/*T* (Figure 4), according to the Arrhenius equation:

$$\eta = A\exp(Ea/RT) \tag{1}$$

where η is the shear viscosity, *A* is a pre-exponential factor, *R* is the universal gas constant, 8.314 J/(K·mol), and *T* is the absolute temperature (K).

In this paper, for calculating E_a, we considered the value of shear viscosity at 100 s^{-1}, this being the shear rate encountered in the case of hardened cells in solution containing albumin [16], and the range of temperatures from 20°C to 60°C.

For BSA solutions, E_a varies between 3.96 kJ/mol for 1 g/dL and 7.6 kJ/mol for 10 g/dL (Figure 5), values similar with those reported for polymer systems [17,18].

The flow behaviour of the protein solutions is governed by the BSA-BSA interactions as well as interactions of the protein with the water and co-solute molecules, the hydrodynamic properties being strongly influenced by pH value and ionic strength of the solution [19], as well as the presence of other polymers [20]. The pH value is correlated with the charge of protein and with the protonation of ionizable amino acids. The presence of ions determines a screening of the electrostatic interactions [8].

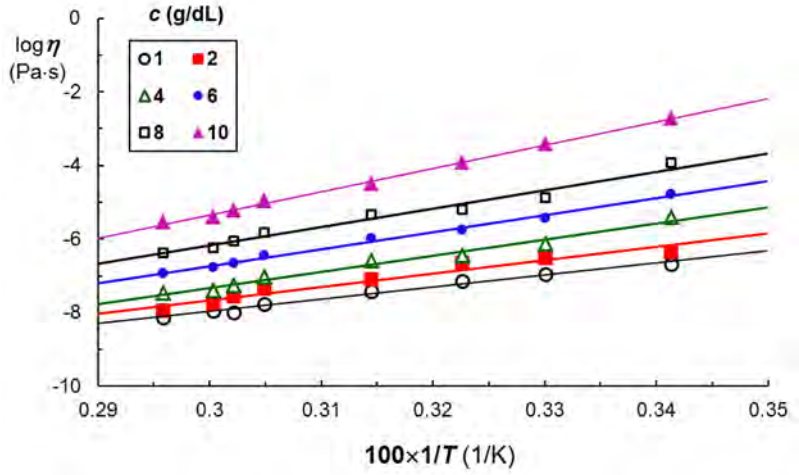

Figure 4. logη *vs*. 1/*T* for BSA solutions of different concentrations

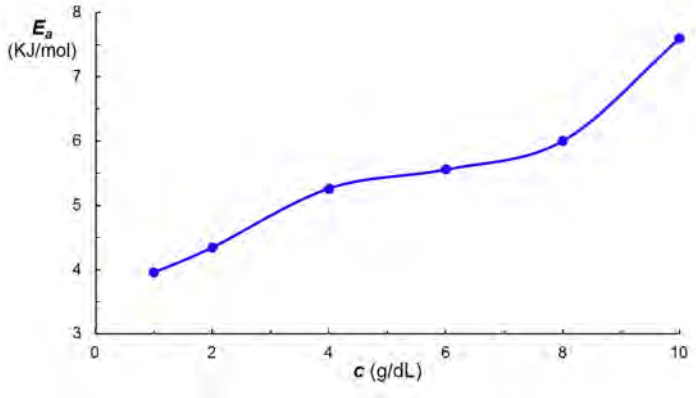

Figure 5. The activation energy of flow (E_a) as a function of BSA concentration

CONCLUSIONS

BSA solutions are complex fluids, their behaviour being influenced by structural factors as well as by the thermodynamic and shear conditions.

At low concentrations of BSA solutions, the electroviscous effects govern the flow behaviour; at high concentrations, the balance between all intermolecular interactions and the shear forces dictates the viscosity value, wherein intermolecular attraction at high temperatures leads to a high solution viscosity. A heat denaturation of BSA occurs above 70°C.

EXPERIMENTAL SECTION

Bovine serum albumin (Sigma-Aldrich) solutions of different concentrations (1 g/dL, 2 g/dL, 4 g/dL, 6 g/dL, 8 g/dL, 10 g/dL) were prepared in physiological serum (pH = 7.4) and refrigerated. They were warmed up to the working temperature and thermostated for 15 minutes before experiments were carried out.

The stationary shear flow investigations were carried out with a MCR 302 Anton-Paar rheometer equipped with Peltier device for temperature control and plane-plane geometry (the upper plate having the diameter of 50 mm, with a gap of 500 μm). For preventing the water evaporation, it was used an anti-evaporation device, which created a saturated atmosphere in the vecinity of the sample.

ACKNOWLEDGMENTS

The financial support of European Social Fund for Regional Development, Competitiveness Operational Program Axis 1 – Project "Petru Poni Institute of Macromolecular Chemistry - Interdisciplinary Pol for Smart Specialization through Research and Innovation and Technology Transfer in Bio(nano)polymeric Materials and (Eco)Technology", InoMatPol (ID P_36_570, Contract 142/10.10.2016, cod MySMIS: 107464) is gratefully acknowledged.

REFERENCES

1. D.C. Carter; J.X. Ho; *Adv. Protein Chem.,* **1994**, *45*, 153–203
2. V.A. Borzova; K.A. Markossian; N.A. Chebotareva; S.Yu. Kleymenov; N.B. Poliansky; K.O. Muranov; V.A. Stein-Margolina; V.V. Shubin; D.I. Markov; B.I. Kurganov; *PLoS One,* **2016**, *11*(4), e0153495 and references cited therein
3. P.D. Ross; A.P. Minton; *J. Mol. Biol.,* **1977**, *112*, 437–452
4. L.R.S. Barbosa; M.G. Ortore; F. Spinozzi; P. Mariani; S. Bernstorff; R. Itri; *Biophys. J.*, **2010**, *98*, 147–157
5. D. Hall; A.P. Minton; *Biochim. Biophys. Acta,* **2003**, *1649*(2) 127–139
6. A. Saluja; D.S. Kalonia; *Int. J. Pharm*., **2008**, *358*(1–2), 1–15
7. R. Chari; K. Jerath; A. Badkar; D.S. Kalonia; *Pharm. Res.,* **2009**, *26*(12), 2607–2618
8. S. Yadav; J. Liu; S. J. Shire; D.S. Kalonia; *J. Pharm. Sci.,* **2010**, *99*(3), 1152–1168

9. J. Jezek; M. Rides; B. Derham; J. Moore; E. Cerasoli; R. Simler; B. Perez-Ramirez; *Adv. Drug Delivery Rev.,* **2011**, *63*, 1107–1117
10. A. Oliva, A. Santovena, J. Farina, M. Llabres, *J. Pharm. Biomed. Anal.,* **2003**, *33,* 145–155
11. V. Sharma; A. Jaishankar; Y.-C. Wang; G.H. McKinley; *Soft Matter*, **2011**, *11*, 5150–5160
12. E.S. Dragan; M. Bercea; L. Sacarescu; *React. Funct. Polym.,* **2018**, *124*, 171–180
13. L.E. Nita; A.P. Chiriac; M. Bercea; M. Asanduleasa; B.A. Wolf; *Int. J. Biol. Macromol.,* **2017**, *95*, 412–420
14. S. Yadav; S.J. Shire; D.S. Kalonia; *Pharm. Res.,* **2011**, *28*, 1973–1983
15. K. Aoki; K.Hiramatsu; K. Kimura; S. Kaneshina; Y. Nakamura; K. Sato; *Bull. Inst. Chem. Res., Kyoto Univ.,* **1969**, *47*(4), 274–282
16. S. Chien; *Science*, **1970**, *168*, 977–979
17. S. Morariu; C.E. Brunchi; C. Hulubei; M. Bercea; *Ind. Eng. Chem. Res*., **2011**, *50*, 9451–9455
18. A. Ghirişan; S. Drăgan; C. Coţa; N.C. Ioica; E.-M. Nagy; V. Miclăuş; *Studia UBB Chemia,* **2018**, *LXIII*(2), 53–62
19. C. Tanford; J.G. Buzzell; *J. Phys. Chem*., **1956**, *60*, 225–231
20. M. Bercea, S. Morariu, L.E. Nita, R.N. Darie, *Polym. Plast. Technol. Eng*., **2014**, *53*, 1354–1361

STUDIA UBB CHEMIA, LXIV, 3, 2019 (p. 129-142)
(RECOMMENDED CITATION)
DOI:10.24193/subbchem.2019.3.11

PHASE BEHAVIOUR CALCULATIONS FOR THE CARBON DIOXIDE + 1,2-DIMETHOXYETHANE BINARY SYSTEM WITH A CUBIC EQUATION OF STATE

SERGIU SIMA[a], RADU C. RACOVIŢĂ[a], AUREL CHIRILĂ[b], DRAGOȘ DEACONU[b], VIOREL FEROIU[a], CATINCA SECUIANU[a,c,*]

ABSTRACT. The ability of different thermodynamic models to predict the phase behaviour of carbon dioxide (1) + 1,2-dimethoxyethane (2) binary system is tested. The model chosen is the General Equation of State (GEOS) coupled with classical van der Waals mixing rules (two-parameter conventional mixing rule, 2PCMR). Comparisons were made with the GEOS3C, Soave-Redlich-Kwong (SRK), and Peng-Robinson (PR) cubic equations of state (EoS) too. A single set of binary parameters for each model was used to predict correctly the global phase behaviour of the system.

Keywords: *carbon dioxide, 1,2-dimethoxyethane, high-pressures, vapour-liquid equilibrium, equations of state, GEOS, GEOS3C*

INTRODUCTION

Over 80% of greenhouse gases (GHGs) are represented by carbon dioxide (CO_2) which enters the atmosphere through burning fossil fuels such as coal, oil, and natural gas, in power plants and energy production facilities as well as solid waste, trees and other biological materials and also as a result of certain chemical reactions in different industry (e.g., cement industry) [1-3].

[a] *University Politehnica of Bucharest, Faculty of Applied Chemistry and Materials Science, Department of Inorganic Chemistry, Physical Chemistry and Electrochemistry, 1-7 Gh. Polizu Street, S1, 011061 Bucharest, Romania*

[b] *University Politehnica of Bucharest, Faculty of Electrical Engineering, Department of Electrical Machines, Drives, and Materials, 313 Spl. Independentei Street, S6, 060042, Bucharest, Romania*

[c] *Imperial College London, Department of Chemical Engineering, South Kensington Campus, SW7 2AZ London, United Kingdom,*

** Corresponding author: catinca.secuianu@upb.ro; c.secuianu@imperial.ac.uk*

Among the many options for carbon mitigation, carbon capture and storage (CCS) is a vital technology for the cost-effective mitigation of anthropogenic CO_2 emissions and could contribute approximately 20% to CO_2 emission reductions by 2050, as recommended by International Energy Agency (IEA) [3,4].

Although CCS holds great potential in many industries and petroleum refineries given their large CO_2 emissions, a key obstacle to its utilization on a large scale remains its cost, being both operating and capital costs [3]. The costs of CCS could be reduced for the cases where industrial processes generate rich CO_2 gas streams or even pure CO_2 but they are still an impediment to its deployment.

In this context, many research focused almost exclusively on the development of improved sorbents with increased CO_2 capacity and/or reduced heat of regeneration [5]. However, recent results [3,5] show that whilst equilibrium CO_2 capacity is a key determinant of process performance, phase equilibria, transport properties (e.g., viscosity, diffusion coefficients, etc.) and other thermophysical properties (e.g., heat capacity, density, etc.) have a significant effect on the capital cost, and thus on the price of the carbon captured.

Therefore, we recently focused on the phase behaviour research of physical solvent for carbon dioxide capture. Phase equilibria at high-pressures of carbon dioxide with different classes of organic substances, such as alkanes [6], cycloalkanes [7,8], alcohols [9-15], ethers [16], esters, ketones, are investigated to illustrate the functional group effect on the solvent ability to dissolve CO_2.

As the experiments are usually expensive and very time consuming, equation of state (EoS) models are the most common approach for the correlation and/or prediction of phase equilibria and properties of the mixtures [17].

In this study we focus on the carbon dioxide (1) + 1,2-dimethoxyethane (DME) binary system. DME is an excellent inert aprotic polar solvent, suitable media for a number of chemical reactions. This ether is a clear, colourless, volatile, flammable liquid, fully miscible with water and a range of other substances such as methanol, ethanol, diethyl ether, acetone, tetrahydrofuran (THF), benzene, toluene, etc., and soluble in aliphatic hydrocarbons. It forms chelate complexes with metal cations and acts as a bidentate neutral ligand. The DME molecule is also of interest as it is the smallest element of the polyoxyethylene (POE), the water soluble polymer with various applications in biomedicine. DME is used as a higher boiling alternative to tetrahydrofuran and diethyl ether being an aprotic neutral polar solvent for chemical reactions. It has also multiple utilizations such as a solvent for oligo- and polysaccharides,

as a solvent for polysilicones, as a low-viscosity component of the solvent for electrolytes of lithium batteries, for etching of PTFE and other fluoropolymers with alkali metal dispersions, as a reaction media in pharmaceutical syntheses, as an entrainer [18,19].

In a previous paper [16], we compared the prediction results by two well-known cubic equations of state (EoS), namely Soave-Redlich-Kwong (SRK) and Peng-Robinson (PR), coupled with both classical van der Waals (2PCMR) and Gibbs excess energy (G^E) mixing rules. A single set of binary interaction parameters for each EoS, determined for the carbon dioxide + 1,2-DME binary system, was used to model the global phase behaviour of the system.

Here, the global phase behaviour of the system was modelled with a general cubic equation of state (GEOS) [20-25] coupled with classical van der Waals mixing rules (2PCMR). This cubic equation is a generalized form with four parameters for all cubic equations of state with two, three, and four parameters. One unique set of binary interaction parameters determined for the carbon dioxide + 1,2-DME system was used to calculate the critical curve and vapour-liquid equilibrium diagrams.

MODELLING

The phase behaviour of this system was modelled with the GEOS equation [20-25] coupled with classical van der Waals mixing rules (2PCMR). The GEOS [20,21] equation of state is:

$$P = \frac{RT}{V-b} - \frac{a(T)}{(V-d)^2 + c} \tag{1}$$

with the classical van der Waals mixing rules

$$a = \sum_i \sum_j X_i X_j a_{ij} \qquad b = \sum_i X_i b_i \tag{2}$$

$$c = \sum_i \sum_j X_i X_j c_{ij} \qquad d = \sum_i X_i d_i \tag{3}$$

$$a_{ij} = \left(a_i a_j\right)^{1/2}\left(1-k_{ij}\right) \quad b_{ij} = \frac{b_i + b_j}{2}\left(1-l_{ij}\right) \qquad c_{ij} = \pm\left(c_i c_j\right)^{1/2} \tag{4}$$

with "+" for c_i, $c_j > 0$ and "–" for c_i, $c_j < 0$. Generally, negative values are common for the c parameter of pure components.

The four parameters *a*, *b*, *c*, and *d* for a pure component are expressed by:

$$a(T) = \frac{R^2 T_c^2}{P_c}\beta(T_r)\Omega_a \qquad b = \frac{RT_c}{P_c}\Omega_b \tag{5}$$

$$c = \frac{R^2 T_c^2}{P_c^2}\Omega_c \qquad d = \frac{RT_c}{P_c}\Omega_d \tag{6}$$

Setting four critical conditions, with α_c as the Riedel criterion:

$$P_r = 1 \quad \left(\frac{\partial P_r}{\partial V_r}\right)_{T_r} = 0 \quad \left(\frac{\partial^2 P_r}{\partial V_r^2}\right)_{T_r} = 0 \quad \alpha_c = \left(\frac{\partial P_r}{\partial T_r}\right)_{V_r} \tag{7}$$

at $T_r = 1$ and $V_r = 1$, the expressions of the parameters Ω_a, Ω_b, Ω_c, Ω_d are obtained

$$\Omega_a = (1-B)^3 \quad \Omega_b = Z_c - B \quad \Omega_c = (1-B)^2 (B - 0.25) \tag{8}$$

$$\Omega_d = Z_c - \frac{(1-B)}{2} \qquad B = \frac{1+m}{\alpha_c + m} \tag{9}$$

where P_r, T_r, V_r are the reduced variables and Z_c is the critical compressibility factor.

The temperature function used is:

$$\beta(T_r) = T_r^{-m} \tag{10}$$

The GEOS parameters *m* and α_c were estimated by constraining the EoS to reproduce the experimental vapour pressure and liquid volume on the saturation curve between the triple point and the critical point [23].

We also used GEOS3C equation [23,24] which is based on the GEOS equation [20,21], but with a new temperature function:

$$\beta(T_r) = 1 + C_1 y + C_2 y^2 + C_3 y^3 \quad \text{for} \quad T_r \le 1 \tag{11}$$

$$\beta(T_r) = 1 + C_1 y \quad \text{for} \quad T_r > 1 \tag{12}$$

$$y = 1 - \sqrt{T_r} \tag{13}$$

The C_1, C_2 and C_3 parameters were obtained by matching points on the saturation curve (vapour pressures together with the corresponding liquid volumes). The objective function for parameters estimation and other details are given elsewhere [24].

The calculations were made using the software package *PHEQ*, developed in our laboratory [26]. The critical curves were calculated using the method proposed by Heidemann and Khalil [27], with numerical derivatives given by Stockfleth and Dohrn [28].

The GEOS equation was used in a semi-predictive approach to obtain a set of binary parameters yielding good results in the binary system carbon dioxide + 1,2-DME. The GEOS parameters, critical data, the acentric factors of the pure substances used in the calculations are presented in **Table 1** [29].

Table 1. Critical data, acentric factor [29], and GEOS parameters for pure compounds

Compound	T_c/K	P_c/bar	V_c/cm^3·mol^{-1}	Ω	α_c	m
CO_2	304.21	73.83	93.90	0.2236	7.0517	0.3146
1,2-DME	536.15	38.71	271.0	0.3475	8.7432	0.3138

RESULTS AND DISCUSSION

The first vapour-liquid equilibrium (VLE) and critical curve data of the carbon dioxide + 1,2-DME binary system were recently published [16]. The mentioned study indicated that this system seems to be type I or type II phase behaviour, according to the according to the classification of van Konynenburg and Scott [30] or the more recent one of Privat and Jaubert [31]. Both type I and type II phase behaviour are very similar and they are characterized by a continuous vapour-liquid critical curve stretching between the critical points of the pure components, the only difference being that in type II phase behaviour an additional liquid-liquid (LL) critical curve intersects a liquid-liquid-vapour three-phase (LLV) equilibrium curve in an upper critical endpoint (UCEP).

In order to calculate the critical curve, the experimental vapour-liquid equilibrium data from [16] were firstly correlated by GEOS/2PCMR and GEOS3C/2PCMR models at each temperature.

Figure 1 illustrates the comparisons of the experimental data [16] at the four available temperatures (313.15, 323.15, 333.15, and 343 K) with the correlation results by GEOS/2PCMR and GEOS3C/2PCMR, as well as by SRK/2PCMR and PR/2PCMR. All models behave similarly, the experimental data are well reproduced, with an overestimation of the critical region. It can be noticed that mixture critical points calculated SRK and PR are overestimated by about 15 bar while the critical pressure by GEOS and GEOS3C is overestimated with less than 8 bar (see **Figure 2**). However, all models fail to

reproduce correctly the critical compositions which are underestimated compared with the experimental ones. In **Figure 3** are shown the average values of the average absolute deviations in bubble-point pressures (AADP, %) for each model. Although all models have similar performances, the smallest errors are obtained by GEOS3C. The optimized binary interaction parameters (BIPs) for GEOS and GEOS3C are presented in **Table 2** together with the average absolute deviations in bubble-point pressures (AADP, %), and the average absolute deviations in the vapour-phase compositions (AADY, %), which are calculated by the equations:

$$AADP(\%) = \frac{1}{N_{\exp}} \sum_{i=1}^{N_{\exp}} \left| \frac{P_i^{\exp} - P_i^{calc}}{P_i^{\exp}} \right| \times 100 \tag{14}$$

$$AADY(\%) = \frac{1}{N_{\exp}} \sum_{i=1}^{N_{\exp}} \left| Y_i^{\exp} - Y_i^{calc} \right| \times 100 \tag{15}$$

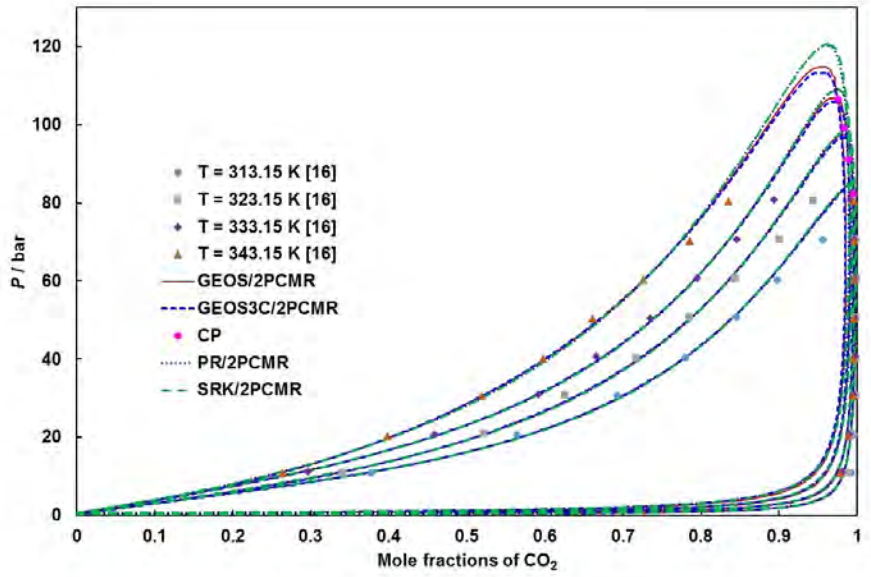

Figure 1. Comparison of literature VLE data [16] and correlations by GEOS (red solid line), GEOS3C (dashed blue line), SRK (dashed green lines), and PR (dotted dark blue line) EoSs for carbon dioxide (1) + 1,2-DME (2) system. CP stands for critical point of the mixture.

Table 2. Optimized binary interaction parameters (k_{12}, l_{12})

EoS/Mixing rule	T / K	k_{12}	l_{12}	*AADP* / %	*AADY* / %
GEOS/2PCMR	313.15	-0.2693	-0.0263	3.66	0.35
	323.15	-0.2603	-0.0118	4.21	0.53
	333.15	-0.2580	-0.0131	2.67	0.89
	343.15	-0.2260	0.0111	2.71	1.54
GEOS3C/2PCMR	313.15	-0.2684	-0.0241	3.51	0.36
	323.15	-0.2584	-0.0094	3.92	0.56
	333.15	-0.2553	-0.0104	2.47	0.97
	343.15	-0.2234	0.0134	2.46	1.70

As the values of optimized BIPs are very similar for GEOS and GEOS3C models, the critical curve was calculated in this study by GEOS EoS. It must be remarked that each set of binary interaction parameters obtained from the correlations at each of the four available temperatures leads to a critical curve.

Therefore, the values of the optimized binary interaction parameters were averaged for GEOS model and then were used to calculate the critical curve for the carbon dioxide (1) + 1,2-DME (2) binary system.

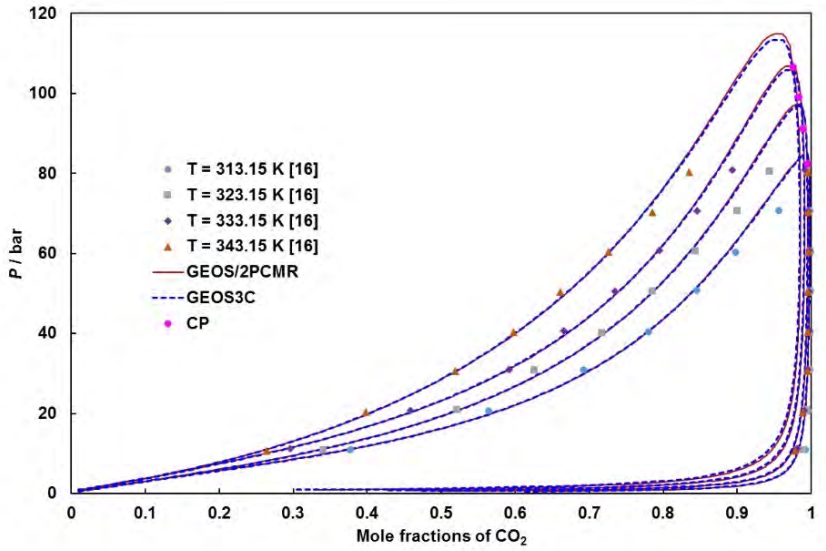

Figure 2. Comparison of literature VLE data [16] and correlations by GEOS (red solid line) and GEOS3C (dashed blue line) models for carbon dioxide (1) + 1,2-DME (2) system.

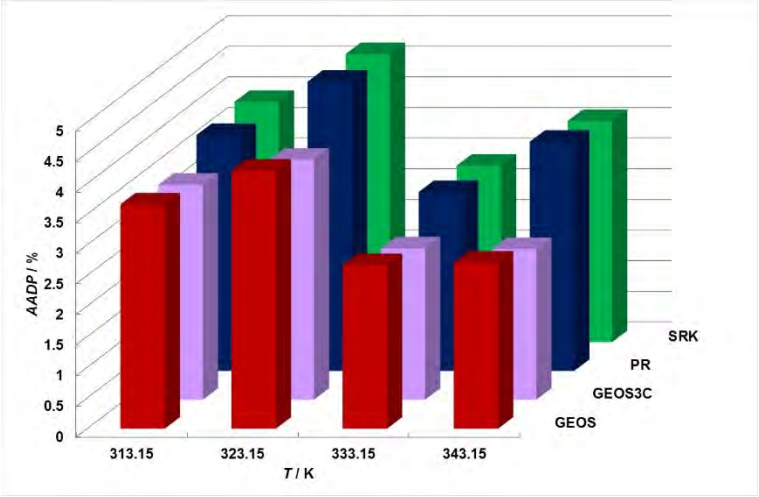

Figure 3. Average absolute deviations in bubble-point pressures (AADP, %) for GEOS (dark red), GEOS3C (purple), PR (dark blue), and SRK (green) models at different temperatures.

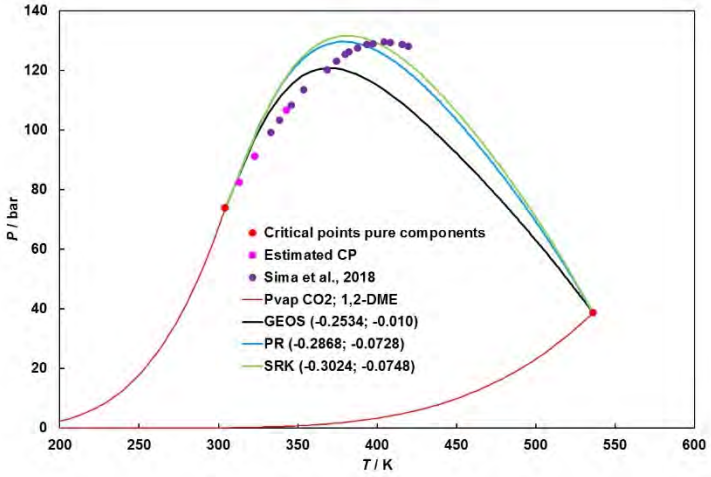

Figure 4. *P–T* fluid phase diagram for CO_2 (1) + 1,2-DME (2) system: (•), critical points of pure components [29]; (•,•), critical curve [16]; (—), vapour pressure curves; (▬), critical curve calculated by GEOS (k_{12} = -0.2534; l_{12} = -0.0100; (▬), critical curve calculated by SRK (k_{12} = -0.3024; l_{12} = -0.0748); (▬), critical curve calculated by PR (k_{12} = -0.2868; l_{12} = -0.0728).

Table 3. Binary interaction parameters (k_{12}, l_{12})

Model	Average BIPs		Modified BIPs[a]	
	k_{12}	l_{12}	k_{12}	l_{12}
GEOS/2PCMR	-0.2534	-0.0100	-0.0140	-0.0010
PR/2PCMR	-0.2868	-0.0728	0.0050	-0.0500
SRK/2PCMR	-0.3024	-0.0748	0.0100	-0.0750

[a]Modified binary interaction parameters are obtained by a trial and error procedure

Table 3 summarizes the average values of BIPs for GEOS, SRK, and PR models. The calculations are compared with the experimental critical data [16] in **Figure 4**.

It can be seen that the critical curves calculated with the average values of BIPs resulted from correlations are not in good agreement with experimental critical curve. While GEOS leads to a critical pressure maximum (CPM) smaller than the experimental one, PR and SRK are slightly overestimate its value. Even though all three models are reproducing relatively well the CPM, the corresponding critical temperatures are much underestimated.

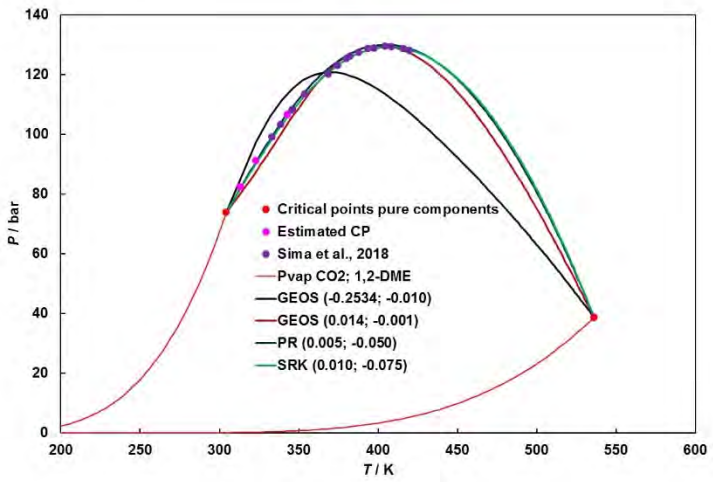

Figure 5. *P–T* fluid phase diagram for CO_2 (1) + 1,2-DME (2) system: (•), critical points of pure components [29]; (•,•), critical curve [16]; (—), vapour pressure curves; (▬), critical curve by GEOS (k_{12} = -0.2534; l_{12} = -0.0100); (▬), critical curve by GEOS (k_{12} = 0.0140; l_{12} = -0.0010); (▬), critical curve by SRK (k_{12} = 0.0100; l_{12} = -0.0750); (▬), critical curve by PR (k_{12} = 0.0050; l_{12} = -0.0500).

In **Figure 5** are presented the predictions of the critical by GEOS, as well as by PR and SRK [16]. The predictions by GEOS, PR, and SRK are almost overlapped, meaning that their CPMs and maximum critical temperatures are comparable. The CPMs predicted by all three models are in very good agreement with the experimental one, the highest difference is ~0.5 bar (PR). The maximum critical temperature is also very well predicted by all equations and the highest difference is ~4 K (GEOS), compared with the experimental value.

Although the predictions by these unique sets lead to small changes in critical pressures and temperatures compared with the experimental critical data, when plotting the critical pressures (**Figure 6**) or critical temperatures (**Figure 7**) against critical compositions, it can be remarked that the differences are exceeding 0.1 in molar composition.

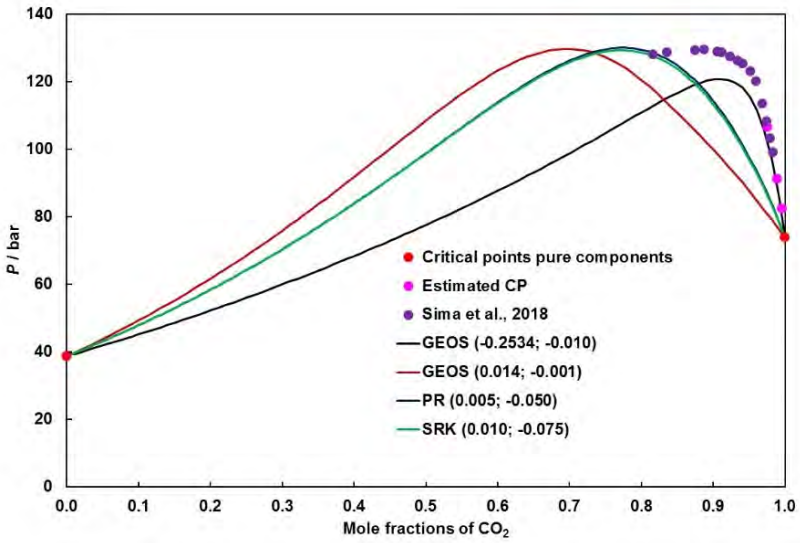

Figure 6. *P–x* projection of the phase diagram for carbon dioxide (1) + 1,2-DME (2) system: (●,●), literature data [16] and calculations by (▬), GEOS (k_{12} = -0.2534; l_{12} = -0.0100); (▬), GEOS (k_{12} = 0.0140; l_{12} = -0.0010); (▬), SRK (k_{12} = 0.0100; l_{12} = -0.0750); (▬), PR (k_{12} = 0.0050; l_{12} = -0.0500).

Consequently, we used a similar semi-predictive approach as in previous studies [8,16] and we obtained an unique set of binary interaction parameters for GEOS that represent very well the experimental critical curve. This set of BIPs (**Table 3**, "Modified BIPs") was estimated by a trial and error procedure, which yield coordinates of critical data closer to the experimental ones.

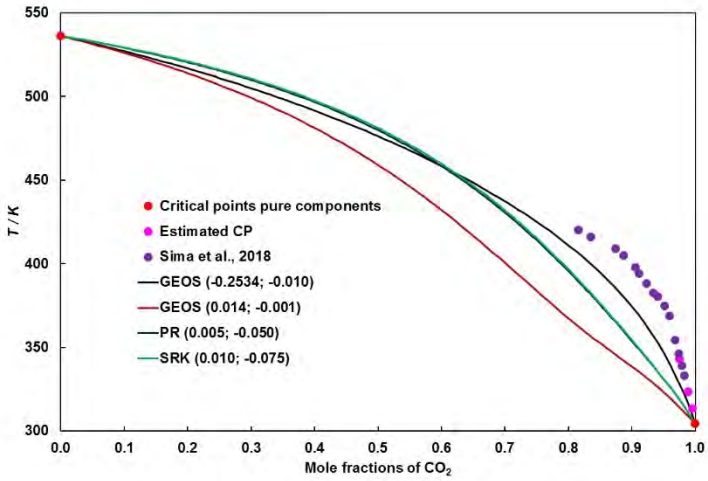

Figure 7. *T–x* projection of the phase diagram for carbon dioxide (1) + 1,2-DME (2) system: (●,●), critical experimental data [16] and calculations by (▬), GEOS (k_{12} = -0.2534; l_{12} = -0.0100); (▬), GEOS (k_{12} = 0.0140; l_{12} = -0.0010); (▬), SRK (k_{12} = 0.0100; l_{12} = -0.0750); (▬), PR (k_{12} = 0.0050; l_{12} = -0.0500).

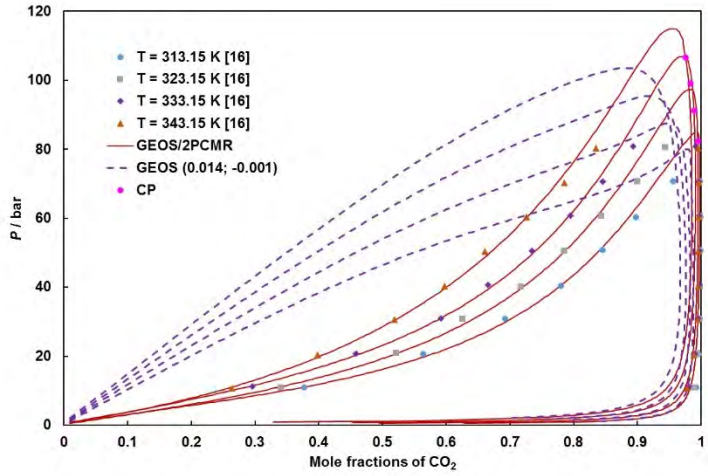

Figure 8. Comparison of correlations and predictions by GEOS for the CO_2 (1) + 1,2-DME (2) system: symbols are the experimental data [16], red solid lines are the correlations, and purple dashed lines are the semi-predictions (BIPs from **Table 3**).

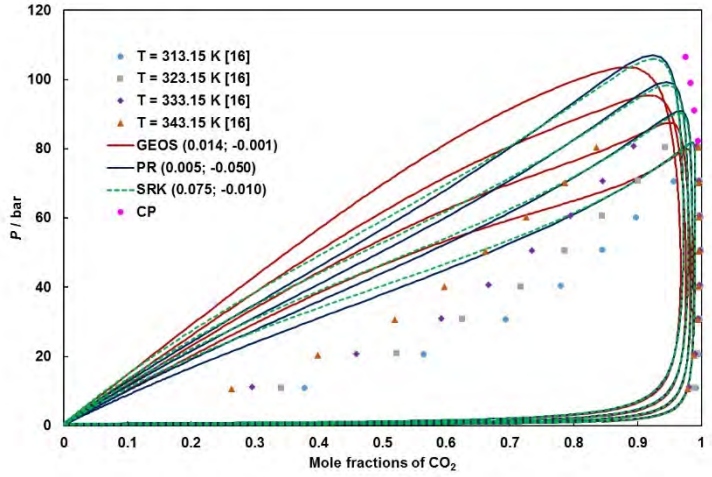

Figure 9. Comparison of experimental data and predictions by GEOS, PR, and SRK EoSs for the carbon dioxide (1) + 1,2-DME (2) system: symbols are the experimental data [16], and the lines are the semi-predictions with the modified parameters in **Table 3** (dark red solid lines, GEOS; dark blue solid line, PR; dashed green line, SRK).

This difference is very well noticed when representing the model results in the pressure-composition diagram. In **Figure 8** are presented the correlations and predictions by GEOS model, while in **Figure 9** are compared the predictions by GEOS, PR, and SRK. It can be seen that the critical pressure of each isotherm is well reproduced, but the compositions, especially the liquid ones, are not.

CONCLUSIONS

The GEOS and GEOS3C, as well as PR and SRK equations of state coupled with classical quadratic van der Waals mixing rules were used to model the phase behaviour of the carbon dioxide (1) + 1,2-DME (2) binary system. The aforementioned models reproduce very well the *P*–*T* critical curve when using a semi-predictive approach, but fail to reproduce well the critical compositions.

The topology of phase behaviour is very well predicted, taking into account the relatively simple models and modelling procedure.

ACKNOWLEDGMENTS

„This work was supported by a grant of Ministry of Research and Innovation, CNCS - UEFISCDI, project number PN-III-P4-ID-PCE-2016-0629, within PNCDI III".

REFERENCES

1. *https://www.epa.gov/ghgemissions/overview-greenhouse-gases*, accessed July 2019
2. IPCC, Climate Change 2014: Mitigation of Climate Change: Contribution of Working Group III to the Fifth Assessment Report of the Intergovernmental Panel on, Cambridge University Press, 2014
3. M.T. Mota-Martinez; J.P. Hallett; N. Mac Dowell, *Sustain. Energ. Fuels*, **2017**, *1*, 2078-2090
4. *https://www.iea.org/geco/emissions/*, accessed July 2019
5. M. Bui; M. Fajardy; N. Mac Dowell; *Fuel*, **2018**, *213*, 164-175
6. C. Secuianu; V. Feroiu; D. Geană; *J. Chem. Eng. Data*, **2010**, *55 (10)*, 4255–4259
7. S. Sima; J.M. Milanesio; J.I. Ramello; M. Cismondi; C. Secuianu; V. Feroiu; D. Geană; *J. Chem. Thermodyn*., **2016**, *93*, 374-385
8. A.V. Crişciu; S. Sima; A.-S. Deaconu; A. Chirilă; D. Deaconu; C. Secuianu; V. Feroiu; *Rev. Chim.-Bucharest*, **2016**, *67 (10)*, 1984-1989
9. S. Sima; S. Ionită; C. Secuianu; V. Feroiu; D. Geană; *J. Chem. Eng. Data*, **2018**, *63 (4)*, 1109-1122
10. S. Sima; R.C. Racoviţă; C. Dincă; V. Feroiu; C. Secuianu; *Univ. Politeh. Buchar. Sci. Bull.-Ser. B-Chem. Mat. Sci.*, **2017**, *79 (4)*, 11-24
11. C. Secuianu; V. Feroiu; D. Geană; *Fluid Phase Equilib.*, **2016**, *428*, 62-75
12. S. Secuianu; S. Ioniţă; V. Feroiu; D. Geană; *J. Chem. Thermodyn*., **2016**, *93*, 360-373
13. S. Ioniţă; C. Secuianu; V. Feroiu; D. Geană; *Univ. Politeh. Buchar. Sci. Bull.-Ser. B-Chem. Mat. Sci.*, **2015**, *77 (1)*, 31-40
14. S. Sima; C. Secuianu; V. Feroiu; D. Geană; *Cent. Eur. J. Chem*., **2014**, *12 (9)*, 953-961
15. S. Sima; C. Secuianu; V. Feroiu; D. Geană; *Cent. Eur. J. Chem*., **2014**, *12 (9)*, 893-900
16. S. Sima; C. Secuianu; V. Feroiu; *Fluid Phase Equilib*., **2018**, *458*, 47-57
17. C. Secuianu; J. Qian; R. Privat; J.-N. Jaubert; *Ind. Eng. Chem. Res*., **2012**, *51*, 11284-11293
18. J. Gujt, H. Dominguez; S. Sokolowski; O. Pizio; *Cond. Matt. Phys.*, **2017**, *20*, 1–14

19. A. Jänes; J. Eskusson; T. Thomberg; T. Romann; E. Lust; *J. Energy Chem*., **2016**, *25*, 609–614.
20. D. Geană; *Rev. Chim. (Bucharest)*, **1986**, *37*, 303-309
21. D. Geană; *Rev. Chim. (Bucharest)*, **1986**, *37*, 951-959
22. D. Geană; *Rev. Chim. (Bucharest)*, **1987**, *38*, 975-979
23. D. Geană; V. Feroiu; *Fluid Phase Equilib*., **2000**, *174*, 51–68
24. D. Geană; V. Feroiu; *Ecuaţii de stare. Aplicaţii la echilibre de faze*, Ed. Tehnică: Bucharest, Romania, **2000**
25. C. Secuianu; V. Feroiu; D. Geană; *J. Supercrit. Fluid.*, **2008**, *47 (2)*, 109-116
26. D. Geană; L. Rus; Phase equilibria database and calculation program for pure components systems and mixtures, in *Proc. Romanian Int. Conf. Chem. Chem. Eng.* (*RICCCE XIV)*, Bucharest, Romania, **2005**; Volume 2, pp.170–178
27. R.A. Heidemann; A. M. Khalil; *AIChE J.,* **1980***, 26*, 769–779
28. R. Stockfleth; R. Dohrn; *Fluid Phase Equilib.,* **1998**, *145*, 43–52
29. Evaluated Standard Thermophysical Property Values, DIPPR Project 801 full version, Brigham Young University, Provo Utah, **2005**
30. P.H. van Konynenburg; R.L. Scott; *Philos. Trans. R. Soc. Lond.-Ser. A*, **1980**, *298*, 495–540
31. R. Privat; J.-N. Jaubert; *Chem. Eng. Res. Des.*, **2013**, *91*, 1807–1839

STUDIA UBB CHEMIA, LXIV, 3, 2019 (p. 143-152)
(RECOMMENDED CITATION)
DOI:10.24193/subbchem.2019.3.12

HEAT TRANSFER INFLUENCE ON FRACTIONATION IN FLOODED PACKED COLUMNS

SIMONA POPA[a], SORINA BORAN[a], GIANNIN MOSOARCA[a,*], COSMIN VANCEA[a]

ABSTRACT. In packed fractionation, the liquid phase can be forced to become continuous, and the vapor phase dispersed, realizing emulsification regime. The paper presents the efficiency comparing results of packed fractionation with respect to the fractionation in an empty flooded column, as well as the influence of the heat flux and of the temperature inside the column's jacket. Experiments for determining the boiling heat transfer of the different methanol – ethanol concentration mixtures were performed. The variation of the boiling heat transfer coefficient at different concentrations of methanol-ethanol mixtures has a minimum, corresponding to the maximum of the difference between concentrations of vapor phase in equilibrium with the liquid phase.

Keywords: *fractionation, flooded columns, boiling heat transfer*

INTRODUCTION

In chemical industry columns are apparatus used in many different technologies, such as fractionation [1-3], polymerization [4-7] or esterification [8, 9]. The main separating process in chemical industry represents fractionation, and it is very important to find means to improve the process or to make it more economic efficient [10] or safety [11].

One of the main reasons of the low efficiency in operating packed columns, under ordinary hydrodynamic conditions, is the non-uniform distribution of the liquid phase over the packing surface. The liquid phase preferred channels when fowling through the packing, which determines a deep decrease of the interfacial area, a growth of the fowling liquid layer thickness and the heat and mass transfer deteriorate.

[a] *Polytechnic University of Timisoara, Victoriei Square, No.2, 30006-Timisoara, Romania*
** Corresponding author: giannin.mosoarca@upt.ro*

When operating a packed column with a large diameter, the liquid can't be uniform distributed on the entire packing surface, causing a decrease of the column's performance, with respect to a smaller diameter packed column, so the height equivalent to a theoretical plate (HETP) is also small [12].

The optimum operating conditions for a packed column are situated in the emulsification regime, which can be observed only in a narrow range of velocities of the liquid and gaseous phases. The upper limit is the column's flooding and the lower limit is when the emulsification disappears. During the emulsification regime, the HETP increases abruptly and the column operates at constant flow velocity. That is why the emulsification regime must be stabilized.

The literature [13-16] presents models for determining the flooding point for different packing. For several decades, the Sherwood-Leva-Eckert correlation chart had been the standard of the industry for predicting flood points and pressure drops for fractionation packed columns. The gas – liquid interaction [13] influences the pressure drop and the flooding, being connected to the maximum of velocity. The point limited by the maximum superficial gas mass flow rate and the superficial liquid mass flow rate is the "limit operating point", and the linking of all these points in the Sherwood-Leva-Eckert diagram represents the "limit operating line" – "flooding line". Many researchers [3, 17-21] tried to establish optimal conditions for fractionating columns.

The boiling heat transfer coefficients are used routinely in calculations and design of industrial boiling equipment. Many researchers calculate boiling heat transfer coefficients using different types of heat surface [22-28]. The literature also presents aspects regarding the control performances improvements [29, 30]. Some of the papers deal with the improvement and optimization of the separation process [30].

Although the heat transfer under flooding conditions and measurements for the holdup are important, only few researchers published in this area [31, 32].

To the best of our knowledge fractionation in flooded packed columns with the study of the influence of the liquid stopper and the calculation of the heat transfer at boiling was not yet been proposed. This is why the present paper proposed to study the separation efficiency when using a flooded column with or without packing material and to evaluate the partial boiling heat transfer coefficient (α) during the process as well as the dependence of boiling heat transfer coefficient on heat flux (q).

RESULTS AND DISCUSSION

In the first part of the experiments, when the efficiency of the flooded column was studied, it was established that, for the same heat flux, the jacket temperature influences the process performance, determining a greater or a

smaller liquid reflux ratio [27]. Empiric equations for the proposed dependences are presented in Table 1. It can be seen that with the increase of the temperature inside the jacket, the concentration of the distillate decreases and the distillate flow rate increases.

Using Fenske relations the height equivalent of a theoretical plate (HETP) was established. The results are presented in Table 2. At 47 and 62 ºC, the results are similar to the ones reported in literature [27].

Table 1. Proposed empiric equations for the dependences of the distillate concentration and distillate flow rate on the jacket temperature for methanol-ethanol mixture in the packed column

Empiric equation of the distillate concentration on the jacket temperature	Empiric equation of the distillate flow rate on the jacket temperature
y = -1.057x + 136.36	y = 1.8876x - 71.6

Table 2. The height equivalent to a theoretical plate (HETP) at different temperatures

Temperature, ºC	HETP, cm
47	7.7
50	7
55	6.4
60	5.2
62	4.7

In the second part of experiments, the efficiency in the flooded column with no packing material was calculated based on Fenske relation. The results are presented in Table 3. It can be observed that the efficiency of a flooded empty column is better than that of a packed column of the same diameter. When the height of the liquid stopper is bigger, the efficiency of the column is also better.

Table 3. Separation efficiency in flooded column with two heights of the liquid stopper for the methanol-ethanol mixture

Height of the liquid stopper (cm)	HETP (cm)
5.5	5.5
7	5.1
10	4.9
14	4.5

When the density of the heat flux (q) at the bottom of the column was increased, the separation efficiency in the flooded column with the liquid stopper of 14 cm increased as well. The performance of the column in this case is presented in Figure 1. It can be seen once more, that the separation process is more efficient by intensifying the heat transfer at the bottom of the fractionating column.

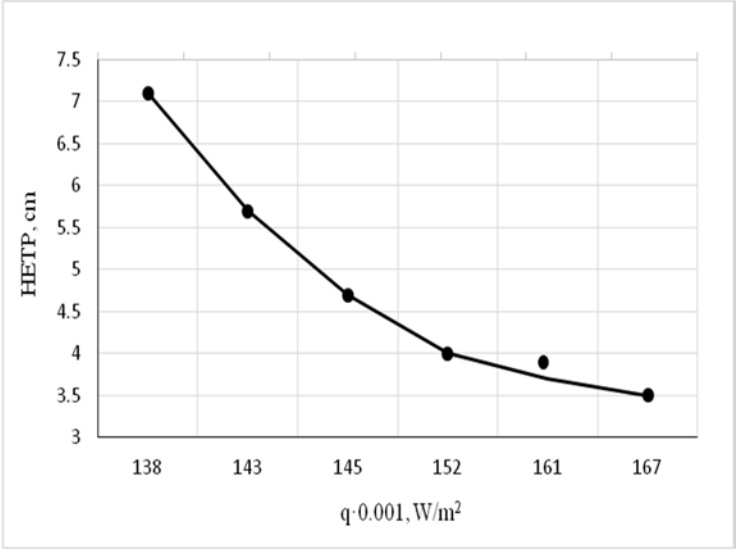

Figure 1. Dependence of the efficiency of a flooded column with the liquid stopper of 14 cm on the thermal flux (q) at separation methanol-ethanol mixture

In order to correlate the efficiency of the column, not only with the heat flux (q), but also with the partial boiling heat transfer coefficient (α), experiments for establishing the variation of α with the heat flux were performed. The experimental results for different concentrations of methanol-ethanol mixtures are presented in Figure 2.

Table 4. Dependent equations between α and q

C, % mol	$\alpha = a \cdot q^{0.56}$
0	$\alpha = 13.68 \cdot q^{0.56}$
42	$\alpha = 12.06 \cdot q^{0.56}$
55	$\alpha = 10.40 \cdot q^{0.56}$
65	$\alpha = 11.13 \cdot q^{0.56}$
100	$\alpha = 13.27 \cdot q^{0.56}$

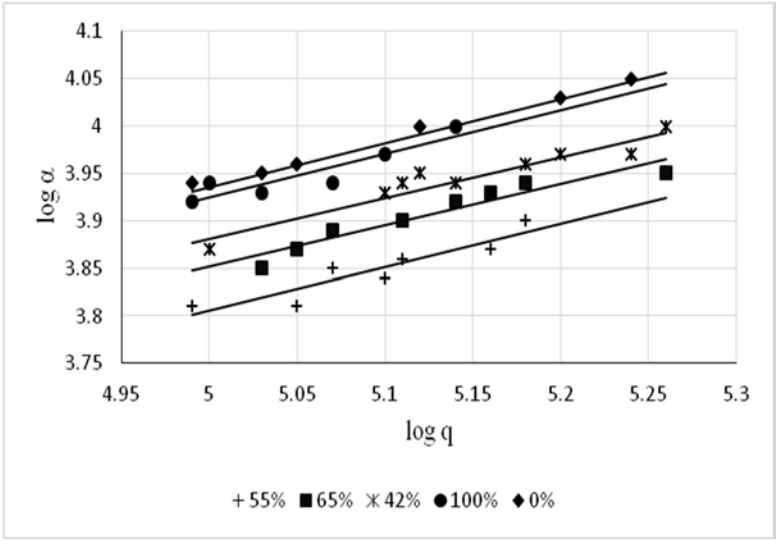

Figure 2. Dependence of boiling heat transfer coefficient (α) on heat flux (q)

The obtained dependences (Table 4) have the general equation:

$$\alpha = a \cdot q^{0.56} \quad (1)$$

where: *a* is concentration depending parameter.

The boiling heat transfer coefficient values decrease at the beginning, but then increase when the concentration increase. This phenomenon was observed even at the different concentrations of boiling ethanol-water mixture [36].

The explanation may be linked to the boiling mechanism. On the basis of the equilibrium data for the methanol-ethanol system, it was established that the variation of the concentration difference between vapor phase in equilibrium to the liquid phase, (y-x), as a function of concentration, has a maximum where the value of the boiling heat transfer coefficient (α) has a minimum. These are represented in Figure 3 and in Figure 4.

It is known that the value for boiling heat transfer coefficient (α) depends on the limit surface phenomena. Thus, if the heat transfer from the boiling surface to the liquid next to it determines a concentration in the low volatility liquid, which is greater if the difference (y-x) increases, the effect is a decrease in the value of α until (y-x) reaches the maximum value, afterwards a new increase of the α-value appears, when (y-x) decreases.

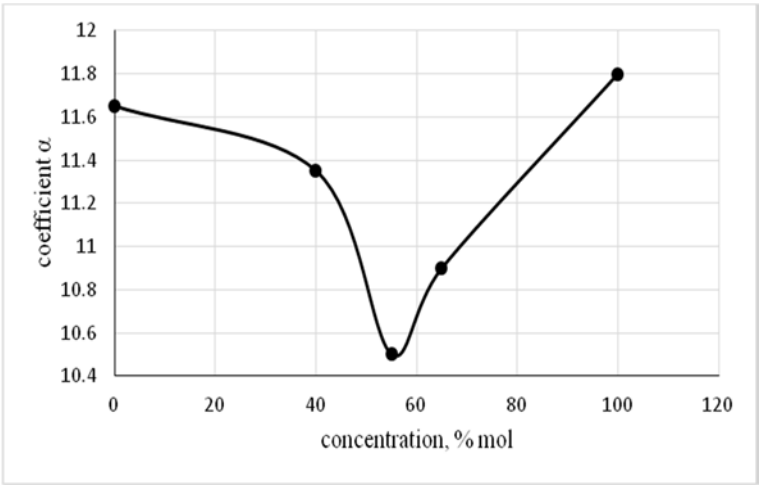

Figure 3. Variation of coefficient α with the concentration

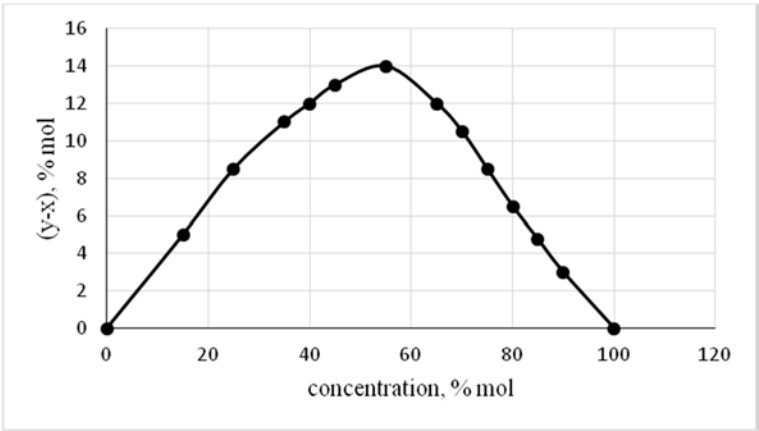

Figure 4. Variation of (y-x) with the concentration

CONCLUSIONS

Experiments show that, during separation of a methanol-ethanol mixture, by raising temperature inside the jacket of a packed flooded column, at the same heat flux, separation efficiency increases. Attempts were made to separate the same mixture of methanol-ethanol into a column with a liquid stopper of different heights, showing an increase in fractional efficiency compared to the filler column.

At the same time, by increasing the thermal flow in the column flap it was once again proved the beneficial influence of the increase of the boiling heat transfer on the performance of the fractionation columns.

Empirical equations for correlating the process parameters are proposed.

The variation of the boiling heat transfer coefficient at different concentrations of methanol-ethanol mixtures has a minimum, corresponding to the maximum of the difference between concentrations of vapor phase in equilibrium with the liquid phase (y-x).

EXPERIMENTAL SECTION

In order to study the fractionation process in flooded columns, an installation, where most of the influencing parameters can be maintained constant was realized [27, 28, 30, 34] (Figure 5). This facilitates the obtaining of constant values for the gas flow rates, corresponding to the mixture concentration.

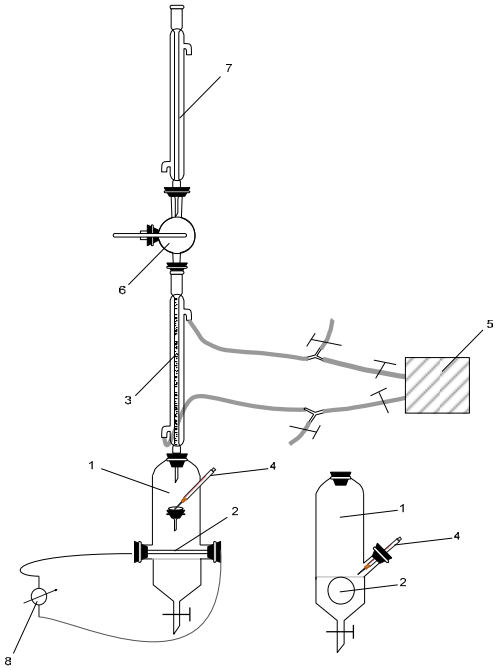

Figure 5. Experimental installation: 1-boiling vessel; 2-heat device; 3-column; 4-pipette; 5-thermostat; 6-dropper separator; 7-refrigerator; 8-current intensity measurement system

Experimental equipment includes a boiling vessel with an inside heater, a packed column provided with a refrigerator and a drops separator.

The boiler is heated by a heating system with internal source, made by a short circuit heating metal, where the heat flux can be measured and reproduced.

The packing material which was in glass Rashig rings (σ = 776 m^2/m^3; Vf = 0.71 m^3/m^3) having a height Hp = 0.3 m.

The inside heater is an horizontal cylindrical stainless steel tube, having the external diameter of 0.01065 m, and the length of 0.0504 m. High amperage alternating current is supplied through thick copper connectors attached to the heating tube. The control of the thermal flux resulting from the Joule — Lenz effect is achieved by adjusting the amperage of the electrical current supplied.

In order to study the efficiency of the flooded column, it was necessary to compare the effectiveness of this column with one whose operation and parameters are established under identical operating conditions. So, at first, the column was performed at total reflux ratio with an ideal methanol-ethanol mixture [35], which has the relative volatility value close to one.

For determining of height equivalent to a theoretical plate (HETP) Fenske relations (1-3) were used [36]:

$$y^* = \frac{\alpha_r \cdot x}{1 + (\alpha_r - 1) \cdot x} \tag{2}$$

where: x is mole fraction of the more volatile component in the liquid phase, y* is molar fraction of the more volatile component in the vapor phase in equilibrium with the liquid phase and α_r represent the coefficient of relative volatility.

$$N = \frac{\lg\left(\frac{x_D}{1-x_D} \cdot \frac{1-x_W}{x_W}\right)}{\lg(\alpha_{med})} - 1 \tag{3}$$

where: N is the minimum number of theoretical plates, x_D, x_W represent mole fraction of the more volatile component in the distillate, and in the still pot respectively and α_{med} is average volatility.

$$\alpha_{med} = \sqrt{\alpha_D \cdot \alpha_W} \tag{4}$$

where: α_D, α_W are relative volatilities in the distillate, and in the still pot respectively.

During the first part of the experiments the temperature ranged between 47 and 62ºC.

In the second part, the experiments were performed at 47ºC with an empty column of the same diameter, at an identical heat flux, where the liquid was maintained at flooding, working with the height of the liquid stopper between 5.5 cm and of 14 cm respectively.

REFERENCES

1. S. Bhatia, A.L. Ahmad, A.R. Mohamed, S.Y. Chin, *Chem. Eng. Sci.,* **2006**, *61(22),* 7436.
2. Z. Olujic, M. Jödecke, A. Shilkin, G. Schuch, B. Kaibel, Equipment improvement trends in distillation, *Chem. Eng. Process*., **2009**, *48(6)*, 1089.
3. A.A. Kiss, Z. Olujic, *Chem. Eng. Process*., **2014**, *86*, 125.
4. S. Popa, C. Csunderlik, S. Florea, V. Jascanu, N. Plesu, *Revista de Chimie*, **2002**, *53(4)*, 259
5. S. Popa, C. Csunderlik, V. Jascanu, D. Jurcau, N. Plesu, *Materiale Plastice*, **2003**, *40(4)*, 177-181.
6. S. Popa, V. Jascanu, D. Jurcau, N. Plesu, *Revista de Chimie*, **2003**, *54(7)*, 595.
7. S. Popa, C. Csunderlik, V. Jascanu, D. Jurcau, N. Plesu, *Materiale Plastice*, **2004**, *41(2)*, 62.
8. E. Özcan, S. Sargin, Y. Göksungur, *Biochem. Eng. J*., **2014**, 92, 9.
9. C.J. Stacy, C.A. Melick, R.A. Cairncross, *Fuel Process. Technol*., **2014**, *124*, 70.
10. P.C. Wankat, *Chem. Eng. Sci.*, **2015**, *137*, 955.
11. L. Bodisz, M. Hahn, A. Rix, J. Schallenberg, *Chem. Eng. Res. Des.*, **2015**, *99*, 208.
12. C. Stratula, "Fractionation. Principles and calculating methods", Editura Tehnica, Bucharest, **1986**.
13. H.Z. Kister, D. R. Gill, *Chem. Eng. Prog*., **1991**, *87(2)*, 32.
14. A.K. Coker, *Chem. Eng. Prog*., **1991**, *87(11)*, 93.
15. M. Leva, *Chem. Eng. Prog*., **1992**, *88(1)*, 65.
16. A. Badea, "Basis of heat and mass transfer", Editura Academiei Romane, Bucharest, **2004**.
17. R.E. Strigle, *Chem. Eng. Prog*., **1993**, *89(8)*, 79.
18. M. Kotora, J. Markos, V. Camaj, *Chem. Eng. Sci*., **2007**, *62*, 5193.
19. L.L. Simon, H. Kencse, K. Hungerbuhler, *Chem. Eng. Process*., **2009**, *48(4)*, 938.
20. Q. Qian, H. Wang, P. Bai, G. Yuan, *Chem. Eng. Res. Des.*, **2011**, *89(12)*, 2560.
21. T. Chen, B. Zhang, Q. Chen, *Energy*, **2014**, *72*, 311.
22. Y.J. Chung, K.H. Bae, K.K. Kim, W.J. Lee, *Ann. Nucl. Eng*., **2014**, *71*, 298.
23. E. Demir, T. Izci, A. S. Alagoz, T. Karabacak, A. Kosar, *Int. J. Therm. Sci.,* **2014**, *82*, 111.
24. G.M. Chen, V.P. Zhelezny, A.V. Melnyk, K.O. Shestopalov, *Int. J. Refrig*., **2015**, *58*, 137.

25. S.J. Thiagarajan, R. Yang, C. King, S. Narumanchi, *Int. J. Heat Mass Transfer*, **2015**, *89*, 1297.
26. X. Zheng, C.W. Park, *Appl. Therm. Eng.*, **2015**, *86*, 14.
27. S. Popa, S. Boran, *Rev. Roum. Chim.*, **2016**, *61(11-12)*, 851.
28. S. Popa, S. Boran, *Thermal Science*, **2017**, *21(5)*, 2031.
29. S. Nanu, T. L. Dragomir, *Control Eng. Appl. Inf.*, **2001**, *3(2)*, 1.
30. S. Popa, S. Boran, *Rev. Roum. Chim*., **2015**, *60(10)*, 991.
31. M. Asadollahzadeh, M. Torab-Mostaedi, R. Torkaman, *Chem. Eng. Process*., **2016**, *109*, 97.
32. P. Amani, J. Safdari, H. Abolghasemi, M.H. Mallah, A. Davari, *Int. J. Heat. Fluid Fl*., **2017**, *65*, 266.
33. T.L. Dragomir, I. Silea, S. Nanu, Control performances improving by interpolator controllers, *6th World Multiconference On Systemics, Cybernetics and Informatics*, Orlando, Florida, USA, **2002**, p.208.
34. D. Kohn, S. Popa, *Exp. Heat Transfer*, **1999**, *12(3)*, 193.
35. R.J.P. Brierley, *Chem. Eng. Progress*, **1994**, *90*, 68.
36. I. Bratu, "Procese si aparate in industria chimica, vol. III. ", Editura Tehnica, Bucharest, **1985**.

STUDIA UBB CHEMIA, LXIV, 3, 2019 (p. 153-162)
(RECOMMENDED CITATION)
DOI:10.24193/subbchem.2019.3.13

LACK OF KINETIC INTERACTION BETWEEN ZOLPIDEM AND DULOXETINE: RESULTS FROM A DRUG-DRUG INTERACTION STUDY IN HEALTHY VOLUNTEERS

ANA-MARIA GHELDIU[a], DANA MARIA MUNTEAN[b], MARIA NEAG[c], ADINA POPA[d], CORINA BRICIU[d,*], LAURIAN VLASE[b]

ABSTRACT. This open-label, non-randomized, two-period and sequential study aimed to evaluate a potential kinetic interaction between zolpidem ((N,N-dimethyl-2-[6-methyl-2-(4-methylphenyl)imidazo[1,2-a]pyridin-3-yl]acetamide), a widely known and used sedative-hypnotic and duloxetine ((3S)-N-methyl-3-naphthalen-1-yloxy-3-thiophen-2-ylpropan-1-amine), an antidepressant. A total of 23 healthy volunteers received the following medications: period 1 (Reference) - zolpidem 5 mg (single dose) and period 2 (Test) - zolpidem 5 mg and duloxetine 30 mg. Non-compartmental method was employed to determine the pharmacokinetic parameters of zolpidem and its main metabolite, zolpidem phenyl-4-carboxylic acid (Z4CA) while analysis of variance (ANOVA) was used to test the differences between study periods. Zolpidem exhibited similar pharmacokinetics with or without duloxetine (C_{max}: 59.64±27.64 ng/mL vs 53.28±22.77 ng/mL, AUC_{0-t}: 239.45±158.26 ng*h/mL vs 217.21±135.95 ng*h/mL, $AUC_{0-\infty}$: 245.87±161.84 ng*h/mL vs 224.61±138.86 ng*h/mL, $t_{1/2}$: 2.97±2.06 vs 3.12±1.86 h). Subsequently, no marked changes were observed for Z4CA. The statistical test confirmed that duloxetine had no significant influence on the exposure to zolpidem and Z4CA ($p<0.05$ for all pharmacokinetic parameters). In conclusion, the study results excluded the possibility of a pharmacokinetic drug-drug interaction between these two drugs. Future investigations should focus on potential undesirable pharmacodynamic effects.

Keywords: *zolpidem, duloxetine, kinetic interaction, healthy volunteers*

[a] *University of Medicine and Pharmacy 'Iuliu Hatieganu', Faculty of Pharmacy, Department of Pharmaceutical Botany, 23 Marinescu str., RO-400337, Cluj-Napoca, Romania*
[b] *University of Medicine and Pharmacy 'Iuliu Hatieganu', Faculty of Pharmacy, Department of Pharmaceutical Technology and Biopharmaceutics, 8 Victor Babes str., RO-400012, Cluj-Napoca, Romania*
[c] *University of Medicine and Pharmacy 'Iuliu Hatieganu', Faculty of Medicine, Department of Pharmacology, Toxicology and Clinical Pharmacology, 23 Marinescu str., RO-400337, Cluj-Napoca, Romania*
[d] *University of Medicine and Pharmacy 'Iuliu Hatieganu', Faculty of Pharmacy, Department of Clinical Pharmacy, 12 Ion Creanga str., RO-400010, Cluj-Napoca, Romania*
* *Corresponding author: corina_briciu@yahoo.com*

INTRODUCTION

A drug-drug interaction (DDI) usually represents the alteration of the expected drug response for a patient, which derives from the exposure of the same patient to another co-administered drug [1]. DDIs usually occur in the body after the drug molecules are absorbed in the systemic circulation and they can be either pharmacodynamic (PD) or pharmacokinetic (PK) [1]. Pharmacokinetic DDIs can emerge at each process (absorption, distribution, metabolism, and elimination) and entail the alteration of the PK profiles of drugs [1,2]

The most prevalent DDIs are those occurring at the level of drug metabolism [3]. The latter represents the process of converting one chemical species to another chemical species, called metabolite, which commonly possesses little or no pharmacological activity when compared to the parent compound [2]. DDIs that involve the inhibition or induction of the metabolism of one drug by another co-administered drug are best understood and evaluated by investigating the specific isoenzymes involved in that particular interaction [4]. This type of DDIs consists of CYP450 enzyme inhibition or induction, both processes involving an alteration in hepatic enzyme activity [5].

A drug acting as an enzymatic inhibitor decreases the metabolism rate of the simultaneously administered drug by several distinct mechanisms, either in a reversible or irreversible manner [1]. The reversible drug inhibition can occur as mutual competitive inhibition, noncompetitive and uncompetitive inhibition [2]. A competitive mechanism refers to a competition between the enzyme inhibitor and the substrate for the same binding site of the metabolizing enzyme. In this case, the two drugs involved seem to have structural similarities and for this reason, they are compatible with the same enzyme [1,6]. The mutual competitive inhibition occurs when the same isoenzyme is responsible for the metabolism of the two compounds, case in which the plasma levels of both inhibitor and substrate will be increased [6]. The noncompetitive inhibition was reported when the inhibitor and the drug behaving as a substrate bind to the same enzyme, but at different binding sites, leading to a conformational change in the proteic structure of the isoenzyme [1,3,6]. For the uncompetitive mechanism of inhibition, the inhibitor does not bind to the free enzyme, but to the complex formed between the enzyme and the substrate. Consequently, the inhibition is more marked when the concentration of the substrate is higher [1,6].

The irreversible inhibition is a consequence of the formation of complexes with the haem portion or the proteic part of the enzyme through covalent bonds [1,6]. Furthermore, the mechanism-based inactivation (also referred to as time-dependent inhibition) occurs more frequently than presumed, partly due to redox cycling-allied enzymatic action of CYPs, and leads to the inactivation of the target enzymes [3].

It is important to evaluate the possibility of metabolic DDIs as their occurrence in the liver and/or gastro-intestinal tract can alter the PK profiles of concomitantly administered drugs and thus potentially leading to therapeutic failure or increased incidence and severity of side effects [3]. Moreover, depending on the localization of the inhibited/induced enzyme(s), an alteration of the bioavailability alongside decreased/increased hepatic clearance can be observed for orally administered drugs [1,3,5].

The degree of inhibition depends on the affinity of the substrate for the inhibited enzyme and on the half-life time ($t_{1/2}$) of the inhibitor [3]. The onset of inhibition and the disappearance of this effect are directly related to the $t_{1/2}$ and the time required to reach the steady-state concentration of the inhibitory drug [1,2]. Thus, metabolic DDIs emerge only after the process of inhibition is completed [1,2,3]. For drugs subjected to intensive first-pass metabolism, the co-administration of an enzyme inhibitor can significantly alter their bioavailability after oral administration [3].

Prior to systemic absorption, inhibition and DDIs can also take place in the gut wall, considering that some of the CYP450 isoforms can be found at this biological site as well [9].

The binding of the inhibitor to the enzyme can take place at the lipophilic domain of the active site, or by ionic bonds with the specific aminoacids from the active site or by hydrogen bonds [1]. Some reversible inhibitors act by binding the haem portion of the enzymes, but the most effective inhibitors are those who, in addition, bind to the hydrophobic site of the active part of the enzymes [2].

From the previously mentioned mechanisms of drug inhibition, the most commonly encountered DDIs are due to reversible inhibition and mechanism-based inactivation [3,10]. Moreover, because a large number of drugs are metabolized via isoenzymes CYP2D6 and CYP3A4, a special attention should be given whenever drug substrates for these isoenzymes are prescribed concomitantly with inhibitors/inducers of the same metabolic pathway [7,8].

Zolpidem (IUPAC name (N,N-dimethyl-2-[6-methyl-2-(4-methylphenyl) imidazo[1,2-a]pyridin-3-yl]acetamide) is a γ-aminobutyric acid $(GABA)_A$-receptor agonist, with an imidazopyridine structure, which exhibits high affinity for the benzodiazepine ω1 receptor [11]. The drug is recommended worldwide for the short-term treatment (<4 weeks) of insomnia at typical dosages that consist of 5-10 mg/day at bedtime [12]. Several CYP450 isoenzymes are involved in the metabolism of this sedative-hypnotic: CYP3A4, CYP2C9, CYP1A2, CYP2D6 and CYP2C19 [11]. In the liver, zolpidem is converted to three pharmacologically inactive metabolites via oxidation and hydroxylation. The 4-carboxy-derivative (zolpidem phenyl-4-carboxylic acid – Z4CA) is the predominant metabolite and accounts for 72 up to 86% of the administered dose [13].

Duloxetine (IUPAC name (3S)-N-methyl-3-naphthalen-1-yloxy-3-thiophen-2-ylpropan-1-amine) is an antidepressant with a dual mechanism of action that acts like a potent norepinephrine and serotonin-reuptake inhibitor (SNRI) [14]. Besides major depressive disorder, it is also used to treat generalized anxiety disorder, diabetic peripheral neuropathic pain, fibromyalgia, and severe stress urinary incontinence [15,16]. This drug undergoes extensive metabolic degradation in the liver mainly via CYP1A2 and CYP2D6, to pharmacologically inactive metabolites that are excreted in the urine [14-16]. Previous studies confirmed that duloxetine is a moderate inhibitor of CYP2D6, thus a risk of drug interaction exists whenever this antidepressant is co-administered with other substances metabolized via the same isoenzyme [14-16], like zolpidem.

Due to a high prevalence of polymedication in patients with depression and sleep disorders, the probability of DDIs is consistent and should be taken into account when drugs belonging to different therapeutic classes are equally needed in clinical practice [17]. In this view, the aim of this study was to investigate whether a pharmacokinetic interaction does occur between zolpidem and duloxetine and, if that is the case, to elucidate the mechanism of the kinetic interaction.

RESULTS AND DISCUSSION

Subject demographics

The study enrolled 23 healthy volunteers (7 women and 16 men) and was completed without any dropouts. The mean age of the subjects was 25.7±3.00 years old (range: 20-35) and they had a mean body mass index (BMI) of 24.00±3.00 kg/m^2 (range: 19-25).

Pharmacokinetic analysis

The mean plasma concentration-time profiles of both zolpidem and its main metabolite, before and after pretreatment with duloxetine are practically similar (**Figure 1**).

In addition, the pharmacokinetics of both analytes (zolpidem and Z4CA) were not influenced by the co-administration of duloxetine (**Table 1** and **Table 2**) as none of the pharmacokinetic parameters presented statistically significant differences between the study periods.

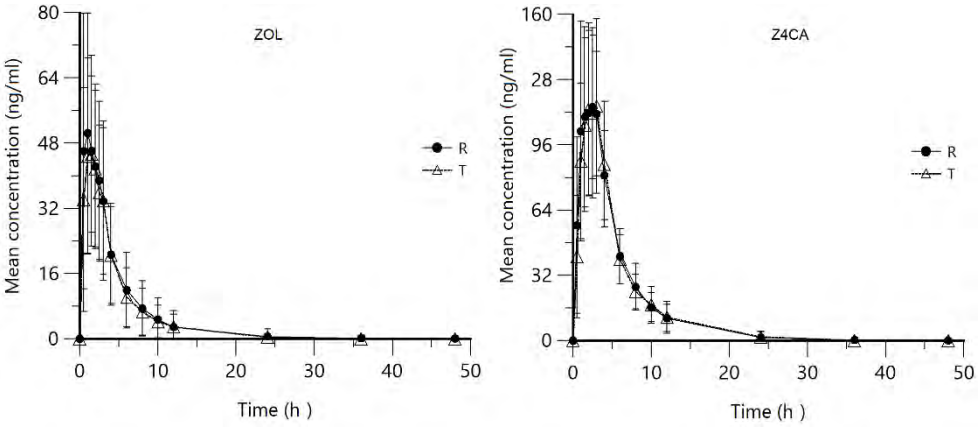

Figure 1. Mean plasma concentrations – time curves of **zolpidem** 5 mg p.o. (**left**) and **zolpidem's main metabolite** (Z4CA, **right**) during both study periods: Reference (**R**), zolpidem administered alone, Test (**T**) zolpidem co-administered with duloxetine, after pre-treatment with duloxetine for 4 days (30 mg/day for 2 days and 60 mg/day for other 2 days). Data are presented as mean ± SD (n=23).

Table 1. Pharmacokinetic (PK) parameters of zolpidem (ZOL) in 23 healthy volunteers after a single oral dose of 5 mg zolpidem, before and after treatment with duloxetine and the statistical evaluation of the differences between treatments (ANOVA test)

ZOL	**Study period**						
	Reference			**Test**			***p** value (ANOVA)**
PK parameter	**Mean**	**SD[a]**	**CV%[b]**	**Mean**	**SD[a]**	**CV%[b]**	
C_{max} (ng/mL)	59.64	27.64	46.35	53.28	22.77	42.73	0.16
t_{max} (h)	1.00	0.69	69.08	1.28	0.77	59.73	0.10
AUC_{0-t} (ng*h/mL)	239.45	158.26	66.09	217.21	135.95	62.59	0.25
$AUC_{0-\infty}$ (ng*h/mL)	245.87	161.84	65.82	224.61	138.86	61.83	0.26
K_{el} (h^{-1})	0.32	0.16	50.64	0.32	0.25	76.91	0.57
$t_{1/2}$ (h)	2.97	2.06	69.27	3.12	1.86	59.53	0.57
Cl_F (L/h)	32.03	30.37	94.81	31.97	20.16	63.06	0.26
Vd_F (L)	99.61	46.27	46.45	105.70	29.39	27.80	0.26

[a]SD – standard deviation; [b]CV% - coefficient of variation; *p** <0.05 statistically significant.

Table 2. Pharmacokinetic (PK) parameters of zolpidem's main metabolite (Z4CA) in 23 healthy volunteers after a single oral dose of 5 mg zolpidem, before and after treatment with duloxetine and the statistical evaluation of the differences between treatments (ANOVA test)

Z4CA	Study period						
	Reference			Test			*p** value (ANOVA)
PK parameter	Mean	SD[a]	CV%[b]	Mean	SD[a]	CV%[b]	
C_{max} (ng/mL)	129.17	45.54	35.26	130.91	41.61	31.79	0.61
t_{max} (h)	2.17	0.86	39.60	2.37	0.79	33.19	0.36
AUC_{0-t} (ng*h/mL)	684.04	170.76	24.96	680.33	209.66	30.82	0.65
$AUC_{0-\infty}$ (ng*h/mL)	717.95	167.09	23.27	712.49	214.92	30.16	0.59
K_{el} (h^{-1})	0.24	0.12	48.11	0.22	0.10	46.57	0.16
$t_{1/2}$ (h)	3.69	2.04	55.15	3.99	1.94	48.55	0.16
Cl_F (L/h)	7.48	2.51	33.52	7.83	3.00	38.28	0.59
Vd_F (L)	37.75	19.20	50.86	41.37	16.76	40.52	0.10

[a]SD – standard deviation; [b]CV% - coefficient of variation; *p** <0.05 statistically significant.

This lack of a pharmacokinetic interaction between zolpidem and duloxetine can be attributed to relatively different metabolic pathways. As mentioned before, only two minor correlations were found in the literature regarding their metabolic profiles: first, duloxetine is a moderate enzymatic inhibitor of CYP2D6 while the same isoenzyme has a minor contribution to the net intrinsic clearance of zolpidem and second, both drugs are metabolized, although not to the same extent, by CYP1A2 (duloxetine - extensively metabolized, zolpidem - 14%) [18,19,20]. In addition, duloxetine is highly plasma protein bound (>90%) and could displace zolpidem and increase the concentration of free drug [21,22]. Despite these potential causal factors, the present study results do not confirm the existence of an interaction between the two molecules. Other pharmacokinetic data supports the outcome of this study. Ruike *et al.* showed that duloxetine has the ability to inhibit the function of P-glycoprotein (P-gp) [23], but there is no evidence to suggest that zolpidem is a substrate of this transport system [24].

Unlike duloxetine, other antidepressants are capable of altering the pharmacokinetics of zolpidem. For example, experimental data demonstrated the existence of a pharmacokinetic interaction between fluvoxamine and the sedative-hypnotic drug [13,25]. These differences in the safety profile of

antidepressants might be useful to clinicians when choosing the most appropriate drugs in patients that require medications from both pharmacological classes. However, even though the pharmacokinetics of zolpidem was unaltered by the combination with duloxetine (at steady-state concentration), a potential pharmacodynamic impact cannot be excluded, especially when a multiple dosing regimen is employed for both substances. Controlled clinical trials reported not only insomnia, but also somnolence during treatment with duloxetine [21,26] and various reports have described patients experiencing hallucinations when taking zolpidem and antidepressants concomitantly [22].

Safety evaluation

No serious adverse events associated with the study medication were reported throughout the clinical trial. Moreover, none of the subjects discontinued the study due to safety concerns.

CONCLUSIONS

To our knowledge, this study is the first to investigate whether duloxetine can influence the pharmacokinetics of zolpidem and its main metabolite. Based on the present findings, the antidepressant did not change the exposure to zolpidem in healthy volunteers which suggests that this drug combination can be considered in clinical practice. However, a pharmacodynamic interaction cannot be excluded and requires further investigation.

EXPERIMENTAL SECTION

Subjects: 23 Caucasian healthy volunteers were enrolled in the present study. The subjects' selection was thoroughly made based on precise inclusion and exclusion criteria. The volunteers were considered eligible for the study based on their medical history, physical examination, vital signs, and clinical laboratory tests. Prospective volunteers were excluded if any clinical abnormalities were identified during the physical examination. All volunteers gave their written informed consent prior to any study procedure. The study was conducted according to the principles of Declaration of Helsinki (1964) and its amendments (Tokyo 1975, Venice 1983, Hong Kong 1989) and Good Clinical Practice (GCP) rules. The clinical protocol was reviewed and approved by the Ethics Committee of the University of Medicine and Pharmacy "Iuliu Hatieganu", Cluj-Napoca, Romania.

Study design: The study was designed as an open-label, single-center, non-randomized, sequential study that consisted of two periods. During the first study period (Reference, R), all volunteers were given a single dose of zolpidem 5 mg (p.o.). In the second period (Test, T), after a 4-day pretreatment regimen with duloxetine (a single daily dose of 30 mg for two days and 60 mg/day (30 mg/12 h) for another two days) in order to achieve steady-state plasma concentrations, the subjects received a combination of zolpidem 5 mg and duloxetine 30 mg. These doses represent a typical dosage regimen for clinical practice.

Study protocol/Drug administration: Each dose of the selected drugs was administered in the morning, after an overnight fast and with at least 150 mL of water.

The pharmaceutical products used were Stilnox® (10 mg film-coated tablets, Sanofi-Aventis, Romania) for zolpidem and Cymbalta® (30 mg hard gastro-resistant capsules, Lilly SA, Spain) for duloxetine, respectively.

Sample collection: On the first and last day of the study, venous blood (5 ml) was drawn into heparinized tubes, before zolpidem administration and after, at the following times: 0.5, 1, 1.5, 2, 2.5, 3, 4, 6, 8, 10, 12, 24, 36 and 48 hours. Blood samples were centrifuged at 5000 rpm for 10 min and the separated plasma was stored frozen (-20°C) until analysis.

Drug analysis from plasma samples: Zolpidem and Z4CA plasma concentrations were determined by using a validated high-throughput liquid chromatography (HPLC) tandem mass spectrometry analytical method. The HPLC system was an Agilent 1100 series (binary pump, autosampler, thermostat) (Agilent Technologies, USA), coupled with a Brucker Ion Trap SL (Brucker Daltonics GmbH, Germany). The chromatographic column used was a Zorbax SB-C18 (100 mm x 3.0 mm i.d., 3.5 µm) (Agilent Technologies). The same bioanalytical method was employed for quantification of zolpidem in other kinetic (PK) study and PK drug-drug interaction study [13,25,27].

Pharmacokinetic analysis: The standard non-compartmental method was employed to calculate the main PK parameters of zolpidem and its metabolite, Z4CA. The maximum plasma concentration (C_{max}, ng/mL) and the time to reach it (t_{max}, h) were directly obtained from the plasma concentration-time curves of each volunteer. The area under the concentration-time profile from time 0 to time of last quantifiable concentration (AUC_{0-t}, ng*h/mL) was calculated by applying the linear trapezoidal method. The total area under the curve ($AUC_{0-\infty}$, ng*h/mL) was obtained by adding C_t/K_{el} to AUC_{0-t}, where C_t (ng/mL) is the last quantifiable concentration of zolpidem and K_{el} (h^{-1}) is the

rate constant of elimination process estimated from the terminal region of the semi-logarithmic curve of plasma concentration-time corresponding to 1st order kinetics of elimination. The half-life time ($t_{1/2}$, h) was determined as $0.693/K_{el}$. All PK calculations were performed with Phoenix WinNonlin 6.1 (Certara, USA) software.

Statistical analysis: Analysis of variance (ANOVA) was used in order to compare the main PK parameters of zolpidem between study periods. All calculations were performed with Phoenix WinNonlin 6.1 (Certara, USA) software. Statistical significance was defined for $p<0.05$.

REFERENCES

1. S.E. Leucuta, L. Vlase, "Farmacocinetica si interactiunile medicamentoase farmacocinetice", Dacia Publishing, Cluj-Napoca, **2005**.
2. L. Lash, "Drug metabolism and transport", Humana Press, **2004**.
3. D. Rodrigues, "Drug-drug interactions", Dekker Inc., New York, **2001**.
4. H. Biswanger, "Enzyme kinetics: principles and methods", Wiley, **2002**.
5. T. Lynch, A. Price, *American Family Physician,* **2007**, *76*, 391.
6. K. Venkatakrishna, R.S. Obach, *Curr. Drug Metab*., **2011**, *12*(9), 871.
7. S.F. Zhou, C.C. Xue, X.Q. Yu, C. Li, G. Wang, *Ther. Drug Monit.,* **2007**, *29*(6), 687.
8. L.K. The, L. Bertlisson, *Drug Metab. Pharmacokinet*., **2012**, *27*(1), 55.
9. K. Thelen, J.B. Dressman, *J. Pharm. Pharmacol*., **2009**, *61*(5), 541.
10. R.L. Walsky, S.E. Boldt, *Curr*. *Drug Metabol*., **2008**, *9*(9), 928.
11. K.J Holm, K.L. Goa, *Drugs*, **2000**, *59*(4), 865.
12. H.T. Swainston, G.M. Keating, *CNS Drugs*, **2005**, *19*(1), 65.
13. A.M. Gheldiu, A. Popa, M. Neag, D. Muntean, C. Bocsan, A. Buzoianu, L. Vlase, M. Achim, I. Todor, C. Briciu, *Farmacia*, **2015**, *63(3)*, 453.
14. M.E. Hunziker, B.T. Suehs, T.L. Bettinger et al., *Clin. Ther.,* **2005**, *27*(8), 1126.
15. M.P. Knadler, E. Lobo, J. Chappell et al., *Clin. Pharmacokinet.,* **2011**, *50*(5), 281.
16. C. Briciu, M. Neag, D.M. Muntean, L. Vlase et al*., Exp. Clin. Cardiol.,* **2014**, *20*(1), 1374.
17. L. Staner, *Sleep Med. Rev.,* **2010**, *14*(1), 35.
18. S. Bleakley, *Prog. Neurolog. Psychiatry*, **2016**, *20*, 21.
19. R.J. Lantz, T.A. Gillespie, T.J. Rash, et al., *Drug Metab. Dispos.,* **2003**, *31*(9), 1142.
20. L.L. von Moltke, D.J. Greenblatt, B.W. Granda, et al., *British J. Clin. Pharmacol.,* **1999**, *48*(1), 89.

21. D.S. Patel, S.S. Deshpande, C.G. Patel, S. Singh, *Indo Glob. J. Pharm. Sci.*, **2011**, *1*(1), 63.
22. T. Inagaki, T. Miyaoka, S. Tsuji, Y. Inami, A. Nishida, J. Horiguchi, *Prim. Care Companion J. Clin. Psychiatry*, **2010**, *12*(6), e1.
23. Z. Ruike, C. Junhua, P. Wenxing, *Hum. Psychopharmacol.*, **2010**, *25*(7-8), 553.
24. J.O. Olubodun, H.R. Ochs, L.L. von Moltke, et al., *British J. Clin. Pharmacol.,* **2003**, *56*(3), 297.
25. L. Vlase, A. Popa, M. Neag, D. Muntean, M. Achim, S.E. Leucuta, *Clin. Exp. Pharmacol. P.*, **2012**, *39*(1), 9.
26. R. Gonçalves, S.M. Guimarães Togeiro, *Sleep Science*, **2013**, *6*(1), 36.
27. A.-M. Gheldiu, A. Csavdari, M. Achim, L. Vlase, I Tomuta, D.M. Muntean, *Studia UBB Chemia,* **2017**, LXII, *2*, Tom II, 179.

STUDIA UBB CHEMIA, LXIV, 3, 2019 (p. 163-180)
(RECOMMENDED CITATION)
DOI:10.24193/subbchem.2019.3.14

HPLC-DAD-ESI$^+$-MS PHYTOCHEMICAL PROFILES OF SEVERAL *ROSMARINUS OFFICINALIS* ACCESSIONS FROM SPAIN AS INFLUENCED BY DIFFERENT ENVIRONMENTAL STRESS CONDITIONS

MONICA BOSCAIU[a], OSCAR VICENTE[b,e], INMACULADA BAUTISTA[c], FLORICUTA RANGA[d], CARMEN SOCACIU[d,*]

ABSTRACT. Rosemary, a native Mediterranean plant is a well-known source of phytochemicals with antioxidant activity attributed mainly to diterpenoids and flavonoids. The aim of the study was to establish an accurate evaluation of the rosemary metabolite profiles from several accessions under changing environmental conditions (water stress and soil salinity) comparing two sampling seasons (summer vs. spring) from four different habitats in Eastern Spain. The methodology was based on the identification and the quantitative evaluation of phytochemicals (phenolic acid derivatives, flavonoids, diterpenes and triterpenes) by HPLC coupled with diode-array detection and electrospray ionization mass spectrometry (ESI$^+$-MS). Phytochemical profiles were statistically compared by factorial ANOVA, cluster analysis, principal component analysis and univariate analysis (Pearson correlations), that allowed the discrimination between the extract composition in correlation to their habitat and stress conditions. Out of twenty-three compounds identified, the major ones were represented by diterpenoids (carnosic acid, carnosol and oxidized metabolites rosmanol, epirosmanol, rosmadial, rosmanol methyl ether) and flavonoids, which showed significant metabolic regulation induced by water stress. The main conclusion of the work is that the diterpene derivatives and their oxidized metabolites may be considered as optimal biomarkers of the environmental stress in *Rosmarinus officinalis*.

Keywords: *Rosmarinus officinalis; environmental stress; high performance liquid chromatography & mass spectrometry; metabolomic profile*

[a] *Universitat Politècnica de València, Instituto de Biología Molecular y Celular de Plantas (UPV-CSIC), Camino de Vera s/n, 46022 Valencia, Spain*
[b] *Universitat Politècnica de València, Instituto Agroforestal Mediterráneo, Camino de Vera s/n, 46022 Valencia, Spain*
[c] *Universitat Politècnica de València, ReForest, Instituto Ingeniería del Agua y Medio Ambiente, Camino de Vera s/n, 46022 Valencia, Spain*
[d] *University of Agricultural Sciences and Veterinary Medicine. 3-5 Manastur Street. 400372 Cluj-Napoca. Romania*
[e] *Universitat Politècnicva de València, Instituto de Conservación y Mejora de la Agrodiversidad Valenciana (COMAV), Camino de Vera s/n, 46022 Valencia, Spain*
** Corresponding author: carmen.socaciu@usamvcluj.ro*

Abbreviation list

DAD - Diode Array Detection
GC- Gas-chromatgraphy
LC- Liquid Chromatography
HPLC - High Performance Liquid Chromatography
ESI^+-MS - Electrospray ionization mass spectrometry
CA - cluster analysis
PCA - principal component analysis
MS – Mass spectrometry
ROS – Reactive Oxygen Species
AsA-GSH – Ascorbate- glutathion

INTRODUCTION

Rosemary (*Rosmarinus officinalis* L., Lamiaceae family) is a woody herb that grows wild in the Mediterranean region, but is also largely cultivated in many areas worldwide as a tasty culinary spice. It has also well-known medicinal uses, such as antimicrobial [1-3] or neuroprotective [4, 5]. Rosemary's high medicinal interest is mainly due to its antioxidant potential brought by its high contents in terpenoids and phenolic derivatives [6-9]. Numerous scientific studies were performed on the chemical composition of rosemary. Advanced techniques, such as high performance liquid chromatography (HPLC) or gas chromatography (GC) coupled with diode array (DAD) or mass spectrometry (MS) detection, are currently used to separate and identify bioactive metabolites in rosemary extracts [10-12]. The major compounds were represented by phenolic diterpenoids (e.g. carnosic acid and carnosol, rosmanol), flavonoids (rosmarinic acid and luteolin derivatives, genkwanin or homoplantaginin) or pentacyclic triterpenoids (oleanolic, betulinic and ursolic acids) [13-16] besides monoterpenes (cineole, camphor and α-pinene). Ultrasound or microwave-assisted procedures have improved the extraction efficiency of rosemary components [15, 17,18]. An HPLC/DAD/MS study [19] showed that drying temperature, storage conditions and extraction procedures can affect the chemical composition of leaf extracts, especially the high antioxidant derivatives e.g. rosmarinic acid and carnosic acid [20, 21].

The phytochemical profile of rosemary was related to its phenological stage [22], geographic location [18, 23], seasonal variation [7] and abiotic stresses, such as drought [24], salinity [25] or photoxidation [26]. Under stressful conditions, including irrigation with effluents that contain high levels of salts and heavy metals, rosemary accumulates reactive oxygen species, which leads to the activation of antioxidant defence mechanisms [13]. Using accessions of rosemary, grown in different field trials and sites in Greece, it was shown that the phenolic chemical profile and the antioxidant behaviour of carnosic acid were affected by stress [27].

Environmental stress has a strong influence on the biosynthesis of bioactive compounds, by generation in excess of ROS, a group of free radicals, reactive molecules and ions derived from oxygen. ROS are normal by-products of cellular metabolisms but under conditions of abiotic and biotic stress the balance between their formation and scavenging is lost, and levels of ROS increase. As they are highly reactive and toxic, when in excess, they produce oxidative stress, affecting cells´ physiology and eventually leading to cellular death. To mitigate oxidative stress, organisms activate their enzymatic and chemic or non-enzymatic defence mechanisms. In plants, the first category is represented by several enzymes, mainly by those involved in the ascorbate–glutathione cycle (AsA-GSH) in chloroplasts, cytosol, mitochondria, apoplast, and peroxisomes. Non-enzymatic antioxidants, include diverse chemical compounds, such as ascorbic acid and E vitamin, carotenoids, reduced glutathione or phenolic compounds, especially the subclass of flavonoids [28]. The antioxidant enzymes represent 'the first line of defence against ROS', but under severe stress their activity may be insufficient for maintaining the ROS homeostasis. At this stage, the biosynthesis of secondary ROS scavenging systems (non-enzymatic compounds) is triggered [29]. As such, plants naturally growing in harsh environmental situations, should have efficient mechanisms to reduce the oxidative damage associated with situations of drought, increased salinity or other types of environmental stress. The role of phenolic compounds in plants is well-known [30, 31]. Out of the wide array of their biological functions, phenolics and especially flavonoids, participate in plant responses to practically all types of abiotic stress: UV radiation, intense light, extreme temperatures, mineral nutrient imbalance, anoxia, ozone exposure, drought, salinity, heavy metals and herbicides [30, 31-35].

In this study, we have analysed samples of rosemary collected in the wild, from different types of environments in South East of Spain. All habitats selected suffer the rigor of Mediterranean climate characterized by dry summers; the combination of drought, high temperatures, risk of salinity and high solar radiation induces a multiple stress, and plants tend to reduce their vegetative activity during this time. There are several well-known strategies developed by Mediterranean plants to with stand the restrictions of the summer stress, such as the syndrome of *Sclerophyllous* leaves or reduction of vegetative activity by the loss of leaves in summer. On the other hand, apart from these anatomic and physiologic adaptations, biochemical responses are triggered, such as osmotic adjustment or activation of antioxidant systems, both chemic and enzymatic, as response to the oxidative stress generated by the activation of ROS, with direct deleterious effects by oxidation of proteins, membrane lipids and nucleic acids. Previously, the content of total phenolics and flavonoids has been determined by spectrophotometric methods in different

plant species, including *R. officinalis*, from these Mediterranean habitats, and a significantly positive correlation between the level of these compounds and soil water deficit was established [36].

The present study aimed to establish phytochemical profiles of four *Rosmarinus officinalis* accessions, as influenced by different environmental growth conditions (two sampling seasons: in spring under favourable climatic conditions vs summer dry conditions**)** in Spain. The hypothesis of work is that the concentrations of main antioxidants will be correlated with environmental parameters, especially those related to the water deficit. The rosemary extracts were analysed by a combined, simultaneous HPLC-DAD and LC-ESI$^+$-MS procedure, in order to evaluate the phytochemicals' fingerprinting and the quantitative analysis of main compounds, followed by statistical analysis. The impact of the environmental stress was established by focusing on the variations of phenolic compounds and terpenoids.

RESULTS AND DISCUSSION

Phytochemicals profile and identification by LC-ESI$^+$-MS

Fig. 1 shows the general fingerprint of thirty-six superposed LC-ESI$^+$-MS chromatograms (peak area *versus* retention time) of rosemary extracts from the sampling groups. Based on their retention times, m/z values and main fragments twenty-three compounds were separated and tentatively assigned.

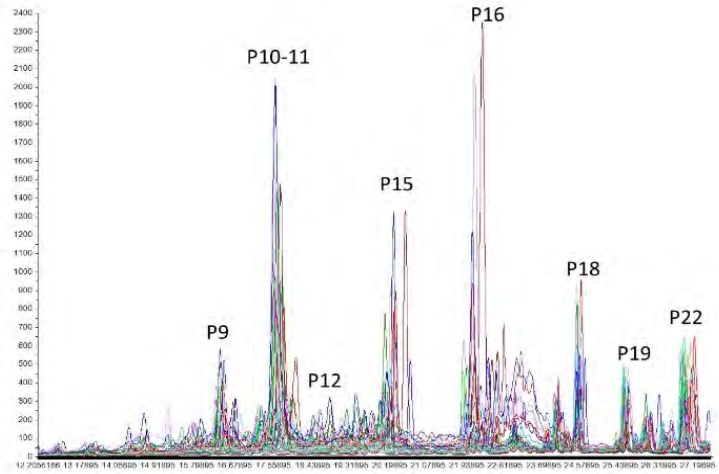

Figure 1. A general view of thirty six superposed LC-ESI$^+$-MS chromatograms (peak area *versus* retention time) obtained from eight sampling groups. The major compounds were marked as P9, P10-11, P12, P15, P16, P18, P19 and P22.

Table 1 includes the retention times (t_R), the specific *m/z* $[M+H]^+$ values, the main fragments derived from the MS analysis, and tentative identification, as compared with the literature data and data bases (Phenol Explorer, KEGG). Three categories of phytochemicals were identified: (1) diterpenoid ethers and other conjugates, (2) phenolic acid derivatives, and (3) flavonoids (luteolin derivatives).

Table 1. LC-ESI$^+$-MS data provided for rosemary extracts: retention time t_R (min)), m/z values used for ESI (+)MS identification, the main fragments and the identified compounds, in agreement with international data bases.

Name	t_R (min)	m/z $[M+H]^+$	Main MS Fragments	Tentative identification
P1	2.91	199.0510	181; 137	Syringic acid
P2	3.90	193.0553	129; 95	p-Coumaric acid ethyl ester
P3	12.02	465.0884	303; 287	Quercetin 3-*O*-glucoside
P4	12.64	523.1320	361; 325	Rosmarinic acid 3-*O*-glucoside
P5	13.49	479.1130	464; 317;302	Nepetrin (6-methoxy-luteolin 7-*O*-glucoside)
P6	14.29	611.1535	303	Hesperidin (Luteolin 7,3'-diglucoside)
P7	14.65	463.1089	285; 163	Homoplantaginin
P8	15.96	463.0798	287	Luteolin3'-glucuronide
P9	16.40	361.0772	199;181;163;137	Rosmarinic acid
P10	17.33	505.0905	401; 287	Luteolin 3'-(3''-acetylglucuronide) Isomer I
P11	17.74	505.0905	445; 287	Luteolin 3'-(4''-acetylglucuronide) Isomer II
P12	18.58	347.1707	303; 285	Rosmanol
P13	19.36	347.1707	285	Epirosmanol (isomer 1)
P14	19.73	285.0611	270	Genkwanin
P15	20.24	331.1863	287	Carnosol
P16	22.06	303.0427	229; 153	Quercetin
P17	24.03	317.1965	287	Rosmaridiphenol
P18	24.54	345.1707	317; 301; 285	Rosmadial
P19	25.66	473.1869	457	Benthamic acid
P20	26.15	361.1966	333; 287	Rosmanol methyl ether
P21	26.63	347.1863	333; 287	12-Methoxy carnosic acid
P22	27.12	333.1864	287	Carnosic acid
P23	27.59	455.1867	-	Micromeric acid

Nine compounds were selected as being major, based on the chromatogram peak intensity higher than 200 and signal/noise ratio of minimum 3 (Fig. 1). These compounds were tentatively identified as follows, P9 (rosmarinic acid), P10 and P11 (two isomers of luteolin acetyl glucuronide), P12 (rosmanol), P15 (carnosol), P16 (quercetin), P18 (rosmadial), P19 (benthamic acid) and P22 (carnosic acid) (Table 1). Fig. 2 shows the chemical structures of the main compounds.

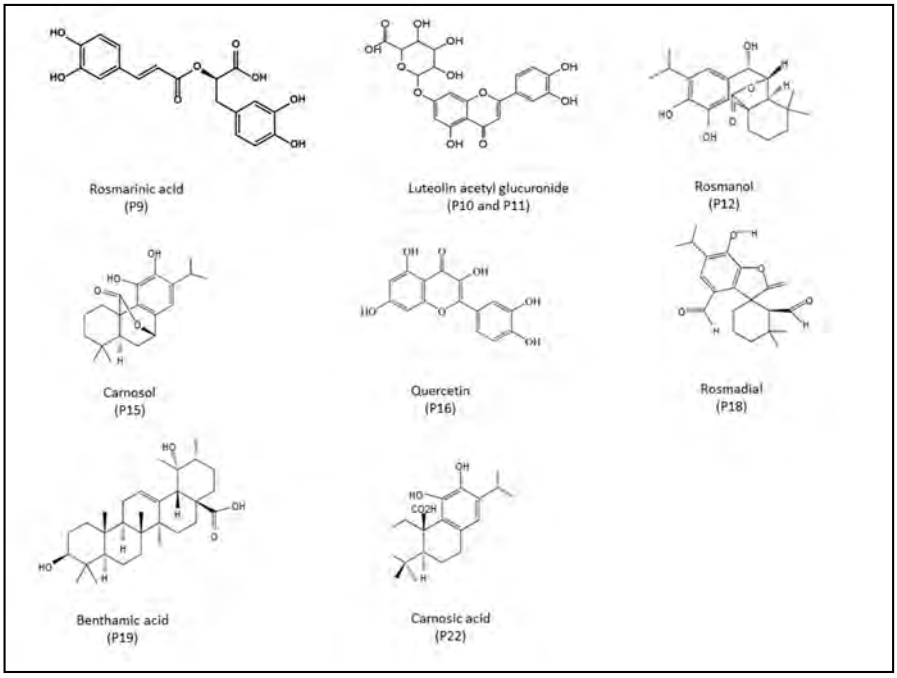

Figure 2. Chemical structure of the major compounds identified in the rosemary samples.

The first major class of compounds from diterpene family were carnosic acid (P22, m/z=333.1864), carnosol (P15, m/z=331.1863), methylcarnosate (P21, m/z=347.1863). Rosmanol (P12, *m/z* 347.1707) and its isomer epirosmanol (P13, *m/z*=347.1707) were formed by oxidative degradation of carnosic acid. Rosmaridiphenol (P17, *m/z* 317.1965, with a fragment of 287), rosmadial (P18, *m/z* 345.1707) and rosmanol methylether (P20, *m/z* 361.1965) were also identified. All these compounds have been previously reported also by other authors [37]. In addition, some minor triterpenes, namely benthamic (P19, *m/z* 473.1869) and micromeric acid (P23, *m/z* 455.1867) were also detected.

The phenolic acid derivatives were represented by rosmarinic acid (P9, *m*/*z* 361.0772), a caffeic acid ester of salvianic acid A and rosmarinic acid 3-*O*-glucoside (P4, *m*/*z* 523.1320S). Syringic acid (P1) and p-coumaric ethyl ester (P2), were also identified, but only as minor components.

Flavonoids such as glucuronic acid derivatives of luteolin, represented by luteolin 3'*O*-(3"*O*-acetyl) β-D-glucuronide (P10-isomer I-, *m/z* 505.0905) and luteolin 3'*O*-(4"*O*-acetyl) β-D-glucuronide (P11-isomer II, *m/z* 505.0905) were also identified. The MS analysis revealed their specific fragmentation and discrimination by fragments of *m*/*z* 410 and 445, respectively. Other minor luteolin derivatives were identified, e.g. nepetrin (P5, *m/z* 479.1130), hesperidin (P6, *m/z* 611.1535), homoplantagin (P7, *m/z* 463.0798), luteolin 3'-glucuronide (P8, *m/z* 463.0798) and genkwanin (P14, *m/z* 285.0611). Flavonols were also identified, including quercetin (P16, *m/z* 303.0427) and quercetin 3-*O*-glucoside (P3, *m/z* 465.0884), in agreement with other reported data [14, 17].

The major fragment, with *m*/*z* = 287, corresponded to glucuronic acid loss, as indicated by previous data found in the literature and databases. For nepetrin (P5) and quercetin 3-*O*-glucoside (P3), the fragment ions with *m*/*z* 317 and 302 were assigned to fragments arising from glucose loss. Similarly, hesperidin (P6) presented a major fragment ion at *m*/*z* 302 due to rutinoside loss.

Quantitative analysis by HPLC-DAD

Based on the preliminary profile evaluations, the flavonoid derivatives (P10, P11 and P16) were the major components of extracts, therefore, we used rutin as a representative flavonoid for the calibration curve. The mean concentrations of all 23 compounds were calculated from the calibration curve equation and expressed as micrograms rutin equivalent/g dry leaf.

Table 2 presents the mean values and standard deviations (x ± SD) of the 23 compounds, as determined by HPLC-DAD, after calibration with rutin. A large variability was observed between these compositions, inside an accession group but especially between the different accession groups, as can be seen for luteolin glucuronide isomers (P10 and P11), rosmarinic acid (P9), carnosic acid derivatives (P15 and P22), rosmanol (P12) and rosmadial (P18), quercetin (P16), and benthamic acid (P19).

Although some of the compounds show significant differences between areas; P7 homoplantagin and P23 micromeric acid, the greatest differences can be found in samples from different seasons. The phenolic acids rosmarinic (P9) and it derivate P4 rosmarinic acid 3-*O*-glucoside increase significantly in summer. Most of the flavonoids also increase significantly in summer time: P5 Nepetrin (6-methoxy-luteolin 7-*O*-glucoside), P6 Hesperidin (Luteolin 7,3'-diglucoside), P8 Luteolin3'-glucuronide, P10 and P11 Isomers I and II of Luteolin 3'-(3"-acetylglucuronide), P14 Genkwanin and P16 Quercetin.

Table 2- Mean values ±standard deviation of the quantified phytochemicals (P1 to P23) in the different areas (A) and sampling date (B- summer and spring). Significant differences by multiple comparison (Two way anova) at P < 0.05 : *, **. ***, significant at P<0.05, 0.01 and 0.001 respectively.

	Gypsum top		Gypsum bottom		Semiarid		Dune		A.	B.
Plot/ season	Spring	Summer	Spring	Summer	Spring	Summer	Spring	Summer		
P1	100 ±12	95 ±60	61 ±76	161 ±35	49 ±42	89 ±49	104 ±48	108 ±60	NS	NS
P2	117 ±54	152 ±18	115 ±66	143 ±20	139 ±21	107 ±64	131 ±19	120 ±69	NS	NS
P3	66 ±53	274 ±115	301 ±69	201 ±59	65 ±32	147 ±93	173 ±65	298 ±65	NS	NS
P4	83 ±42	303 ±243	119 ±83	298 ±95	77 ±72	304 ±56	178 ±99	219 ±96	NS	**
P5	77 ±36	329 ±185	105 ±55	334 ±92	101 ±43	286 ±58	237 ±92	286 ±94	NS	***
P6	84 ±40	378 ±373	70 ±21	432 ±98	79 ±54	168 ±54	328 ±99	388 ±89	NS	**
P7	62 ±12	275 ±171	450 ±97	478 ±78	149 ±86	562 ±67	608 ±98	873 ±97	*	NS
P8	164 ±87	723 ±306	731 ±76	948 ±87	417 ±78	749 ±65	549 ±76	672 ±65	NS	*
P9	165 ±54	1561 ±564	688 ±76	1391 ±372	516 ±68	1522 ±95	1565 ±78	1551 ±87	NS	***
P10	464 ±24	1118 ±521	807 ±369	1159 ±339	716 ±95	1240 ±543	996 ±294	1759 ±150	NS	*
P11	331 ±20	4730 ±337	1865 ±142	4145 ±165	831 ±90	4870 ±297	3681 ±255	4695 ±514	NS	**
P12	399 ±85	1418 ±102	1048 ±785	849 ±691	725 ±96	1844 ±120	1141 ±139	349 ±219	NS	NS
P13	146 ±15	693 ±485	455 ±203	890 ±419	496 ±25	1040 ±341	875 ±350	1336 ±695	*	**
P14	182 ±17	936 ±495	374 ±191	1122 ±335	361 ±22	911 ±481	912 ±488	1330 ±599	NS	***
P15	989 ±90	2483 ±180	982 ±44	1971 ±805	988 ±92	2104 ±974	2424 ±111	2645 ±157	NS	NS
P16	258 ±98	3399 ±392	322 ±144	2178 ±722	728 ±82	3924 ±401	2171 ±157	1839 ±226	NS	*
P17	507 ±64	747 ±319	539 ±72	773 ±323	639 ±73	765 ±122	482 ±192	515 ±276	NS	NS
P18	956 ±82	2094 ±606	496 ±140	1475 ±327	890 ±20	2062 ±237	579 ±243	1573 ±521	*	**
P19	998 ±92	727 ±311	1121 ±213	1042 ±321	985 ±91	1259 ±147	1072 ±371	785 ±76	NS	NS
P20	747 ±87	800 ±332	743 ±96	768 ±93	834 ±94	883 ±287	527 ±76	798 ±87	NS	NS
P21	821 ±95	492 ±301	584 ±83	800 ±95	73 7±94	718 ±115	449 ±86	667 ±89	NS	NS
P22	2296 ±427	2089 ±955	2854 ±343	1703 ±446	999 ±93	1551 ±464	1949 ±856	1799 ±345	NS	*
P23	425 ±23	394 ±177	437 ±89	566 ±83	512 ±90	635 ±236	397 ±32	410 ±20	*	NS

The water stress (summer drought) induced a significant increase of diterpenoids rosmadial (P18) in all plots, whereas carnosic acid (P22) had higher content in spring. Differences in compounds are more significant in the two plots subjected to greater water stress, that are one from the gypsum area, on top of the hill and the semiarid area.

In the dune area, these differences were not as significant. This pattern can be explained by a constant environmental stress in this habitat, independent on the season: similar salinity and low water retention of the sandy substrate.

When comparing the two plots in the gypsum area, the mean concentrations of these compounds are related to water stress. In spring, due to humidity and rains, the site at the bottom of the hill became more stressful for plants because the gypsum soil concentration (salt stress) was higher than at the top. Generally, non-significant effects of altitude were detected in summer time.

The concentrations of minor components ranged between 90 and 130 micrograms rutin eq./g dry leaf. Such components were represented by rosmarinic acid derivatives (P13, P17, P20), micromeric acid (P23), methoxycarnosate (P21) luteolin derivatives (P8, P14), glycosylated flavonoid derivatives (P3-P7) and phenolic acids (P1 and P2).

Comparing the concentrations of different phytochemical classes, the most significant differences were observed for flavonoids and rosmarinic acid derivatives, positively correlated with water stress.

Significant increases were noticed in summer compared with spring for flavonoid glycosides (P4-P6, P13, P17) in the gypsum zone and in the semiarid area but no differences were observed for triterpenes and diterpenes. The levels of the some compounds increased in summer in the dune sand, especially epirosmanol (P13) and genkwanin (P14). These data suggest that specific synthesis of flavonoids and terpenes, as well their oxidation is up-regulated by the environmental stress, in agreement with other data [38]. The most significant effects on rosemary metabolites from different accession groups studied here were mainly related to water stress (summer *vs* spring) and, to a lesser extent, to salt stress (sea *vs* gypsum).

The potent antioxidant properties of *R. officinalis* extract is attributed to its diterpene, carnosic acid, that under drought conditions scavenges free radical within the cloroplast giving highly oxidized diterpenes such as carnosol, rosmanol and isorosmanol [7, 13]. The antioxidant protection mechanism by carnosic acid is especially relevant in rosemary [13, 26]. In this context, our data reflected similar findings: not only an up-regulation of flavonoid synthesis is induced by water stress, but also a post-synthesis oxidation of carnosic acid to its metabolites (carnosol, methoxy carnosate).

Statistical correlations and significance of phytochemicals' modifications induced by environmental stress

The Cluster analysis (CA) allowed the identification of the similarities and discriminations between the different accession groups of rosemary. The Euclidian distance among the accession groups shows good discriminations between the profiles of samples A1, B1, C1, D1 collected in summer (water stress - dry season) and samples D2, B2, A2, B2 collected in spring (humid season).

Table 3. Pearson correlation factors (R) and their significance (S), considering the differences between the mean values (x ± SD) of phytochemicals' total concentrations found in accession groups. The significant correlations are bolded.

		A1	B1	A2	B2	C1	C2	D1	D2
A1	R	1	**0.9663**	0.2890	0.5726	**0.97551**	0.5568	**0.9043**	**0.9326**
	S	--	7.2E-14	0.1809	0.0043	2.6E-15	0.0057	3.2E-09	9.2E-11
B1	R	**0.9663**	1	0.2996	0.6264	**0.94429**	0.56064	**0.96137**	**0.9493**
	S	7.2E-14	--	0.1648	0.0013	1.3E-11	0.0053	3.0E-13	4.9E-12
A2	R	0.2890	0.2996	1	0.7804	0.2134	0.8909	0.2629	0.3310
	S	0.1809	0.1648	--	1.1E-05	0.3281	1.2E-08	0.2255	0.1228
B2	R	0.5726	0.6264	0.7804	1	0.5029	0.8016	0.5918	0.6777
	S	0.0043	0.0013	1.1E-05	--	0.0144	4.2E-06	0.0029	3.8E-04
C1	R	**0.9755**	**0.9442**	0.2134	0.5029	1	0.4902	0.8618	**0.9049**
	S	2.6E-15	1.E-11	0.3281	0.0144	--	0.0175	1.2E-07	3.0E-09
C2	R	0.5568	0.5606	0.8909	0.8016	0.4902	1	0.5376	0.6282
	S	0.0057	0.0059	1.2E-08	4.2E-06	0.0177	--	0.0081	0.0013
D1	R	**0.9043**	**0.9613**	0.2629	0.5918	0.8618	0.5376	1	**0.9243**
	S	3.2E-09	3.0E-13	0.2255	0.00293	1.2E-07	0.0081	--	2.8E-10
D2	R	**0.9326**	**0.9493**	0.33101	0.67773	**0.90496**	0.62812	**0.9247**	1
	S	9.2E-11	4.9E-12	0.1228	3.8E-04	3.0E-09	0.0013	2.8E-10	--

The metabolites responsible for statistical discrimination were P11 (luteolin 3'*O*-(4"*O*-acetyl) β-D-glucuronide), P22 (carnosic acid), P15 (carnosol), P16 (quercetin), P9 (rosmarinic acid), and P19 (benthamic acid).

Table 3 presents the Pearson correlation factors (R) and their statistical significance (S), considering the mean total concentrations of all twenty-three phytochemical found in rosemary accession groups. Significant correlations (R > 0.90) were noticed among "summer" accession groups A1-B1-C1-D1 but no significant correlations inside "spring" groups A2, B2 and C2. No correlations between the profiles of phytochemicals in spring season versus summer season in gypsum and semi-arid areas (e.g. A1 vs A2, B1 vs B2, C1 vsC2) were noticed, excepting the saline dune with significant positive correlations (D1 *vs* D2).

Metabolic relevance of phytochemicals' profile and their stress-regulated pathways

According to the qualitative and quantitative data, the specific biosynthetic pathways for phenolics and terpenoids in rosemary were affected by the environmental stress factors (water stress/salinity/altitude).

Mainly the water stress (soil aridity) during the dry summer season and the salt stress, to a lesser extent, were key factors that up-regulated the synthesis of phenolics, especially the flavonoids pathways and their glycosylation, for the protection of cell membranes against dryness. Water stress was signalised as the factor inducing significant changes in the metabolites profiles in this species [13] and salinity increased total amount of antioxidants in rosemary plants grown under increasing concentratiosn of NaCl [39].

The diterpene synthesis was also affected, especially by the oxidative degradation of carnosic acid to rosmanol and its derivatives, induced and amplified by dryness and salinity, in agreement with previous published data on rosemary [7, 13]. Antioxidant properties of carnosic acid in *in vitro* sytems were used in food technology and medicine [40]. It has been recently establishing that oxidation of carnosic acid is an efficient ROS scavenger mechanism and fulfils an important antixodant role in this species in *planta* [26]. The oxidized metabolites of carnosic acid, such as carnosol, acid carnosol, rosmanol, and epirosmanol are also strong antioxidants. As such, carnosic acid oxidation is a "cascade-type process", generating different secondary antioxidants, and constitutes a very efficient anti-oxidant mechanism in labiates. To confirm the impact of environmental stress on phenolics and diterpene metabolism, a principal component analysis (PCA) was carried out (Fig. 3).

The PCA biplot shows the relationships and variance between the environmental factors (altitude, rainfall, temperature and soil humidity) and the concentrations of the nine major compounds presented in Table 2. The three main components with eigenvalues equal to or higher than 1 explain a significant cumulative variance of 86.46%. The first component, that explain 64.77 % of the variance is positively correlated with water availability (rainfall and soil humidity). The second component which explain an additional 15.50% is related to altitude. These findings are in agreement with previous observations [36] where positive correlations were found between total phenolics and flavonoids and water stress. It is therefore strongly supported the idea that the phenolics' synthesis is intensified by water stress and may contribute to the drought tolerance in *R. officinalis*, as it has been reported in many other plant species [41].

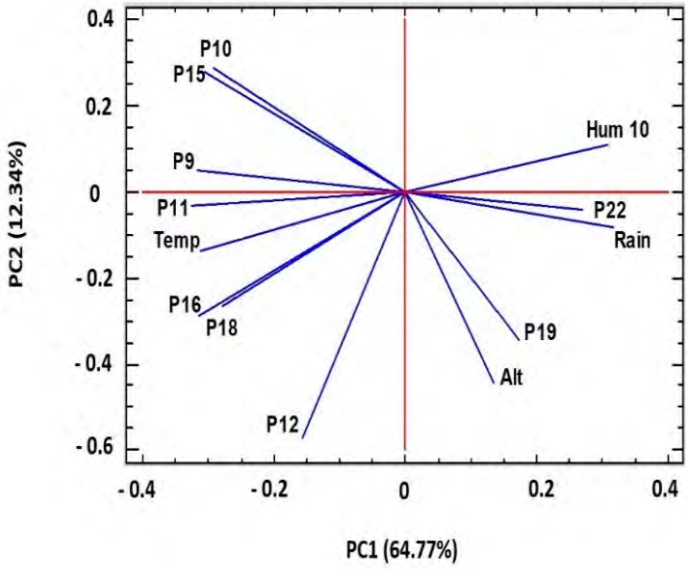

Figure 3. Biplot by the principal component analysis showing the relationships and variance between the environmental factors (altitude, rainfall, temperature and soil humidity) and the concentrations of the nine major compounds identified expressed as micrograms rutin/g dry leaf. For compound identification and quantification see Table 1.

CONCLUSIONS

Using an advanced methodology, HPLC-DAD-ESI+-MS, the phytochemical profiles of several *Rosmarinus officinalis* accessions from four different habitats in Spain, at two seasons (summer vs. spring), as influenced by different environmental stress (water stress and soil salinity), were established.

There were separated and quantified 23 molecules, nine being major: rosmarinic acid, two isomers of luteolin acetyl glucuronide, rosmanol, carnosol, quercetin, rosmadial, benthamic acid, carnosic acid. According to the qualitative and quantitative data, the specific biosynthetic pathways for these phenolics and terpenoids were affected by the environmental stress factors (water stress/salinity/altitude).

The diterpene derivatives and their oxidized metabolites were more sensitive than flavonoids to environmental stress and can be considered good biomarkers of water stress in wild *R. officinalis* grown in areas affected by the Mediterranean climate. By Cluster Analysis and Principal Component Analysis, the differences between the accession groups were determined,

being dependent on the environmental conditions. These data underline the key role of carnosic acid and its up-regulated biosynthesis by water and its degradation to oxidized derivatives, as an adaptation to water stress.

EXPERIMENTAL SECTION

Environmental conditions and sample harvesting

Rosemary leaves were harvested from different areas in the province of Valencia (Spain) growing in distinct environmental growth conditions: a plot in a sea sand dune; a plot in a semiarid area on limestone substrate at 200 m altitude, and two plots on a hill in a gypsum area at an altitude of about 700 m. To assess the climatic conditions from each area, data on mean temperatures from the previous month and accumulated rainfall were collected on a daily basis from the nearest agroclimatological stations, located in Benifaió (less than 6 km from the dune zone), Bétera (10 km from the semiarid zone) and Chulilla (18 km from the gypsum area). Soil water content was monitored through several sensors for soil moisture installed to 10 cm depth, connected to data loggers. For a more extensive description of the soil and climatic characteristics of the experimental zones, see [36].

The dune area is a stressful environment given its proximity to the sea, but plants were also affected by a constant water stress due to the low water retention by sand and the moderately saline shallow water table. In the semiarid zone, the plants were grown on a thin soil over a stony bedrock, the main stress factor being the water deficit in the dry season. In the gypsum area, it was a combination of salt and water stress (since gypsum soils are found always under arid climatic conditions). In this area, different environmental conditions were found at the top (with low gypsum, drier soil) and bottom areas of a hill (more gypsum, more humid, even during the summer season). In order to investigate the effect of different levels of water stress, the samples were collected from the same plants, during two seasons: summer, after a month without rainfall, and spring, after a rainy period.

Young shoots of flowering rosemary plants were sampled separately from five individuals from each locality, cooled on ice and transported to the laboratory, where leaves were separated from branches and dried in an oven at 45ºC for 72 h until constant weight. The harvested rosemary samples are indicated in Table 4.

Table 4. The rosemary accessions coding according to habitat and sampling season. Temperature values and accumulated rainfall were recorded by the nearest agro-climatological stations and correspond to the month before sampling date. Soil humidity was measured by electronic sensors installed at 10 cm depth.

Habitat	Code (m)	Sampling date	Number of samples	Mean T (ºC)	Cumulated rainfall (mm)	Soil humidity cm^3/cm^3
Gypsum Top 710 m	A1	Summer (I)	5	24.8	7	0.111
	A2	Spring (II)	5	12.0	113	0.194
Gypsum Bottom 690 m	B1	Summer (I)	4	24.8	7	0.139
	B2	Spring (II)	4	12.0	113	0.258
Semiarid 220 m	C1	Summer(I)	4	25.9	3	0.008
	C2	Spring (II)	5	14.1	35	0.242
Sand sea dune	D1	Summer (I)	4	21,0	1	0.073
	D2	Spring (II	5	13.5	50	0.138

Extraction protocols

Aliquots of rosemary dried leaves (2 g) were mixed with aq. methanol 95% (20 ml) containing 1% HCl (aq.), stirred and kept in an ultrasonic bath (XUB5 model, at operating frequency of 32 KHz and power supply of 100 W), for 24 h at 25°C. After centrifugation (2000 rpm), the supernatant was filtered through a 0.25-µm nylon filter. All the extractions were done in duplicate for each sample.

UV-VIS spectrometry

As a preliminary evaluation of extracts, the UV absorption profiles were determined by recording the spectra from 200 to 400 nm (using a UV/Vis Lambda 25 Perkin Elmer spectrophotometer), looking to the peaks at 280 and 340 nm, as markers of the phenolic acid and flavonoids, respectively.

HPLC-DAD and LC-ESI^+-MS analysis

A simultaneous evaluation (qualitative and quantitative) of phytochemicals was done using an Agilent 1200 HPLC Series system (Agilent Technologies, Santa Clara, CA. USA). The extract components were separated in a Zorbax Eclipse XDBC18 column (4.6 x 150 mm; 5 µm particle), at 25°C. The mobile phase consisted of a mixture of water:acetonitrile:acetic acid (99:0.9:0.1, v/v/v) (solvent A) and acetonitrile:acetic acid (99.9:0.1, v/v) (solvent B). The linear gradient for solvent B was as follows: 0-2 min.: 5% B,

2- 18 min. (from 5 to 40% B), 18 - 40 min (from 40 to 90% B) 20-24 min (isocratic 90% B), 24-27.5 min. (from 90 to 5% B). The flow rate was 0.5 mL/min and the injection volume of the sample dissolved in methanol was 5 µL. Before injecting, all the samples were filtered through a PTFE filter (13 mm i.d., 0.22 µm). The HPLC system was equipped with a diode array (DAD-G1315D) detection at specific wavelengths (280 and 340 nm). The system was coupled online with a single quadrupole mass spectrometer (MS) (Agilent Technologies 6110 system, Santa Clara, USA), in the ESI$^+$ mode. The MS settings were: dry gas N_2 at a flow rate of 8 L/min; drying temperature at 350°C, nebulizer pressure at 65 psi, capillary voltage of 3000 V, scan range of *m/z* from 150 to 1000.

The HPLC-DAD analysis was applied for the optimization of the phytochemicals separation and for the quantitative evaluation, based on chromatograms recorded at 340 nm.

For an accurate identification of the metabolites, the HPLC-DAD separation protocol was optimized using pure standards of phenolic acids (p-coumaric, caffeic and syringic acid) absorbing at 280 nm, and flavonoids (quercetin and rutin), carnosic acid and betulinic acid of 95-99% purity (purchased from Sigma Aldrich), at 340 nm. All pure standards were dissolved in methanol and injected individually and as a mixture in the HPLC column and their specific retention times (t_R) and UV absorption spectra were recorded.

For the quantification of metabolites, the optimized HPLC-DAD separation protocol was applied using pure rutin (quercetin 3-*O*-rutinoside) standard to build a calibration curve, based on five different concentrations (10, 5, 2.5, 1.25 and 0.625 micrograms rutin/mL). The calibration curve was represented by a regression equation y=32.846+273.7; R^2=0.9983 used to calculate the concentrations of metabolites separated by HPLC-DAD (expressed as micrograms rutin equivalents/ gram of dry sample).

The LC-ESI$^+$-MS analyses aimed to fingerprint and identify the metabolites based on their m/z values and fragmentation features, compared with literature reports and databases (Phenol Explorer, KEGG) finalized by tentative identification consistent with published data.

Statistical Analysis

The qualitative data derived from LC-ESI+-MS data were processed by non-targeted statistical analysis (Cluster Analysis and Principal Component Analysis), to discriminate the profile differences between the sampling groups depending on the environmental conditions. The mean values of identified compounds were compared by the Pearson correlation test, the significance of differences being established at 3E-9.

ACKNOWLEDGMENTS

We acknowledge the contribution of our collaborators from the Applied Biotechnology Centre BIODIATECH-Proplanta SRL, as well the funding from the Spanish Ministry of Science and Innovation (Project CGL2008-00438/BOS) and the contribution of European Regional Development Fund.

REFERENCES

1. S. Moreno; T. Scheyer; C.S. Romano; A. Vojnov; *Free Rad. Res*. **2006**, *40*, 223-231.
2. B. Bozin; N. Mimica-Dukic; I. Samojlik; E. Jovin; *J. Agric. Food. Chem*. **2007**, *55*, 7879-7885.
3. E. Issabeagloo; P. Kermanizadeh; M. Taghizadieh; R. Forugh; *Afr. J. Microbiol. Res*. **2012**, *6,* 5039-5042.
4. T. Kayashima; K. Matsubara; K.Ayashima; K. Matsubara; *Biosci. Biotechnol. Biochem.* **2012**, *76*, 115-119.
5. S. Habtemariam; *Evid. Based Complement. Alternat. Med*. **2016**, 2680409.
6. G. Zgórka; K. Glowniak; *J. Pharm. Biomed. Anal*. **2001**, *26*, 79–87.
7. J.C. Luis; C.B. Johnson; *Span. J. Agric. Res*. **2005**, *3*, 106–112.
8. European Medicines Agency. Community herbal monograph on *Rosmarinus officinalis* L. *aetheroleum.* **2010**, Available from: http//www.ema.europa.eu/WC500101493.pdf
9. I. Cocan; E. Alexa; C. Danciu; I. Radulov; A. Galuscan; D. Obistioiu; A.A. Morvay; R.M. Sumalan; M.A. Poiana; G. Pop; C.A. Dehelean; *Exp. Ther. Med*. **2018**, *15*, 1863-1870.
10. M.B.Hossain; D.K. Rai; N.P. Brunton; D.A.B. Martin; C. Barry-Ryan; J. *Agric. Food. Chem*. **2010**, *58***,** 10576–10581.
11. K. Hcini; J.A. Sotomayor; M.J. Jordan; S. Bouzid; *Asian J. Chem. part B* **2013**, 25, 9299–9301.
12. A. Vallverdú Queralt; J. Regueiro; M. Martìnez Huélamo; J.F. Rinaldi Alvarenga; L. Leal; N. Lamuela Raventos; *Food Chem*. **2014**, *154*, 299–307.
13. S. Munne Bosch; L. Alegre; *Planta* **2000**, *210*, 925-931.
14. M.J. Del Baño; J. Lorente; J. Castillo; O. Benavente García; M.P.Marín; J.A. Del Río; A. Ortuño; I. Ibarra; *J. Agric. Food Chem.* **2004**; *52*, 4987–4992.
15. C. Bicchi; A. Binello; P. Rubiolo; *Phytochem Anal.* **2010**, *11*, 236–242.
16. P. Mena; M. Cirlini; M. Tassotti; K.A. Herrlinger; C. Dall'Asta; D. Del Rio; *Molecules* **2016**, *21*, 1576-1587;

17. M. Herrero; M. Plaza; A. Cifuentes; E. Ibañez; *J. Chromatogr.* **2010**, *1217*, 2512–2520.
18. I. Borrás Linares; Z. Stojanović; R. Quirantes Piné; D. Arráez Román; J. Švarc Gajić; A. Fernández Gutiérrez; A. Segura Carretero; *Int. J. Mol. Sci.* **2014***, 15,* 20585–20606.
19. M. Mulinacci; M. Innocenti; M. Bellumori; C. Giaccherini; V. Martini; M. Michelozzi; *Talanta,* **2011**, *85,* 167–176.
20. C.R.L. Wellwood; R.A. Cole; *J. Agric. Food Chem.* **2004,** *52*, 6101–6107.
21. L. Almela; B. Sánchez Muñoz; J.A. Fernández López; M.J. Roca; V. Rabe; *J. Chromatogr.* **2006***, 1120*, 221–229.
22. M.J. Jordan; V. Lax; M.C. Rota; S. Loran; J.A. Sotomayor; *Ind. Crops Prod*. **2013**, *48*, 144–152.
23. D. Meziane Assami; V. Tomao; K. Ruiz; B.Y. Meklati; F. Chemat; *Food Anal. Meth*. **2013**, *6*, 282–288.
24. M.H. Mehrizi; H. Shariatmadari; A.H. Khoshgoftarmanesh; F. Dehghani; *J. Agr. Sci. Technol*.-Iran **2012**, *14*, 205–212.
25. T. Tounekti; A.M. Vadel; M. Ennajeh; H. Khemira; S. Munné-Bosch; *J. Plant Nutr. Soil Sci.* **2011**, *174, 504-514*.
26. M. Loussouarn; A. Krieger-Liszkay; L. Svilar; A. Bily; S. Birti; M. Havaux; *Plant Physiol*. **2017**, *175*, 1381–1394
27. V. Papageorgiou; C. Gardeli; A. Mallouchos; M. Papaioannou; M. Komaitis; *J. Agric. Food Chem.* **2008**, *56*, 7254–7264.
28. A. Caverzan; A. Casassola; S. Patussi Brammer; In *Abiotic and biotic stress in plants. Recent advances and future perspectives*. **2016**, Arun Shanker, IntechOpen, pp.463-481
29. A. Fini; C. Brunetti; M. Di Ferdinando; F. Ferrini; M. Tattini; *Plant Signal. Behav.* **2011**, *6*, 709–711.
30. K.S. Gould; C. Lister; In Andersen ØM, Marham KR (eds) *Flavonoids, chemistry, biochemistry and application*, Boca Raton, FL: CRC Press, **2006,** 397–442.
31. D. Treutter; *Environ. Chem. Lett.* ***2006****, 4*, 147–157.
32. B. Winkel-Shirley; *Curr. Opin. Plant Biol.* **2002**, *5*, 218–223.
33. M. Di Ferdinando; C. Brunetti; A. Fini; M. Tattini; In Ahmad P, Prasad MNV (eds) *Abiotic stress responses in plants: metabolism, productivity and sustainability*, New York: Springer, **2012**, 159–179.
34. J. Mierziak; K. Kostyn; A. Kulma; *Molecules* **2014**, *19*, 16240-16265;
35. J. Grassmann; *Vitam. Horm*. **2005**, *72*, 505–535.
36. I. Bautista; M. Boscaiu; A. Lidón; J.V. Llinares; C. Lull; M.P. Donat; O. Mayoral; O. Vicente; *Acta Physiol. Plant.* **2016**, *38,* 9-16.
37. Y. Zhang; J.P. Smuts; E. Dodbiba; R. Rangarajan; J.C. Lang; D-W. Armstrong; *J. Agric.Food Chem.* **2012**, *60*, 9305–9314.
38. N. Bai; K. He; M. Roller; C. Lai; X.Shao; M. Pan; C.T.Ho; *J. Agric. Food Chem.* **2010**, 58, 5363–5367.

39. K. Kiarostami; R. Mohseni; S. Azra; *J. Stress Physiol. Biochem*. **2010**, *6*, 114-122.
40. S. Birtić; P. Dussort; F.X. Pierre; A.C. Bily; M. Roller; *Phytochemistry* **2015**, *115*, 9–19.
41. L. Yang; K.S. Wen; X. Ruan; Y.-X. Zhao; F. Wei; Q.Wang; *Molecules* **2018**, *23,* 762-769.

STUDIA UBB CHEMIA, LXIV, 3, 2019 (p. 181-192)
(RECOMMENDED CITATION)
DOI:10.24193/subbchem.2019.3.15

SIMPLE AND FAST PROCEDURE TO INCORPORATE DOXORUBICINE IN SMALL UNILAMELLAR LIPOSOMES: EFFECTS ON LIPOSOME SIZE AND ZETA POTENTIAL

MIHAI ADRIAN SOCACIU[a], ZORITA DIACONEASA[b], CARMEN SOCACIU[b,c,*]

ABSTRACT. This study aimed to find alternative, cheap and fast procedures to incorporate Doxorubicin in small unilamellar nanoliposomes made of Dipalmitoyl Phosphatidyl Choline and Cholesterol. It was compared the entrapment efficiency of doxorubicin in "home-made" liposomes (1) and in ImmunoSOME liposomes (2), a commercial, expensive formulation. It was obtained an entrapment efficiency of 27.6 % *vs* 12.1% for formulatios (1) *vs* (2). The liposomes' size and zeta-potential of formulation (1) ranged from 116 and 120 nm, being smaller than in formulation (2). The zeta potential was negative for both formulations and showed a better stability and monodispersibility also for formulation (1). This fast procedure is convenient and assure efficient doxorubicin entrapment in the monodisperse nanoliposomes. Such simple formulations, easier to be obtained, can offer also good quality/ price ratios and can be produced at larger scale, with higher incorporation efficiency for experimental *in vivo* studies which aims the targeted delivery of Doxorubicin to cancer tumors in animals.

Keywords: *Liposomes, Doxorubicin encapsulation, size and zeta potential*

[a] *University of Medicine and Pharmacy "Iuliu Haţieganu" 12, Victor Babeş str., RO-400028, Cluj-Napoca, Romania*
[b] *University of Agricultural Sciences and Veterinary Medicine, 3-5 Mănăştur str., RO-400372 Cluj-Napoca, Romania*
[c] *Research Center for Applied Biotechnolgy in Diagnosis and Molecular Therapy, BIODIATECH, str. Trifoiului 12G, 400478 Cluj-Napoca, Romania*
* *Corresponding author: carmen.socaciu@usamvcluj.ro*

INTRODUCTION

Anthracyclines such as doxorubicin (DOXO), epirubicin and daunorubicin are among the most active cytotoxic agents, a highly potent chemotherapeutic agent for the treatment of a wide variety of solid tumors and hematological malignancies. Since the secondary effects associated with their chronic administration induce cardiomyopathy and congestive heart failure, new, less toxic formulations (pegylated or nonpegylated liposomal formulations) demonstrated the superiority of liposomal doxorubicin in comparison to conventional non-liposomal doxorubicin. Therefore, liposomal formulations with entrapped DOXO are currently the best-known alternatives to improve the index and spectrum of anticancer activity and decrease cardiotoxicity [1].

Liposomes are prepared, characterized and used since decades as potent drug delivery carriers, being largely characterized for their physico-chemical properties, highly dependent on their qualitative and quantitative phospholipid composition, pH, size [2-5]. Mostly used is Dipalmitoyl Phosphatidyl Choline (DPPC) in combination with other types of phospholipids and in different ratios with cholesterol, which confers stability and modulate membrane fluidity [6, 7]

It is well documented, that drug delivery using carriers like liposomes provides several advantages, e.g. increased solubility, improved tumor targeting, enhanced accumulation in tumor tissues and cells, decreased systemic toxicity and increased maximum tolerated dosage [8, 9].

Nowadays, new formulations containing doxorubicin encapsulated in liposomes are available and produced, at high prices, by some specialized companies. For example, Doxosome is a DOXO-entraped liposomal suspension and Doxil, commercially known as Caelyx, is a Polyethyleneglycol-coated liposomal formulation including DOXO, used for the treatment of ovarian cancer, sarcoma and multiple myeloma. In spite of showing reduced DOXO-related toxicity, Doxil showed a lower clinical efficiency, since the PEGylated liposomal doxorubicin was sequestered in the cellular lysosomes, with a lower bioavailability of DOXO [10]. Another comparative study of the antitumor activity of free DOXO and Doxil in mouse lymphoma models concluded contrasting effects, e.g. free DOXO was more efficient by i.p administration while Doxil was superior by i.v. administration [11]. Another commercial formulation is ImmunoSOME, a surface reactive product without DOXO, which include PEG-conjugated liposomes linked to biotin. This product offers possibilities to link avidine-conjugated microbubble and target tumors by ultrasounds (US), recommending DOXO-liposomes as good nanotheranostic agents [12].

In this context, our experimental study aimed to find a fast and cheap procedure to incorporate DOXO in small unilamellar liposomes (SUV) as simple formulations made of Dipalmitoyl Phosphatidyl Choline (DPPC) and Cholesterol (CHOL) (1). Comparatively, ImmunoSOME, an expensive commercial PEGylated liposomal suspension was used to incorporate similar quantities of DOXO (2). The results were monitored by measuring the DOXO entrapment efficiency (EE), the liposomes' size and zeta-potentials, after DOXO incorporation in both formulations (1) and (2).

RESULTS AND DISCUSSION

Evaluation of DOXO entrapment efficiency

The influence of liposomal lipid composition on liposome size, zeta potential and liposome-induced dendritic cell maturation using a design of experiments approach was recently reported [13]. Another novel approach on drug delivery refers to the key-role of the lipid composition and nano-formulation of liposomal DOXO in relation to the biological evaluation of entrapped DOXO [14]. The antiproliferative long-circulating liposomes co-encapsulating DOXO and curcumin, through the use of a quality-by-design approach was also reported, recently. Six parameters, namely the phospholipid, curcumin and DOXO concentrations, the phospholipid: cholesterol molar ratios, the temperature during evaporation, buffer's pH and hydration steps were identified as potential risk factors for the quality of the final product. The influence of these variables was monitored by the particle size, zeta potential, drug loading and entrapment efficiency [15].

To intensify the accumulation of DOXO inside SUV *vs* ImmunoSOME liposomes, we tried either the classical procedure using only Hepes buffer at pH 7.4 (a) or a combination of Hepes buffer and gradients of ammonium sulfate to obtain a more 'active' loading of amphipathic weak bases into the aqueous compartment of liposomes (b), approach being applied previously to encapsulate anthracyclines inside the liposomes at very high efficiency [16]. The results were superior in our case using procedure (b) and are presented in Table 1 which includes the comparative values (mg of DOXO added to liposomal suspension (DOXOadded), DOXO found in the supernatant (DOXOout), found in the pellet (DOXOin, calculated as the difference DOXO added - DOXOout (column 4) or by direct determination after the dissolution of the pellet (DOXOin* - column 5). The encapsulation efficiency (EE) was calculated as a ratio DOXOin*/DOXOadded.

Table 1. The encapsulation efficiency (EE) of DOXO inside liposomes, taking into account the DOXO before and after encapsulation. *For sample abbreviations see the Experimental Section.*

Sample	DOXO added (mg)	DOXOout (mg)	DOXOin (calculated) (mg)	DOXOin* (determined) (mg)	EE (%)
L1 (SUV)	1	0.73	0.27	0.276	27.60
L2 (SUV)	1.4	1.31	0.09	0.068	4.85
L3(ImmunoSOME)	1.4	1.28	0.12	0.110	7.85
L4(ImmunoSOME)	1	0.86	0.14	0.121	12.1
L5(ImmunoSOME)	1.4	1.24	0.16	0.125	8.92
L6 (SUV)	1.4	0.89	0.51	0.375	26.78

Significant differences were observed between the six samples: The SUV liposomes (L1 and L6) showed higher incorporation yields than ImmunoSOME. When sucrose was added, the incorporation decreased significantly (L2<L1 and L3<L5). No significant differences between EE values were observed when DOXO was added as 1 or 1.4 mg (see L1 *vs* L6), suggesting that the liposomal membrane structure is mainly responsible for the limitations of DOXO incorporation.

The more complex composition of ImmunoSOME membrane determined a limited incorporation of DOXO, at around 50% comparing to SUV liposomes (L4 *vs* L1).

Liposomes Size and Polydispersibility index

Fig. 1 shows the values of liposome sizes for samples L1 (SUV-DOXO liposomes), comparative to L3, L4, L5 (ImmunoSOME-DOXO liposomes).

The DOXO-SUV liposomes from samples L1 and L6 had similar sizes, of 116 and 120 nm, respectively. Also, their polydispersity index (PDI) is good (0.162-0.170), with values less than 0.2, suggesting a good monodispersion of liposomes. For samples containing DOXO- ImmunoSOME liposomes (L3, L4 and L5) the sizes ranged from 148 to 163 nm (larger size), and PDI values from 0.119 to 0.214 (still monodisperse).

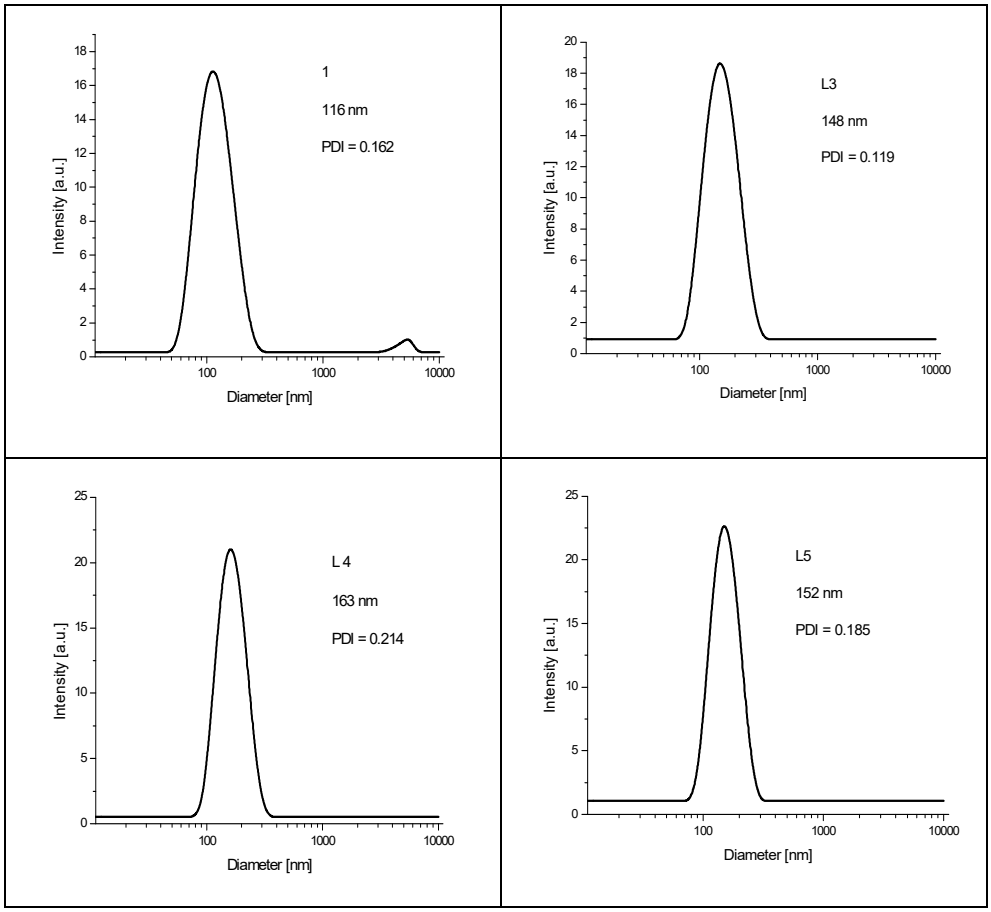

Figure 1. The liposome size for samples L1 (SUV-DOXO liposomes), comparative to L3,L4, L5 (ImmunoSOME-DOXO liposomes)

Zeta-potential of DOXO liposomes

The measurements of zeta potential of the six samples (L1 and L6 containing DOXO-SUV liposomes and L3-L5 containing DOXO-ImmunoSOME liposomes) showed negative values in all cases, as shown in Fig.2.

The zeta potential of the SUV-DOXO and ImmunoSOME-DOXO liposomes was negative (ranging from -26 to -48mV), due to their charge and pH of the buffer, The higher values were noticed for L1 (-48 mV) suggesting the best stability, followed by L2 and L6 (-30 and -26mV, respectively). The samples L3-L5 corresponding to DOXO-ImmunoSOME liposomes had closer values, from -27 to -29 mV.

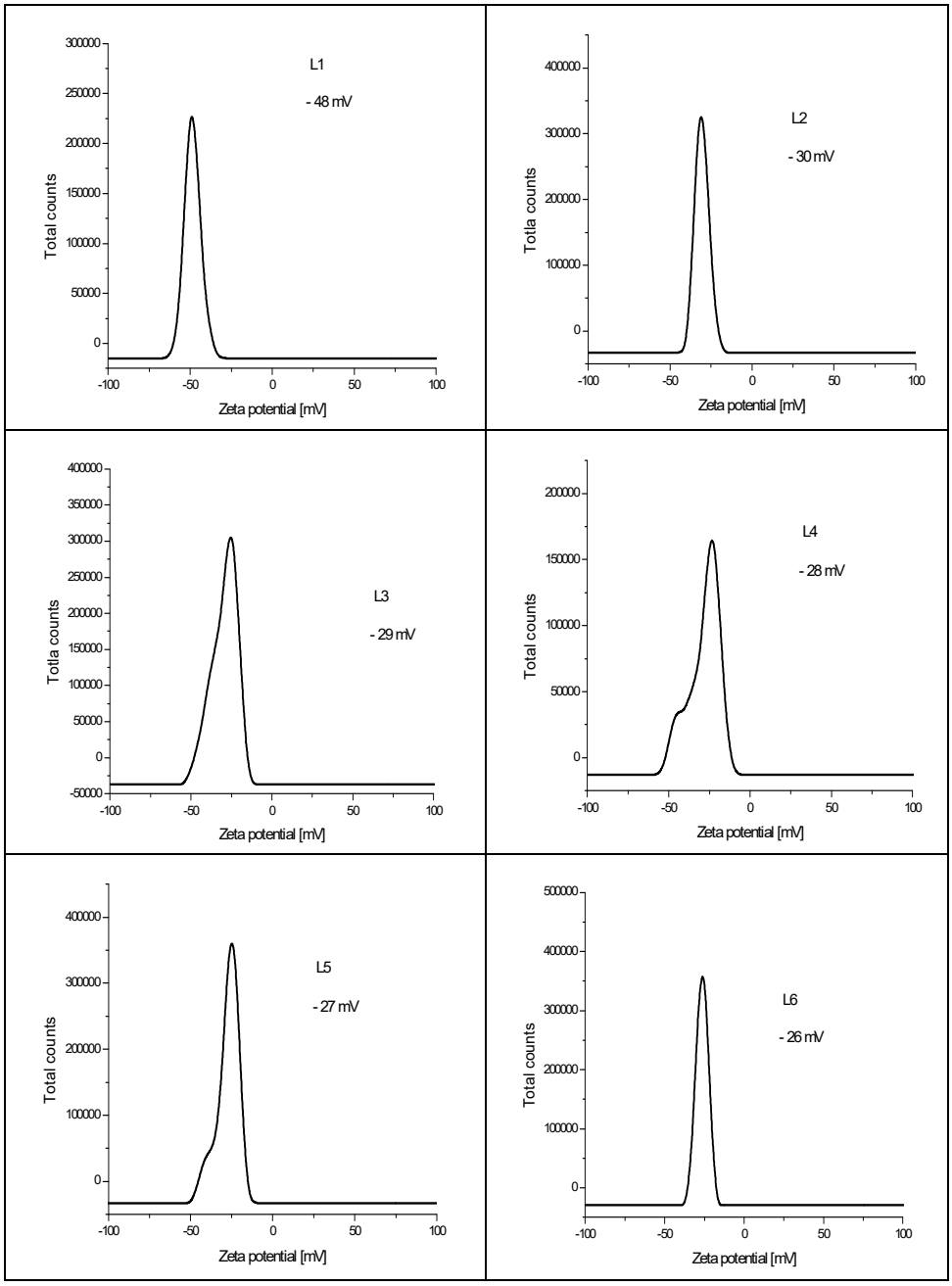

Figure 2. The values of zeta potential for the six samples (L1 to L6).
For abbreviations see the Experimental Section Table 2.

The significance of the zeta potential is related to the short- and long-term stability of emulsions and liposomal suspensions. Zeta potential becomes more negative when pH increases and is a measure of magnitude of charges on liposomal vesicles. Recently such assumptions were demonstrated for DPPC and 1,2-dioleoyl-sn-glycero-3-phosphatidylcholine (DOPC) liposomes investigated in 1 mM NaCl (pH 6.2) and phosphate buffer (pH 8.1) in relation to the liposome size, polydispersity index, and zeta potentials [17]. The higher the value of the zeta potential is (positive or negative), the more stable the colloid dispersion is. Normally, a value of > 30 mV indicates good stability [17]. Our data are in agreement with recent reports which demonstrated the superiority of liposomal doxorubicin in comparison to conventional non-liposomal doxorubicin [18], especially in SUV formulations with high zeta potentials.

Considering these data, sample L1 (SUV-DOXO liposomes) showed best stability and dispersibility. The ImmunoSOME-DOXO samples had inferior properties comparing to SUV-DOXO.

CONCLUSION

The results of this study show that simple and fast procedures can be applied to incorporate DOXO in “home-made” SUV-unilamellar nanoliposomes containing cheap and simple lipid composition. We have shown that entrapment efficiency of DOXO into SUV-liposomes (L1) was higher than into ImmunoSOME liposomes (L4), having values of 27.6% vs 12.1% respectively, when the same initial DOXO quantity was added.

The addition of sucrose decreased significantly the entrapment efficiency, but no significant differences.

Meanwhile, no significant differences between the entrapment efficiency were observed when DOXO was added as 1 or 1.4 mg, suggesting that the liposomal membrane structure is mainly responsible for the limitations of DOXO incorporation.

The more complex composition of ImmunoSOME membrane may explain the lower incorporation rate of DOXO, at around 50% comparing to SUV liposomes. This is an expensive commercial liposomal formulation, using the transmembrane ammonium ion gradient procedure and its complex structure seems to hinder the DOXO incorporation.

Considering the liposomes’ size and the zeta potential, SUV-DOXO liposomes showed best stability and dispersibility and is recommended to be obtained at larger scale by this simple, cheap and fast procedure.

Finally, we consider this simple and fast procedure to prepare SUV-DOXO liposomes can be upgraded, in order to obtain higher quantities of this liposomal suspension. Such simple formulations with high entrapment efficiency of DOXO may offer good quality/price ratios and can be produced at larger scale for experimental studies *in vivo*, for a targeted delivery to cancer tumors in small animals.

EXPERIMENTAL SECTION

Chemicals, reagents and materials

1,2-dipalmitoyl sn-glycero-3-phosphatidylcholine (DPPC, MW=734), Cholesterol (Roth puritate 99%, (CHO L, MW=386), Doxorubicin clorhydrate (DOXO) 2 mg/ml saline solution, ImmunoSOME (5 ml, Encapsula Nanoscienes) a mixture of HSPC:CHOL:DSPE-PEG: DSPE-PEG-Biotin (55:40:4:1) representing 5.96 mg lipids/ml in 100 nm liposomes. Buffer HEPES 10mM (pH 7.4), buffer Ammonium Sulphate pH 5.5 (Sigma-Aldrich).

Instrumentation

BENACOR rotavapor with automatic regulation of vacuum, temperature and rotation, ultrasonic generator UP200St-G (Hielscher Ultrasonics GmbH) 200W, 26kHz with an S26d2 sonotrode of 2 mm and ultrasonic bath, thermostate with recirculated water, extrusion system of LiposoFast-50, crio-centrifuge Hettich 460R, Eppendorf centrifuge (max. 15000 rpm), Cell Media mixer. The spectrophotometric measurements were made on a Perkin Elmer UV WinLab Spectrophotometer (200-700 nm at 1 nm/min).

Preparation of Unilamellar liposomes

To a mixture of 375 mg lecithin and 125 mg cholesterol, in a molar ratio 61.5:38.5 it was added a solvent mixture of chloroform:methanol 2:1 (v:v), in a glass round bottom flask of 50 ml. The solvent was evaporated under vacuum in the Rotavapor at 43°C, for 30 min. The lipid layer was then dehydrated in an exicator containing anhydrous Calcium chloride, during 48 hrs. The lipid layer was suspended in 20 ml $(NH_4)_2\ SO_4$ 300 mM, pH 5.5, and strongly vortexed. The liposome suspension was taken from the flask and centrifuged at 4°C, 4600 rpm, 20 min. The upper, opalescent phase containing multilamellar liposomes was retained and extruded successively through

polycarbonate filters of 400 and 100 nm, using the Lipofast system. The extruded suspension contained small unilamellar liposomes (SUV), whose size was determined, as mentioned below.

Incorporation of DOXO in SUV and ImmunoSOME liposomes

The incorporation of DOXO in unilamellar liposomes was realized by the transmembrane ammonium ion gradient procedure, as follows: under mix in the ultrasonic bath at 65°C, 30 min, to a volume of 0.3 ml liposome suspensions (SUV or ImmunoSOME) there were added 0.5 or 0.7ml DOXO and 0.5 ml Hepes 10 mM pH 7.4. as mentioned in Table 2. The mixture was maintained 10 min at 4°C in the refrigerator, then a volume of 0.8 Ammonium sulphate 300 mM pH 5.5 was added to the suspension, kept 10 min at room temperature and centrifuged at 15000 rpm, 10 min. The supernatant was separated and the DOXOout (the non-incorporated DOXO) was determined by UV-Vis spectrometry. The pellet was washed with Hepes buffer two times and then re-suspended in 0.7 ml Hepes pH 7.4, mixed for 15 min at 45°C.

Fig. 3 reflect the differences between the two types of liposomes used for DOXO entrapment, as well the mechanisms behind the DOXO loading using a transmembrane ammonium ion gradient in the unilamellar liposomes.

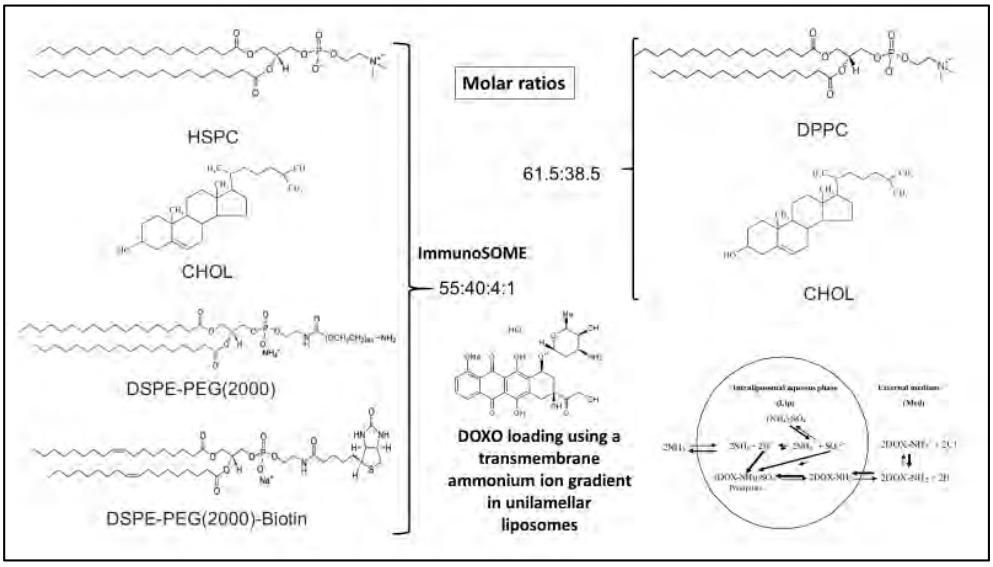

Figure 3. The composition of the SUV and ImmunoSOME liposomes used for DOXO entrapment and the mechanisms behind the DOXO loading using a transmembrane ammonium ion gradient.

Table 2 represents the volumes of liposome suspensions (SUV and ImmunoSOME) and Hepes buffer, with or without addition of sucrose, used to incorporate DOXO (volumes of 0.5 or 0.7 ml representing 1 and 1.4 mg, respectively).

Table 2. Incorporation of DOXO (using 0.5 or 0.7 ml from a solution of 2 mg/ml) into SUV or ImmunoSOME liposomes, in 0.5 ml Hepes buffer 10 mM (pH 7.4), with or without sucrose 10%.

Abbreviation	Liposome type and volume	DOXO (ml)	+/- sucrose 10% (ml)
L1	0.3 ml SUV	0.5	-
L2	0.3 ml SUV	0.7	2 ml sucrose
L3	0.3 ml ImmunoSOME	0.7	2 ml sucrose
L4	0.3 ml ImmunoSOME	0.5	-
L5	0.3 ml ImmunoSOME	0.7	-
L6	0.3 ml SUV	0.7	-

After the incorporation procedure, a volume of 0.5 ml from each final suspension was taken to determine the liposomes size and zeta potential > concomitantly, to 0.2 ml suspension, a volume of 0.1 ml methanol and 0.8 ml Hepes buffer was added and the absorption intensity was recorded at 480 nm, in order to evaluate the DOXO incorporated in liposomes (DOXOin). In parallel, the empty liposomes were dissolved, and considered as blank.

Evaluation of DOXO entraped in SUV or ImmunoSOME liposomes

First, a calibration curve was built, using different dilutions of the initial DOXO solution (2 mg/ml), the curve factor ($f= c/A_{480nm}$) having the value f=0.133 .

The formula used to calculate the quantity of DOXOin and DOXOout was the following:

DOXO (mg) = f x dilution factor x total volume of the solution collected (from supernatant or dissolved liposomes containing DOXO).

Evaluation of liposomes' size and zeta potential

The liposome hydrodynamic diameter and polydispersity index (PDI) were determined at 25 ºC by dynamic light scattering (DLS) using a Malvern Zetasizer Nano ZS-90 (Malvern Instruments) with a He–Ne laser operating at a wavelength of 633 nm and an avalanche photodiode detector. The zeta

potential of the liposomes was determined also at 25 ºC by the laser Doppler microelectrophoresis technique using the same Malvern equipment. Before measurements, the samples were diluted 5 fold with ultrapure water.

ACKNOWLEDGMENTS

This study was supported by the Grant nr. 4945/12/2016 funded by the University of Medicine and Pharmacy "Iuliu Haţieganu" Cluj-Napoca. The authors would like to thank Prof. Dr. Simion Aştilean and Dr. Monica Potara (Interdisciplinary Research Institute in Bio-Nano-Sciences, University "Babeş-Bolyai") for their kind support and help related to the measurements of liposomes'size and zeta potential.

REFERENCES

1. H. Cortes-Funes; C. Coronado; *Cardiovasc. Toxicol*., **2007**, *7*, 56-60.
2. A. Akbarzadeh; R. Rezaei-Sadabady; S. Davaran; S.W. Joo; N. Zarghami; Y. Hanifehpour; M. Samei; M. Kouhi; K. NejatiKoshki; *Nanoscale Res. Lett.*, **2013**, *8*, 1-9.
3. N. Bergstrand; PhD diss. *Acta Univ. Upsaliensis*, Uppsala, **2003**.
4. J.S. Dual; A.C. Rana; A.K. Bhandari; *Int. J. Pharm. Sci. Res.,* **2012**, *3*, 14-20.
5. Y. P. Patil; S.Jadhav; *Chem. Phys. Lipids*, **2014**,*177*, 8-18.
6. H. Ohvo-Rekila; B. Ramstedt; P. Leppimaki; J.P. Slotte; *Prog. Lipid Res.*, **2002**, *41*, 66-97.
7. C. Socaciu; R. Jessel; H. Diehl; *Chem. Phys. Lipids*, **2000**, *106*, 79-88.
8. A. Gabizon; R. Shiota; D. Papahadjopuulos; *J. Natl. Cancer I.,* **1989**, *81*,1484-1488.
9. A. Gabizon; R. Catane; B. Uziely; B. Kaufman; T. Safra; R. Cohen; *Cancer Res.,* **1994**, *54*, 987-992.
10. A.L. Seynhaeve; B.M. Dicheva; S. Hoving; G.A. Koning; T.L. Ten Hagen; *J. Control. Release, **2013***, 172, 330-340.
11. Cabanes A; Tzemach D; Goren D; Horowitz AT; Gabizon A. *Clin. Cancer Res.,* **1998**, *4*, 499-505.
12. P. Mohan; N.Rapoport; *Mol. Pharm.* **2010**, 7, 1959-1973.
13. P. C. Soema; G-J. Willems; W. Jiskoot; J-P. Amorij; G.F. Kersten; *Eur. J. Pharm. Biopharm.,* **2015**, *94*, 427-435.
14. F. Haghiralsadat; G. Amoabediny; M.H. Sheikhha; T. Forouzanfar; J.M. Arough; M.N. Helder; B. Zandieh-doulabi; *Cell Journal* (*Yakhteh*), **2017**, *19*, 55-65.

15. L.R. Tefas; B. Sylvester; I. Tomuta; A. Sesarman; E. Licarete; M. Banciu; *Drug Des. Dev. Ther.*, **2017**, *11*, 1605-1621.
16. G. Haran; R. Cohen; L.K. Bar; Y. Barenholz; *Biochim. Biophys. Acta,* **1993**, *1151*, 201-215.
17. E. Chibowski; A. Szczes; *Adsorption*, **2016**, *22*, 755-765.
18. Y.H. Ngan; M. Gupta; *Arch. Pharm. Pract.,* **2016**, *7*, 1-13.

STUDIA UBB CHEMIA, LXIV, 3, 2019 (p. 193-202)
(RECOMMENDED CITATION)
DOI:10.24193/subbchem.2019.3.15

SYNTHESIS, STRUCTURE AND LUMINESCENT PROPERTIES OF A MONONUCLEAR ZINC(II) COMPLEX WITH A BICOMPARTMENTAL LIGAND

MIHAI RĂDUCĂ[a], AUGUSTIN M. MĂDĂLAN[a]*

ABSTRACT. A mononuclear complex of Zn(II) with the Schiff base ligand derived from *o*-vanillin and 2,2-dimethyl-1,3-diaminopropane (H_2valdmpn) was obtained and structurally characterized by X-ray diffraction on single crystal. In the [Zn(valdmpn)(H_2O)] complex the metal ion is pentacoordianated with a square pyramidal geometry. The luminescent properties of the complex were investigated in solid state and solution following the influence of the solvent.

Keywords: *Zinc complexes, bicompartmental ligands, luminescence*

INTRODUCTION

The reactions between *o*-vanillin and diamines can generate various Schiff base podands, that were extensively used as ligands. The morphologies of the resulting complexes depend basically on the flexibility or rigidity of the diamines. The relatively rigid podands derived from hydrazine, 4,4'-methylenedianiline or 4,4'-diaminodiphenyl ether are easily engaged in multiple bridging and helical binding modes [1-4]. Schiff-bases derived from *o*-vanillin and flexible diamines (ethylenediamine; 1,3-diaminopropane; 2,2-dimethyl-1,3-diaminopropane) usually behave as bicompartmental ligands, allowing the synthesis of mono- and binuclear complexes (Scheme 1).

These ligands are suitable for the synthesis of heterobinuclear 3d-4f complexes [5-7] or 3d-3d' complexes [7-10]. In the 3d-4f complexes, the 3d metal ion is located into the N_2O_2 compartment, while the oxophilic lanthanide cation occupies the larger, open $O_2O'_2$ compartment. In the binuclear complexes, the phenoxo oxygen atoms act as bridges between the two metal ions. In mononuclear complexes with the metal ion hosted into the

[a] *Inorganic Chemistry Department, Faculty of Chemistry, University of Bucharest, 23 Dumbrava Rosie, 020464-Bucharest, Romania*
* *Corresponding author: augustin.madalan@chimie.unibuc.ro*

N_2O_2 compartment, the larger vacant $O_2O'_2$ compartment can act as a receptor not only toward other metal ions, but also toward hydrogen bond donors (e.g. the aqua ligand arising from another complex, identical [11] or different [12], amino groups [13-14], ammonium cation [15]).

In zinc-lanthanide complexes, this type of ligands can act as sensitizers for excitation of lanthanide ions (antenna effect), overcoming the disadvantage presented by the very small molar absorption coefficient of f-f transitions [16]. In mononuclear zinc complexes, the metal ion (hosted into the N_2O_2 compartment) plays basically a structural role rigidifying the organic fragment, which can present photoluminescent properties [17].

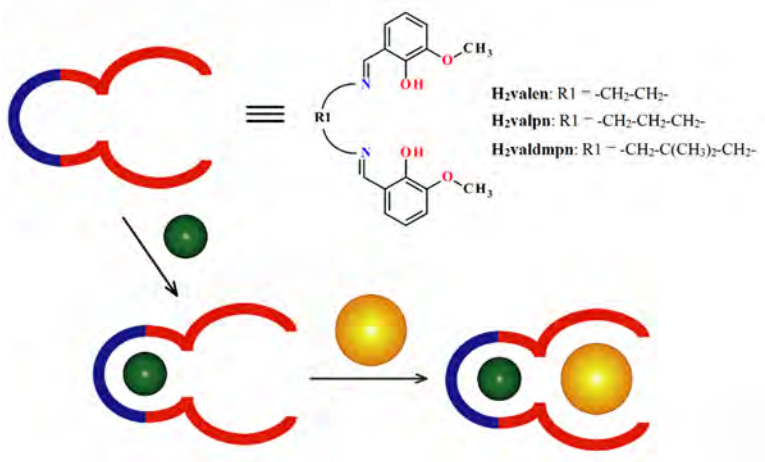

Scheme 1

In this paper, we report synthesis, structure and luminescent properties of a mononuclear complex of Zn(II) with the Schiff base ligand derived from *o*-vanillin and 2,2-dimethyl-1,3-diaminopropane. The luminescent properties of the complex were investigated both in solid state and solution. In solution, we were particularly interested by the solvent influence on the photoluminescent properties.

RESULTS AND DISCUSSION

Reaction of *o*-vanillin with 2,2-dimethyl-1,3-propylenediamine and Zn(II) nitrate in the presence of triethylamine affords yellow crystals, which were structurally characterized by X-ray diffraction on single crystal. The

crystals contain mononuclear Zn(II) complexes, [Zn(valdmpn)(H_2O)], and crystallization water molecules. The general formula of the compound is [Zn(valdmpn)(H_2O)]·H_2O. In the mononuclear complex, the zinc ion is pentacoordinated with a square-pyramidal geometry (Figure 1). The basal plane is formed by the two imino nitrogen atoms and the two phenoxo oxygen atoms of the Schiff base ligand. In the apical position is coordinated the oxygen atom of the water molecule. The basal bond lengths are Zn1-N1 = 2.119(5), Zn1-N2 = 2.109(5), Zn1-O2 = 2.017(5), and Zn1-O3 = 2.032(5) Å, longer than the apical one, Zn1-O5 = 1.980(6) Å. The organic ligand has a 'butterfly' shape with the dihedral angle between the mean planes of the two aromatic fragments (including the imino and phenoxo groups) of 118.2º.

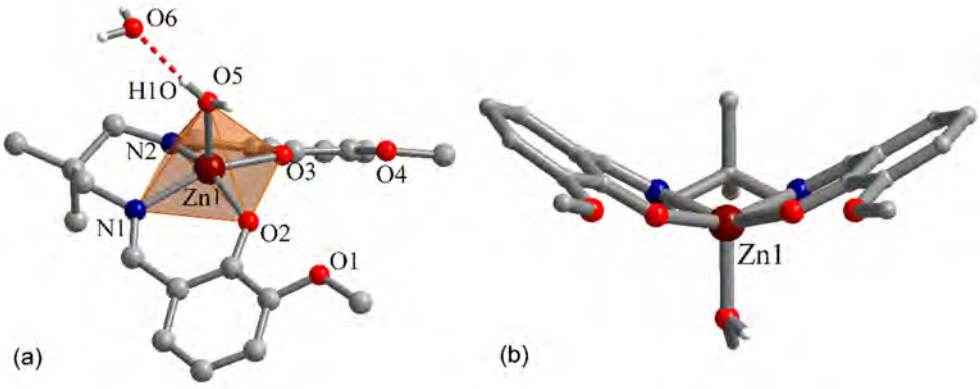

Figure 1. Perspective views of the asymmetric unit (a) and the mononuclear complex showing the 'butterfly' shape of the Schiff base ligand (b)

The coordinated water molecules are involved in hydrogen bonding with crystallization water molecules generating supramolecular double chains (Figure 2). Coordinated water molecules act only as hydrogen bond donors towards crystallization water molecules: O5-H1O···O6 = 1.82 Å, O5-H2O···O6' = 1.94 Å, < O5-H1O···O6 = 167.8º and < O5-H2O···O6' = 146.9º (symmetry code: ' = -0.5+x, 1.5-y, -z). The crystallization water molecules are hosted in the outer compartment of the organic ligand making donating bifurcated hydrogen interactions with the phenoxo and methoxy oxygen atoms.

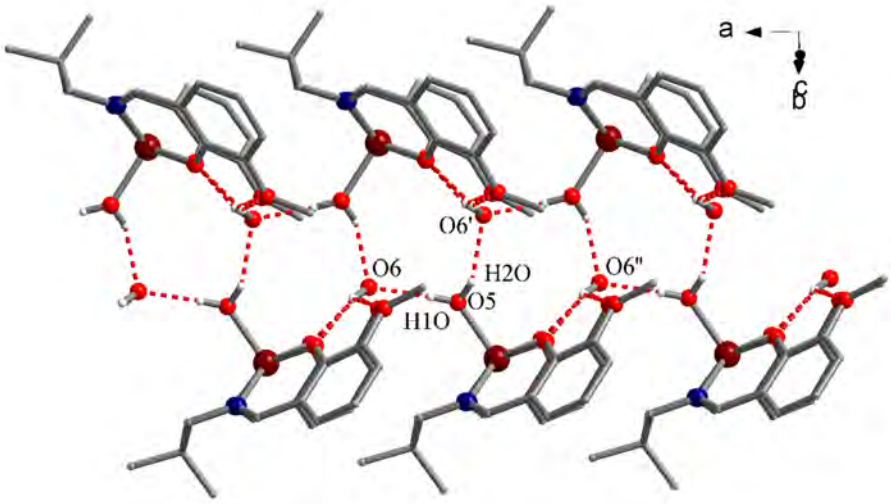

Figure 2. View of the supramolecular chain formed by hydrogen interactions (symmetry codes: ' = -0.5+x, 1.5-y, -z and " = -1+x, y, z)

An interesting feature of the packing is that the supramolecular double chains are oriented with 2,2-dimethyl-1,3-propylene fragments in the same direction and are running parallel along the crystallographic *a* axis (Figures 2 and 3). This type of packing explains the crystallization in a chiral space group, *orthorhombic P212121*.

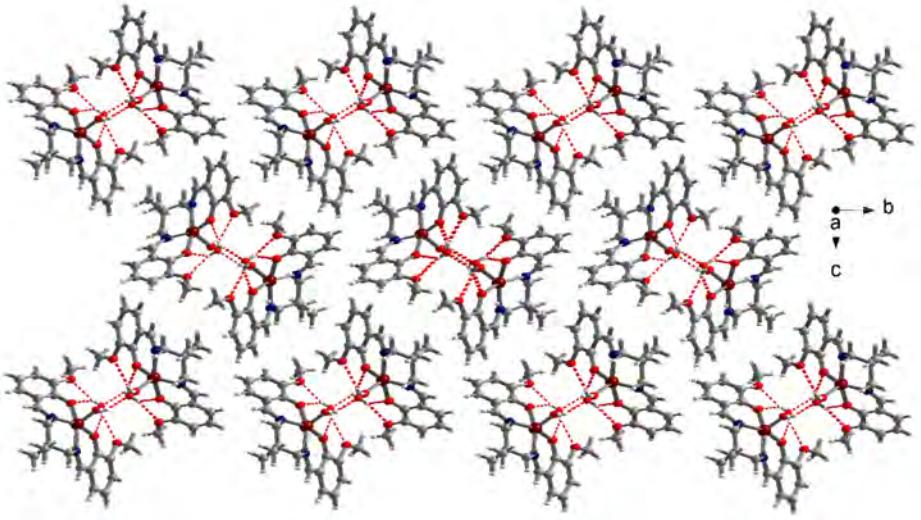

Figure 3. View of the packing diagram along the crystallographic *a* axis

Spectroscopic studies

The electronic spectrum of compound [Zn(valdmpn)(H_2O)]·H_2O, acquired over a wavelength range from 200 to 1800 nm on solid sample (using the diffuse reflectance technique), displays a band with the maximum at 410 nm. The room temperature photoluminescence of crystalline compound [Zn(valdmpn)(H_2O)]·H_2O was investigated using different wavelengths for excitation in the 330-430 nm range. The resulting emission spectrum displays an asymmetric band (tailed to the lower energy side) with a maximum at 460 nm. The highest intensity of this band is obtained when λ_{ex} = 350 nm. The corresponding excitation spectrum (λ_{em} = 460 nm) reveals a complex band within the 250-440 nm domain (Figure 4).

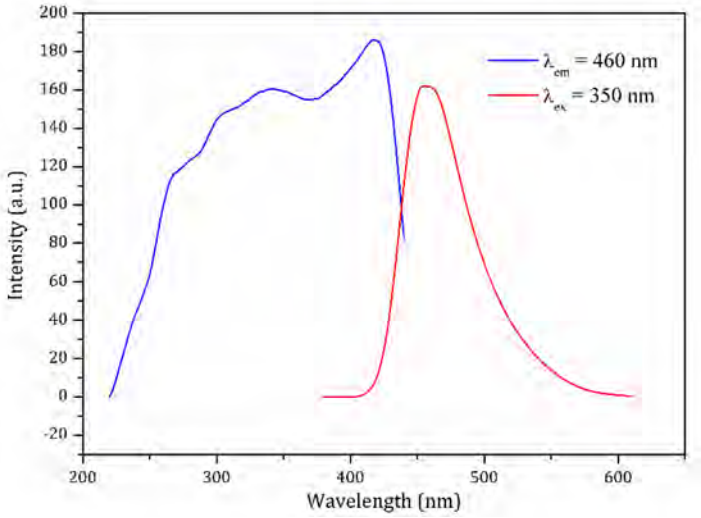

Figure 4. Emission (right) and excitation (left) spectra for the compound [Zn(valdmpn)(H_2O)]·H_2O

The influence of the solvent on the absorption properties (solvatochromism) was already studied for similar compounds [17]. We investigated the effect of the solvent on the emissive properties of the compound [Zn(valdmpn)(H_2O)]. All solutions were prepared using 2.3 mg of compound and 4 mL of solvent (1.22 mM) and were ultrasonicated for 2 minutes for a proper solubilization. The solvents used were: dimethylsulfoxide (DMSO), tetrahydrofuran (THF), N,N-dimethylformamide (DMF), acetonitrile (ACN), chloroforme ($CHCl_3$), methanol (MeOH), ethanol (EtOH), 2-propanol (iPrOH), ethyl acetate (EtAc) and 2-methoxy ethanol (MeOEtOH).

The emission spectra were recorded using λ_{ex} = 350 nm, and the respective pure solvents as references. The solvents used were of different polarities, protic (MeOH, EtOH, iPrOH and MeOEtOH) or aprotic (DMSO, THF, DMF, ACN, $CHCl_3$ and EtAc). The highest intensity of the emission was observed in the case of THF solution (more than double comparing with the next ones, DMF and EtAc – Figure 5). Using the less polar aprotic solvents, THF and EtAc, is also observed a blue shift of the emission with the maxima at 465 nm and 457 nm, respectively. The emission maxima for the other solutions range between 471 and 479 nm. For the ACN solution a quenching phenomenon is observed. In this context, no correlation can be done with the protic or aprotic nature of the solvent, since the highest and lowest intensities of the emission were observed for aprotic solvents (THF and ACN, respectively).

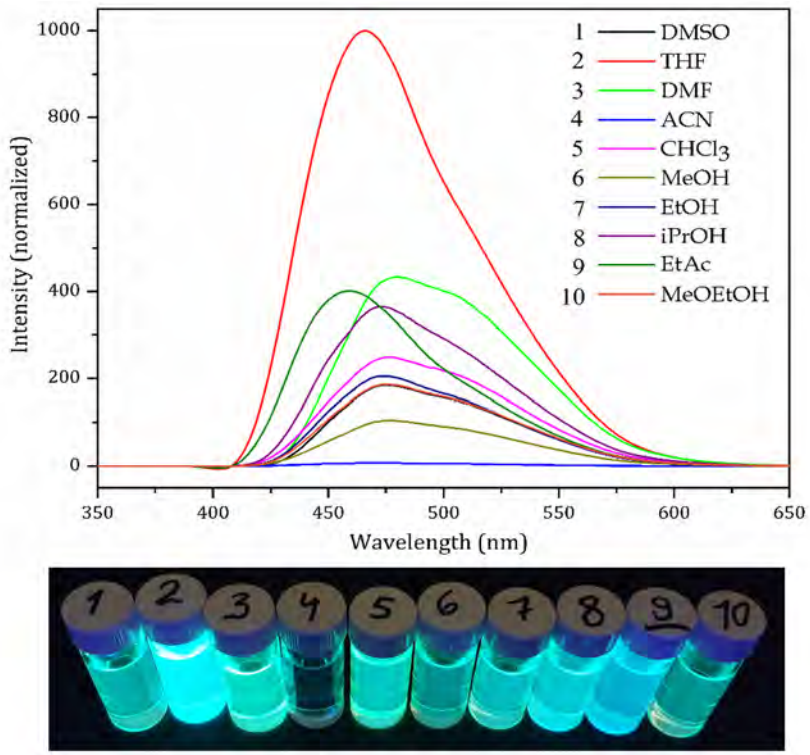

Figure 5. The emission spectra for [Zn(valdmpn)(H_2O)] in different solvents (1.22 mM) excited at 350 nm (top) and the comparative aspect of the solutions under 365 nm UV light (bottom)

CONCLUSIONS

The mononuclear complex of Zn(II) with the bicompartmental Schiff base ligand derived from *o*-vanillin and 2,2-dimethyl-1,3-diaminopropane confirmed the ability of this type of complexes to act as receptor for hydrogen bond donors (a water molecule in this particular case). The hydrogen interactions between the water molecules coordinated to the Zn(II) ions and that ones hosted in the larger vacant $O_2O'_2$ compartments of the complexes generate an oriented 1D supramolecular array. The photoluminescent properties of the complex are influenced by the solvent, but no clear correlations can be done with the polarity and protic or aprotic nature of the solvent.

EXPERIMENTAL SECTION

Synthesis. 5 mmol of $Zn(NO_3)_2 \cdot 6H_2O$ were added to an ethanolic solution (75 mL) containing 10 mmol of 3-methoxysalicylaldehyde and 5 mmol of 2,2-dimethyl-1,3-propylenediamine. Subsequently 20 mmol triethylamine were added. The mixture was stirred for 1 hour at 60 ºC. The slow evaporation at room temperature of the resulting mixture affords yellow single crystals after 3-4 days. Selected IR data (KBr pellet, cm^{-1}): 3051 (m), 2950 (m), 1620 (vs), 1546 (w), 1471 (s), 1418 (s), 1402 (w), 1390 (w), 1326 (m), 1242 (m), 1222 (s), 1070 (m), 970 (w), 858 (w), 738 (m).

Physical measurements. The IR spectra (KBr pellets) were collected on a Bruker Tensor 37 spectrophotometer in the 4000-400 cm^{-1} range. The UV-Vis-NIR spectra (diffuse reflectance technique) were recorded on a JASCO V-670 spectrophotometer. The fluorescence spectra were collected on a JASCO FP-6500 spectrofluorometer.

X-ray crystallography. Single crystal X-ray diffraction measurements were performed on a STOE IPDS II diffractometer operating with Mo-Kα (λ = 0.71073 Å) X-ray tube with graphite monochromator. The structure was solved by direct methods and refined by full-matrix least squares techniques based on F^2. The non-H atoms were refined with anisotropic displacement parameters. Calculations were performed using SHELX-2014 crystallographic software package. A summary of the crystallographic data and the structure refinement is given in Table 1. CCDC reference number: 1952966.

Table 1. Crystallographic data, details of data collection and structure refinement parameters for [Zn(valdmpn)(H_2O)]·H_2O

Compound	**[Zn(valdmpn)(H_2O)]·H_2O**
Chemical formula	$C_{21}H_{28}N_2O_6Zn$
M (g mol^{-1})	469.82
Temperature (K)	173(2)
Wavelength (Å)	0.71073
Crystal system	Orthorhombic
Space group	*P212121*
a (Å)	6.7049(4)
b (Å)	15.9853(11)
c (Å)	20.2309(14)
α (°)	90
β (°)	90
γ (°)	90
V (Å^3)	2168.3(2)
Z	4
D_c (g cm^{-3})	1.439
μ (mm^{-1})	1.172
F(000)	984
Goodness-of-fit on F^2	0.937
Final R_1, wR_2 [I>2σ(I)]	0.0490, 0.0629
R_1, wR_2 (all data)	0.1041, 0.0765
Largest difference in peak and hole (e Å^{-3})	0.341, -0.510

The X-ray powder diffraction measurements (XRPD) were carried out on a Proto AXRD Benchtop using the Cu-Kα radiation with a wavelength of 1.540593 Å in the range 5-35º *2θ*. In the figure 6 are presented the experimental and single-crystal simulated XRPD patterns of the compound [Zn(valdmpn)(H_2O)]·H_2O showing the purity of the solid sample.

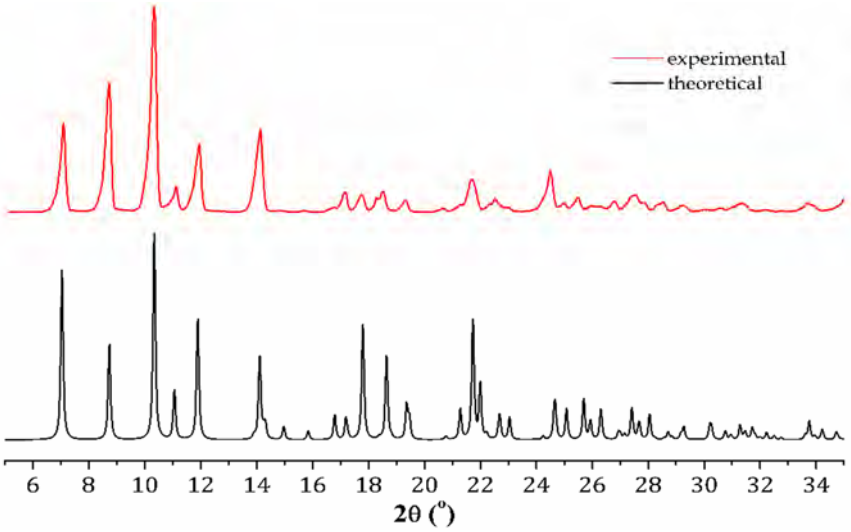

Figure 6. Comparison between the experimental (in red) and single-crystal simulated (in black) XRPD patterns of $[Zn(valdmpn)(H_2O)]\cdot H_2O$

ACKNOWLEDGMENTS

Financial support from University of Bucharest (project 72/2013) is highly acknowledged.

REFERENCES

1. J. Wu; L. Zhao; P. Zhang; L. Zhang; M. Guo; J. Tang; *Dalton Trans.*, **2015**, *44*, 11935-11942.
2. P. Cucos; F. Tuna; L. Sorace; I. Matei; C. Maxim; S. Shova; R. Gheorghe; A. Caneschi, M. Hillebrand; M. Andruh; *Inorg. Chem*., **2014**, *53*, 7738-7747.
3. D. Jiang; X. Yang; H. Chen; F. Wang; S. Wang; T. Zhu; L. Zhang; S. Huang; *Dalton Trans.*, **2019**, *48*, 2206-2212.
4. G. Novitchi; J.-P. Costes, J.-P. Tuchagues; L. Vendier; W. Wernsdorfer; *New J. Chem.*, **2008**, *32*, 197-200.
5. J.-P. Costes; F. Dahan; A. Dupuis; J.-P. Laurent; *Inorg. Chem.*, **1996**, *35* 2400-2402.
6. M. Andruh; *Chem. Commun.*, **2007**, 2565-2577.

7. M. Andruh; *Chem. Commun.*, **2011**, *47*, 3025-3042.
8. D.G. Branzea; A. Guerri; O. Fabelo; C. Ruiz-Pérez; L.-M. Chamoreau; C. Sangregorio; A. Caneschi; M. Andruh; *Cryst. Growth Des.*, **2008**, *8*, 941-949.
9. D.G. Branzea; L. Sorace; C. Maxim; M. Andruh; A. Caneschi; *Inorg. Chem.*, **2008**, *47*, 6590-6592.
10. M. Nayak; R. Koner; H.-H. Lin; U. Flörke; H.-H. Wei; S. Mohanta; *Inorg. Chem.*, **2006**, *45*, 10764-10773.
11. S. Nastase; F. Tuna; C. Maxim; C.A. Muryn; N. Avarvari; R.E.P. Winpenny; M. Andruh; *Cryst. Growth Des.*, **2007**, *7*, 1825-1831.
12. A.M. Madalan; N. Avarvari; M. Andruh; *New J. Chem.*; **2006**, *30*, 521-523.
13. A.M. Madalan; C.D. Ene; *Inorg. Chim. Acta*, **2018**, *475*, 184-192.
14. M. Nayak; S. Sarkar; P. Lemoine; S. Sasmal; R. Koner; H.A. Sparkes; J.A.K. Howard; S. Mohanta; *Eur. J. Inorg. Chem.*, **2010**, 744-752.
15. A. Cucos; A. Ursu; A.M. Madalan; C. Duhayon; J.-P. Sutter; M. Andruh; *CrystEngComm*, **2011**, *13*, 3756-3766.
16. T.D. Pasatoiu; C. Tiseanu; A.M. Madalan; B. Jurca; C. Duhayon; J.P. Sutter; M. Andruh; *Inorg. Chem.*, **2011**, *50*, 5879-5889.
17. S.S. Sreejith; N. Mohan; M.R. Prathapachandra Kurup; *Polyhedron*, **2017**, *135*, 278-295.

STUDIA UBB CHEMIA, LXIV, 3, 2019 (p. 203-216)
(RECOMMENDED CITATION)
DOI:10.24193/subbchem.2019.3.17

PRE-COATED MERCURY FILM ON GLASSY-CARBON ELECTRODE FOR THE SIMULTANEOUS DETERMINATION OF Cu^{2+}, Zn^{2+}, Cd^{2+}, AND Pb^{2+} IN WATER

JINGXUAN PEI[a], XIANG YU[a,*] XINGJU LIU[b] AND CHAO ZHANG[c]

ABSTRACT. A mercury film was pre-coated on glassy-carbon electrodes to improve the precision and detection limit of the electrodes in anodic stripping voltammetry. A mixed solution containing 0.1 mg/l Zn^{2+}, 0.01 mg/l Pb^{2+}, 0.01 mg/l Cd^{2+}, and 0.5 mg/l Cu^{2+} was used to investigate the simultaneous detection of these ions by the electrode. The influence of the base solution pH and the accumulation time on the electrochemical reactions of Cu^{2+}, Zn^{2+}, Cd^{2+}, and Pb^{2+} were investigated, as well as the effect of the concentration of the film coating solution and the number of mercury coating step on the stripping signals of the four ions. Optimizing the parameters of the pre-coated mercury film improved the precision of the glassy-carbon electrode in evidence. When the base solution pH was 4.68, and the accumulation time was 300 s, the positions of the stripping peaks were optimal, and the peak signals were at a maximum. When the concentration of the film coating solution was 0.03 mol/l $HgCl_2$, and the mercury coating step was repeated three times, the prepared electrode showed a moderately high elution peak with little noise. The optimized electrode demonstrated superior precision and detection limits in the simultaneous detection of Zn^{2+}, Cd^{2+}, Pb^{2+}, and Cu^{2+}, compared with the uncoated electrode. The calibration curves were highly linear with determination coefficients (R^2) of 0.9913 (Cu^{2+}), 0.9939 (Pb^{2+}), 0.9933 (Cd^{2+}), and 0.9962 (Zn^{2+}); the detection limits (μg/l) were 5 for Cu^{2+}, 1 for Pb^{2+}, 0.1 for Cd^{2+}, and 10 for Zn^{2+}, and the relative standard deviations obtained from five replicate experiments were 4.1% (Cu^{2+}), 2.1% (Pb^{2+}), 2.7% (Cd^{2+}), and 3.4% (Zn^{2+}). It is reasonable to suppose that the precision and detection limits of this mercury film electrode may meet the requirements for the simultaneous detection of multiple heavy metal ions in water in the natural environment.

Keywords: *Glassy-Carbon Electrode, Mercury Film, Heavy Metal Ions, Anodic Stripping Voltammetry*

[a] *University of Geosciences (Beijing), School of Materials Science and Technology, Beijing Key Laboratory of Materials Utilisation of Nonmetallic Minerals and Solid Wastes, National Laboratory of Mineral Materials, 29 Xueyuan Road, Haidian, Beijing 100083, China*

[b] *China University of Geosciences (Beijing) School of Engineering and Technology, 29 Xueyuan Road, Haidian, Beijing 100083, China*

[c] *University of Science and Technology Beijing, School of Mechanical Engineering, Tianjin College, No.1, North Ring Road, Zhujiang, Beijing-Tianjin New City, Baodi District, Tianjin 100083, China*

** Corresponding author: yuxiang@cugb.edu.cn*

INTRODUCTION

Zn^{2+}, Cd^{2+}, Pb^{2+}, and Cu^{2+} are four heavy metal ions commonly found in natural water bodies, and anodic stripping voltammetry is the preferred method used for their detection. The problem is that the precision and detection limits of conventional glassy-carbon electrodes cannot meet the requirements needed for the simultaneous detection in practical applications. A typical case is the groundwater pollution incident of heavy metals in the Dabaoshan area of China in 2013. The detected concentrations of Cu^{2+}, Pb^{2+}, Zn^{2+}, and Cd^{2+} were 28.4, 4.4, 41.39 and 26.7 times the upper limits in the Chinese standard: Quality standard for groundwater (GB/T 14848-93). Such high concentrations of heavy metal ions may lead to severe soil contamination and damage to the health of residents via the food chain. Indeed, cancer mortality rates in Dabaoshan residents have increased to 84% of the total death rate [1]. Conventional detection methods such as high-performance liquid chromatography (HPLC) are limited by high-cost equipment and sophisticated procedures, and cannot achieve in-situ measurements of heavy metal ions in complicated water bodies [2-4]. The portability of the device and in-situ measurement capability allows anodic stripping voltammetry to achieve rapid detection of heavy metal ions in water, and so it can be employed in online monitoring and pre-alerts of heavy metal ions in complicated water bodies [5, 6]. As a core component for stripping analysis, glassy-carbon electrodes are limited by insufficient precision and detection limits for the simultaneous detection of different ions. The good chemical stability and high hydrogen over-potential of the glassy-carbon electrode means that improvements in the precision and detection limits can be achieved through a pre-plated mercury film, allowing the simultaneous detection of Cu^{2+}, Zn^{2+}, Cd^{2+}, and Pb^{2+} in water.

The mercury film coating on the glassy carbon electrode consists of a myriad of tiny mercury droplets; dense and uniform mercury droplets are prerequisites for good electrode performance [7]. The working environment affects the extent of reactions on the electrode surface, and the coating parameters affect the mercury load on the electrode surface and the distribution of the mercury micro-drops. Recent studies to improve the precision and detection limit of glassy-carbon electrodes by mercury film pre-coating have focused on a single internal or external factor, such as coating potential, electrode rotation rate, etc. There have been few systematic studies of how the external working environment of the electrode and the internal coating parameters affect its electrochemical performance. These variables include: 1) the effects of base solution pH and electrode accumulation time on the stripping curves of the electrode. The base solution pH (denotes the working environment

of the mercury film coated electrode) and the accumulation time (a working parameter of the electrode) has a direct effect on the reaction rates of heavy metal ions on the mercury film. 2) The effects of coating solution concentration and the number of mercury coating steps on the stripping curves of the electrode. The coating solution concentration and the number of mercury film coating steps determine the mercury load on the electrode surface, and so affects the surface state and stability of the mercury film. 3) Electrochemical performance test. An electrochemical performance test can reflect the overall performance of the electrode and evaluate its practical applicability. Without intensive studies of base solution pH, electrode accumulation time, coating solution concentration, the number of mercury film coating steps and the electrochemical performance of the electrode, it is impossible to fully understand the effect of a pre-coated mercury film on the precision and detection limit of glassy-carbon electrodes.

In this study, stripping curves of Cu^{2+}, Zn^{2+}, Cd^{2+}, and Pb^{2+} were obtained to reflect electrode performance. We investigated the effect of base solution pH and accumulation time on the electrochemical reactions of Cu^{2+}, Zn^{2+}, Cd^{2+}, and Pb^{2+} (at different concentrations) on the mercury film, as well as the effect of the coating solution concentration and number of coating step on the stripping signals of the different ions. Additionally, mercury film coated glassy-carbon electrodes were prepared under optimized parameters, and their electrochemical performance was tested.

RESULTS AND DISCUSSION

Effects of base solution pH and electrode accumulation time on the stripping curves of the electrode

Effects of base solution pH on the stripping curves of the electrode

The base solution pH affects the reaction rates of the target ions on the electrode surface, and thus affects the peak potential and the current of the stripping curves. The base solution used was a sodium acetate-acetic acid buffer containing 0.125 mol/l sodium acetate and 0.25 mol/l KCl, and its pH value ranged from 4.00 to 5.00 for gradient tests. The accumulation time was 350 s, and the concentration of the coating solution was 0.04 mol/L, with three coating steps.

Fig. 1 shows anodic stripping voltammetry curves of mercury film coated electrodes in base solutions with different pH values. The pH value of the base solution had no significant effect on the stripping current but did affect the stripping peak positions. The pH value of the base solution affected the collection of the data at the bottom of the stripping peaks in the scanning range,

thus affecting the detection accuracy. With a base solution pH of 4.00 (see Fig. 1a), the stripping peak potential was shifted to the right for all four ions tested, and the stripping peak of Cu^{2+} was out of the scanning range. With a base solution pH of 4.50 (see Fig. 1b), the stripping peak potential shifted slightly left, and the stripping peak of Cu^{2+} was within the scanning range, although its peak pattern was not complete and the data at the bottom of stripping peaks could not be collected. With a base solution pH of 4.68 (see Fig. 1c), the stripping peak potential was moderate, the stripping peak pattern was complete, and the data at the bottom of stripping peaks was fully collected for all four ions tested. Hence, the detection accuracy was improved. With a base solution pH of 5.00 (see Fig. 1d), the stripping peak potential shifted to the left, and the data at the bottom of the stripping peak of Zn^{2+} was not collected, which was attributed to the over-fast reaction of Zn^{2+} on the electrode surface.

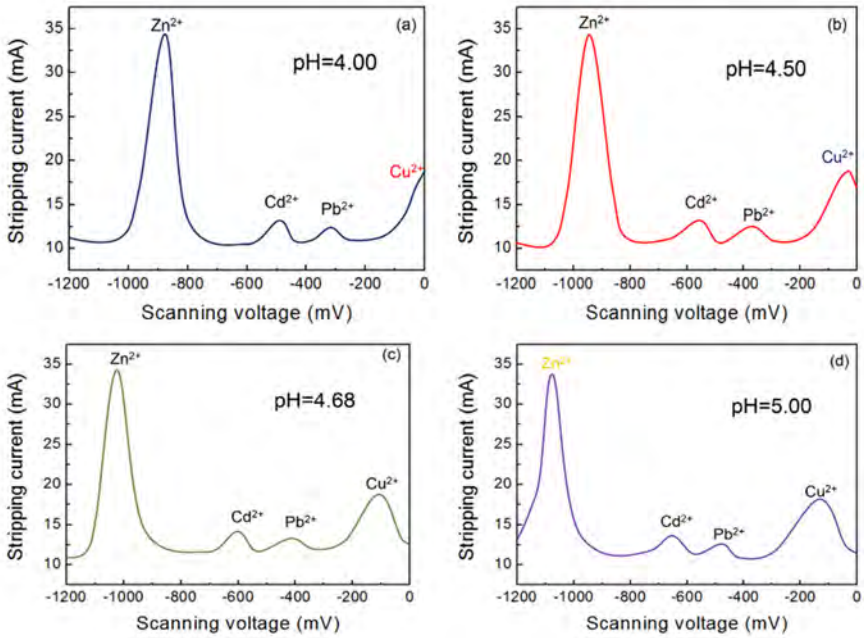

Figure 1. Stripping current curves of the electrode in different base solutions.

Contrary to the predictions of the Nernst equation, changes in the pH of the base solution affected the stripping peak position of the four ions. There were two possible reasons for this unexpected behavior. The first was competition between H^+ and the metal ions [8, 9]. Base solutions with different pH values have different concentrations of H^+. When the concentration of H^+ was too high, the stripping process of heavy metal ions was inhibited

and resulted in a shift of the stripping peak position. The second was the formation of acetate [10]. The reversible ionization reaction of acetic acid occurs readily in solution, and the CH_3COO^- ion would like to combine with heavy metal ions. The concentration of CH_3COO^- decreased with decrease in pH. Consequently, the decrease in the concentration of acetate induces a shift in the position of the stripping peak. At a base solution pH of 4.68, the stripping peak potentials and currents are distinct, and the ion concentrations measured were closest to the standard solution. Hence, it was concluded that 4.68 was the optimum pH value of the base solution.

Effects of accumulation time on the stripping curves of the electrode

Target ions were enriched on the electrode, followed by reverse stripping. The accumulation time had a direct effect on the stripping peak current intensity. Scanning voltages were applied under the corresponding stripping potentials for Cu^{2+}, Zn^{2+}, Cd^{2+}, and Pb^{2+}. The other three parameters selected were: a base solution pH = 4.68, a coating solution concentration of 0.04 mol/l, and three coating steps.

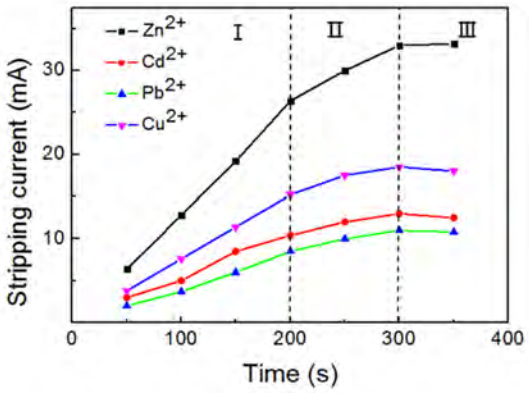

Figure 2. Effect of accumulation time on stripping currents for different ions.

Fig. 2 shows the effect of accumulation time on the stripping currents of the different ions. The effect of accumulation time on the stripping currents of the four ions can be divided into three stages. Stage I (50–200 s): the stripping peak currents of all ions increased rapidly with the accumulation time. This was attributed to the amalgam formed by the reduction of heavy metal ions on the mercury film. This was rapid as the concentrations of the heavy metal ions being reduced were low. Stage II (200–300 s): the enrichment of heavy metal ions on the mercury film was less rapid, resulting in lower rates of increase of the peak currents. Stage III (after 300 s):

amalgam on the mercury film approached saturation, and increases in accumulation time no longer led to increases in the current intensity of the stripping peak. Therefore, 300 s was the optimum accumulation time.

Effect of film coating parameters on the stripping curves of glassy-carbon electrodes

Effect of coating solution concentration

The coating solution concentration affects the mercury load on the electrode surface and thus affects the electrode stability. Glassy-carbon electrodes were coated in different $HgCl_2$ coating solutions (0.01–0.04 mol/l $HgCl_2$) for 70 s, and used for detection in different standard solutions (0.101 mg/l Zn^{2+}, 0.011 mg/l Cd^{2+}, 0.011 mg/l Pb^{2+}, and 0.056 mg/l Cu^{2+}). The other three parameters selected were a base solution pH = 4.68, an accumulation time of 300s, and three coating steps.

Fig. 3 shows the stripping curves of the four metal ions on the electrode prepared under different coating solution concentrations.

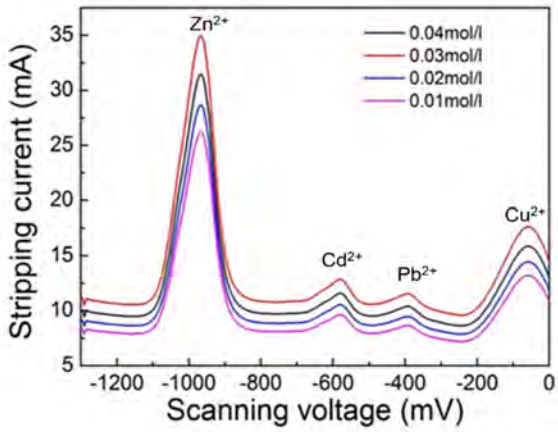

Figure 3. Stripping curves of different metal ions on electrodes prepared under different coating solution concentrations.

The stripping peak intensity increased and then decreased as the coating solution concentration increased, but the peak position remained constant. At a coating solution concentration of 0.01 mol/l, the stripping peak current intensities of all ions were smallest. At a coating solution concentration

of 0.02 mol/l, the stripping peak current intensities of all ions increased slightly. However, the intensities were still insufficient for adequate detection. At a coating solution concentration of 0.03 mol/l, the stripping peak current intensities of all ions were largest. At a coating solution concentration of 0.04 mol/l, the stripping peak current intensities of all ions decreased, and the accuracy also decreased. As the coating solution concentration increased, the mercury load on the electrode surface and the mercury micro-drop size increased, but the stability and detection accuracy of the mercury film increased and then decreased. As the coating solution concentration increased from 0.03 mol/l to 0.04 mol/l, the stripping peak value decreased. This can be attributed to the over-large size of mercury micro-drops, which degraded the stability of mercury film [11, 12]. In other words, peak values of all ions were maximized at a coating solution concentration of 0.03 mol/l, and little signal noise was observed, thus guaranteeing high stripping peak current intensity and good detection accuracy. Therefore, 0.03 mol/l was the optimum coating solution concentration.

Effects of coating step number

The coating step number was an important parameter that can reflect both the coating time and film formation cycle. When the mercury film was prepared with different coating numbers, the increase of the coating step number represents an extension of the coating time as well as the filming cycle. The coating time affects the size of the micro-mercury droplets, and the coating cycle affects the uniformity and compactness of the mercury film.

After the initial film formation, the micro-mercury droplets continued to form a film on the basis of the original film; the distribution of mercury micro-drops determines the amount of noise in the stripping curves. This study investigated stripping peak signals for glassy-carbon electrodes with one, two, and three coating steps for Cu^{2+}, Pb^{2+}, Zn^{2+}, and Cd^{2+}. The concentration of the coating solution was 0.03 mol/l, the pH of the base solution was 4.68, and the accumulation time was 300 s.

Fig.4 shows the stripping currents for electrodes prepared with different numbers of coating steps. Dual peak phenomena and large background waves were observed for the stripping potential of Zn^{2+}, and the stripping peak of Cd^{2+} was not observed. This can be attributed to the low density of mercury micro-drops on the electrode and poor electrode stability, leading to significant noise. With two coating steps, the density of mercury micro-drops increased, but the distribution was not uniform, resulting in excessive sensitivity of the electrode and significant noise. With three coating steps, peak values were reasonable, and the signal shapes were symmetric with little noise observed. Both the

density and distribution of mercury micro-drops on electrode were acceptable, resulting in good electrode stability and high detection precision. Therefore, the optimum number of coating steps was three.

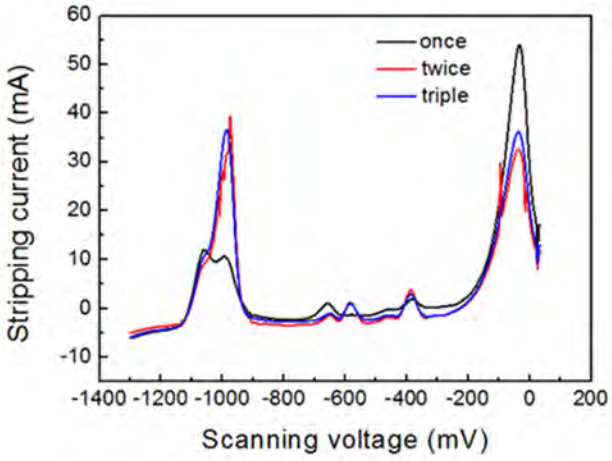

Figure 4. Stripping currents by electrodes prepared with different coating cycles.

Electrochemical performance test

The electrochemical performance of mercury film coated electrodes prepared under the optimized parameters discussed above was evaluated. In addition to overall performance, calibration curves, detection limits, and reproducibility were investigated.

Calibration curve

Standard solutions with a concentration gradient of 0.02 mg/l were prepared and measured. Taking Zn^{2+} as an example, a calibration curve was drawn based on the linear relationship between the Zn^{2+} concentration and the peak current. Fig. 5 shows linear correlation of Zn^{2+} concentration (0.03–0.15 mg/l) *vs.* peak current. The calibration curve obtained was $y = 78.2142x + 14.4464$, and the determination coefficient (R^2) was 0.9913. Similarly, R^2 for Cd^{2+}, Pb^{2+}, and Cu^{2+} were 0.9939, 0.9933, and 0.9962, respectively.

The calibration curve is a guarantee of the detection accuracy of the electrode. The closer the determination coefficient is to 1, the better the electrode performance. Joanna Smajdor *et al.* [13] proposed a renewable glassy-carbon electrode, and the R^2 reported was 0.99. The R^2 values of all electrodes prepared in this study were > 0.99, indicating high detection accuracy.

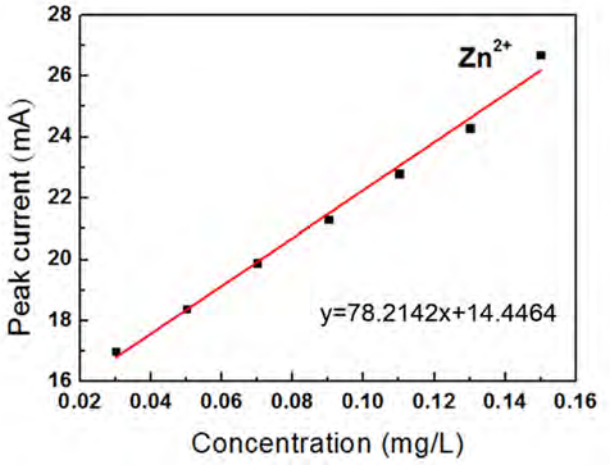

Figure 5. The calibration curve of Zn^{2+}.

Detection limit

The lower detection limit of the electrode was determined by the ratio of the response signal to the noise (signal-to-noise ratio), and the critical level defined as a signal-to-noise ratio = 3. A suitable amount of pure sub-boiling distilled water was used as a blank solution for a control experiment, and the mercury film electrode prepared under the optimal parameters was used to scan the blank solution. The standard deviation of the scan for ten equipotential differences in the scanning curve was used as the electrode noise. Fig. 6 shows the scanning results of a blank solution at 100 mV intervals. The stripping currents were within 9–12.5 mA, the range was concentrated, and the electrode noise was small. The detection limits ($D = 3N/S$, D for detection limit, N for noise and S for sensitivity) calculated were 5 µg/l, 10 µg/l, 1 µg/l, and 0.1 µg/l for Cu^{2+}, Zn^{2+}, Cd^{2+}, and Pb^{2+}, respectively.

The lower detection limit of an electrode determines its application range. Arancibia, V *et al.* [14] proposed a Nafion-mercury coated glassy-carbon electrode for the detection of Cd^{2+}. The detection limit reported for Cd^{2+} was 0.8 µg/l at pH = 3.5 and an accumulation time of 100 s. This method was similar to that proposed in our study, but the detection limit in our study was similar. In another study, a complex polymer modified glassy-carbon electrode was used to detect Pb^{2+} in soft water by stripping voltammetry [15]. The detection limit for Pb^{2+} measured at an accumulation time of 45 min, and a base solution pH of 4.5 was 1.2 µg/l. In our study, a lower detection limit for Pb^{2+} was achieved (0.1 µg/l) with a much shorter accumulation time of 300 s, indicating significant improvements in detection efficiency.

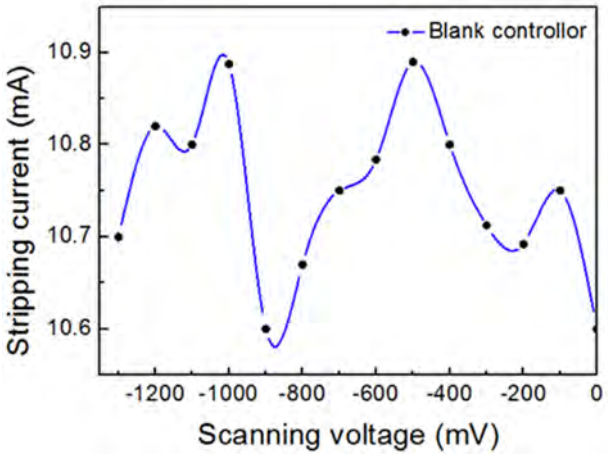

Figure 6. Scanning results of a blank solution.

Reproducibility

The mercury load on the mercury film coated electrode decreased as the number of detection cycles increased. The stability of the electrode was evaluated by multiple repeatability tests. Table 1 summarizes the test results using a mixed solution containing 0.1 mg/l Zn^{2+}, 0.01 mg/l Pb^{2+}, 0.01 mg/l Cd^{2+}, and 0.5 mg/l Cu^{2+}, and also gives the concentration confidence intervals at the 95% confidence level. The step potential was 4 mV. As shown in Table 1, the RSDs for the detection of Zn^{2+}, Cd^{2+}, Pb^{2+} and Cu^{2+} were 3.4%, 2.7%, 2.1% and 4.1%, respectively. The mean concentrations measured were (mg/l) 15.15 -- 15.17 for Zn^{2+}, 1.01 -- 1.04 for Cd^{2+}, 1.45 -- 1.48 for Pb^{2+} and 6.65 -- 6.66 for Cu^{2+}, respectively.

Table 1. Repeatability test results and confidence interval with 95% confidence level of the mixed solution containing 0.1 mg/l Zn^{2+}, 0.01 mg/l Pb^{2+}, 0.01 mg/l Cd^{2+}, and 0.5 mg/l Cu^{2+}.

	1	2	3	4	5	RSD (%)	Mean concentration (mg/l)
Zn^{2+}	14.72	14.96	14.85	15.26	15.99	3.4	(15.15, 15.17)
Cd^{2+}	0.99	0.98	1.04	1.03	1.03	2.7	(1.01, 1.04)
Pb^{2+}	1.44	1.43	1.44	1.48	1.50	2.1	(1.45, 1.48)
Cu^{2+}	6.77	6.77	6.19	6.70	6.87	4.1	(6.63, 6.66)

Currently, great efforts are being made to improve the repeatability of detection by electrodes. A typical example is Jesid Lara *et al.* [16]. They used a polymer-modified glassy-carbon electrode and simultaneously measured Pb^{2+} and Cd^{2+} in a 9.0 μg/l mixed solution. At a base solution pH of 4, an RSD of 2.0% for cadmium and 2.5% for lead were obtained from seven replicate experiments. By comparison, our electrode was prepared by a more convenient preparation method and had similar repeatability.

Recovery degree represents the degree of ion loss during the detection process, and it reflects the accuracy of the electrode. The recovery degree was not applicable in our study due to the absence of impurity ions in the solution system [17, 18].

CONCLUSIONS

Improvement of the precision and detection limit of glassy-carbon electrodes by mercury film coating is critical for water body monitoring and pre-alerts for the natural environment. In this work, a systematic investigation was conducted of the working environment, and the coating parameters for a mercury film coated electrode. The electrochemical performance of the optimized electrode was evaluated in the simultaneous detection of Cu^{2+}, Zn^{2+}, Cd^{2+}, and Pb^{2+}.

1. The pre-coated mercury film parameters were optimized. At a base solution pH of 4.68 and an accumulation time = 300 s, stripping peaks for all ions exhibited complete peak shapes and maximum peak values. At a coating solution concentration of 0.03 mol/l and after three coating steps, the prepared electrode exhibited advisable stripping peak intensities for all ions with a low signal-to-noise ratio.

2. The mercury film coated electrode prepared and operating under optimized parameters demonstrated admirable electrochemical performance. R^2 values of the four ions were all greater than 0.99, and the highest value was 0.9962. The detection limits were all lower than 10 μg/l, and was as low as 0.1 μg/l for Pb^{2+}, with RSD values in the range 2.1% to 4.1%.

As a core component of a rapid detector, such precision and detection limits may enable the mercury film coated electrode to be applicable in simultaneously detecting multiple heavy metal ions in complicated water bodies.

EXPERIMENTAL SECTION

Equipment and reagents

Film coating and testing used an electrochemical analyzer (Safeda Technologies, China). The working electrode was a glassy-carbon electrode (diameter = 3 mm), the reference electrode was Ag/AgCl (3M KCl), and the auxiliary electrode was Pt. The base solution pH was measured with a pH meter (Mettler Toledo, China) and an electronic balance used for weighing was purchased from Jingtian electronic equipment, Shanghai, China.

All reagents used were Guaranteed Reagent (GR) grade. The coating solution used was a $HgCl_2$ solution, and the standard solution was a mixed solution of Cu^{2+}, Zn^{2+}, Cd^{2+}, and Pb^{2+}. These solutions were prepared by adding sub-boiled distilled water into a 1000 mg/l standard solution for atomic absorption. The base solution was a sodium acetate-acetic acid buffer prepared from sodium acetate, potassium chloride, and acetic acid (purchased from Shanghai Pharmaceuticals Holding Co., Ltd). The pH of the solution was set by adjusting the amount of acetic acid added.

Preparation of mercury film coated glassy-carbon electrode

The mercury film coated glassy-carbon electrode was prepared using an electrochemical analyzer. In pre-treatment, the electrode was polished using buckskin until no scratches were observed, rinsed with deionized water, and wiped with filter paper. Then, the electrode was manually polished for 60 s, using a polishing medium of Al_2O_3 powder (particle size of 30 μm) mixed with deionized water, and rinsed. The film was removed after each testing cycle to minimize errors.

At the coating stage, 5 ml of pure water and 5 ml of film coating solution ($HgCl_2$) were injected into the detector cell of the electrochemical analyzer, a backward voltage was applied on the working electrode for 60 s and then left untouched for 10 s with no voltage applied. The concentration (mol/l) of $HgCl_2$ solution used was 0.1, 0.2, 0.3 and 0.4. The number of coating steps ranged from 1 to 3.

Detection of heavy metal ions

The heavy metal ions in a mixed solution containing Cu^{2+}, Zn^{2+}, Cd^{2+}, and Pb^{2+} were detected using the mercury film coated glassy-carbon electrode prepared under optimized parameters. The stripping frequency and the working voltage of the electrochemical analyzer were set at 2 ms and -1.3 V,

respectively, and the step potential was 4mV. 1 ml of standard solution, 5 ml of electrolyte, a 1 ml test sample, 5 ml of pure water, and 5 ml of film coating solution were added together and mixed.

ACKNOWLEDGMENTS

This work was supported by the National Natural Science Foundation of China (Grant No. 51571183) and the Fundamental Research Funds for the Central Universities of China.

REFERENCES

1. P.Y. Li, R. Tian, C.Y. Xue, J.H. Wu, *Environ. Sci. Pollut. R.*, **2017**, 24, 13224.
2. Q.W. Zhou, B.H. Liao, L.N. Lin, W.W. Qiu, Z.G. Song, *Sci. Total Environ.*, **2018**, 615, 115.
3. J.J. Wan, W.X. Duan, K. Chen, *Sensor. Actuat B-Chem.,* **2018**, 255, 49.
4. T. Fujiyoshi, T. Ikamib, K.J. Kikukawaa, M. Kobayashia, R. Takaib, D. Kozakib, A. Yamamotob, *Food Chem.*, **2018**, 240, 386.
5. L.C. Nunes, G.G.A. de Carvalho, D. Santos, F.J. Krug, *Spectrochim. Acta B-Atomic Spectroscopy*, **2014**, 97, 42.
6. E. Flores, J. Pizarro, F. Godoy, R. Segura, A. Gomez, N. Agurto, P. Sepulveda, *Sensor. Actuat B-Chem.*, **2017**, 251, 433.
7. C. Liu, W.X. Cheng, Q. Zeng, X.J. Huang, L.S. Wang, *J. Electroanal. Chem.*, **2017**, 784, 145.
8. N.B. Li, H.Q. Luo, G.N. Chen, *Anal. Sci.*, **2004**, 20, 825.
9. H.B. Li, J. Li, Z.J. Yang, Q. Xu, C.T. Hou, J.Y. Peng, X.Y. Hu, J. *Hazard. Mater.*, **2011**, 191, 26.
10. E. Nagles, V. Arancibia, C. Rojas, R. Segura, *Talanta*, **2012**, 99, 119.
11. N. Nunez-Dallos, C. Cuadrado, J. Hurtado, E. Nagles, O. Garcia-Beltran, *Int. J. Electrochem. Sci.*, **2016**, 11, 9855.
12. S. Armalis, E. Kubiliene, *Chemia Analityczna*, **2001**, 46, 715.
13. J. Smajdor, R. Piech, M. Rumin, B. Paczosa-Bator, Z. Smajdor, *Electroanal.*, **2016**, 28, 394.
14. V. Arancibia, E. Nagles, O. Garcia-Beltran, J. Hurtado, *Int. J. Electrochem. Sci.*, **2018**, 13, 8711.
15. G.G. Vasile, G.L. Arnold, G.O. Buica, E. Diacu, E.M. Ungureanu, C. Dinu, *Rev. Chim. Bucharest*, **2018**, 69, 21.

16. J. Lara, J.F. Torres, O.G. Beltran, E. Nagles, J. Hurtado, *Int. J. Electrochem. Sci.*, **2017**, 12, 6920.
17. L.F. Ribeiro, J.C. Masini, *Electroanal.*, **2014**, 26, 2754.
18. S. Vasanthi, M. Devendiran, S.S. Narayanan, *Appl. Surf. Sci.*, **2017**, 422, 138.

STUDIA UBB CHEMIA, LXIV, 3, 2019 (p. 217-228)
(RECOMMENDED CITATION)
DOI:10.24193/subbchem.2019.3.18

THE PHENOLIC COMPOUNDS, ANTIOXIDANT AND ANTICHOLINESTERASE ACTIVITIES OF *CYCLOTRICHIUM ORIGANIFOLIUM* (LABILL.) MANDEN & SCHENG AND *THYMUS SIPYLEUS* BOISS TEAS FROM TURKEY

ZÜLEYHA ÖZER[a]*

ABSTRACT. In this study, phenolic compounds, antioxidant and anticholinesterase activities of *Cyclotrichium origanifolium* (Labill.) Manden & Scheng and *Thymus sipyleus* Boiss teas were investigated. Two methods were used for the preparation of the teas: infusion and decoction. The quantitative amounts of the phenolic contents were determined by LC-MS/MS. Anticholinesterase activity was measured by Ellman method. Also, the antioxidant activity of the tea samples was determined by three methods: 2,2-diphenyl-1-picrylhydrazyl (DPPH) free radical scavenging, *β*-carotene linoleic acid and CUPRAC assays. Flavonoids and derivatives were the most abundant components of the *C. origanifolium* and *T. sipyleus* teas. The infusion of *C. origanifolium* and decoction of *T. sipyleus* were found to be rich in phenolics. The tea samples exhibited beneficial antioxidant and anticholinesterase activities. There is a useful relationship between the antioxidant capacity and polyphenolic composition of the decoction and infusion of *C. origanifolium* and *T. sipyleus*. This study supported that *C. origanifolium* and *T. sipyleus* used as tea traditionally, are source of natural antioxidant.

Keywords: *Cyclotrichium origanifolium; Thymus sipyleus; phenolics; anticholinesterase; antioxidant.*

INTRODUCTION

For centuries, traditional plants have been presented as an alternative medicine. Herbal remedies are often consumed in the form of tea, which often prepared as decoction and infusion.

Lamiaceae (Labiatae) family is represented 45 genera and 546 species and totally 731 taxa in the Flora of Turkey [1, 2]. *Cyclotrichium* and *Thymus* species are a large genus belonging to the Lamiaceae family. In Turkey, *Cyclotrichium* is presented by 6 species [3]. Some members of this genus,

[a] *Balikesir University, Altinoluk Vocational School, Programme of Medicinal and Aromatical Plants, 10870, Altinoluk, Edremit-Balikesir, Turkey*
** Corresponding author: zuleyhaozer@balikesir.edu.tr*

especially *Cyclotrichium origanifolium* (dağ nanesi), have been widely used as tea, flavoring agents in soups and salads in Eastern and Southern Anatolia [4]. *Thymus* is represented by 39 species with 64 taxa and has been used for a long time as spice or drugs. Members of this genus are called ‘‘kekik’’ in Turkish and used as herbal tea and condiments [5].

Many studies have been conducted to investigate the chemical essential oil content of *Cyclotrichium* and *Thymus* species [4, 6-18]. *C. origanifolium* has rich essential oil content, dominated usually by pulegone which is monoterpene ketone and has various biological activities [4, 11, 12]. There are some reports about biological activities of essential oils and various extracts of *C. origanifolium* [4, 6, 11, 17] and *T. sipyleus* [13, 14, 19]. The essential oil of *C. origanifolium* and *T. sipyleus* were analyzed the first time by Baser *et al*. (Table 1) [12]. Apart from these studies, antioxidant flavonoids of hexane, ethyl acetate, and *n*-butanol extracts of *C. origanifolium* have been reported [20]. Also, Tepe *et al*. reported that the amount of the total phenolics was highest in the dichloromethane extract. The lowest amount of total phenolics was recorded in deodorized hot water extract. Especially polar extracts exhibited stronger activity than non-polar ones [11]. There are many studies in the literature on the phenolics and biological activities of *Cyclotrichium* and *Thymus* extracts [5, 19-25]. (Table 1).

A correlation between the phenolic contents and antioxidant activity of plants have been demonstrated by several studies in medicinal plants. So there is an increasing interest about infusion and decoction of medicinal plants have been presented about phenolics and flavonoids which have strong antioxidant activity in the literature [26-28].

The aim of this study was to determine phenolic compounds, antioxidant and anticholinesterase activity of decoction and infusion of *C. origanifolium* and *T. sipyleus*. To the best of our knowledge, in the literature, there is no study on the chemical composition and biological activities of teas prepared from *C. origanifolium* (CO) and *T. sipyleus* (TS).

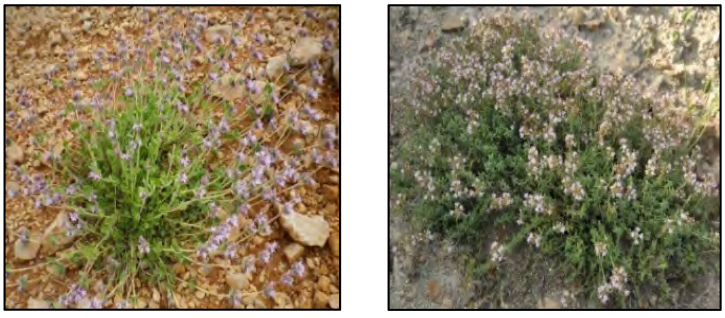

(a) (b)

Figure 1. (a) *C. origanifolium* and (b) *T. sipyleus*

Table 1. Previous studies on *C. origanifolium* and *T. sipyleus*

	Main compounds of EO	**Phenolics, Flavonoids and derivatives**	**Biological Activity**
C. origanifolium	Pulegone, Cis-isopulegone Isomenthone, Isomenthol [12] Isopinocamphone, β-pinene Limonene, Spathulenol [7] Bicyclo[3.1.l]hepten-3-one 2,6,6-trimethyl-,(l.α, 2.*β*, 5.α), pulegone 2-cylohexen-1-ol 1-methyl-4-(1-methylethyl) [17] Pulegone, Menthone Limonene [11] Isopinacamphone Menthone *β*-Pinene [6]	Isosakuranetin Eriodictyol Luteolin Naringenin Apigenin [20]	Antioxidant [11,20] Antimicrobial activities of extracts and EO [11,17] Antibacterial and Antifungal activity of EO [6].
T. sipyleus	Geranial, Neral Linalool, α-Terpineol [16] Borneol, α-Muurolol *β*-Caryophyllene Geranial Neral [13] Thymol, *p*-Cymene γ-Terpinene [14] 1,8-Cineol Linalool Borneol α-Pinen *β*-Pinen Carvone Camphor Carvacrol [18]	Chlorogenic acid Caffeic acid Rosmarinic acid Apigenin [5] Ursolic acid Rosmarinic acid Luteolin, Luteolin 7-*O*-(6”-feruloyl)-*β*-glucopyranoside Luteolin 5-*O*-*β*-glucopyranoside Luteolin 7-*O*-*β*-glucuronide [19]	Antioxidative activity of EO [13] Anti-inflammatory and antibacterial activities of EO [14]. Antioxidant activity of extracts [5,19]. Memory-vitalizing effect of extracts [25]

RESULTS AND DISCUSSION

The results of the studied phenolic compounds of decoction and infusion of CO and TS by LC-MS/MS are shown in Table 2. All the phenolic compounds of samples decoction and infusion were classified into three groups: flavonoids and derivatives, coumaric acids and derivatives and simple phenolics and others. Total 22 compounds, composed of 13 flavonoids

and derivatives, 4 coumaric acids and derivatives and 5 simple phenolics and others were determined in the decoction and infusion of CO and TS. Rutin (1143.27; 517.08 mg/kg dried herb), kaempferol (648.36; 552.11 mg/kg dried herb) and kaempferol-3-O-rutinoside (323.61; 205.92 mg/kg dried herb) were found to be the main phenolic compounds in infusion sample of CO (COI) and decoction sample of CO (COD), respectively. Rosmarinic acid (992.18 mg/kg dried herb), fumaric acid (669.64 mg/kg dried herb) and quercitin (399.12 mg/kg dried herb) were found to be the main phenolic compounds in decoction sample of TS (TSD), whereas fumaric acid (682.17 mg/kg dried herb), rosmarinic acid (643.43 mg/kg dried herb) and kaempferol (255.24 mg/kg dried herb) were found to be the main phenolic compounds in infusion sample of TS (TSI).

Flavonoids and derivatives were the dominant group (2640.01 mg/kg) in the COI with rutin (1143.27 mg/kg), kaempferol (648.36 mg/kg) and kaempferol-3-O-rutinoside (323.61 mg/kg), luteolin (166.82 mg/kg) and penduletin (136.04 mg/kg). Cumaric acids and derivatives were represented with 152.87 mg/kg with rosmarinic acid (85.04 mg/kg), chlorogenic acid (50.79 mg/kg) and caffeic acid (17.04 mg/kg). While simple phenolics and others were detected in scarce amounts (119.91 mg/kg) with fumaric acid (114.24 mg/kg) and syringic acid (5.67 mg/kg).

Similarly, phenolic compounds of COD were characterized by the presence of flavonoids and derivatives (1654.31 mg/kg), with kaempferol (552.11 mg/kg), rutin (517.08 mg/kg) and kaempferol-3-O-rutinoside (205.92 mg/kg). Coumaric acids and derivatives were represented with 175.24 mg/kg. Simple phenolics and others were detected in scarce amounts (73.84 mg/kg) as compared to the flavonoids and derivatives.

Flavonoids and derivatives were the dominant group in the TSD (1506.23 mg/kg) with quercitin (339.12 mg/kg), kaempferol (366.27 mg/kg), luteolin-5-*O*-glucoside (179.38 mg/kg) and luteolin (178.39 mg/kg). Cumaric acids and derivatives were represented with 1163.88 mg/kg and rosmarinic acid (992.18 mg/kg) was the dominant compound in decoction *T. sipyleus*. While simple phenolics and others were represented with 737.26 mg/kg with fumaric acid (669.64 mg/kg).

On the contrary, In TSI, flavonoids and derivatives (872.92 mg/kg), cumaric acids and derivatives (771.44 mg/kg) and simple phenolics and others (707.36 mg/kg) were detected in equal amounts. Kaempferol (255.24 mg/kg) was detected as main flavonoid, rosmarinic acid (643.43 mg/kg) was detected as main coumaric acid derivative and fumaric acid (682.17 mg/kg) was detected as main simple phenolic.

The antioxidant activities were determined with three methods: DPPH, *β*-carotene linoleic acid and CUPRAC. Butylated hydroxytoluene (BHT) and

butylated hydroxyanisole (BHA) were used as standard compounds in DPPH and *β*-carotene linoleic acid assays. DPPH and *β*-carotene analyzes were performed at four concentrations: at 10, 25, 50 and 100 µg/mL.

Table 2. Phenolic contents of CO and TS decoction and infusion

	COD	**COI**	**TSD**	**TSI**
Flavonoids and derivatives				
Pelargonin (1)	42.89±4.36	82.21±4.18	117.51±11.96	117.51±11.96
Penduletin (2)	106.11±10.76	136.04±13.79	35.13±3.56	35.13±3.56
Luteolin (3)	39.48±10.14	166.82±21.43	178.39±45.82	178.39±45.82
Apigenin (4)	32.64±2.63	56.87±4.58	72.46±5.84	4.49±0.36
Quercitin (5)	-	-	**399.12±25.47**	208.5±13.3
Quercetagetin-3,6-dimethylether (6)	112.3±21.03	12.26±2.3	-	-
Luteolin-7-*O*-glucoside (7)	11.22±1.14	30.81±1.57	115.16±11.72	67.79±3.45
Luteolin-5-*O*-glucoside (8)	6.81±0.44	11.04±0.71	179.38±11.54	160.57±10.33
Kaempferol (9)	**552.11±38.97**	**648.36±45.76**	366.27±25.85	**255.24±18.02**
Rutin (10)	**517.08±33.87**	**1143.27±74.88**	18.36±1.2	62.08±4.07
Kaempferol-3-O-rutinoside (11)	**205.92±18.61**	**323.61±29.25**	8.73±0.79	9.39±0.85
Salvigenin (12)	12.8±0.87	14.65±1.00	-	-
Isoquercetin (13)	14.95±4.29	14.07±4.04	15.72±4.51	22.023±6.38
Total (mg/kg dried herb)	**1654.31**	**2640.01**	**1506.23**	**872.97**
Coumaric acids and derivatives				
Caffeic acid (14)	28.29±5.6	17.04±3.37	153.97±30.47	98.86±19.56
Chlorogenic acid (15)	27.86±3.86	50.79±7.03	9.12±1.26	21.36±2.96
t-Ferulic acid (16)	-	-	8.61±0.6	7.79±0.54
Rosmarinic acid (17)	119.09±9.13	85.04±6.52	**992.18±76.08**	**643.43±49.34**
Total (mg/kg dried herb)	**175.24**	**152.87**	**1163.88**	**771.44**
Simple phenolics and others				
Syringic acid (18)	18.12±1.22	5.67±0.38	11.49±0.77	2.66±0.18
Fumaric acid (19)	55.72±3.86	114.24±7.92	**669.64±46.44**	**682.17±47.31**
Gallic acid (20)	-	-	4.59±0.32	4.76±0.33
Pyrogallol (21)	-	-	16.24±1.08	17.77±1.18
Ellagic acid (22)	-	-	35.3±2.36	-
Total (mg/kg dried herb)	**73.84**	**119.91**	**737.26**	**707.36**
Curcumin*				
	1903.39	**2912.79**	**3407.37**	**2351.77**
*** Used as internal standard**				

In DPPH-free radical scavenging activity assay, CO and TS teas at all concentrations (10, 25, 50 and 100 µg/mL) showed very high activity (up to 60%). In the literature, aqueous extracts of *C. niveum* and *T. praecox*

subsp. *caucasicus* var. *caucasicus* had weak scavenging ability 9.96% and 11.36% at 2.0 mg/mL, respectively [23]. Also, the percentage inhibition of free radical scavenging activity by 15 µg/mL concentration of *C. niveum* (Boiss.) Manden and Scheng water extract was found as 31.8% [21]. In view of these tea samples are rich in flavonoids, it can be said that these compounds to be hight antioxidant capacity (Figure 2).

Furthermore, *β*-carotene linoleic acid assay, for all concentrations, COD, COI and TSD showed good activity results while TSI had relatively lower activity (Figure 3). The TSI has showed best inhibition result at a concentration of 100 µg/mL (67.44%). Especially, the richest of the phenolic compounds, the TSD and COI have had good activity values like as the standard compounds (BHA and BHT). For the CUPRAC method, the tea samples showed good activity. Especially, TSD were showed higher activity (3.20 mmol TR g^{-1}), while the lowest activity was showed by COD (1.15 mmol TR g^{-1}), which is the lowest tea sample in terms of phenolic compounds. Curcumin was used as a standard compound (0.9 mmol TR g^{-1}). The results are given in the Figure 4.

The acetyl-cholinesterase (AChE) and butyryl-cholinesterase (BChE) activities of decoction and infusion of CO and TS were determined at 200 µg/mL concentration, for which galanthamine was used as a standard compound. The best inhibition values against AChE and BChE enzymes were shown by COI (58.40% and 60.73%, respectively) and TSD (56.65% and 48.76%, respectively) as compared to galanthamine. The results are given in the Table 3. The aqueous extract of *C. niveum* were also tested for their inhibitory effect aganist AChE and was reported to have 9.68% at 2.0 mg/mL [23]. In the another study, *T. serpyllum* water extract was found to have a low AChE inhibition [29].

The amount of phenolics extracted in TSD and COI are very high comparison with TSI and COD (3407.37 and 2912.79 mg/kg dried herb, respectively). In DPPH, *β*-carotene linoleic acid and CUPRAC assays, the high antioxidant capacity of the TSD and COI is associated with the amount of phenolic compounds.

Considering that decoction sample of TS, rosmarinic acid and fumaric acid were determined as the main compounds, it can be said that these compounds are responsible for the significant antioxidant activity of the tea. Rosmarinic acid, which has antiviral, antibacterial, antiinflammatory and antioxidant activities, is very important phenolic compound [5, 30]. The presence of rosmarinic acid in medicinal plants, herbs and spices has beneficial and health promoting effects.

COI consisted of rutin and kaempferol as main compounds. The effective antioxidant and anticholinesterase activities of COI might be due to the high level of those phenolic compounds. According to previous studies,

rutin and kaempferol had antioxidant, antimicrobial, diabetic, anti-inflammation, antiproliferative, antibacterial, anticancer, antidiabetic, anticarcinogenic, antitumor and antiglycation activities [31, 32]. These results are consistent with the literature.

Previous studies have been showed that, CO solvent extracts were rich in flavonoids (isosakuranetin, eriodictyol, luteolin, naringenin, apigenin) [20] and TS solvent extracts were rich in triterpenic acid (ursolic acid), phenolic acid (rosmarinic acid, chorogenic acid, caffeic acid), and flavonoids (luteolin, luteolin 7-O-(6"-feruloyl)-*β*-glucopyranoside, luteolin 5-O-*β*-glucopyranoside, and luteolin 7-O-*β*-glucuronide, apigenin) [5, 19].

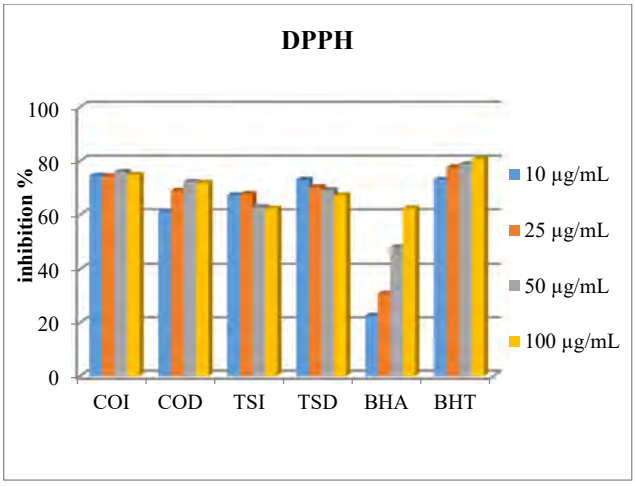

Figure 2. DPPH results of CO and TS.

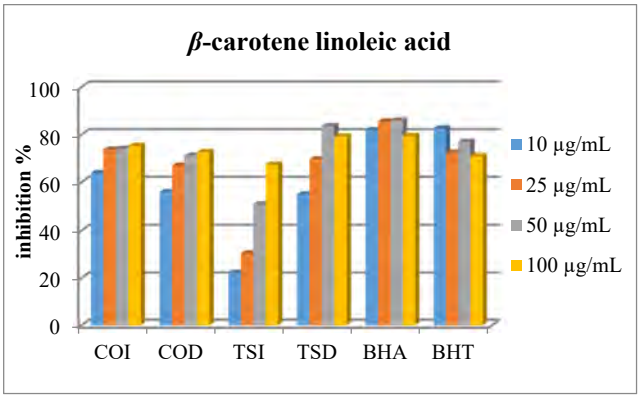

Figure 3. *β*-carotene-linoleic acid assay results of CO and TS.

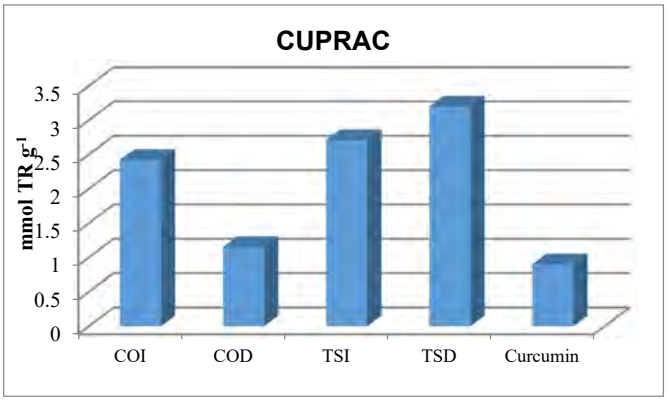

Figure 4. CUPRAC assay results of CO and TS.

Table 3. Anticholinesterase activity of CO and TS (200 µg/mL)

Tea samples	AChE*	BChE*
COI	58.40±1.12	35.21±0.99
COD	40.94±2.52	60.73±4.70
TSI	56.65±5.36	22.93±0.64
TSD	52.82±3.15	48.76±2.64
Galantamine**	86.73±5.25	77.13±4.31

* % inhibition of 200 µg/mL concentration of tea samples
** Galantamine was used as a standard.

CONCLUSIONS

In conclusion, we examined and reported the main phenolic components, antioxidant and anticholinesterase activity of decoction and infusion of CO and TS. The decoction and infusion of the samples were found to be a rich source of phenolics, while rutin and kaempferol were found to be the major units of the composition in CO. Also, rosmarinic acid and fumaric acid were found to be the major units of the composition in TS. Considering the antioxidant capacity determination assays, such as DPPH, *β*-carotene linoleic acid, and CUPRAC methods, there is a good relationship between the antioxidant capacity and polyphenolic composition of the decoction and infusion. This study supports that *C. origanifolium* and *T. sipyleus*, used in tea, food, pharmaceutical and cosmetic industry, are a source of natural antioxidant.

EXPERIMENTAL SECTION

Plant material

The aerial parts of *C. origanifolium* were collected from Antalya, Alanya, Mahmutlar-Hadim road, rocky slopes, (36°34'36.30"N, 32°22'12.05"E, 1298 m) during the full-flowering season in July 2016, Turkey (Herbarium number SV 1543).

The aerial parts of *T. sipyleus* were collected from Balıkesir, Kazdağları, Sarıkız location, rocky slope, (39°42'12.39"N, 26°50'6.55"E, 1648 m), during the full-flowering season in July 2016, Turkey (Herbarium number SV 2466).

The species were identified by Assoc. Prof. Dr. Selami Selvi at Balikesir University. Voucher specimens were deposited at the Herbarium of the Altinoluk Vocational School, Balikesir University, Balikesir, Turkey. The plant samples were allowed to dry in the shade.

Preparation of decoction and infusion samples

4 g of aerial parts of the plant, dried (30 ^{0}C) in the shade and chopped into small pieces. The teas were prepared as following two methods; infusion and decoction.

Infusion; 2 g of the plant were added to 98 mL of distilled boiling water and allowed to stay for 15 minutes.

Decoction; 2 g of the plant were added to 98 mL of distilled water and heated together in a steel kettle and allowed to stay for 15 minutes after boiled.

The teas were filtered with an ashless filter paper. The filtrates were diluted with 25 mL of distilled water. Phenolic compounds were determined by LC-MS/MS. Infusion samples were named as **COI** and **TSI**, decoction was **COD** and **TSD**.

Liquid chromatography-mass spectrometry

LC-MS/MS experiments were performed by a Zivak® HPLC and Zivak® Tandem Gold Triple quadrupole (Istanbul, Turkey) mass spectrometry equipped with a Synergy Max C18 column (250 x 2 mm i.d., 5µm particle size). The mobile phase was composed of water (A, 0.1% formic acid) in methanol (B, 0.1% formic acid), the gradient programme of which was 0-1.00 minute 55% A and 45% B, 1.01-20.00 minutes 100% B and finally 20.01-23.00 55% A and 45% B. The flow rate of the mobile phase was 0.25 mL/min, and the column temperature was set to 30 ^{o}C. The injection volume was 10 µL.

The detailed information on preparation of test solution and evaluation of uncertainty has been reported in the literature [33, 34].

Antioxidant activities

The antioxidant activities were measured based on 2,2-diphenyl-1-picrylhydrazyl (DPPH) free radical scavenging activity [33-38], *β*-carotene linoleic acid assays [33, 34, 37] and cupric (Cu^{2+}) ion reducing power assay (CUPRAC) [33, 34, 39, 40]. The detailed experimental procedure was given in the “Supplementary data”.

Anticholinesterase activity

Inhibitory activities of acetyl- and butyrylcholinesterase were measured by a slightly modified spectrophotometric method, developed by Ellman, Courtney, Andres and Featherston [41-44]. Acetylthiocholine iodide and butyryl thiocholine iodide were used as substrates of the reaction, and DTNB method was applied for the measurement of the anticholinesterase activity [41, 42]. Detailed procedure was given in “Supplementary data”.

Supplementary Supporting information will be provided by the author upon request.

REFERENCES

1. P.H. Davis; *Flora of Turkey and the East Aegean Islands*, 7th ed. London, Edinburgh University Press, **1982**.
2. P.H. Davis; R.R. Mill; K. Tan; *Flora of Turkey and the East Aegean Islands*, 10th ed. London, Edinburgh University Press, **1988**.
3. F. Satıl; A. Kaya; T. Dirmenci; *Nord. J. Bot*., **2011**, *29*, 38-48.
4. K.H. C. Baser; N. Kirimer; G. Tümen; *J. Essent. Oil. Res.,* **1998**, *10*, 1-8.
5. A. Gökbulut; *Trop. J. Pharm. Res*., **2015**, *14*,1871-1877.
6. T. Kilic; A. Karahan; T. Dirmenci; T. Arabaci; E. Kocabas; A.C. Goren; *Chem. Nat. Compd.,* **2007**, *43*, 733-735.
7. S. Aslan; M. Firat; B. Konuklugil; *Chem. Nat. Compd.,* **2007**, *43*, 724-725.
8. A. Alim; I. Goze; A. Cetin; A.D. Atas; N. Vural; E. Donmez; *Afr. J. Microbiol. Res.,* **2009**, *3*, 422-425.
9. K.H.C. Baser; B. Demirci; F. Demirci; N. Kirimer; I.C. Hedge; *Chem. Nat. Compd.,* **2001**, *37*, 336-338.
10. K.H.C. Baser; S. Sarikardasoglu; G. Tümen; *J. Essent. Oil Res.,* **1994**, *6*, 9-12.
11. B. Tepe; M. Sokmen; A. Sokmen; D. Daferera; M. Polissiou; *J. Food Eng.,* **2005**, *69*, 335-342.

12. K.H.C. Baser; N. Kirimer; M. Kürkçüoglu; T. Özek; G. Tümen; *J. Essent. Oil. Res*., **1996**, *8*, 569-570.
13. B. Tepe; M. Sokmen; H.A. Akpulat; D. Daferera; M. Polissiou; A. Sokmen; *J. Food Eng.*, **2005**, *66*, 447-454.
14. F. Demirci; N. Karaca; M. Tekin; B. Demirci; *Microb. Pathog.,* **2018**, *122*, 117-121.
15. C. Ballester-Costa; E. Sendra; J. Fernández-López; J.A. Pérez-Álvarez; M. Viuda-Martos; *Ind. Crop. Prod.,* **2013**, *50*, 304-311.
16. K.H.C. Baser; M. Kürkçüoglu; T. Özek; G. Tümen; A. Akgül; *J. Essent. Oil Res.,* **1995**, *7*, 411-413.
17. R.S. Gokturk; O. Sagdic; G. Ozkan; O. Unal; A. Aksoy; S. Albayrak; M.Z. Durak et al. *J. Essent. Oil Bear. Pl.,* **2013**, *16*, 795-805.
18. G. Yilmaz; I. Telci; N. Kandemir; N. Kaya; *Asian J. Chem.*, **2004**, *16*, 841.
19. U. Özgen; A. Mavi; Z. Terzi; C. Kazaz; A. Asçi; Y. Kaya; H. Seçen; *Rec. Nat. Prod.,* **2011**, *5*, 12.
20. A. Guzel; H. Aksit; M. Elmastas; R. Erenler; *Phcog. Mag*., **2017**, *13*, 316.
21. I. Gulcin; A.Z. Tel; E. Kirecci; *Int. J. Food Prop*., **2008**,*11*, 450-471.
22. A. Ozdemir; M. Yildiz; F.S. Senol; Y. D. Şimay; B. Ibişoglu; A.Gokbulut; I.E. Orhan; M. Ark; *Food Chem. Toxicol.* **2017**,*109*, 898-909.
23. I. Orhan; F.S. Şenol; A.R. Gülpinar; M. Kartal; N. Şekeroglu; M. Deveci; K. Kan; B. Şener; *Food Chem. Toxicol.,* **2009**, *47*, 1304-1310.
24. S. Emen; B. Çeken; G. Kızıl; M. Kızıl; *Pharm. Biol.,* **2009**, *47*, 219-229.
25. F.S. Senol; I.E. Orhan; U. Ozgen; G. Renda; G. Bulut; L. Guven; E.S. Karaoglan; H.G. Sevindik; K. Skalicka-Wozniak; U.K. Caliskan; N. Sekeroglu; *S. Afr. J. Bot.,* **2016**, *102*, 102-109.
26. Y. Kiselova; D. Ivanova; T. Chervenkov; D. Gerova; B. Galunska; T. Yankova; *An International Journal Devoted to Pharmacological and Toxicological Evaluation of Natural Product Derivatives*, **2006**, *20*, 961-965.
27. E.W.C. Chan; Y.Y. Lim; K.L. Chong; J.B.L. Tan; S.K. Wong; *J. Food Comp. Anal.,* **2010,** *23*, 185-189.
28. H.D. Dorman; M. Koşar; K. Kahlos; Y. Holm; R. Hiltunen; *J. Agric. Food Chem.,* **2003**, *5116*, 4563-4569.
29. A.T. Mata; C. Proença; A.R. Ferreira; M.L.M. Serralheiro; J.M.F. Nogueira; M.E.M. Araújo; *Food Chem.,* 2007, *104*, 510–517.
30. M. Petersen; M.S. Simmonds; *Phytochem.,* **2003**, *62*, 121-125.
31. B. Gullón; T.A. Lú-Chau; M.T. Moreira; J.M. Lema; G. Eibes; *Trends Food Sci. Tech.*, **2017**, *67*, 220-235.
32. Q. Lu; M. Hao; W. Wu; N. Zhang; A. T. Isaac; J. Yin; X. Zho; L. Du; X. Yin; *Acta Biochim. Pol.*, **2018**, *65*, 35-41.
33. Z. Ozer; *J. Turk. Chem. Soc., Sect. A: Chem*., **2018**, *5*, 445-456.
34. Z. Ozer Sagir; S. Carikci; T. Kilic; A.C. Goren; *Int. J. Food Prop*., **2017**, *20*, 2994-3005.
35. E. Köksal; E. Bursal; I. Gülçin; M. Korkmaz; C. Çağlayan; A.C. Gören; S.H. Alwasel; *Int. J. Food Prop*., **2017**, *20*, 514–25.

36. A. Ertaş; A.C. Gören; N. Haşimi; V. Tolan; U. Kolak; *Rec. Nat. Prod.,* **2015**, *9*, 105-115.
37. H.E. Miller; *J. Am. Oil Chem. Soc.,* **1971**, *48*, 91.
38. M.S. Blois; *Nature,* **1958**, *181*,1199-2000.
39. R. Apak; K. Güçlü; M. Özyürek; S.E. Karademir; *J. Agr. Food Chem.,* **2004**, *52*, 7970-7981.
40. M. Bener; Y. Shen; Z. Xu; R. Apak; *Rec. Nat. Prod.,* **2016**, *10*, 794–9.
41. A.C. Goren; G. Bilsel; M. Bilsel; *J. Chem. Metrol.,* **2007**, *1*, 1-10.
42. P. Kalin; I. Gulcin; A.C. Goren; *Rec. Nat. Prod*., **2015**, *9*, 496-502.
43. G.L. Ellman; K.D. Courtney; V. Andres; R.M. Featherstone; *Biochem. Pharma.*, **1961**, *7*, 88-95.
44. A. Yılmaz; M. Boga; G. Topçu; *Rec. Nat. Prod*., **2016**, *10*, 530-541.

STUDIA UBB CHEMIA, LXIV, 3, 2019 (p. 229-237)
(RECOMMENDED CITATION)
DOI:10.24193/subbchem.2019.3.19

COMPARATIVE ANALYSIS OF WALNUTS AND PEANUTS OILS

SABINA NIȚU[a], MIRABELA PĂDURE[a], ANDRA TĂMAȘ[a,*], LUCIAN MIRCEA RUSNAC[a]

ABSTRACT. In this paper, a comparative study of the physico-chemical properties and composition of walnuts and peanuts oils obtained by cold pressing or Soxhlet extraction in hexane was performed. The physical properties (color, density, refractive index, acidity, saponification, iodine and peroxide values, rheological behavior), the distribution of the major fatty acids in oils (through gas-chromatographic analysis) and the metal content were determined.

Keywords: *cold pressing, extraction, oil, peanuts, viscosity, walnuts*

INTRODUCTION

Peanuts or hazelnuts are the fruits of a leguminous plant (*Arachis Hipogaea*) which are often included in the walnut category, due to their composition, properties and similar benefits.

Although walnuts are the fruits of the walnut tree (*Juglans regia L.*), they do not have a characteristic sweet taste of fruits and are noted for their high content of fats and nutrients (vitamin E and B1, Mg, Ca, Cu, Mn, P, fiber), which gives them an appreciated nutritional value and multiple benefits for health. Recent studies have shown that walnuts, due to their high content of polyphenols, have an antioxidant capacity superior to fish oil [1]. The main benefits of walnuts consumption on health are: lowering of cholesterol and serum triglycerides [2], reducing blood pressure and the risk of heart attack [3,4], hypoglycemic action for type 2 diabetes, anti-inflammatory action [5], antimicrobial activity [6].

Peanut oil, is quite rich in vitamin E, which is an essential vitamin for human beings. It is particularly important for the maintenance and health of the skin, protecting it from the effects of free radicals that cause wrinkles, blemishes, and other signs of premature aging [7].

[a] *Politehnica University of Timișoara, Faculty of Industrial Chemistry and Environmental Engineering, 6 Vasile Pârvan Bv., RO-300223, Timișoara, Romania*
** Corresponding author: andra.tamas@upt.ro*

The pleasant taste, nutritional value and health benefits recommend the consumption of nuts as such or in the form of oil, especially that obtained by cold pressing.

The current policy of the European Union is directed towards stimulating nuts production by granting non-refundable financial aid for the establishment and development of nut tree cultures [8].

In this paper, a comparative study of the composition and physico-chemical properties between walnuts and peanuts oil was carried out.

RESULTS AND DISCUSSION

For a number of three samples of walnuts/peanuts with known mass, the average moisture content is shown in Table 1.

Table 1. The moisture content of the raw nuts

Type of nuts	Humidity (wt.%)
Walnuts	2.0
Peanuts	1.1

The final separation yields compared to the amount of processed nuts are presented in Table 2, and the main properties of the oils are shown in Table 3.

Table 2. The final separation yields

Oil obtained (wt.% relative to nuts)			
Walnuts		Peanuts	
Cold pressing	Soxhlet extraction	Cold pressing	Soxhlet extraction
34	41	30	32

Table 3. The main properties of the oils

Property	Walnuts		Peanuts	
	Cold pressing	Soxhlet extraction	Cold pressing	Soxhlet extraction
Appearance	Pale yellow	Yellowish	Yellowish	Yellowish
Density, g cm^{-3}	0.927	0.926	0.918	0.908
Refractive index (n_D 20°C)	1.478	1.475	1.4714	1.4722
Acidity index (mg KOH g^{-1})	1.09	1.34	4	2.99
Saponification value (mg KOH g^{-1})	188	193	182.53	161.12
Iodine value, g I_2/100 g	151.8	158.6	80.27	78.88
Peroxide value, (mmol O_2 kg^{-1}, max)	8.2	8.9	0.05	3.61

The density of peanuts oil is slightly lower than that of the walnuts oil, and the values obtained for the refractive index are almost identical for both types of oils, regardless of the obtaining method.

The iodine values are higher for walnuts oil than for peanuts oil, which proves a higher content of unsaturated triglycerides.

The peroxide values were higher for walnuts oil, the differences being justified by the higher content in unsaturated fatty acids demonstrated by the higher iodine values.

The results of the elemental analysis are presented in Table 4.

Table 4. The metal content of the oils

mg kg^{-1} oil	**Walnuts oil**		**Peanuts oil**	
	Cold pressing	Soxhlet extraction	Cold pressing	Soxhlet extraction
Pb^{2+}	0.081	0.059	<0.06	-
Cu^{2+}	0.268	0.256	0.184	0.276
Zn^{2+}	55.93	42.35	29.9	33.5
Fe^{n+}	22.87	21.46	69.7	56.3
Ca^{2+}	40.5	32.65	23.2	30.1
Mg^{2+}	16.75	22.85	37.6	47.8
Cr^{3+}	0.089	0.084	2.91	2.43
Mn^{2+}	0.0029	0.0028	-	-
Cd^{2+}	0.0021	0.0019	1.51	1.66

Although the content of macroelements (Ca^{2+}, Mg^{2+}, K^{+} and Na^{+}) in nuts is important [9], these being linked to proteins, much smaller quantities pass into the oil. Potentially toxic elements (As, Cd, Pb) indicate the degree of soil pollution in the area of origin.The higher Fe and Zn content for pressed oils can be explained by contamination from moving metal elements in direct contact with the oleaginous material. The presence of metals (even non-toxic) in the oil may affect in time its quality by the action of catalyzing of some oxidative degradation processes. To minimize oxidative degradation it is necessary to avoid metal contamination from pressing elements.

The IR spectra of the two oils are presented in Figure 1a, b.

The spectral bands for both types of oil are: $\vartheta_{C=O}$esteric = 1742.85cm^{-1}; $\vartheta^{as}_{CH_2}$= 2922.56cm^{-1}; $\vartheta^{as}_{CH_2}$= 2921.54 cm^{-1}, $\vartheta^{s}_{CH_2}$= 2853.18 cm $^{-1}$, ϑ_{C-O}= 1160.54 cm^{-1}; 1095.70 cm^{-1}. These spectral bands illustrate the vibrations of the functional groups (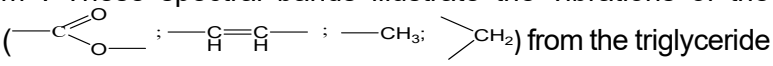) from the triglyceride structure, the majority components of all oils.

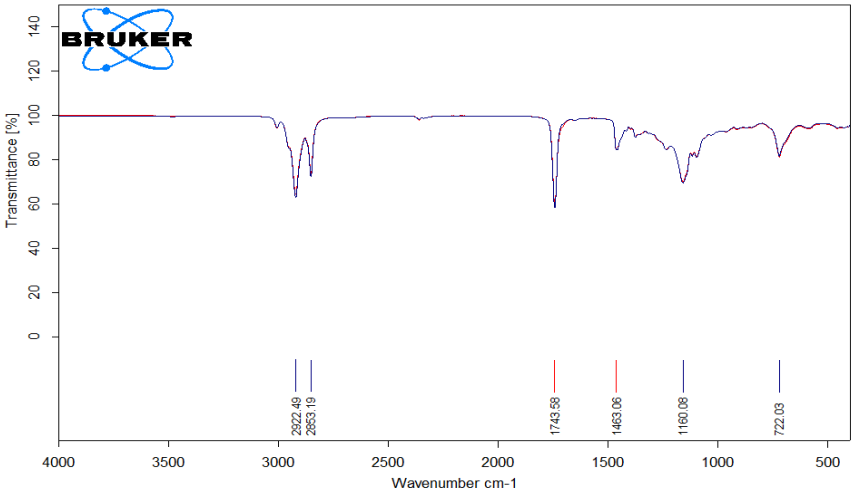

Figure 1a. The IR spectrum of walnuts oils

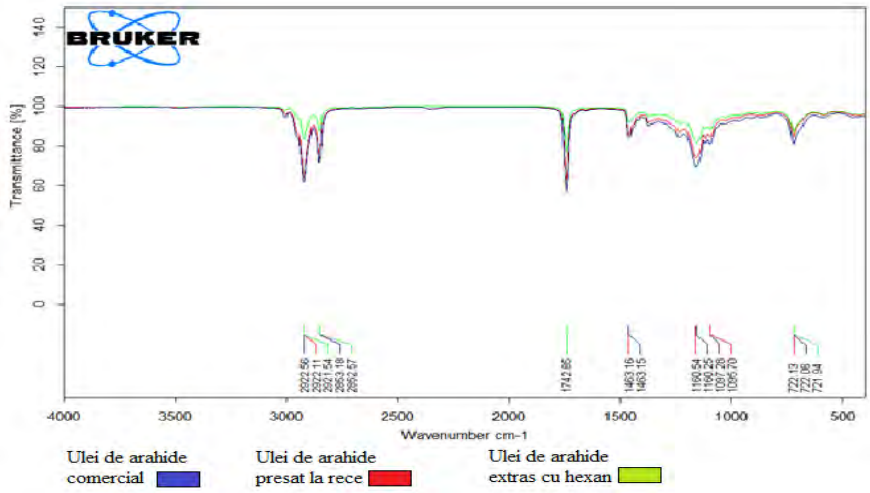

Figure 1b. The IR spectrum of peanuts oils

The IR spectra overlap perfectly regardless of the oil and the obtaining method, the distribution of fatty acids not influencing the position of the bands.

The distribution of the fatty acids in the oils is presented in Table 5.

Table 5. The distribution of fatty acids in the oils

		C16:0	C18:2	C18:1	C18:0	C20:0
Walnuts oil	Cold pressing	5.08	62.75	29.50	1.96	0.71
	Soxhlet extraction	5.08	62.75	29.50	1.96	0.71
Peanuts oil	Cold pressing	5.19	14.68	73.64	-	-
	Soxhlet extraction	3.57	17.08	69.75	-	-

For walnuts and peanuts oils obtained by cold pressing, the $\tau = f(\dot{\gamma})$ dependence is shown in Figure 2.

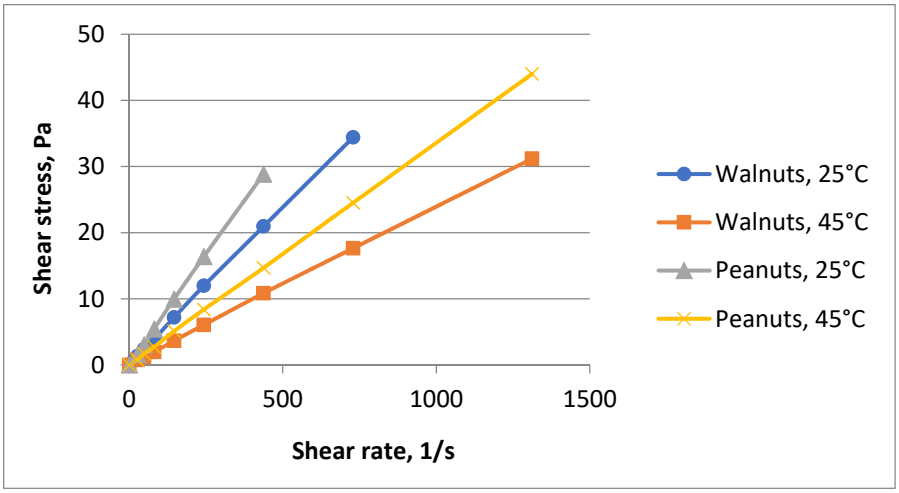

Figure 2. Shear stress (τ) *vs.* shear rate ($\dot{\gamma}$) for walnuts and peanuts oils at different temperature values

It is noted that for both oils the dependence $\tau = f(\dot{\gamma})$ is linear, which shows a Newtonian behaviour. Increasing temperature led to a decrease in the viscosity of the samples but without change of the Newtonian behaviour.

Using the TableCurve 2D program, the rheological equations corresponding to these dependences were established (Table 6). From the slopes of the obtained straight lines, it was observed that the peanuts oil has a higher dynamic viscosity, on average 41,5%, compared to that of walnuts oil.

The exponential decrease of the samples viscosity with temperature is described by an Arrhenius-type equation:

$$\eta = A \cdot \exp\left(\frac{E_a}{R \cdot T}\right) \quad (1)$$

where: E_a - the activation energy of viscous flow, $J \cdot mol^{-1}$; R - the universal gas constant $J \cdot mol^{-1} \cdot K^{-1}$; T - the absolute temperature, K; A - material constant, $Pa \cdot s$ [10,11].

Table 6. Rheological equations for cold-pressed walnuts and peanuts oils

Temperature, °C	**Eq.** $\tau = \eta \cdot \dot{\gamma}$		Viscosity increasing*, %
	Walnuts oil	Peanuts oil	
25	$\tau = 0.0476 \cdot \dot{\gamma}$	$\tau = 0.0664 \cdot \dot{\gamma}$	39.5
35	$\tau = 0.033 \cdot \dot{\gamma}$	$\tau = 0.0477 \cdot \dot{\gamma}$	44.5
45	$\tau = 0.024 \cdot \dot{\gamma}$	$\tau = 0.0337 \cdot \dot{\gamma}$	40.4

*Peanuts oil compared to walnuts oil

Through the measurements at different temperatures, it was possible to establish the dependence ln η = f(1/T) and to calculate the E_a values. Particular expressions of eq.(1) for the two oils are given in Table 7.

Table 7. Arrhenius-type equations for walnuts and peanuts oils

Oil type	**Eq. (**$\eta = A \times 10^6 \exp(E_a / R \cdot T)$**)**	**E_a,** $kJ \cdot mol^{-1}$
Walnuts (cold-pressed)	$\eta = 0.86 \exp(3251/T)$	27.0
Walnuts (Soxhlet)	$\eta = 2.25 \exp(2860/T)$	23.8
Peanuts (cold-pressed)	$\eta = 1.41 \exp(3207/T)$	26.6

CONCLUSIONS

The low humidity of walnuts and peanuts is a prerequisite for long-term storage stability under appropriate conditions and, consequently, of properly obtained oils.

Gas chromatographic analysis of the fatty acid methyl esters revealed a higher content (62.57 wt.%) of linoleic acid in walnuts than in peanuts (35.33 wt.%) where the majority is oleic acid (69÷73 wt.%).

Linoleic acid (Omega-6) is one of the essential fatty acids that enter the structure of cell membranes and is involved in the structure of prostaglandins. The lower linoleic acid content of peanuts oil is expected to provide better thermal stability.

By the composition and the ratio of the fatty acids contained, both oils are valuable components of a balanced diet.

Although the oil yields are slightly higher for solvent extraction compared to pressing, it must be taken into account that the first method involves an additional desolvation operation and the oil contamination with traces of solvent. Regarding pressing, the efficiency can be improved by using more efficient pressing machines.

EXPERIMENTAL SECTION

The raw materials were of Romanian origin: walnuts from Caransebeș area, and peanuts from southern Oltenia (Bratovoiești, Dolj).

The oils were obtained by two methods: cold pressing (Piteba press) and extraction in hexane by the Soxhlet method, followed by desolvation through the vacuum evaporation of hexane.

In order to obtain the oils, the moisture content of the nuts was determined by means of a MA X2 moisture analyzer.

Before the oils were obtained, the walnuts/peanuts were dried in the oven at 60˚C for 12 hours. Cold pressing was carried out with the Piteba press after a preliminary grinding of nuts. To increase the separation efficiency, the remaining oil in the press cake was separated by vacuum filtration at 5 mmHg. In the case of extraction, a Soxhlet apparatus was used. Two samples of 100 g dried and crushed nuts were extracted, successively, with 400 mL of hexane (for each sample 6 siphons). The hexane was removed by means of a rotary evaporator at 270 mmHg and bath temperature 60˚C (boiling temperature 40˚C).

At 20ºC, the density (Method no. 920.213) and the refractive index (Method no.921.08) were determined following AOAC methods [12].

The acidity of the oils was determined by titration with KOH solution toward phenolphthalein (Method no. 972.28). The saponification values were determined by refluxing with an excess of KOH alcoholic solution and retitrating the excess of KOH with hydrochloric acid toward phenolphthalein (Method 920.160). The degree of unsaturation of the oils was determined as iodine value (g I_2/100 g oil) (Method no. 993.20) [12].

The peroxid values were determined by titration with 0.1N sodium thiosulphate solution using starch as an indicator (Method 965.33), according to [12].

To determine the content of metals the oils were calcined at 550°C for 5 hours to remove the organic part. The ash resulted after calcination was mineralized with 10 mL of concentrated HCl and 5 mL of concentrated HNO_3. After the ash dissolution the sample was filtered, washed with distilled water and brought to a volume of 50 mL (volumetric flask).

The elemental analysis was performed by flame atomic absorption spectrometry using the Varian AAS 280 FS atomic absorption spectrometer.

The evaluation of the fatty acids profile of the oils was performed by GC/MS analysis. A Brucker SCION 436-GC system was used (Bruker Co., Billerica, MA, USA). The acquisition and processing of GC/MS data was accomplished using the MS Workstation 8 software package for SCIONTM (Bruker Co., Billerica, MA, USA). Chromatograms and mass spectra corresponding to the chromatographic peaks were recorded using the gas chromatograph system GC/MS Thermo Scientific TRACE 1310, ITQ 1100 Ion Trap MS. The column used was TG-5MS 30 x 0.25mm x 0.25µm, Thermo Scientific. The MS parameters were: the transfer line temperature at 310˚C, the reading range 35-700 m/z. Specifically, the methyl esters obtained through the transesterification of the oils with methanol in the presence of BF_3, were used. As internal standard was used hexadecane.

The rheological characterization of the oils was carried out under thermostatic conditions (temperature range 25÷45°C), using a rotation viscometer Rheotest-2. The device allows the measurement of the torsion moment appeared thanks to the ring-shaped substance layer placed between a fixed cylinder and a rotating one with known revolution. The torsion moment is correlated with the shear stress (τ). The revolution and the ring-shaped layer thickness determine the shear rate ($\dot{\gamma}$). The flow curves $\tau = f(\dot{\gamma})$ of the oil samples were plotted by increasing (forward measurements) and decreasing (backward measurements) the shear rate in the range 3÷1312 s^{-1}. Average shear stresses were calculated.

REFERENCES

1. C. Hudthagosol; E. Haddad; R. Jongsuwat; *J. Med. Assoc. Thai,* **2012**, *95(6)*, S179-S188
2. H. Jamshed; F.A. Sultan; R. Iqbal; A.H. Gilani; *J. Nutr.,* **2015**, *145(10),* 2287-2292
3. L.Wu; K. Piotrowski; T. Rau; E. Waldmann; U.C.Broedl; H. Demmelmair et al., *Metabolism*, **2014**, *63(3)*, 382-391

4. P. Lopez-Uriarte; R. Nogues; G. Saez; M. Bullo; M. Romeu; L. Masana; C. Tormos; P. Casas-Agustench; J. Salas-Salvado, *Clin.Nutr.,* **2010**, *29(3)*, 373-380
5. G. Grosso; R. Estruch, *Maturitas*, **2016**, *84*, 11-16
6. R. Saxena; D.D. Joshi; R. Singh, *Int. J. Essent. Oil Ther.,* **2009**, *3*, 1-4
7. https://www.organicfacts.net/health-benefits/oils/peanut-oil.html, accessed on 16.03.2019
8. www.afir.ro, accessed on 27.10.2018
9. Juranovic, M. Zeiner, D. Hlebec, *Int. J. Environ. Res. Public Health*, **2018**, *15*, 2674-2682
10. T. Budtova; P. Navard, *Nord. Pulp & Pap.Res.J.*, **2015**, *30(1),* 99-104
11. S. Goh; E. Giap, *Int. J. Phys. Sci.,* **2010**, *21(1)*, 29-39
12. *Official Methods of Analysis of AOAC International*, edited by P. Cunniff, 16th ed., AOAC International, Arlington, **1995**, Methods 920.213, 921.08, 972.28, 920.160, 993.20, 965.33.

STUDIA UBB CHEMIA, LXIV, 3, 2019 (p. 239-247)
(RECOMMENDED CITATION)
DOI:10.24193/subbchem.2019.3.20

HPLC ANALYSIS OF EXTRACTS OF FRESH PETALS OF *PAPAVER RHOEAS* L.

JASMINA M. VELICKOVIC[a], MILAN N. MITIC[b], BILJANA B. ARSIC[b], DUSAN Đ. PAUNOVIC[a], BRANKA T. STOJANOVIC[a], JOVANA N. VELJKOVIC[b], DANICA S. DIMITRIJEVIC[a], SLAVICA D. STEVANOVIC[a], DANIJELA A. KOSTIC[b]*

ABSTRACT. *Papaver rhoeas* L. (Papaveraceae) is an annual grass native to many regions of the world, which is known to possess several pharmacological activities. It is also known that represent a rich source of anthocyanins. In this study, the content of the anthocyanin was determined in the examined various extracts of fresh petals by HPLC analysis. The most represented anthocyanins in the extracts of *Papaver rhoeas* L. are delphinidin-3-*O*-glucoside, cyanidin-3-*O*-glucoside, cyanidin-3-*O*-rutinoside, peonidin-3-*O*-glucoside, petunidin-3-*O*-glucoside, petunidin-3-acetylglucoside, and delphinidin-3-*p*-coumaroylglucoside. Acyl derivatives of anthocyanins in the water extract have not been identified. By comparing the contents of individual anthocyanins, the glycosides (polar) are better extracted with 50% alcohol solution, and their acyl derivatives are better extracted with pure alcohol. The water solution is the least suitable for anthocyanin extraction.

Keywords: *anthocyanins, Papaver rhoeas L., HPLC analysis.*

INTRODUCTION

Medicinal plants and their extracts deserve special attention because of the vital influence they have on human health. For the majority of the world population, medicinal plants represent the primary source of health care. According to the World Health Organization (WHO) report, almost 80% of people in marginal communities use only medicinal plants for the treatment of various diseases [1].

[a] *University of 'Union – Nikola Tesla' Beograd, Department of Advanced Food Technologies, Faculty of Applied Sciences, Dušana Popovića 22a, 18 000 Niš, Republic of Serbia*
[b] *University of Niš, Faculty of Sciences and Mathematics, Višegradska 33, 18000 Niš, Republic of Serbia*
** Corresponding author: danijelaaakostic@yahoo.com*

Papaver rhoeas L. (family: Papaveraceae) is commonly known as corn poppy and found wild in various parts of the world. *Papaver rhoeas* L. has a long history of medicinal usage. Extracts derived from this plant have been used for the treatment of a wide range of diseases including inflammation, diarrhea, sleep disorders, cough, analgesia and also the reduction of withdrawal signs of the opioid addiction [2, 3]. The flowers of corn poppy have a long history of medicinal usage, especially for ailments in the elderly and children. However, the plant does contain alkaloids, which are still under investigation, and so should only be used under the supervision of a qualified herbalist. The flowers and petals are anodyne, emollient, expectorant, hypnotic, slightly narcotic, and sedative [4]. An infusion is taken internally in the treatment of bronchial problems and coughs, insomnia, poor digestion, nervous, digestive disorders, and minor painful conditions. The flowers are also used in the treatment of jaundice. The petals are harvested as the flowers opened and dried for later use. They should be collected on a dry day and can be dried or made into syrup. The plant has been suggested to have anticancer properties [5].

Anthocyanins which are natural pigments widely distributed in nature, responsible for the colors of innumerable fresh petals. The common anthocyanidins found in the majority of colored plants are pelargonidin, cyanidin, delphinidin, peonidin, petunidin, and malvidin. The proportion and amount of each anthocyanidin are significantly influenced by cultivar type and agricultural conditions [5].

The effects of concentration methods such as vacuum, microwave and conventional heating methods on total phenolic and anthocyanin contents, antiradical activity, antioxidant capacity and color of *Papaver rhoeas* L. (poppy) sorbet, a traditional beverage of Turkey, were investigated. The lowest initial anthocyanin content was found to be 571.31 mg cyn-3-glu/kg using the conventional method, and the highest anthocyanin content was determined to be 774.49 mg cyn-3-glu/kg in the vacuum treated sorbet at the beginning of the storage. Their results revealed that the poppy sorbet was an excellent source of phenolics and anthocyanins. Storage degradation of poppy anthocyanins followed the first-order reaction kinetics. The concentration method and storage temperature had a significant effect on the bioactivity and color of sorbets [6].

The variation in anthocyanins content of the petals of red poppy (*Papaver rhoeas* L.) during the development of the flower from the closed bud stage has been investigated by thin-layer chromatography. The densitograms were recorded at 465 nm; they show gradually increasing peaks of red anthocyanins in the petals of closed buds, partly opened buds and fully developed flower and changes in the proportions of several anthocyanins, with various R_F values, during the growth of the flower [7].

In our previous work, the contents of total phenols, flavonoids, anthocyanins in different extracts of petals of *P. rhoeas* L. were determined, and it was found to contain high concentrations of these compounds. Their antioxidant activity was also tested using the DPPH method, and it was found to exhibit high antioxidant activity. The examined extracts show both antibacterial and antifungal activity [8]. *P. rhoeas* L. was the subject of the investigation earlier [9], but our previous study is complementary to the investigations by other research groups.

Anti-oxidant and anti-radical *in vitro* properties and *in vivo* topical anti-inflammatory activity of ten hydroalcoholic extracts of edible plants including poppy (*Papaver rhoeas* L. ssp.), from the Calabria region (Italy) were reported as well [10].

Antioxidant, antimutagenic and anticarcinogenic properties of *P. rhoeas* L. extract have been studied recently on *Saccharomyces cerevisiae.* Based on the well-expressed properties obtained in this work, the *P. rhoeas* L. extract could be recommended for further investigations and possible use as a food additive [11].

Qualitative and quantitative determinations of the contents of flavonoids and anthocyanins in various extracts obtained from *P. rhoeas* L. using the HPLC method was not performed before, so we are the first research group who has investigated, and reported the results. The influence of solvent on the extraction of these compounds was investigated in order to find the best solvent for the extraction which can be used in food industry.

RESULTS AND DISCUSSION

Red pigment, a natural antioxidant present in the petals of the red poppy, belongs to anthocyanins. Anthocyanin is the general name applied to the glycosides of anthocyanidin chromophores which are the origin of the red, violet, and blue colors found throughout the plant kingdom, such as the colors of petals, leaves, and fruits. Only a few anthocyanidin nuclei have been found despite the great variety of plant colors. The major anthocyanidins found in nature are pelargonidin, cyanidin, peonidin, delphinidin. The content of anthocyanins in our previous work ranged from 4.72-5.193 mg/g of fresh petals in different extracts of *P. rhoeas* L. from South-east Serbia [8].

The content of total anthocyanins determined by the pH differential method does not provide a complete picture of the quantity and quality of anthocyanins in the extracts of the investigated plant species due to the possible presence of interfering compounds.

Using HPLC-DAD techniques, a comparative analysis of the quantities of anthocyanins in investigated extracts was performed. The phenolic components present in samples were identified by the comparison of the retention times and spectra of the standards for each component. Quantitative determination was performed by the method of the external standard. The following standards were used: delphinidin-3-*O*-glucoside, cyanidin-3-*O*-glucoside, cyanidin-3-*O*-rutinoside, peonidin-3-*O*-glucoside, petunidin-3-*O*-glucoside, petunidin-3-*O*-glucoside acylated, delphinidin-3-*O*-glucoside-*p*-coumaroyl, chlorogenic acid, caffeic acid, quercetin, myricetin. For each standard, the first standard was prepared with the mass concentration 1.0 mg/ml, by dilution in 10 % methanol solution. The calibration curve was constructed on the basis of the obtained areas depending on the mass concentration of the standard. From the obtained equation of linear dependence, the mass concentrations of components were calculated in the samples. For the components without available standards, the quantification was performed on the basis of the calibration curve according to the structure of the corresponding standard. All analyses were performed in triplicates.

Figure 1 shows a chromatogram of 50% ethanol extract of petals of *P. rhoeas* L.

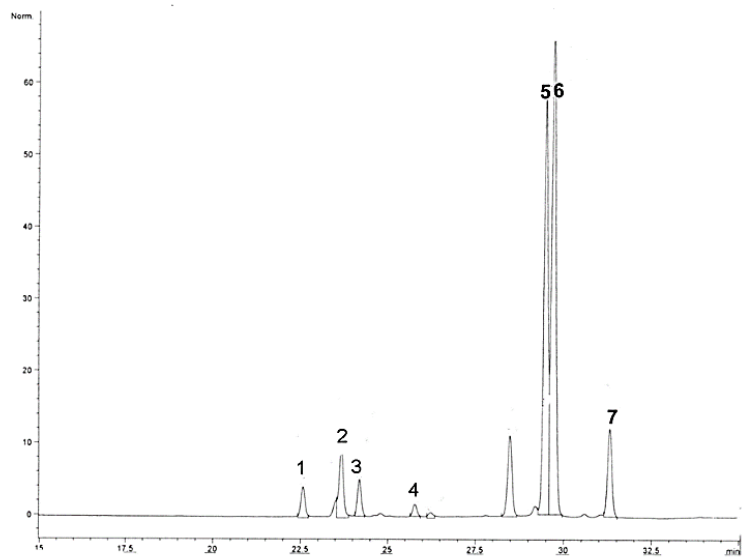

Figure 1. *Anthocyanins content in the ethanol 50% extracts of fresh petals (Papaver rhoeas L.): delphinidin-3-O-glucoside (1), cyanidin-3-O-glucoside (2), cyanidin-3-O-rutinoside (3), peonidin-3-O-glucoside (4), petunidin-3-O-glucoside (5), petunidin-3-O-acetylglucoside (6), delphinidin-3-O-p-coumaroylglucoside (7).*

Seven phenolic compounds were identified as anthocyanins due to the information provided by their UV–Vis spectra. Thus, five glucosylated anthocyanins (λ_{max}= 520 nm) were identified: delphinidin-3-*O*-glucoside, cyanidin-3-*O*-glucoside, cyanidin-3-*O*-rutinoside, petunidin-3-*O*-glucoside, peonidin-3-*O*-glucoside, and acylglucosylated anthocyanins: petunidin-3-*O*-acetylglucoside and delphinidin-3-*O*-*p*-coumaroylglucoside. Structures of identified anthocyanins in extracts of fresh petals of *P. rhoeas* L. are shown in Table 1.

Table 1. Structure of identified anthocyanins in extracts of fresh petal of *P. rhoeas* L.

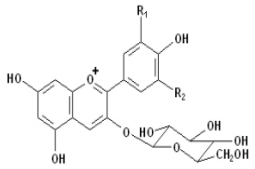	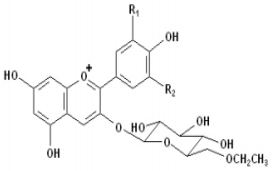	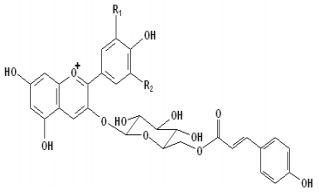
R_1=R_2=OH delphinidin-3-*O*- glucoside	R_1=OCH_3, R_2=OH petunidin-3-*O*-acetyl-glucoside	R_1=R_2=OH delphinidin-3-*O*-*p*-coumarylglucoside
R_1=OH, R_2=H cyanidin-3-*O*- glucoside		
R_1=OCH_3, R_2=OH, petunidin-3-*O*- glucoside		
R_1=OCH_3,R_2=H, peonidin-3-*O*- glucoside		

The content of anthocyanins in different extracts of fresh petals of *P. rhoeas* L. was shown in Table 2.

In investigated extracts of fresh petals of *P. rhoeas* L. plants, glucosides of four anthocyanins were identified: delphinidin, cyanidin, petunidin, peonidin and acyl derivatives of petunidin (petunidin-3-*O*-acetylglucoside) and malvidin (delphinidin-3-*O*-*p*-coumarylglucoside).

Order of anthocyanins by content in methanol extracts and methanol 50%:

Methanol: Ptgl<Dpgl<Cyrut<Cygl<Dpgl-coum<Pngl<Ptgl-ac

Methanol 50%: Ptgl<Dpgl<Cyrut<Cygl<Dpgl-coum<Pngl<Ptgl-ac

The content of polar anthocyanins is larger in extracts of 50% methanol, and less polar anthocyanins in pure methanol.

Order of anthocyanins by content in ethanol extracts and ethanol 50%:

Ethanol: Ptgl-ac<Pngl<Dpgl-coum<Cygl<Cyrut<Dpgl<Ptgl

Ethanol 50%: Ptgl-ac<Pngl<Dpgl-coum<Cygl<Cyrut<Dpgl<Ptgl

Table 2. Content of anthocyanins in the different extracts of fresh petals of *Papaver rhoeas* L.

	Anthocyanins	Methanol mg L^{-1}	Methanol 50% mg L^{-1}	Ethanol mg L^{-1}	Ethanol 50% mg L^{-1}	Water mg L^{-1}
1	Delphinidin-3-*O*-glucoside (Dpgl)	1.96±0.02	2.02±0.02	1.39±0.07	1.44±0.03	1.20±0.02
2	Cyanidin-3-*O*-glucoside (Cygl)	4.45±0.4	4.64±0.04	3.33 ±0.05	3.60±0.04	0.57±0.02
3	Cyanidin-3-*O*-rutinoside (Cyrut)	2.46±0.03	3.30±0.15	2.58±0.06	2.62±0.01	0.34±0.02
4	Petunidin-3-*O*-glucoside (Ptgl)	0.75±0.05	0.95±0.02	0.72±0.02	0.85±0.02	0.56±0.05
5	Peonidin-3-*O*-glucoside (Pngl)	20.50±0.35	18.4±0.40	14.89±0.32	33.26±0.09	0.68±0.03
6	Petunidin-3-*O*-acetylglucoside (Ptgl-ac)	27.80±0.65	19.42±0.30	18.20 ±0.40	15.29±0.70	
7	Delphinidin-3-*O*-*p*-coumaroyl glucoside (Dpgl-coum)	5.56±0.06	4.194±0.02	3.65±0.20	3.22±0.3	-

The content of polar anthocyanins is higher in ethanol of 50%, and the content of less polar anthocyanins is more abundant in pure ethanol.

The smallest content of the anthocyanin is in the water extract of fresh petals. The acyl derivatives are the least polar and not identified in the aqueous extract.

The differences in anthocyanins content depend on the used extraction medium as a consequence of different polarity of used organic solvents and their mixtures [12]. The content of anthocyanins represents the pharmacological characteristic of the plant. Based on numerous studies, it is known that the content of anthocyanins depends on genotype, soil conditions, and the difference in plant ripening [13-15]. Also, outdoor conditions, like altitude, light, temperature, the content of feeding material in the soil might affect phenylpropanoid metabolism [16].

CONCLUSION

The results revealed that the different extracts of fresh petals of *Papaver rhoeas* L. were an excellent source of anthocyanins. The differences in anthocyanins content depend on the used extraction medium as a consequence of different polarity of used organic solvents and their mixtures. The retention times of anthocyanins on the chromatogram are following their polarity; glycosides initially occur, and their acyl derivatives at the end. The highest content of anthocyanins glucosides was determined in methanol and methanol 50% solution, and the smallest in aqueous solution. By comparing the contents of individual anthocyanins, the glycosides (polar) are better extracted with 50% alcohol solution and their acyl derivatives are better extracted with pure alcohol. The water solution is the least suitable for anthocyanin extraction.

This investigation is significant because the anthocyanins and their derivatives are vital herbal pigments and have a significant contribution to the antioxidant, antimicrobial, and other positive effects shown by extracts of *P. rhoeas* L.

EXPERIMENTAL

Preparation of materials

Fresh petals samples of *Papaver rhoeas* L. collected throughout May 2018, were used for the investigation. This region of Serbia (Soko Banja) at the foothills of the Rtanj Mountain is said to be free of harmful environmental influences, as it is mostly devoid of industries and major highways. A voucher specimen 13636 was deposited in the herbarium of the Faculty of Sciences and Mathematics, University of Nis. The plant species were identified by Marija Markovic, Department of Biology, University of Nis.

Preparation of herbal extracts

Fresh petals samples of *Papaver rhoeas* L. were grounded in a blender, and 2 g was extracted by the following solvents: ethanol and ethanol 50%, methanol, and methanol 50% and water.

Extraction was carried out in an ultrasonic bath for 15 min three times in succession with 30 ml of the solvent, respectively. The extract was filtered through a Buchner funnel and filter paper (blue-collar) (CHMLAB, Spain), transferred into a 100 ml flask and made up to mark with the same solvent.

High-performance liquid chromatography (HPLC) analysis

The fruit extracts were analyzed by the direct injection of the extracts, previously filtered through a 0.45 μm pore size membrane filter, into the Agilent Technologies 1200 chromatographic system equipped with the Agilent photodiode array detector (DAD) 1200 with RFID tracking technology for flow cells and a UV lamp, an automatic injector, and Chemstation software. The column was thermostated at 30 °C. After injecting 5 μL of the sample extract, the separation was performed in an Agilent-Eclipse XDB C-18 4.6 mm×150 mm column. Two solvents were used for the gradient elution: A – (H_2O + 5% HCOOH) and B – (80% ACN + 5% HCOOH + H_2O). The used elution program was as follows: from 0 to 28 min, 0.0% B, from 28 to 35 min, 25% B, from 35 to 40 min, 50% B, from 40 to 45 min, 80% B, and finally for the last 10 min again 0% B. The detection wavelengths were 320 and 520 nm. The identification and quantification of individual compounds were performed using calibration curves obtained with standard solutions of pure anthocyanins. The results are expressed as mg L^{-1} of plant extracts.

Statistical analysis

The experimental results were expressed as mean value ± standard error of the mean value of three replicates. In order to estimate statistically any significant differences among mean values, where applicable, the data were subjected to a one-way analysis of variance (ANOVA test) [17].

REFERENCES

1. WHO. *WHO Guidelines on Safety Monitoring of Herbal Medicines in Pharmacovigilance Systems*. Geneva, Switzerland: World Health Organization **2004**.
2. A. Zargari, Medicinal Plants. 6th ed. Tehran University Press; **1995**, pp. 145-150.
3. A. Zargari, Medical Plants, Tehran University, Tehran, **1994**, vol. 1, pp. 91–102.
4. R. Soulimani, C. Younos, S. Jarmouni-Idrissi, D. Bousta, F. Khalouki, A. Laila, *J. Ethnopharmacol.*, **2001**, *74*, 265-274.
5. A. Castañeda-Ovando, M. Pacheco-Hernández, M.E. Páez-Hernández, J.A. Rodríguez, C.A. Galán-Vida, *Food Chem.,* **2009**, *13,* 859-871.
6. L. Ekici, *LWT-Food Sci.Technol.,* **2014**, *56*, 40-48.
7. G. Matysik, M. Benesz, *Chromatographia*, **1991,** *32* (1-2), 19–22.

8. D.A. Kostić, S.S. Mitić, M.N. Mitić, A.R. Zarubica, J.M. Veličković, A.S. Dordević, S.S. Randelović, *J. Med. Plants Res.,* **2010**, *4*, 1727-1732.
9. J.P. Rey, J. Levesque, J.L. Pousset, F. Roblot, *J. Chromatogr. A*, **1992**, *596* (2), 276-280.
10. T. Todorova, M. Pesheva, F. Gregan, S. Chankova, *J. Med. Food*, **2015**, *18*, 460-467.
11. F. Conforti, S. Sosa, M. Marrelli, F. Menichini, G.A. Statti, D. Uzunov, A. Tubaro, F. Menichini, *Food Chem.,* **2009**, *112*, 587 – 594.
12. H. Eng Khoo, A. Azlan, S. Teng Tang, S. Meng Lim, *Food Nutr. Res.,* **2017**, *61*(1), 1361779, DOI:10.1080/16546628.
13. D.D. Orhan, A. Hartevioğlu, E. Küpeli, E. Yesilada, *J. Ethnopharmacol.,* **2007**, *112(2)*, 394-400.
14. N. Gougoulias, N. Mashev, *Oxid. Commun.*, **2015**, *38(1),* 25-34.
15. N. Gougoulias, *Oxid. Commun.,* **2015**, *38*(*1)*, 35-45.
16. R.A. Dixon, N.L. Paiva, *Plant Cell*, **1995,** *7(7),* 1085-1097.
17. Statistical Analysis and Reporting System, ser Guide, Version 1.0, IBM **1999**.